Scuola di Ingegneria Civile e Ambientale
Corso di laurea magistrale in Ingegneria per l'Ambiente e il Territorio
Environmental and Land planning engineering

POLITECNICO
MILANO 1863

ANALYSIS OF SLAKED LIME SPREADING METHODOLOGIES FOR OCEAN ALKALINITY ENHANCEMENT

Supervisor: Prof. Stefano Caserini
Co-supervisor: Ing. Selene Varliero

Candidates:
Elisa Gentile 945720
Fabio Tarantola 944955

Academic Year 2020-2021

TABLE OF CONTENTS

LIST OF FIGURES

LIST OF TABLES

LIST OF SYMBOLS

α	Ratio between mass transfer to the bulk and mass loss of the particle
α_h	Rainbowing spray angle with respect to the water surface
α_l	Rainbowing longitudinal spray angle
α_T	Temperature coefficient of variation
γ_w	Seawater specific weight
γ_i	Ionic-specific activity coefficient
δ	Net CO_2 removed per unit of SL discharged
δ_{th}	Theoretical CO_2 removed per unit of SL discharged
ε	Dielectric constant of water
η	Pump efficiency
η_p	Penalty
θ	Generic angle in Navier-Stokes equations
μ_f	Air viscosity
μ_w	Seawater viscosity
ρ_p	Slaked lime particle density
ρ_s	Slaked lime slurry density
ρ_w	Seawater density
σ_i	Seawater conductivity at temperature i
ϕ	Scalar quantity in the fluid dynamic model
ϕ_0	Diffusion potential
χ_0	Chemical gradient for calcium ions dissolution
ω	Stirrer angular velocity
Ω	Saturation state
A	Total surface of slaked lime particles
A', B'	Temperature-dependent coefficient (Debye-Hückel formula)
a_i, b_i	Ionic-specific fit parameter (Debye-Hückel formula)
A_p	Surface area of each particle
b	Base of the rainbowing imprint area
c_d	Average daily shipping cost
c_e	Energy cost
c_f	Specific fuel price
c_{fuel}	Fuel consumption

c_i	Ionic-specific concentration
$CO_{2,th}$	Theoretical amount of CO_2 removed
$C_{opex,}$	Total Opex
$C_{opex,p}$	Total pumping Opex
$C_{opex,s}$	Total shipping Opex
$c_{SL,max}$	Maximum slaked lime concentration in water
d	Travelled distance
D	Linear dissolution rate of SL particles (Bernard et al. model)
D_f	Seawater calcium ion diffusivity coefficient
d_p	Slaked lime particle diameter
d_R	Vessel diameter
D_ϕ	Generic molecular diffusion coefficient in the fluid dynamic model
e	Eccentricity of the rainbowing imprint area
$E_{A\,i}$	Activation energy of the forward/backward reaction
E_{CO_2}	Total carbon dioxide emissions
E_{LTO}	Total emissions during the LTO cycle
EF_{climb}	Climb phase emission factor
EF_{cruise}	Cruise phase emission factor
$EF_{descent}$	Descent phase emission factor
EF_{HFO}	Heavy fuel oil emission factor
EF_{ship}	Vessel emission factor
f	Practical activity coefficient (Johannsen and Rademacher model)
fCO_2	Carbon dioxide fugacity
f_i	Fraction of the rainbowing discharging area
f_{max}	Fraction of the rainbowing discharging area related to the maximum load
g	Gravitational acceleration
Ga	Galileo number
H	Pump total head
h	Rainbowing arc apex height
$\{i\}$	Ion activity
$[i]$	Ion concentration
I	Ionic strength
k	Constant rate for a generic reaction
K_1^*	First stoichiometric equilibrium constant for carbonic acid dissociation

K_2^* Second stoichiometric equilibrium constant for carbonic acid dissociation

K_B Boltzmann constant

k_b Backward constant rate for slaked lime dissolution

k_d Mass transfer coefficient

k_f Forward constant rate for slaked lime dissolution

K_{H,CO_2} Henry's carbon dioxide constant

K_{SL} Thermodynamic equilibrium constant for slaked lime dissolution

K_w^* Seawater ionic product

l Rainbowing distance

L_i Slaked lime load per unit area

LHV Lower heating value

$\dot{M}$ Total mass transfer

m_d Total dissolved slaked lime mass

M_p Slaked lime molar mass

m_p^0 Slaked lime mass at time 0

m_p Slaked lime mass at time t

M_{SL} Slaked lime total transported mass

$M_{SL,y}$ Yearly slaked lime mass discharged

Mol_d Total moles of dissolved slaked lime

Mol_p^0 Moles of slaked lime at time 0

N Number of rainbowing discharging area fractions

n_0 Initial number of slaked lime particles

P Atmospheric pressure

p Pressure of a generic fluid

pCO_2 Carbon dioxide partial pressure

$P_{eff,disc}$ Effective power of the rainbowing discharging system

$P_{eff,suction}$ Effective power of the rainbowing water suction system

pH Measure of acidity of an aqueous solution

P_p Pumping power

Q_s Slaked lime slurry discharge rate

Q_{SL} Slaked lime discharge rate

Q_w Water discharge rate

q_r Flux of the fluid in the radial direction

q_{z_a} Velocity of the fluid in the axial direction

q_θ	Velocity of the fluid in the tangential direction
R	Gas constant
r	Radius
r_0	Initial slaked lime particle radius
R_d	Net rate of slaked lime particle dissolution (Johannsen and Rademacher model)
Re	Reynolds number
r_p	Slaked lime particle radius
r_r	Generic reaction rate
S	Seawater salinity
Sc	Schmidt number
SI	Saturation index
S_ϕ	Source term in the fluid dynamic model
t	Time/duration
T	Temperature
t_p	Pumping time
U	Solid concentration
u_r	Velocity of the fluid in the radial direction
v	Vessel average speed
V	Sinking particle's total water volume
V_0	Initial slaked lime particle volume
V_L	Volume of the liquid phase
V_N	Sinking particle's water volume for each fraction
V_p	Slaked lime particle volume
v_{TS}	Terminal settling velocity in air/in water
V_{und}	Volume of undissolved slaked lime
z	Sinking depth of rainbowing jet
z_a	Vertical quote
z_i	Ionic-specific charge number
Z_0	Slaked lime dosed concentration

LIST OF CHEMICAL SYMBOLS

$B(OH)_3$	Boric acid
$B(OH)_4^-$	Borate ion, tetrahydroxyborate
Ca^{2+}	Calcium ion
$CaCO_3$	Calcium carbonate
CaO	Calcium oxide, quicklime, burnt lime
$Ca(OH)_2$	Calcium hydroxide, slaked lime, hydrated lime
CH_4	Methane
Cl^-	Chloride ion
CO_2	Carbon dioxide
CO_3^{2-}	Carbonate ion
F^-	Fluoride ion
Fe	Iron
H^+	Hydrogen ion, hydron
H_2	Molecular hydrogen, dihydrogen
HCO_3^-	Bicarbonate, hydrogencarbonate
H_2CO_3	Carbonic acid
H_2O	Water
HPO_4^{2-}	Hydrogen phosphate ion, monohydrogen phosphate
H_3PO_4	Phosphoric acid
$H_2PO_4^-$	Dihydrogen phosphate
HS^-	Bisulfide ion
$H_3SiO_4^-$	Orthosilicic ion
HSO_4^-	Hydrogen sulphate ion
K^+	Potassium ion
Mg^{2+}	Magnesium ion
$MgCO_3$	Magnesium carbonate, magnesite
$Mg(OH)_2$	Magnesium hydroxide, brucite
Mg_2SiO_4	Magnesium orthosilicate, forsterite
Na^+	Sodium ion
$NaCl$	Sodium chloride, table salt
Na_2CO_3	Soda ash, sodium carbonate
NH_3	Ammonia
NH_4^+	Ammonium

N_2O	Nitrous oxide
OH^-	Hydroxyl ion
PO_4^{3-}	Phosphate, orthophosphate ion
SF_6	Sulphur hexafluoride
Si	Silicon
SiO_2	Silicon dioxide, silica
SO_4^{2-}	Sulphate ion

ACRONYMS

ACC Antarctic Circumpolar Current

ACGIH American Conference of Governmental Industrial Hygienists

AEED Aircraft Engine Emissions Databank

AN32 Antonov AN-32P

AR Afforestation and Reforestation

AR5 5th IPCC Assessment Report

AR6 6th IPCC Assessment Report

B737 Boeing 737-700C

BA Borate Alkalinity

BADA Base of Aircraft Data

BECCS Bioenergy with Carbon Capture and Storage

BFC Bromofluorocarbon

CA Carbonate Alkalinity

CCAC Climate and Clean Air Coalition

CCD Climb/Cruise/Descent cycle

CCN Clouds Condensation Nuclei

CCS Carbon Capture and Storage

CCT Cirrus Cloud Thinning

CDR Carbon Dioxide Removal

CFC Chlorofluorocarbons

COP Conference Of the Parties

DACCS Direct Air Carbon Capture and Storage

DIC Dissolved Inorganic Carbon

DWBC Deep Western Boundary Currents

DWCC Deadweight Cargo Capacity

DWT Deadweight Tonnage

ECBM Enhanced Coal Bed Methane

ECMWF European Centre for Medium-Range Weather Forecasts

EDGAR Emission Database for Global Atmospheric Research

EEA European Environment Agency

EF Emission Factor

EMEP European Monitoring and Evaluation Programme

EOR Enhanced Oil Recovery

EW Enhanced Weathering

FAA Federal Aviation Administration

GHG Greenhouse Gas

HFO Heavy Fuel Oil

ICAO International Civil Aviation Organisation

IMO International Maritime Organization

IND Indian Ocean

IPCC Intergovernmental Panel on Climate Change

JRC Joint Research Centre

LC50 Lethal Concentration of half population

LES Large Eddy Simulation

LRIT Long Range Identification and Tracking

LTO Landing to Take-Off cycle

MABL Marine Atmospheric Boundary Layer

MD11 McDonnell Douglas MD-11

NDC Nationally Determined Contribution

NET Negative Emissions Technology

NFPA National Fire Protection Association

NOAEC No Observed Adverse Effect Concentration

OAE Ocean Alkalinity Enhancement

OF Ocean Fertilization

PA Practical Alkalinity

QL Quicklime, Calcium Oxide

RCP Representative Concentration Pathway

SCS Soil Carbon Sequestration

SL Slaked Lime, Calcium Hydroxide

SML Sea Surface Microlayer

SO Southern Ocean

SPNA Subpolar North Atlantic region

SPNP Subpolar North Pacific region

SR15 Special Report on Global Warming 1.5 °C

SST Sea Surface Temperature

STNA Subtropical North Atlantic region

STNP Subtropical North Pacific region

STSA Subtropical South Atlantic region

STSP Subtropical South Pacific region

TA Total Alkalinity

THC Thermohaline Circulation

TSHD Trailing Suction Hopper Dredger

UN United Nations

UNCED United Nations Conference on Environment and Development

UNFCCC United Nations Framework Convention on Climate Change

USDT United States Department of Transportation

WHO World Health Organization

WMO World Meteorological Organization

ABSTRACT

To limit global warming within the limit defined in the Paris Agreement, there is the need to remove huge quantity of CO_2 from the atmosphere by the implementation of the Negative Emission Technologies to remain below 1.5 °C from the Preindustrial Level. Among the various strategies, there is a solution that prevents both global warming and ocean acidification: the so-called Ocean Alkalinity Enhancement. This technology is based on atmospheric CO_2 sequestration by the addition of alkaline materials into seawater (slaked lime, SL).

The first part of the thesis is focused on the assessment of the discharging's configurations with the implementation of different discharging scenarios in ships' wake, through "rainbowing" and by aircraft. However, their viability depends on many variables, such as fleet size and characteristics needed (i.e.: load capacity, discharge rate). These assessments address the mitigation potential, costs, logistics, as well as the concentrations of SL in seawater or the temporary increase in pH that could have harmful effects on the marine ecosystem.

The various analyses examining each OAE discharging option show a higher CO_2 removal efficiency in the scenarios with SL discharge from ships and rainbowing. They have a penalty (CO_2 emitted during spreading / CO_2 removed) varying between 1-4 % and costs between € 6-9 per ton of CO_2 removed; aircraft, depending on the scenario, have a penalty varying between 28-77 % and costs between € 30-1846 per ton of CO_2 removed. It is clear that aircraft have huge limitations due to significant fuel consumption, which implies large economic drawbacks.

In the second part of the thesis, a chemical-fluid dynamic modelling analysis is carried out to evaluate the dissolution rate of SL in seawater, a key parameter for its diffusion in ship's wake. The evaluation shows how the coupling of the unloading in the ships' wake and the use of rainbowing systems can allow widening the sea area affected by the unloading, reducing the SL load per surface unit and therefore the potential impacts.

SOMMARIO

Per limitare il riscaldamento globale entro i limiti definiti dall'Accordo di Parigi è necessario rimuovere ingenti quantità di CO_2 dall'atmosfera grazie all'adozione di tecnologie per le emissioni negative; fra queste l'alcalinizzazione artificiale degli oceani permette contemporaneamente il sequestro chimico della CO_2 e il contrasto dell'acidificazione degli oceani, mediante lo spargimento di materiali alcalini, come l'idrossido di calcio (slaked lime, SL).

La prima parte della tesi è incentrata sulla valutazione di diverse configurazioni di spargimento di SL, considerando diversi scenari di scarico nelle scie delle navi, tramite "rainbowing" e per mezzo di aerei. La fattibilità di queste diverse configurazioni dipende da molte variabili, come il numero di aerei o di navi e le loro caratteristiche (i.e.: capacità di carico, rateo di scarico). Sono stati valutati il potenziale di mitigazione, i costi, la logistica dello spargimento, nonché le concentrazioni di SL nell'acqua di mare o l'aumento temporaneo del pH che potrebbe avere effetti nocivi sull'ecosistema marino.

Le analisi effettuate hanno mostrato una maggiore efficienza sia in termini di rimozione di CO_2 sia economici negli scenari di scarico nella scia delle navi e con il rainbowing. Queste metodologie hanno una penalità (CO_2 emessa nello spargimento/CO_2 rimossa) variabile tra l'1-4 % e costi variabili tra 6-9 € per ton di CO_2 rimossa; gli aerei, in funzione degli scenari, hanno una penalità variabile tra il 28-77% e costi tra € 30-€ 1846 per ton di CO_2 rimossa. Lo scarico tramite aerei mostra quindi molte limitazioni, soprattutto a causa dell'ingente consumo di carburante che ha notevoli riflessi anche sui costi.

Nella seconda parte è stata effettuata un'analisi modellistica chimico-fluidodinamica finalizzata a valutare la velocità di dissoluzione di SL in acqua di mare, parametro chiave per la diffusione di SL nella scia di una nave. Dalle valutazioni condotte emerge come l'accoppiamento dello scarico nella scia di una nave e dell'uso di sistemi di rainbowing può permettere di ampliare l'area di mare interessata dallo scarico, riducendo il carico per unità di superficie e quindi i potenziali impatti.

1. INTRODUCTION

Since the era of Industrial Revolution in 1750 human activities (like fossil fuel burning for energy production, deforestation, and agriculture) emitted tremendous quantity of greenhouse gases (GHGs) into the atmosphere, including more than 2,400 Gt of carbon dioxide (CO_2), warming the planet, and causing consequential deleterious impacts like climate change (IPCC, 2021). While emissions from fossil fuels started before the Industrial Era, they became the dominant source of anthropogenic emissions to the atmosphere from around 1950 and their concentration has continued to rise (Friedlingstein et al., 2020).

Its main future impacts are global surface temperature rise, more intense storms and weather extremes, more often heat waves, glacial retreat and sea ice loss, sea-level rise with vigorously impacts on biodiversity, human health and natural resources. In particular, the World Health Organization (WHO) defined climate change as the greatest threat to global health in the 21st century (WHO, 2015). Climate change causal chain is explained in Figure 1.1.

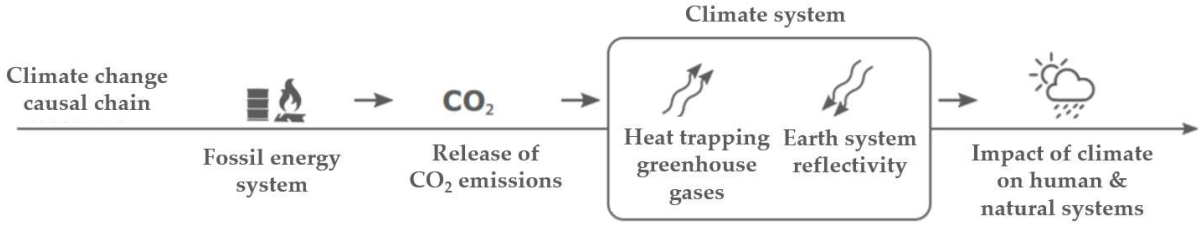

Figure 1.1: Causal chain of the climate change problem (Minx et al., 2018).

It is worth noting that the oceans absorbed about a third of emitted CO_2 (Watson et al., 2021) mainly due to chemical and biological processes, inducing ecophysiological effects and threatening vital ecosystem services, and causing the deleterious effect commonly known as ocean acidification (Riebesell and Gattuso, 2015; Gao et al., 2020). Moreover, it has been estimated that the shift in ocean pH due to uptake of anthropogenic CO_2, since the pre-industrial period is unprecedented in the last 65 million of years (Diffenbaugh and Field, 2013).

The 2015 Paris Agreement aims to limit global temperature well below 2 °C above pre-industrial levels. The Intergovernmental Panel on Climate Change (IPCC) stated that alongside the reduction in GHGs emissions, other mitigation strategies are necessary; the drawdown of large quantities of CO_2 needs to be implemented through upscaling of Carbon Dioxide Removal (CDR) techniques, also called Negative Emissions Technologies (NETs), removing about 10-20 GtCO_2 yr^{-1} by 2100 (IPCC, 2018).

Among these, the so-called Ocean Alkalinity Enhancement (OAE) method plays an important role. It consists in discharging alkaline substances into the ocean, in order to promote atmospheric CO_2 sink into the ocean, and secondly to increase seawater pH.

The expected result of this thesis is a feasibility analysis of different methodologies for the discharge of slaked lime (SL) for OAE. This study analyses pros and cons of each option with the ambition to understand which is the best suitable technology between the available

portfolio, without neglecting the economic viewpoint. Nowadays, many researchers and scientists evaluated the dispersion of alkaline slurry in the wake of ships (Renforth et al., 2013; Caserini et al., 2021; Mongin et al., 2021). Moreover, a new kind of marine vessels for SL shedding is investigated, the so-called rainbowing method. In addition, given the success achieved in the past with the liming lakes with aircraft, the latter were also considered for the discharge on larger area like oceans. Finally, it is also on-topic to assess the SL dissolution dynamic in seawater, and then evaluating the pH change due to the release of OH^- ions that could give side effects on the marine ecosystem in a short time scale.

1.1 GREENHOUSE EFFECT AND CLIMATE CHANGE

Excessive human activities since the Industrial Revolution caused an uncontrolled rising of GHGs concentration in the atmosphere, breaking its frail energy balance leading temperatures to rise indiscriminately.

In addition to CO_2, other relevant GHGs are methane (CH_4), sulphur hexafluoride (SF_6), nitrous oxide (N_2O), chlorofluorocarbons (CFCs) and bromofluorocarbons (BFCs). In particular, CO_2 emissions come mostly from coal- and gas-fired power stations, motorized vehicles (cars, trucks, and aircraft), and industrial operations (i.e.: smelting, manufacture of cement). CH_4 emissions come from the production of fossil fuels (escape from coal mining and from gas and oil production and processing), livestock farming (mostly beef), landfills, wastewater, and wetland rice farming. Agricultural activities are the main cause of N_2O emissions, but also industrial activities, combustion of fossil fuel, and wastewater management play an important role. Finally, CFCs and HCFs are gases used in refrigeration, air-conditioning and foam applications (EPA, 2021). Certain chemicals within HCFs class of compounds are acceptable alternatives to CFCs and HCFCs on a long-term basis; because the HFCs contain no chlorine they do not directly affect stratospheric ozone (NOAA, 2021).

It is worth noting that GHGs have a strong effect on the energy budget of the Earth system, even though they constitute only a small fraction of all atmospheric gases. These gases lead to an amplification of the natural greenhouse effect, which itself would allow the Earth's system to maintain an average surface temperature of about 15 °C, ideal for the development of life as we know it, by the absorption of infrared radiation emitted from Earth's surface and reradiating it back to Earth's surface.

The effect of each GHG depends on its capacity for absorbing infrared radiations that is linked to its chemical nature, to the size of the increase in atmospheric concentration, and its residence time in the atmosphere once emitted. Some GHGs have long atmospheric residence times, and consequently they are well-mixed throughout the atmosphere. In particular, gas lifetime can be defined as the ratio between the total amount of the gas in the atmosphere and its removal rate. It is worth noting that, due to the different rates of uptake by different removal processes no single lifetime can be defined for CO_2; some CO_2 is absorbed very quickly, while some remain in the atmosphere for thousands of years (IPCC, 2001). This necessitates complex modelling of the decay curve; because such decay curve depends on the

model used and the assumptions incorporated therein, it is difficult to specify an exact atmospheric lifetime for CO_2.

Pre-industrial and current concentrations, and atmospheric lifetime for the major GHGs considered are reported in Table 1.1, while the related trends are shown in Figure 1.2.

Table 1.1: Pre-industrial and current concentrations measured at Mauna Loa Observatory, and atmospheric lifetime of the major GHGs (concentrations data from NOAA, 2021; atmospheric lifetime data from CDIAC, 2016).

GHG	Pre-industrial concentration	Concentration in 2021	Concentration increase	Atmospheric lifetime
CO_2	280 ppm	417 ppm	49 %	-
CH_4	700 ppb	1,895 ppb	171 %	12 yr
N_2O	270 ppb	335 ppb	24 %	114 yr
SF_6	~ 0	11 ppt	-	3,200 yr
CFC-11	~ 0	223 ppt	-	45 yr
CFC-12	~ 0	494 ppt	-	100 yr

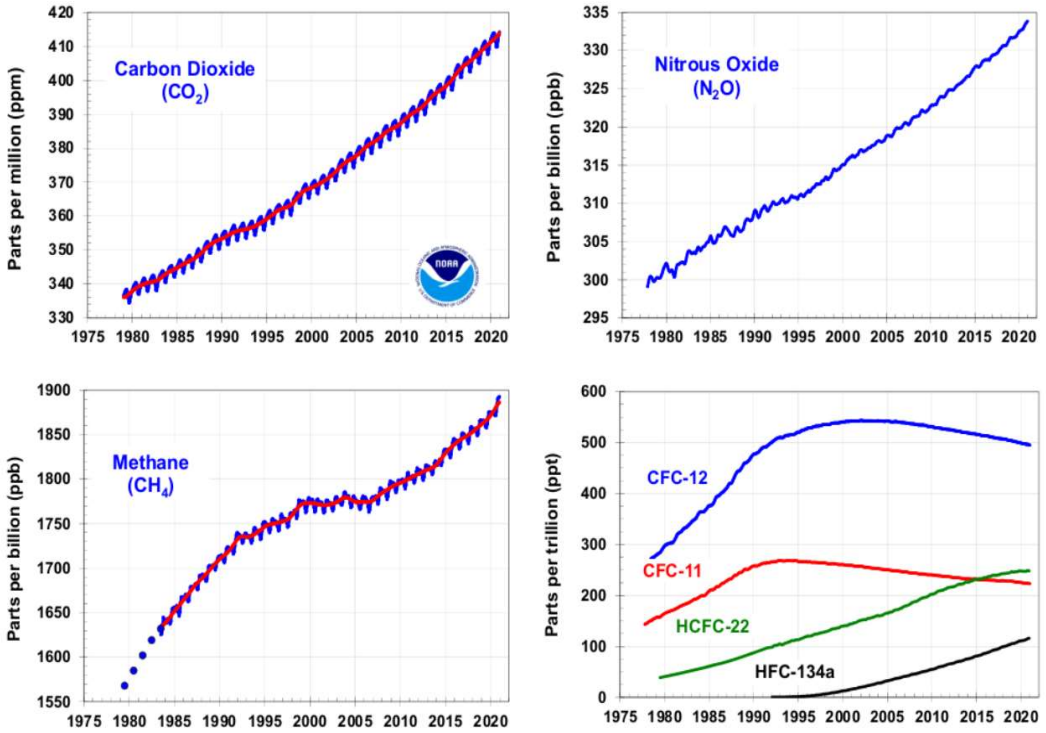

Figure 1.2: Global average abundances of the major GHGs: carbon dioxide, methane, nitrous oxide, and different CFCs and HFCs from the NOAA global air sampling network since the beginning of 1979 until 2020 (NOAA, 2021).

The biggest anthropogenic contributor to global warming is CO_2, which accounts for 56% of positive forcing in the period 1750-2018; CH_4 accounts for 32%, and the halocarbon gases and N_2O account for 6% each (Earle, 2019).

It is worth noting that, while in general GHGs concentrations are increasing in the atmosphere, the concentration of CFCs is instead decreasing in the last 20 years, as can be seen in Figure 1.3 (NOAA, 2021). That is due to the Montreal Protocol, an international treaty signed in 1987, designed to protect the ozone layer. Such a treaty forced to phase out the

production of numerous substances responsible for ozone depletion, including a wide range of CFCs (UN, 1987).

To basically understand how our climate may change in future, the IPCC adopted the Representative Concentration Pathways (RCPs). These graphs describe different climate futures, depending on the GHGs quantity emitted in the years to come, ranging from very high (RCP8.5) through to very low (RCP2.6) future concentrations, as shown in Figure 1.3. The numerical values of the RCPs (2.6, 4.5, 6.0 and 8.5) indicate the radiative forcing, in terms of W m^{-2}, that the Earth surface will reach in 2100. According to the worst scenario (the so-called business-as-usual scenario or RCP8.5, which assumes that normal circumstances can be expected to continue unchanged so there will not be no significant change in people's attitudes and priorities, or no major changes in technology, or policies) carbon emissions might lead to atmospheric CO_2 levels of ~2000 ppm by year 2300 (IPCC, 2021).

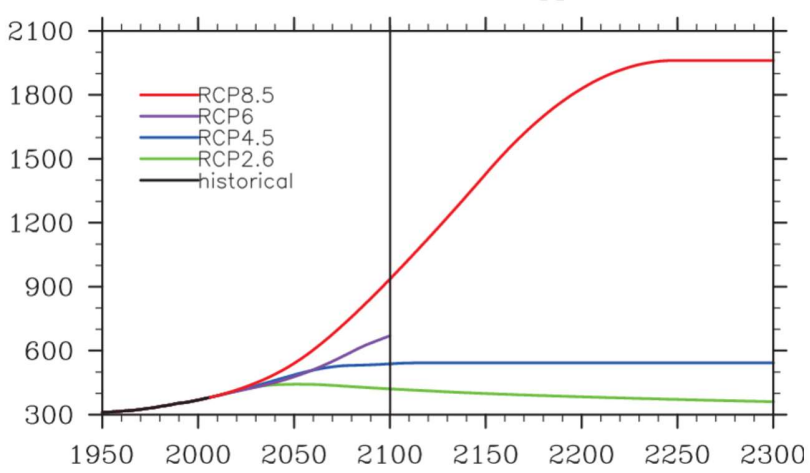

Figure 1.3: Time series of CO_2 concentration, in terms of ppm, under different RCP scenarios (Xin et al., 2013).

1.2 INTERNATIONAL TREATIES AND PANELS

Since humanity stated out the climate change problem in the XX century, the United Nations (UN) began to define a series of panels and international agreements in order to fight against this global climatic issue and to find mitigation strategies.

One of the first actions to be made was the establishment of the IPCC in 1988. IPCC is a UN intergovernmental body that aims to improve the knowledge concerning human-induced climate change, founded with the World Meteorological Organization (WMO). Such panel, headquartered in Geneva, Switzerland, includes 195 member states. It does not conduct original research but provides a systematic review of all the published studies, discussing natural, political, and economic impacts related to such a global issue. Scientists and experts review the available data, realizing the so-called "Assessment Reports", aiming to inform policymakers and even the general public in a scientific and most comprehensive way. Each report is made up of three different volumes, that are related to three working groups dealing with distinct topics (physical and scientific basis, socio-economic and natural systems vulnerability, and mitigation).

A few years after the IPCC foundation, at the United Nations Conference on Environment and Development (UNCED) held in Rio de Janeiro in 1992, 154 states signed the United Nations Framework Convention on Climate Change (UNFCCC). It is an international treaty aiming to combat human interference with the climate system. Currently, UNFCCC has 197 signatory Parties, that meet periodically in the so-called Conference of the Parties (COP) dealing with climate change. The first of these conferences, the COP1, was held in Berlin in 1995, while the COP3 led to the adoption of the Kyoto Protocol in 1997; this last treaty was the first implementation of measures under the UNFCCC. Presently, the last conference is the 26th COP (COP26), held in Glasgow in 2021.

1.2.1 PARIS AGREEMENT

In order to address climate change and its negative impacts, the 21st UNFCCC COP in Paris (COP21) developed the Paris Agreement in December 2015. It is the first universal and legally binding treaty on climate change, and entered into force on 4th November 2016, following the fulfilment of the condition of ratification by at least 55 countries representing at least 55% of global GHGs emissions.

In particular, Article 2 sets a limit on the global average temperature: "*the increase in the global average temperature to well below 2 °C above pre-industrial levels and to pursue efforts to limit the temperature increase to 1.5 °C above pre-industrial levels"* (UNFCCC, 2015).

A mitigation target is also needed: countries aim to reach the global emission peak as soon as possible and to achieve rapid emission reductions. In this regard, the signatory countries have to submit their national contributions for climate action every 5 years through plans, called Nationally Determined Contributions (NDCs). Figure 1.4 represents future scenarios after the Paris Agreement NDCs, before COP26 was held.

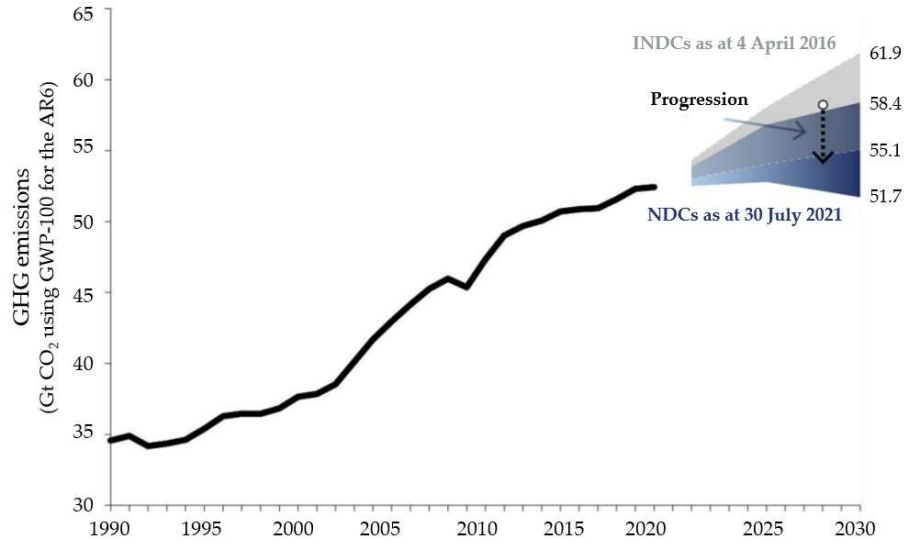

Figure 1.4: Projected ranges cover the higher-emission end for unconditional elements of NDCs to the lower-emission end when also taking conditional elements of NDCs into account (UNFCCC, 2021).

These lately submitted NDCs, before the 26th COP in Glasgow, would lead to a temperature increase of 2.7 °C by 2100. Such value does not respect the target set up by the Paris Agreement, but it is a significant improvement if compared to the business-as-usual scenario.

UNFCCC recognizes that the Parties have a different responsibility and not the same capability to reduce GHGs emissions in a short time. In this regard, the emissions peaking should be delayed for developing country Parties, achieving later an equilibrium between emissions and carbon removals. The Paris Agreement acknowledges that the reduction of emissions is not a sufficient tool against climate change. In fact, all the Parties should "*take action to conserve and enhance, as appropriate, sinks and reservoirs of greenhouse gases, including forests*". As a result, UNFCCC stated out the importance of natural carbon sinks and artificial carbon removal technologies.

Furthermore, UNFCCC claims the usefulness of voluntary cooperation among Parties, aiming at the realization of more ambitious mitigation plans. These collaborations should be engaged respecting a set of principles, including development sustainability, environmental integrity, and transparency. From this point of view, the Paris Agreement recommends developed country Parties to sustain developing countries also financially, supporting them in elaborating ambitious and functional policies for a climate-resilient future.

In addition to emissions reduction and improvement of removal sinks, the Article 7 asserts the importance of adaptation, "*enhancing adaptive capacity, strengthening resilience and reducing vulnerability to climate change, with a view to contributing to sustainable development and ensuring an adequate adaptation response*". Adaptation has a key role in the global response to climate change, in order to protect people, livelihoods, and ecosystems. Adaptation, as well as mitigation, should be guided by the best available science and technologies, without neglecting traditional and local knowledge in a sustainable and efficient developing system suitable for each specific country.

1.2.2 GLASGOW CLIMATE PACT

As mentioned in the previous section, COP26 is currently the last UNFCCC conference held; hosted in the city of Glasgow, Scotland, from 31st October to 13th November 2021, it has been delayed for a year due to the COVID-19 global pandemic. Actually, it was the third meeting of the Parties to the Paris Agreement and the 16th meeting of the Parties to the Kyoto Protocol. COP26 was the first conference since 2015 COP21 that expected Parties to make enhanced commitments in mitigating climate change; it should have been held exactly 5 years later COP21, that's the time range that Parties should await between different submissions of national pledges. The result of this 26th conference was the Glasgow Climate Pact, negotiated by the representatives of the 197 attending Parties.

The Glasgow Climate Pact reaffirmed the Paris Agreement 1.5°C warming limit, in fact COP26 "*recognizes that limiting global warming to 1.5 °C requires rapid, deep and sustained reductions in global greenhouse gas emissions, including reducing global carbon dioxide emissions by 45% by 2030 relative to the 2010 level and to net zero around mid-century, as well as deep reductions in other greenhouse gases*" (UNFCCC, 2021). Before the Paris Agreement was struck, the world was on

a 4 °C warming trajectory by 2100, significantly higher than the subsequently stated 1.5 °C limit. Currently, by the end of COP26 in Glasgow, 151 countries have submitted their climate plans, most of them already updated; these plans should put the world on track for about 2.5 °C warming by the end of the century, examining the 2030 targets. Such NDCs show an improvement, but the situation is still extremely critical, and the actual plans are not sufficient, as shown in Figure 1.5, which demonstrates that no countries have actually submitted sufficiently challenging pledges.

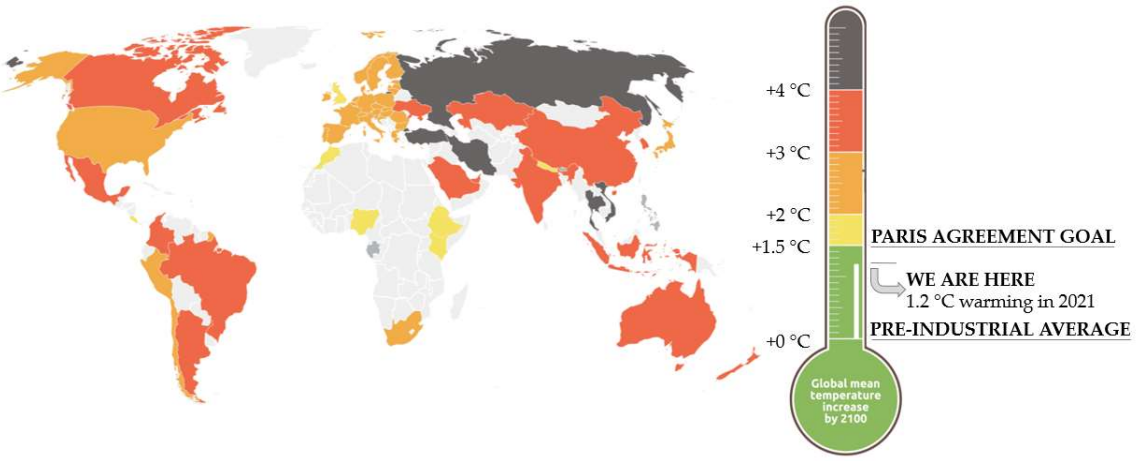

Figure 1.5: Global map showing how much global warming is each country's pledge leading to after Glasgow's NDCs (Climate Action Tracker, 2021).

Nevertheless, considering countries' commitments to achieving net-zero emissions by around 2050, analysis shows that the temperature rise could stay below approximately 2.1 °C, while extremely optimistic studies assess a value of 1.8 or 1.9 °C: however, many major emitters' 2030 targets are so weak, without offering convincing pathways to reach net-zero targets (Mountford et al., 2021). These results are though similar, or even lower, to the 2 °C minimum target by the end of the century, showing goodwill from a large part of the Parties. Furthermore, many countries have not yet submitted their pledges to achieve net-zero emissions by half of the century. The Glasgow Climate Pact recommended signatory Parties to revisit and strengthen their 2030 targets by the end of 2022 to align them with the COP21 temperature goals: 2050 net-zero and 2030 targets could be achieved only following a revising of the submitted NDCs. Moreover, COP26 stated out that carbon budgets assessed in the Paris Agreement are presently small and being rapidly depleted.

The COP26 emphasizes the necessity to "*phase down unabated coal*" and "*phase-out fossil fuel subsidies*". A group of 46 countries made pledges to phase out domestic coal, while other 29 countries committed to ending new direct international public support for unabated fossil fuels by the end of 2022. Some countries haven't shown the willingness to phase-out coal usage, but they have still declared the necessity of a phase-down of such a resource. This agreement is the first-ever climate deal to explicitly outline the requirement to reduce unabated coal power. Parties are indeed urged to accelerate the development, deployment, and dissemination of technologies to transition towards low-emission energy systems. The importance of rapidly scaling up the deployment of clean power generation has been pointed out (UNFCCC, 2021).

In addition to CO_2 emissions, Parties discussed even methane emissions. More than 100 countries have voluntarily signed the Global Methane Pledge: a global reduction target that declares the intent to reduce methane emissions by at least 30% from 2020 levels by 2030. According to signatory countries, the Global Methane Pledge would reduce global warming by at least 0.2 °C by 2050. Moreover, the Global Methane Assessment from the Climate and Clean Air Coalition (CCAC) examine that realizing this target would prevent over 200,000 deaths and many related diseases (European Commission, 2021).

Furthermore, COP26 stated the importance of nature for reducing emissions and building resilience to the climate change impacts. More than 100 countries (including around 85% of the world's forests) have committed to reversing deforestation: one of the crucial points of the COP26 has been the announcement of the Glasgow Leaders' Declaration on Forests and Land Use (UNFCCC, 2021), in which many countries pledged to end forest loss and land degradation by 2030. Countries agreed to "*halt and reverse forest loss and land degradation by 2030 while delivering sustainable development and promoting an inclusive rural transformation*", but without specifying the concrete measures that will be engaged. Ending deforestation by 2030 within all signatory countries would avoid the emission of around 18.9 GtCO_2 (Taylor et al., 2021).

Moreover, UNFCCC declared that developed countries failed the goal of mobilizing an amount of $100 billion yr^{-1} to support climate efforts in developing countries in 2020; the Parties so agreed to a robust process to develop a new finance goal to go into effect after 2025. Countries also agreed to improve the funding in adaptation, which currently amounts to only a quarter of total climate finance. Wealthy country Parties are recommended by the 18th article of the Glasgow Climate Pact to *"at least double their collective provision of climate finance for adaptation to developing country Parties from 2019 levels by 2025"* (UNFCCC, 2021).

Another COP26 key point was the so-called "Loss and Damage". Climate change is already causing losses of lives, land, and livelihoods; many of these damages are permanent. Various climate-vulnerable countries asked for a new finance facility dedicated to such an issue. A new loss and damage fund has been established, and Scotland became its first contributor. Although the progress in COP26, what has been done is largely insufficient; however, it offers space to develop concrete solutions, and it will be one of the bigger issues leading up to the COP27 summit in Egypt in 2022 (Mountford et al., 2021).

1.2.3 LONDON CONVENTION AND PROTOCOL

Since OAE aims to discharge a huge quantity of alkaline materials in the oceans, it is also fundamental to analyse the current legislation about the disposal of substances into the marine environment.

In the 1950s-1970s many countries became aware of the environmental impacts of human activities on the marine environment, mainly due to the uncontrolled disposal of wastes into the oceans. At this purpose, in 1972 the Inter-Governmental Conference on the Convention on the Dumping of Wastes at Sea adopted the Convention on the Prevention of Marine Pollution by Dumping of Wastes and Other Matter, also known as London Convention. It is one of the

first global conventions that provides frameworks for protecting marine environment from human activities; it contributes to the international control and prevention of marine environment pollution by prohibiting the deliberate disposal at sea of hazardous materials (i.e.: wastes) from vessels, aircraft, and platforms (ECOLEX, 1972). It entered into force from 1975 and starting from 1977 it has been administered by the International Maritime Organization (IMO). Nowadays, there are 87 countries that are Parties to this Convention (IMO, 2021).

In 1996, the Parties decided to modernize and eventually replace the London Convention toward a new, free-standing treaty, the so-called London Protocol, that entered into force in 2006 and it is currently signed by 53 different Parties (ECOLEX, 1996). This Protocol represents a major change of approach for regulating the use of the sea as a depository for waste materials, it prohibits dumping of all wastes, except for possibly acceptable ones listed in Annex I, the so-called reverse list:

- dredged material;
- sewage sludge;
- fish waste, or material resulting from industrial fish processing;
- inert/inorganic geological material;
- organic material of natural origin;
- carbon dioxide streams for capture processes for sequestration in sub-seabed geological formations.

Other types of waste are regulated in the "black and grey list", dealing with wastes whose disposal could be allowed according to their environmental hazard. Grey-listed materials dumping necessitates a special permit from the national; on the other hand, the disposal of waste from the so-called blacklist is always forbidden. Since waste dumping is a critical issue about marine pollution, the Protocol makes no distinction concerning the different possible discharging methodologies; moreover, the sea discharge is considered the same as the disposal at the bottom of the sea or the marine underground.

A precautionary approach is the base of the London Protocol: it claims that preventive measures are fundamental when wastes or other matter introduced into the marine environment are likely harmful, even if there is no conclusive evidence about it. The Protocol's purpose is similar to the Convention's, but it is more restrictive.

Recently, the contracting Parties to that Protocol have taken steps about climate mitigation, while ensuring that new technologies aiming to engineer the climate are properly controlled and regulated. The regulatory instruments used have been the most advanced addressing carbon capture and sequestration in sub-sea geological formations, and others climate engineering such as ocean fertilization (IMO, 2006).

In addition to the waste dumping at sea, the London Protocol deals even with other issues. In more details, it forbids:

- the perforation of vessels, aircraft, platforms, or other marine artificial infrastructures aiming to sink them;

- to abandon or overturn marine platforms with the only aim to eliminate them;
- the waste incineration overseas and oceans.

1.2.4 IPCC: THE 6TH ASSESSMENT REPORT ON CLIMATE CHANGE

The 6th Assessment Report (AR6), published by the IPCC in 2021, describes how men and their activities caused unequivocally the CO_2 increase in the atmosphere from 1750, reaching the current atmospheric CO_2 concentration of about 417 ppm. Compared to 1850, the global average temperature increase appears to be between 0.8 and 1.3 °C, with a best estimate of 1.07 °C (IPCC, 2021): the harmful temperature trend to the present day is reported in Figure 1.6, while Figure 1.7 shows possible future scenarios.

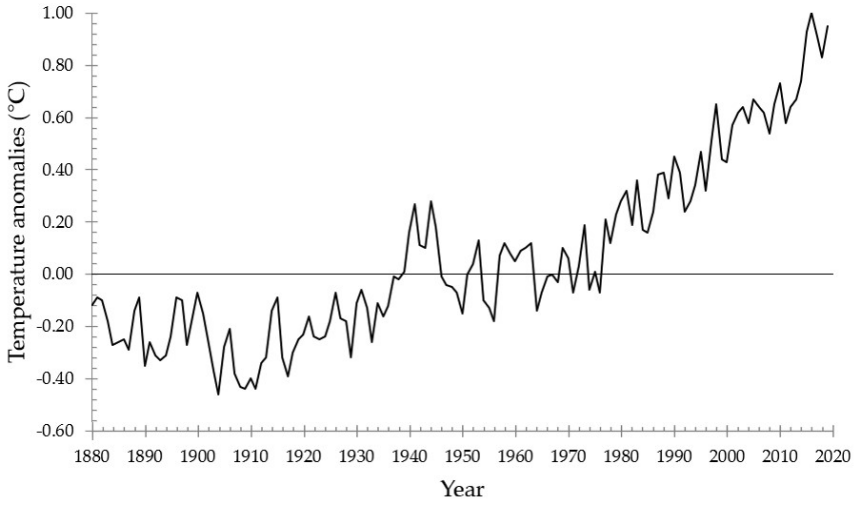

Figure 1.6: Change in global surface temperature, global temperature anomalies referred to the global average temperature in the period from 1901 to 2000 (reworked from NOAA, 2021).

In this report, the IPCC stated that even assuming the most aggressive emissions reduction scenario (RCP2.6), the surface temperature will continue to increase until at least 50 years. The esteemed warming rate is unprecedented in at least the last two millennia (Ming et al., 2021).

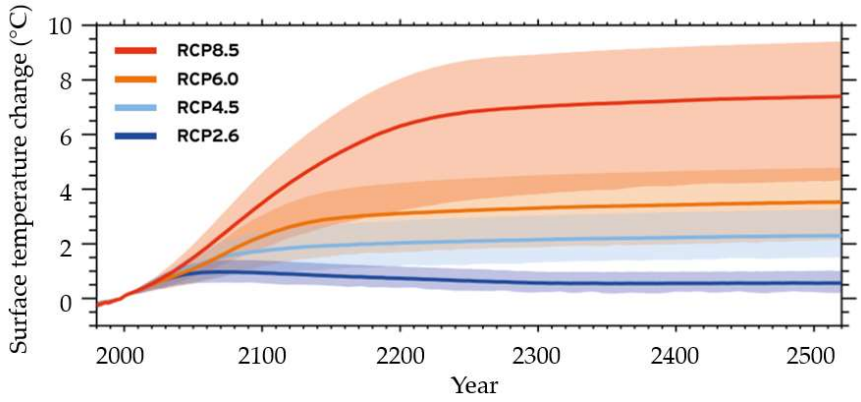

Figure 1.7: Projected global mean surface temperature change for the four RCPs (IPCC, 2014).

The temperature increase is the cause of many deleterious mechanisms, such as ice coverage loss and sea-level rise. The AR6, asserted that the September Arctic Sea ice area has decreased by 40% in the 2010-2019 period compared to 1979-1988 (while this value is 10% in March).

Humans are also responsible for the decrease in Northern Hemisphere spring snow cover since 1950, and for the observed surface melting of the Greenland Ice Sheet in the last 20 years. Ice melting and thermal expansions of the oceans are the issues implied in the observed sea-level increase; the global mean sea level appears to be raised by about 0.20 m between 1901 and 2018. The current increasing rate is the astonishing value of 3.7 mm yr^{-1}. Even the most optimistic IPCC scenario predicts the mean sea level to increase by 0.28 to 0.55 m by 2100. Also, the ice coverage loss has other harmful effects. For instance, permafrost melting releases gaseous compounds such as methane, which is an intense GHG.

AR6 shows more confidence in the human influence about the increased frequency of extreme weather events, if compared to the 5th Assessment Report (AR5) published by IPCC in 2013. Heatwaves, heavy precipitation, droughts, and tropical cyclones have been more frequent and severe since the 1950s in almost every region across the globe. Differently from hot extremes, the cold ones (such as cold waves) are becoming less frequent and less severe.

For limiting climate change and its consequences it is crucial to limit the use of carbon and it is also important to implement technologies to limit the impact of carbon use on the atmospheric CO_2 concentration even if using fossil fuel (i.e.: carbon capture and storage) and also technology for CO_2 removal (Renforth and Henderson, 2017). According to IPCC (2021), there is still time to avoid the most deleterious results of climate change, but it is important to operate in the shortest possible period. However, the effects of reducing emissions and carbon removal would be felt within decades.

Since artificial activities have emitted around 2,400 GtCO_2 in the atmosphere, IPCC (2021) asserted that to have a 50% chance of staying below the Paris Agreement 1.5 °C warming limit, humans can emit a maximum of 500 GtCO_2 from 2020 (the so-called carbon budget). In fact, each 1,000 Gt of emitted CO_2 is responsible for a temperature increase that ranges between 0.27 and 0.63 °C, with a best estimate of 0.45 °C, following a near-linear relationship between cumulative CO_2 emissions and the related global warming.

1.3 CARBON DIOXIDE REMOVAL TECHNOLOGIES

Article 4.1 of Paris Agreement states that *"counties must reach peak emissions as soon as possible so as to achieve a balance between anthropogenic emissions by sources and removals by sinks of GHG in the second half of this century"* (UNFCCC, 2015). As a result of the COP26 in Glasgow, over 140 countries pledged to reach net-zero carbon emissions during the century. Since many countries decided to achieve the net-zero emissions goal by 2050, some of the largest emitters set a later target. For instance, China had committed to net-zero carbon emissions by 2060, while India established the latest target data planning, setting such a goal in 2070.

In particular, IPCC stated "*CDR approaches could be used to compensate for residual emissions from sectors that are difficult or costly to decarbonize. CDR could also be implemented at a large scale to generate global net negative CO_2 emissions (i.e.: anthropogenic CO_2 removals exceeding anthropogenic emissions), which could compensate for earlier emissions as a way to meet long-term climate stabilization goals after a temperature overshoot*" (IPCC, 2021). At this purpose, CDR technologies play an outstanding role in both limiting global warming and climate change mitigation, and

over years climate policies integrated them. Rather than using only one technology it is always recommended to use a different portfolio of CDR techniques.

According to the SR15, the "Special Report on Global Warming 1.5 °C" (IPCC, 2018), it is indeed fundamental to develop on a large scale the CDR technologies to stay below a 1.5 °C increase. Even in the best future scenario, considering a global emission peak in 2020 and a subsequent very rapid decrease, it is essential to remove from the atmosphere more than 100 GtCO_2 by the end of the XXI century. This amount achieves the huge value of 1,000 GtCO_2 in the worst scenarios (without neglecting mitigation from all economic sectors). Evaluations and estimates about the necessary CO_2 removal rate are various, and Figure 1.8 graphically shows them: a minimum of few GtCO_2 yr^{-1} until 2050, up to a maximum of 10-20 GtCO_2 yr^{-1} by the end of the century.

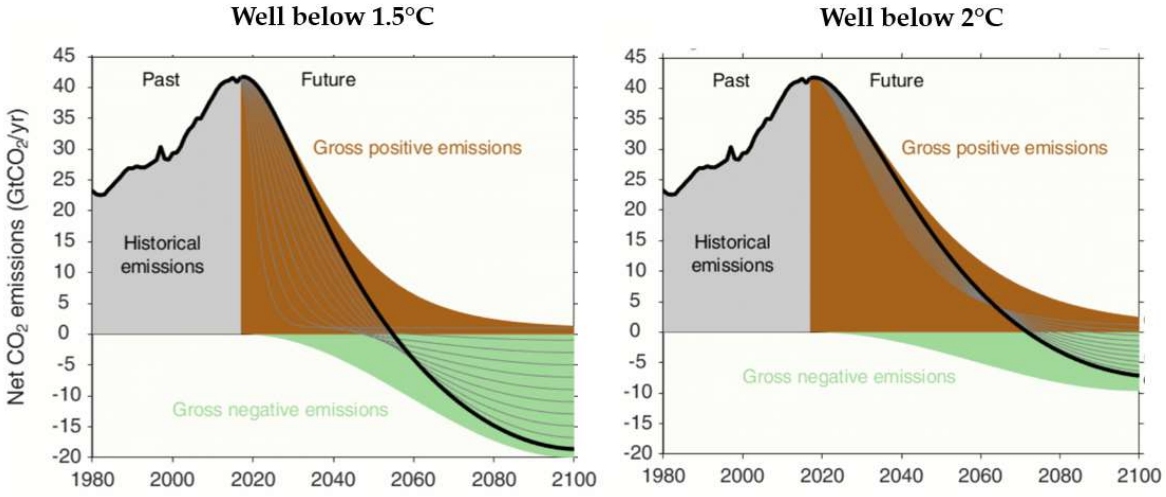

Figure 1.8: Pathways of global net anthropogenic CO_2 emissions limiting global warming well below 1.5°C or below 2°C (Peters, 2018).

Their main aim is removing anthropogenic CO_2 from the atmosphere, through photosynthesis or chemical processes and storing it in a permanent way (i.e.: geological sequestration, carbon mineralization). The CDR portfolio includes: afforestation and reforestation (AR), biochar, soil carbon sequestration (SCS), bioenergy with carbon capture and storage (BECCS), direct air carbon capture and storage (DACCS), enhanced weathering (EW), ocean fertilization (OF), ocean alkalinity enhancement (OAE), and seaweed cultivation (EASAC, 2018; Gao et al., 2022). These solutions can be divided into three main categories: nature-based solutions, measures that aim to enhance natural processes, and technology-based solutions.

Nature-based solutions incorporate AR, involving the repurposing of land use by growing forests where there was none before (afforestation) or re-establishing a forest where there was one in the past (reforestation).

Enhanced natural processes include land management approaches to increase the carbon content in soil. This can incorporate the addition of biochar (charcoal obtained from the pyrolysis of biomass) to soils, where the carbon can remain stored for hundreds or thousands of years. EW permits the acceleration of the natural processes that absorb CO_2 by adding

mineral silicate rocks powder to soils. In OF nutrients are added to the ocean to increase its biological capacity to absorb CO_2.

Technology-based solutions, like BECCS and DACCS, permit the CO_2 capture directly from the atmosphere. Both of these solutions rely on geological storage of CO_2 for large-scale carbon removal. Another solution could be OAE, by spreading alkaline materials into oceans and seas.

One postulated CDR technology is Ocean Alkalinity Enhancement (OAE). In 1995, Kheshgi developed the idea of discharging alkaline materials, like calcium carbonate ($CaCO_3$) or calcium hydroxide ($Ca(OH)_2$), into mixed-layer seawater allowing CO_2 removal from the atmosphere via chemical sequestration, according to the simplified scheme in Figure 1.9 (Kheshgi, 1995; Renforth and Henderson, 2017; Moras et al., 2021). Its main aim is to enhance a natural process that would require tens of thousands of years. Additionally, researchers consider OAE one of the CDR technologies with the highest potential since modelling suggests that between 264 and 790 GtCO_2 could be removed by 2100 (Feng et al., 2017).

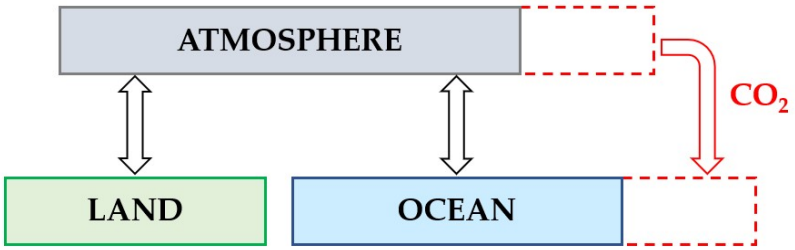

Figure 1.9: Scheme of the Ocean Alkalinity Enhancement process.

Furthermore, this practice also allows increasing ocean alkalinity, ameliorating the effects of seawater acidification, which poses a serious threat to marine life (Hoegh-Guldberg et al., 2007). By the way, the addition of alkaline materials into the seawater causes localised and elevated pH level around the point of addition; sustained elevated pH will be detrimental to some organisms so this aspect should be better investigated. Moreover, it could result in carbonate precipitation which would lower the effectiveness of OAE. In past times, between 1989 and 1990, this technology allowed the recovery by liming of a small lake in Italy, Orta Lake (Calderoni et al., 1994) and many lakes and watersheds in Sweden, Norway, Canada, and in the USA (Olem, 1991).

On the other hand, CDR technologies have many drawbacks, implications and issues of scale that in-depth studies should better investigate; in particular, large-scale deployment will indeed have non-trivial impacts on water use, land footprints and nutrient use (Smith et al., 2016). The development potential of these technologies on a large scale depends on a lot of factors: the geophysical capacity of the global system to allow such growth, the environmental possibility to supply the needed natural resources, the ability of such technologies to rise and diffuse in short periods, the economic and financial availability, the presence of social and cultural implications on human behaviour, risks management and the capability of governments to rule that technologies' evolution (Honnegger et al., 2020). Nowadays, CDR

utilization is inadequate, many of them are still in the research and development stage; their cost is elevated and not yet easily affordable.

1.4 OCEANS AND CARBON CYCLE

Oceans play a key role in climate change mitigation, covering about 70% of the Earth's surface with an average depth of 3,800 m. In the last 50 years, oceans stored the 93% of the energy surplus from global warming; without this kind of natural mitigation, global temperature increase would be much more intense. Furthermore, they can absorb a large part of CO_2 in the atmosphere, thanks to gaseous exchange with the water surface. According to the IPCC "Special Report on the oceans and cryosphere in a changing climate" (IPCC, 2019), oceans serve as an important sink of CO_2 emitted to the atmosphere, absorbing about 30% of the entire emitted CO_2 in the last 40 years. In more detail, it absorbed about 7 GtCO_2 yr^{-1} over the 20 years from 1980 to 2000, with ocean uptake over the past 200 years estimated to be more than 500 GtCO_2 (IPCC, 2005).

It is worth noting that ocean's capacity to absorb increasing amounts of anthropogenic CO_2 is not uniformly distributed worldwide: this suggests that there is a contribution of different underlying mechanisms in different regions. In particular, cold seawater can store more dissolved CO_2 than warm water, that is because gas solubility decreases as temperature increases (Diamond and Akinfiev, 2003). Takahashi et al. (2009) estimated the annual average air-sea CO_2 fluxes, displayed in Figure 1.10: cold waters (i.e.: poleward-moving western boundary currents) tend to take up carbon, and waters that are upwelling and warming (i.e.: coastal zones and the tropics) tend to emit carbon.

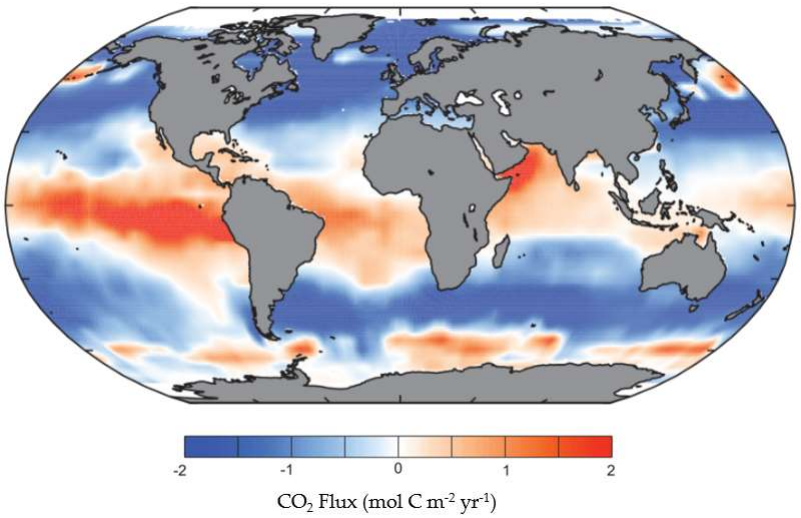

Figure 1.10: Global annual average air-sea CO_2 fluxes, in terms of molC m^{-2} yr^{-1}. The positive fluxes represent the exchange from ocean to atmosphere, while the negative ones are from the atmosphere to the ocean (McKinley Ocean Carbon Group, 2021).

Increasing CO_2 emissions from human activities are causing ocean warming, acidification and oxygen loss with severe changes in nutrient cycling and primary production, posing a serious threat to marine life and causing relevant impacts on economies and societies.

Gaseous CO_2 tends to reach equilibrium between oceans' surface and the atmosphere, transferring in the dissolved phase according to the well-known Henry's law (1.1).

$$[CO_{2(aq)}] = K_{H,CO_2}\, fCO_2 \tag{1.1}$$

The equilibrium concentration of dissolved CO_2 in water (or a general gaseous component), $[CO_{2(aq)}]$, is equal to its fugacity (fCO_2) multiplied by Henry's constant (K_{H,CO_2}), which is the solubility coefficient of CO_2 in seawater. Fugacity is an effective partial pressure, closely related to thermodynamic activity: for a general purpose, it is very similar to partial pressure. This last parameter is proportional to the gaseous mole fraction, and it is a portion of the total pressure in the atmosphere.

However, the time needed to reach this equilibrium is very large, because of the huge volume of the oceans; furthermore, a lot of chemical reactions happen subsequently, delaying this equilibration. CO_2 reacts with water molecules during the so-called CO_2 hydration (reaction (1.2)), leading to the formation of carbonic acid (H_2CO_3, a weak acid), which dissociates in bicarbonate (HCO_3^-) and H^+ ions (reaction (1.3)); bicarbonate ions are so in equilibrium with carbonate ions (CO_3^{2-}). This sequence of reactions takes place in less than one minute (Zeebe et al., 1999). The consequent H^+ molecules can so easily react with carbonate ions already present in water, becoming again bicarbonates (reaction (1.4)). Carbon is so partitioned in water in the form of different species, which are in equilibrium: this balance is strictly related to the water pH, temperature T, practical salinity S, and pressure.

$$CO_2 + H_2O \rightleftarrows H_2CO_3 \tag{1.2}$$

$$H_2CO_3 \rightleftarrows H^+ + HCO_3^- \tag{1.3}$$

$$H^+ + CO_3^{2-} \rightleftarrows HCO_3^- \tag{1.4}$$

The equilibrium constants of the described carbonate system are related to the standard free energy of the reactions. A variation of temperature or pressure leads to a change in energy, and hence of the thermodynamic equilibrium constants. Reactions (1.3) and (1.4) show why such constants depend on the pH, while the effect of salinity is not so immediate; Figure 1.11 explains graphically how these dependencies act on equilibrium constants. The reason for the salinity dependence is that equilibrium constants are generally calculated as stoichiometric and not entirely thermodynamic. The cause is that such constants are generally obtained through the usage of the concentration of chemical species and not their activity, because this value is not easily measurable. The activity of an ion is a sort of effective concentration, better describing the behaviour of ions in a solution, but very similar to the concentration value; in general, it depends on long-range electrostatic interactions between the ions, and ion-pairing and complex formation. It is roughly considered as the fraction of the total concentration that participates in the reactions (Langmuir, 1997). As a result, ions' activity is smaller than the correspondent concentration. To calculate the ion-specific activity, the knowledge of the activity coefficient is fundamental. The ion activity coefficient, generally denoted as γ_i, is a value that correlates ions' concentration $[i]$ to their activity $\{i\}$ (equation (1.5)): in a theoretical infinite diluted solution, this coefficient is equal to 1.

$$\{i\} = \gamma_i\, [i] \tag{1.5}$$

Stoichiometric constants are denoted by K^*, while K expresses thermodynamic constants. Usually, equilibrium constants are described with pK^* value instead of K^*, which is the negative common logarithm of the equilibrium constant (equation (1.6)).

$$pK^* = -log_{10}(K^*) \tag{1.6}$$

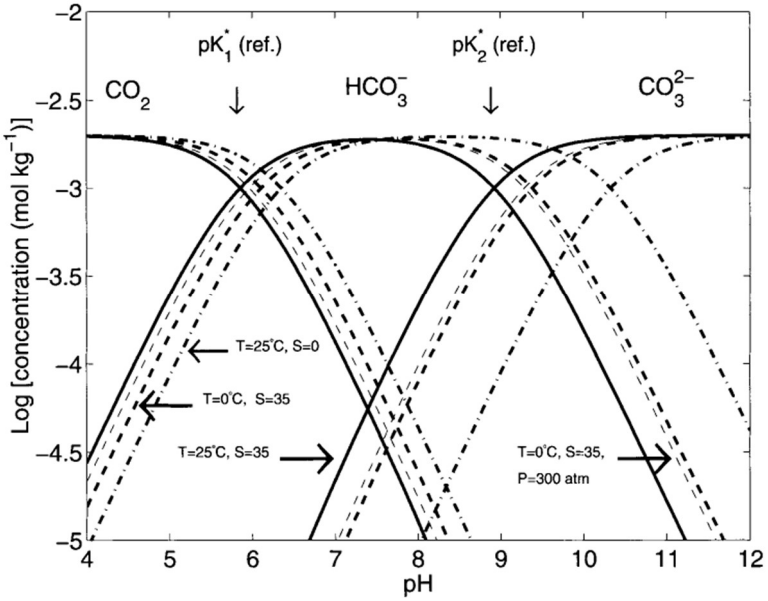

Figure 1.11: pK values of CO_2, HCO_3^-, and CO_3^{2-} depending on the pH level. Different curves refer to different conditions of temperature and water salinity (g kg^{-1}), (Zeebe and Wolf-Gladrow, 2003).*

The pH of the oceans has a strong effect on the CO_2 partial pressure (pCO_2), which drives the dissolved inorganic carbon (DIC) concentration in seawater; DIC is considered as the sum of dissolved CO_2, HCO_3^- and CO_3^{2-} (equation (1.7)), (Zeebe and Wolf-Gladrow, 2003). The sum of the two neutral forms (aqueous CO_2 and H_2CO_3, which are chemically inseparable) is usually denoted by CO_2.

$$DIC = [CO_2] + [HCO_3^-] + [CO_3^{2-}] \tag{1.7}$$

The importance of the oceans in the global carbon cycle is clear because seawater masses contain about 38,000 Gt of carbon, 45 times more than the atmosphere, especially in the form of bicarbonate ions (Sabine and Tanhua, 2010).

While CO_2 is a dissolved species and can evaporate, bicarbonates and carbonates are ions, and so they can't be in the gaseous phase. As a result, carbon is stored as bicarbonate ions: therefore, the oceans can stock more CO_2 compared to what they would absorb in a simple equilibrium with the atmosphere.

Thanks to the reactions described above, CO_2 dissolves in seawater and then mineralizes slowly, thanks to the presence of calcium or magnesium carbonate minerals in the ocean. These carbonates dissociate in calcium and carbonate ions, leading to the formation of carbonate anions (reaction (1.8)). The formation and dissolution of $CaCO_3$ in the oceans is strictly related to the control of atmospheric CO_2 on various time scales.

$$CaCO_3 \rightleftarrows Ca^{2+} + CO_3^{2-} \tag{1.8}$$

Calcium carbonate is a particular salt because its solubility increases at lower temperatures. However, this effect is small: predominant is instead the fact that solubility increases with pressure. The peculiarity of calcium carbonate in seawater is its great abundance in terms of concentration. For this reason, oceans are generally supersaturated concerning such a chemical, and it could stay in the form of marine sediments for a long time. Nevertheless, the supersaturation decreases with depth because $CaCO_3$ solubility increases. With the word lysocline, is named the depth at which the dissolution rate of $CaCO_3$ increases dramatically because of the pressure effect, separating poorly preserved and well-preserved calcium carbonate assemblages (Zeebe and Wolf-Gladrow, 2003).

Carbonates could derive from the dissolution of carbonate rocks in the deep oceans, but also living microorganisms could produce them. Furthermore, the weathering of silicate rocks on the Earth's surface, reacting with CO_2 and forming carbonate rocks (reaction (1.9)), leads to the presence of carbonates on the surface, then transported by the rivers into the oceans.

$$CaSiO_3 + CO_2 \rightleftarrows CaCO_3 + SiO_2 \tag{1.9}$$

Weathering is a naturally slow phenomenon (because of strong bonding in such materials), but temperature, runoff, available surface area, and biological activity (West et al., 2015; Cockell, 2011) accelerate it. The weathering rate of CO_2 removal is estimated at about 0.25 GtC yr^{-1}. This process is generally in balance with volcanic emissions.

A different process involving CO_2 is the direct reaction with solid carbonates ($CaCO_3$), (reaction (1.10)); the dissolution of carbonate rocks on the ocean's floor is a natural mechanism removing CO_2 from the ocean (and from the atmosphere consequently), but it lasts thousands of years.

$$CO_2 + H_2O + CaCO_3 \rightleftarrows Ca^{2+} + 2HCO_3^- \tag{1.10}$$

A sum-up of the global carbon cycle is shown in Figure 1.12, where all carbon fluxes are indicated with their estimated quantitative value in terms of mass.

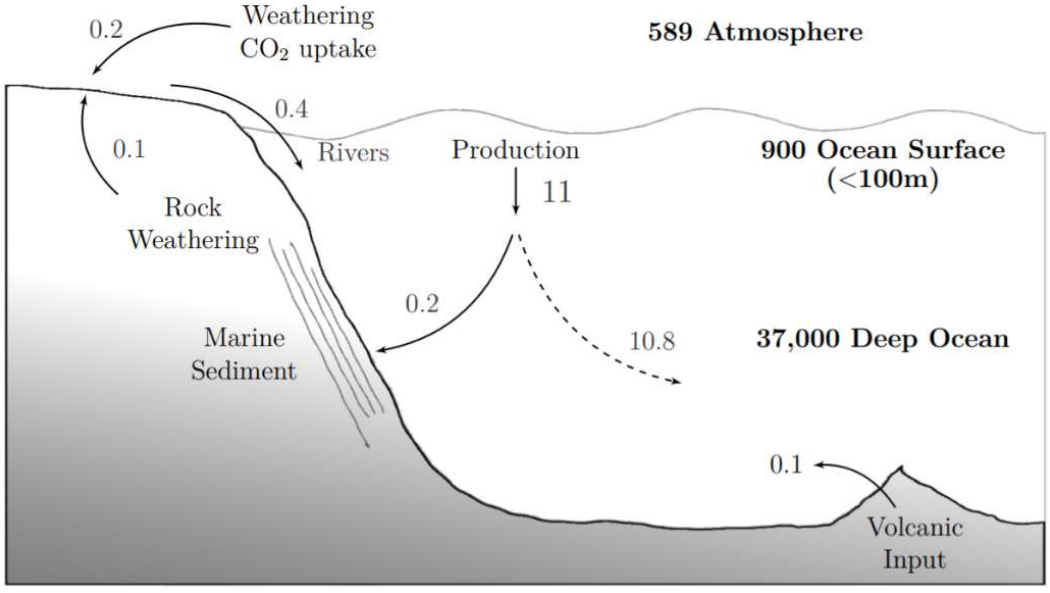

Figure 1.12: Scheme of the global carbon cycle; fluxes are expressed in GtC yr^{-1} (Renforth and Henderson, 2017).

As mentioned before, other natural processes reducing the CO_2 in the atmosphere are removals by biological mechanisms. The so-called "biological pump" has two main drivers: the first consists in the formation of photosynthetic organic matter consuming CO_2, the latter involves calcification processes thanks to microorganisms such coccolithophorids or foraminifera. Organic matter production from oceanic photosynthesis leads to the consumption of CO_2 in the surface layers: this carbonic matter is then transported at major depths after the organisms' death, during a process called "soft tissue pump". Even the formation of calcium carbonates by living microorganisms takes place in the higher depths, and then they sink to the ocean's floor; this mechanism is known as "carbonate pump": coccolithophorids and foraminifera produce calcium carbonates in the form of calcitic and aragonitic shells and skeletons (Marinov et al., 2008). Then coral reefs are responsible for up the 50% of the global $CaCO_3$ production, although they occupy a small portion of the ocean (Mackenzie and Andersson, 2013).

Marine plants and animals have hence the ability to precipitate $CaCO_3$: this is possible assimilating C and removing Ca^{2+} from the ocean. A consequence is the reduction of the surface alkalinity, better described in Chapter 2.1. However, in deep water there is remineralization of organic carbon, causing a pH decrease; the dissolution of $CaCO_3$, enhanced in lower temperature and higher pressure, compensates this phenomenon (as a result, it increases in deep water).

The removal of CO_2 by the natural processes is too slow if compared to the release of CO_2 from human activities, causing an unbalance affecting the global climate. Therefore, anthropogenic CO_2 accumulation in the atmosphere is the latter mechanism ruling the global carbon cycle, and its effect is one of the most relevant in the global equilibrium system.

2. OCEAN ALKALINITY ENHANCEMENT

The OAE has complex chemistry dynamics, so this chapter aims to investigate all the chemical reactions taking place in the ocean surface during SL discharging, also evaluating the effect on the natural carbon cycle and investigating the OAE efficiency. Moreover, a brief focus explored the consequences of seawater acidification on the marine ecosystems.

Additionally, a description of the SL characteristics is necessary, focusing on its production and distribution methods and on the necessity to store the huge amount of CO_2 emitted during its production process. After all, a further analysis examined the main side issues of this technology, both on biology and humans, to better understand its viability.

2.1 OCEAN ACIDIFICATION AND ALKALINITY

Reactions (1.2) and (1.3) show that the presence of dissolved CO_2 in seawater increases the concentration of H^+ ions. This fact would naturally reduce the pH of the oceans, leading to the effect known as acidification, as can be seen from equation (2.1).

$$pH = -log_{10}[H^+] \tag{2.1}$$

It is worth noting that $[H^+]$ represents not only the concentration of free hydrogen ions, but mainly a group of hydrate complexes associated with H_3O^+ and $H_9O_4^+$. In fact, free hydrogen ions don't exist in any significant amount in natural water. More accurate definitions of pH should consider H^+ ion activity instead of its concentration, but these parameters are very similar in natural water ranges.

In a naturally balanced process, the carbonate system described in Chapter 1.3 would buffer this surplus of acidity (Zeebe and Wolf-Gladrow, 2003). The capacity of a water body to counteract the pH oscillations is known as alkalinity, and it is closely related to the presence of carbonates, which buffer the acidity increase by reacting with H^+ and forming bicarbonates.

Alkalinity is a fundamental concept in describing the seawater carbonate system. Despite its importance, it is a complex issue, subject to many discussions and not always well understood: alkalinity is *"one of the most central but perhaps not the best understood concept in aquatic chemistry"* (Morel and Hering, 1993). For these reasons, scientific literature offers many different alkalinity definitions, more or less similar to each other. The proposed study examines deeply a couple of alkalinity definitions, the ones accurately described by Zeebe and Wolf-Gladrow (2003).

Dickson (1981) provided the current definition of alkalinity: *"The total alkalinity of a natural water is thus defined as the number of moles of hydrogen ion equivalent to the excess of proton acceptors in one kg of sample"*. Furthermore, Zeebe and Wolf-Gladrow (2003) stated that "*alkalinity keeps track of the charges of the ions of weak acids*". Total alkalinity is a conservative quantity such as DIC. If it is expressed in mol kg^{-1}, alkalinity doesn't change alongside variations of temperature and pressure. This parameter is historically measured in terms of acid added to a solution neutralizing it, and this is the operational definition of total alkalinity; due to this calculating process, TA is also called "titration alkalinity".

While total alkalinity (TA) depends on a lot of different ions in seawater, the practical alkalinity (PA) is defined as the sum of carbonate alkalinity (CA), borate alkalinity (BA), and water alkalinity (equation (2.2)). At natural seawater pH, usually above 8, PA describes the system alkalinity with a very good approximation. In more detail, BA is the concentration of borate ions ($B(OH)_4^-$) while water alkalinity is equal to the concentration of OH^- minus the H^+ ions. The concentration of species with a double negative charge is counted twice, because of their valence.

$$PA = [HCO_3^-] + 2[CO_3^{2-}] + [B(OH)_4^-] + [OH^-] - [H^+] \tag{2.2}$$

CA is of major interest in the present study, since it is the sum of bicarbonate and carbonate ions (equation (2.3)): it measures indeed the charge concentration of the anions of the carbonic acid.

$$CA = [HCO_3^-] + 2[CO_3^{2-}] \tag{2.3}$$

The PA evaluation does not consider many anions in natural seawater because of their minor concentration. However, some of these anions have a role in determining TA: phosphates (PO_4^{3-}) and hydrogen phosphates (HPO_4^{2-}), orthosilicic ions ($H_3SiO_4^-$), bisulfides (HS^-), and hydrogen sulphates (HSO_4^-). Furthermore, even ammonia (NH_3), hydrofluoric acid (HF), and phosphoric acid (H_3PO_4) have a role in the TA evaluation in seawater. The presence of these last three uncharged species in TA definition is counterintuitive, but it is related to the so-called proton condition, which is a mass balance for hydrogen ions. The proton condition determines which species are proton donors and acceptors in a specific acid-base system (Zeebe and Wolf-Gladrow, 2003). Indeed, phosphoric acid and hydrofluoric acid become proton donors when converted respectively in dihydrogen phosphate ($H_2PO_4^-$) and fluoride ion (F^-), while ammonia becomes a proton acceptor if converted in ammonium ion (NH_4^+).

Alkalinity can be furthermore defined as the difference between conservative cations (Na^+, Mg^{2+}, Ca^{2+}, K^+) and anions (Cl^-, SO_4^{2-}) in seawater; the sum of CA and $[B(OH)_4^-]$ balances the small excess charge of conservative cations over anions, the principle of electroneutrality is therefore applied, as can be seen in Figure 2.1. The result of this charge imbalance is a buffered system. Adding a strong base in a sample, TA increases, because the corresponding cation concentration becomes higher. Drever (1982) defines as conservative such ions whose concentrations are unaffected by changes in pH, pressure, or temperature.

Since the sum of CA and BA is almost equal to the practical alkalinity, the difference between the conservative ions is basically the same value of PA. As a result, the investigated definitions provide approximately the same results in terms of alkalinity.

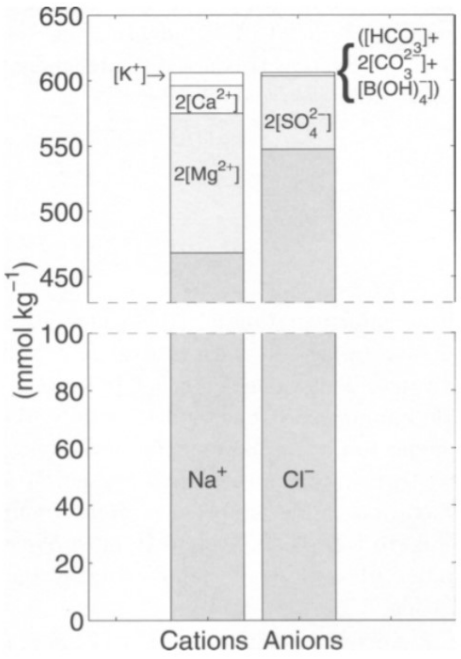

Figure 2.1: Charge balance of the major ions in seawater. Carbonate and borate alkalinity offset the charge excess of conservative cations over anions (Zeebe and Wolf-Gladrow, 2003).

It can also be deduced that alkalinity is the excess of bases (proton acceptors) over acids (proton donors) in seawater: as alkalinity increases, more carbonic acid tends to dissociate, and a larger amount of carbon is drawn into the oceans. The carbonate ions availability is indeed the limiting factor of the ocean buffer capacity against climate change.

2.1.1 ACIDIFICATION IMPACTS ON OCEAN BIOLOGY

Anthropogenic CO_2 concentrations in the atmosphere have increased too rapidly, and the oceans' alkalinity has not completely buffered this increase; as a result, the acidification of the oceans is occurring. According to the AR6, the ocean's pH is decreased from an average value of 8.12 in 1950 to the current value of about 8.05: such shift is unprecedented in the last 65 million years (Diffenbaugh and Field, 2013).

Another drop of 0.3–0.4 units by 2100 has been predicted (Feely et al., 2004). It is worth noting that a 0.1 pH units change, since it is a logarithmic scale, represents roughly a 30% increase in acidity (NOAA, 2020). An example is reported in Figure 2.2, that represents seawater pH variation at a global scale between almost three centuries, from the 1700s and the 1900s.

In SR15, IPCC stated that "*The level of ocean acidification due to increasing CO_2 concentrations associated with global warming of 1.5 °C is projected to amplify the adverse effects of warming, and even further at 2 °C, impacting the growth, development, calcification, survival, and thus abundance of a broad range of species, for example, from algae to fish (high confidence)*" (IPCC, 2018). For these reasons, ocean acidification is often referred to as the "evil twin" of climate change (Cooke and Kim, 2018).

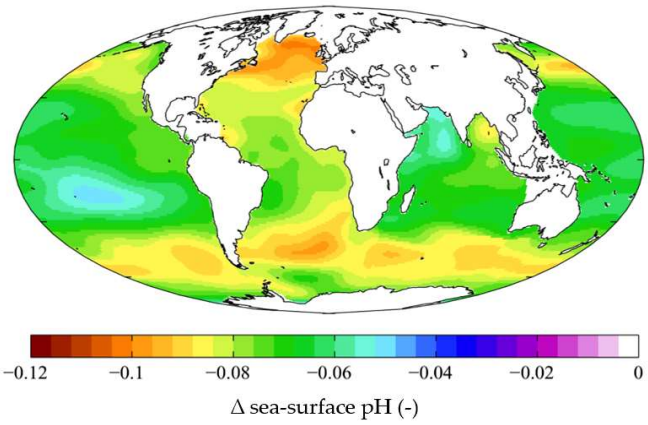

Figure 2.2: Estimated change in annual mean sea surface pH between the pre-industrial period (1700s) and 1990s (Pinnegard et al., 2012).

One of the main consequences of water acidification is the limitation of the formation of calcium carbonate, the main constituent of the exoskeletons and the shells of many organisms (such as corals, oysters, plankton, and also calcifying micro-organisms); global warming amplifies considerably that problem: varying the temperature of the system results in a change of the thermodynamic equilibrium constant, thus having implications for the carbonate formations. As a result, calcifying organisms can hardly build and maintain their shells and skeletons, because of the lack of available calcium carbonate ions in seawater. If the pH gets too low, such biological calcium carbonate structures can even begin to dissolve (NOAA, 2020). Studies carried out on *Thecosomata*, a taxonomic suborder of small pelagic swimming sea snails (the so-called "sea butterflies"), show that if they are placed in seawater with the pH and carbonate levels projected for the year 2100, the shells dissolve after only 45 days (Bednaršek et al., 2012).

Additionally, ocean acidification improves coral mortalities, whose ecosystems are already endangered because of the well-known coral bleaching effect, determining coral reefs' disruption. The coral bleaching problem is mainly linked to the ocean temperature increase, causing the death of such marine organisms: excessive warm water breaks down the symbiotic relationship between corals and the microscopic algae (*zooxanthellae*) living their tissues, forcing corals to expel these algae (Jokiel and Coles, 1990). After corals expelled most zooxanthellae, the underlying white calcium carbonate coral skeleton becomes visible through the transparent coral tissue: this phenomenon is known as bleaching (Liu et al., 2018). However, a bleached coral is not dead, but it is more stressed and subjected to increased mortality (Hussain and Ingole, 2020); bleached corals suffer starvation and a larger number of diseases: if temperatures stay too warm for a prolonged time, corals could easily die. Furthermore, their reproduction rate decreases, and even their growth is reduced; this latter aspect is probably due to the minor energy supply, previously provided by the algae. A temperature increase of only 1-2°C can induce mass bleaching events (Marshall and Schuttenberg, 2006).

Coral bleaching is one of the most relevant deleterious aspects of global warming: the increase in sea surface temperature (SST) during the past few decades has caused unprecedented mass

bleaching worldwide, including the three major episodes in 1998, 2010 and 2015/16 (Heron et al., 2016; Hussain and Ingole, 2020). In more details, in 2016 the Great Barrier Reef proportion experiencing extreme bleaching was over four times higher compared to 1998 or 2002. In such a year, bleaching killed 30-50% of Great Barrier Reef corals (Hughes et al., 2017). Moreover, in 1998, 80% of the Indian Ocean's reefs were bleached, and subsequently, 20% died (Knowlton and Cairns, 2018).

Oceans' acidification, related to the increasing CO_2 emissions, is another issue linked to climate change that improves the coral reefs' disruption. As acidified waters drop down calcium carbonate levels, existing coral structures start to dissolve away. This dissolution includes corals' skeletons and even the sediment platforms which form the bulk of the reefs. At current rates of acidification, seawaters are expected to reach a tipping point in 2080, at which reefs will start to dissolve faster they can build up. As a result, coral reefs will completely disappear (Harvey, 2018).

It is worth noting that some coral species are more resilient than others, and impacts vary between regions, but the deterioration due to climate change is currently inevitable, with severe consequences for other marine and coastal ecosystems, like loss of coastal protection for many islands and loss of biodiversity. Redistribution of marine species due to direct and indirect effects of climate change may also disrupt existing marine resource sharing and governance (Pinsky et al., 2018). Other marine problems linked to acidification are reproductive and metabolic fish diseases, and it causes the killing of food for animals at the higher end of the food chain. Studies demonstrated that the ability of some fish to detect predators decreases in more acidic waters, while certain larval fishes become less able to locate suitable habitats (Simpson et al., 2011). Furthermore, ocean acidification could differently affect the growth of marine algae, like diatoms. Acidification may interfere with the silicification of diatoms, and it can inhibit their growth; this later effect is related to the sunlight exposure of such algae. Instead, other algae could also be positively affected by ocean acidification, such as macroalgae without CO_2 concentrating mechanisms (Gao et al., 2020).

The IPCC Special Report on Global Warming 1.5 °C states: "*Limiting global warming to 1.5 °C compared to 2 °C is projected to reduce increases in ocean temperature as well as associated increases in ocean acidity and decreases in ocean oxygen levels (high confidence). Consequently, limiting global warming to 1.5 °C is projected to reduce risks to marine biodiversity, fisheries, and ecosystems, and their functions and services to humans, as illustrated by recent changes to Arctic Sea ice and warm-water coral reef ecosystems (high confidence)"* (IPCC, 2018).

2.2 OAE CHEMISTRY: EQUILIBRIUM AND KINETICS

"*CO_2 dissolves in seawater and is mineralised slowly, ultimately descending to deep ocean sediments (2000–8000 years is needed for this system to reach equilibrium). The critical factor is calcium (or magnesium) carbonate minerals entering the ocean after weathering on land where their alkalinity compensates for the initial acidification when CO_2 dissolves. Accelerating this could thus increase the rate of CO_2 absorption by the oceans*" (EASAC, 2018).

The OAE aims to accelerate the process of CO_2 absorption, transferring carbon into bicarbonates. By adding alkalinity in seawater, CO_2 molecules react with the discharged calcium carbonates or hydroxides, leading to the formation of HCO_3^-. Furthermore, the artificial increasing of alkalinity can reduce the oceans' acidification, buffering the H^+ excess: this effect has to be applied several times to reduce acidification problems in freshwater. OAE has so a double beneficial effect on the global system.

A practical example of liming in freshwater is the recovery of the polluted Orta Lake in Italy performed from May 1989 to June 1990, discharging alkaline materials. The liming profoundly changed the acid-base system of the whole body; the first effect was an increase of pH to neutrality and a decrease in the mean acidity of the lake (Calderoni et al., 1994). In addition, alkalinity was absent before the liming because bicarbonate into water was insufficient to compensate the H^+ ions. After the liming, the concentration of bicarbonates and carbonates was large enough to neutralize the low pH level and offset the theoretical acidity (Calderoni and Tartari, 2000).

The best way to practice OAE appears to be the discharge of SL ($Ca(OH)_2$). One mole of this compound could theoretically remove two moles of aqueous CO_2 (reaction (2.4)), increasing the alkalinity of the water body by two-mole equivalents. This consumption of dissolved CO_2 does not correspond immediately to removal of atmospheric CO_2, which depends on the difference in CO_2 partial pressure (ΔpCO_2) between sea and near-surface atmosphere.

$$Ca(OH)_2 \rightleftarrows Ca^{2+} + 2OH^- \tag{2.4}$$

Dissolved CO_2 reacts with OH^- ions forming bicarbonates in less than a minute (reaction (2.5)), and only later the oceans absorb CO_2 from the atmosphere thanks to the mentioned partial pressure gradient, as described in Figure 2.3.

$$CO_2 + OH^- \rightleftarrows HCO_3^- \tag{2.5}$$

This event is sped up the more the discharge takes place near the surface, because superficial waters are well equilibrated with the atmosphere: the presence of upwelling currents could enhance this situation, transporting alkaline materials in the upper oceans' layers (Harvey, 2008; Renforth et al., 2013). For these reasons, the CO_2 removal occurs without a long lag time: the equilibration time of CO_2 in water varies according to pH, DIC, temperature T, and salinity S; however, it is generally between 10 and 30 seconds (Zeebe and Wolf-Gladrow, 2003).

The DIC concentration changes in the carbonate system are related to the environmental conditions in the specific location, and advective and diffusive processes remove a portion of the discharged alkalinity from the surface. The resulting partial pressure of CO_2 in seawater and pH also depends on local temperature T, salinity S, and pressure P. On the other hand, pH neutralization effects would become evident only after several SL releases because to counteract acidification is fundamental that the entire water body reaches an equilibrium (Butenschön et al., 2020).

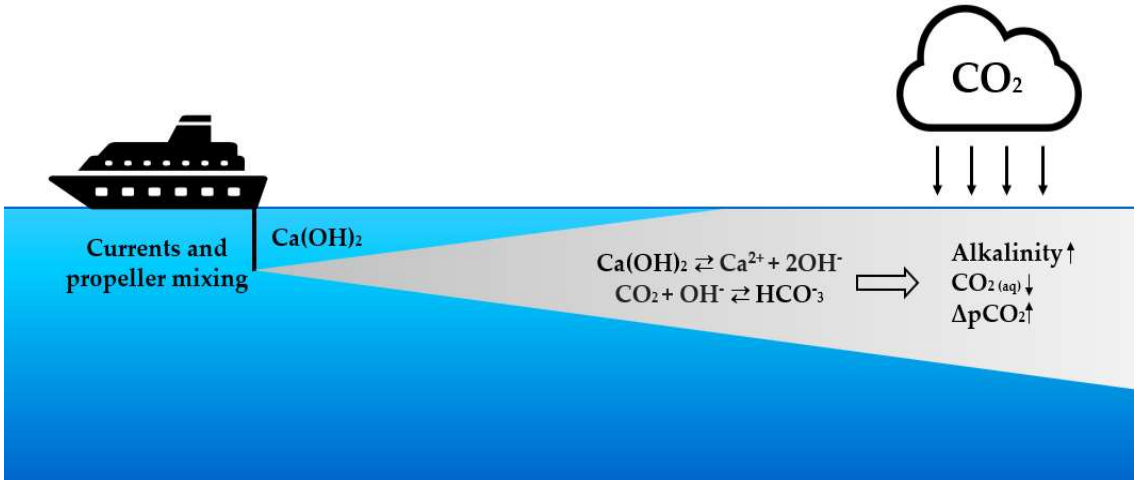

Figure 2.3: Example of slaked lime discharge via ships and principal occurring phenomena in short time scale.

The release of OH^- ions right after the disposal of SL causes a rapid increase in pH. This increase could last only a couple of minutes (Caserini et al., 2021), but it could be consistently high, also reaching values like 10-11. After that increase, OH^- ions react with the dissolved CO_2, and so the pH level decreases again. Furthermore, mixing thanks to oceans' currents helps to reduce such pH spike, dispersing SL but even hydroxyl groups in the water bodies. Also, when SL is discharged in the wake's ships, the vessel propeller increases such mixing efficiency, diminishing the biological impact.

2.3 OAE EFFICIENCY

Since SL reaction in water modifies the carbonate system equilibrium, because of the redistribution of inorganic dissolved carbon species, the process efficiency decreases; moreover, dynamic exchanges with the underlying waters amplify the reduction of the CO_2 uptake efficiency.

In this regard, this chapter aims to deeply investigate the efficiency of the OAE basing on existing literature studies (Köhler et al., 2010; Renforth et al., 2013; Keller et al., 2014; Lenton et al., 2018; Butenschön et al., 2020; Burt et al., 2021; Moras et al., 2021).

Literature suggests that this efficiency does not depend on SL particle size (Keller et al., 2014; Butenschön et al., 2020), proposing a 70% removal efficiency. The result of this assumption is that OAE carbon removal rate is about 0.83 kgCO_2 kgSL^{-1}, because one mole of $Ca(OH)_2$ removes two moles of CO_2, associated with the related molecular weights (44 g mol^{-1} for CO_2 and 74 g mol^{-1} for $Ca(OH)_2$), and multiplied by the described efficiency. The current study adopts this value, which is lower than the estimate defined by Renforth et al. (2013), who neglected the latter described phenomenon, assuming that 1 mole of $Ca(OH)_2$ could remove about 1.6-1.8 moles of CO_2. Even Köhler et al. (2010) assumed a more optimistic efficiency, considering that about 1.6 moles of CO_2 could be taken up by spreading 1 mole of SL.

Regional aspects

Keller et al. (2014) and later Lenton et al. (2018) simulated the spreading of 10 GtSL yr^{-1}. In more detail, Keller et al. (2014) investigated an increase of the total surface alkalinity between 70° N and 60° S, to avoid potential seawater icing during the entire year. In this modelling, OAE has been evaluated as a maximum intensity scenario based on current transport capacity. They considered a situation where 1 mole of SL removes approximately 1.4 moles of CO_2: the result of this simulation is a reduction in atmospheric CO_2 of 78 ppm, a surface air temperature cooling of 0.26°C, and a global increase in ocean pH of 0.06. Even Lenton et al. (2018) stated the necessity to discharge at tropical latitudes and modelled a situation with similar assumptions to Keller et al.'s studies. According to different emissions scenarios, this modelling demonstrated a reduction of atmospheric CO_2 levels between 53 and 86 ppm by 2100. The global mean cooling in the worst emissions scenario is about 0.16°C, while the estimated pH increase is 0.06.

Influence of ocean currents

Additionally, a key role in the OAE is related to ocean currents. In this situation, it is important to avoid areas with descendant currents, which are linked to the thermohaline circulation (THC). Winds are the cause of the surface ocean currents, while THC drives the vertical moving of the water masses. This circulation is caused by water density differences, which depend on temperature and salinity. The THC consists of more phenomena, taking place in the oceans on a global scale. A schematic currents pathway is given in Figure 2.4.

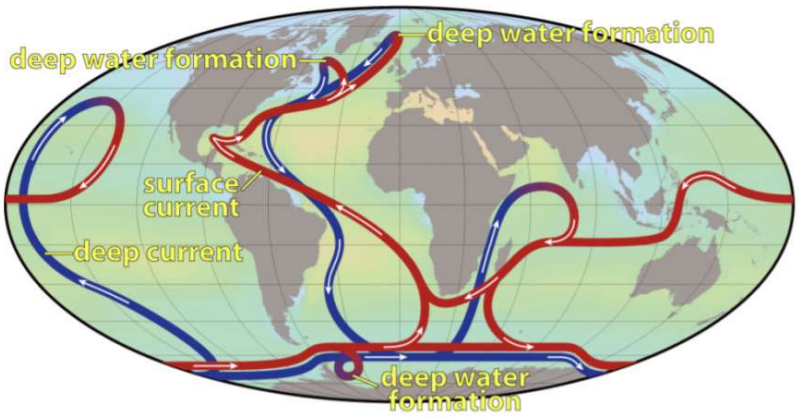

Figure 2.4: Scheme of the thermohaline circulation (Webb, 2019).

The first event taking place in the THC is the sinking of water masses, strictly related to convection; this dropping occurs in the coldest areas of the ocean, since cold waters are heavier than the hottest. This happens above all in the high latitude regions, and it is the engine of the THC. However, also high salinity increases the seawater density, and that's why also near the Mediterranean Sea opening into the Atlantic Ocean, there are dropping down water masses. The sunk waters are then spread in the deep ocean, mainly in the form of deep western boundary currents (DWBC). Because of the convection effect and thanks to the winds, the so-called upwelling drives the movement of deep waters; this occurs especially in the Antarctic Circumpolar Current (ACC) region. The result of the THC is noticeable from the pattern of

the near-surface currents. In general, it is possible to state that the coldest and heaviest water masses tend to settle to the ocean floor, while the hottest currents go up and stay near the surface until a subsequent cooling at high latitudes. The main ocean upwelling currents that could be investigated for OAE are the Humboldt, Canary, Benguela, California, and Somalia currents (Garcia-Reyes et al., 2015), additionally the Gulf Stream might also be evaluated.

Lenton et al. (2018) assessed better results in increasing the surface alkalinity discharging SL in not subpolar regions, between 70° N and 60° S (blue, green and red area in Figure 2.5). The subduction effect is the main cause of this fact because it is less efficient in this tropical area. In subpolar oceans, alkalinity could show a small increase, reflecting the strong connection between surface and deep waters. Furthermore, in this region, there is the risk of ice formation, reducing the dispersion of SL in water.

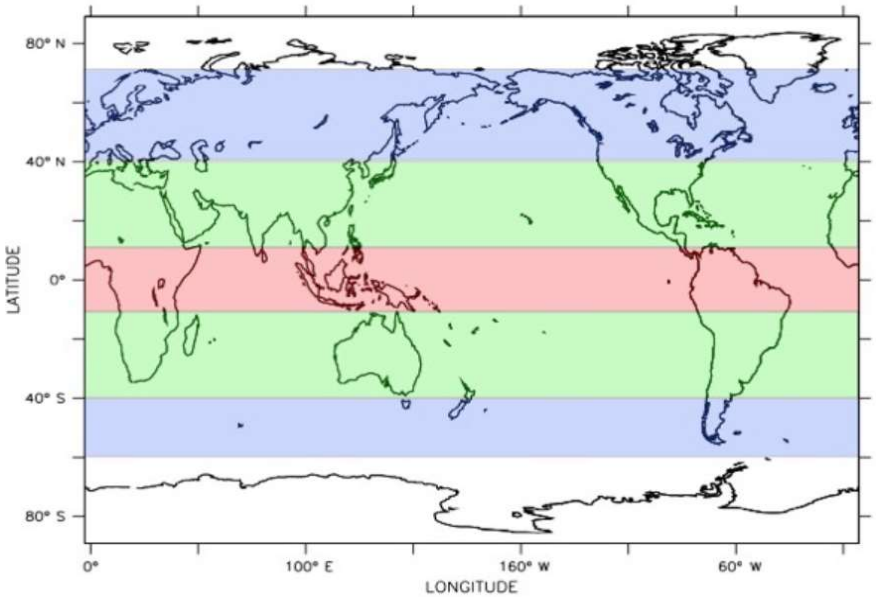

Figure 2.5: Ocean regions usable for alkalinity injection. Blue denotes the subpolar regions, green regions represent the subtropical gyres, the red area represents the tropical ocean, the white regions represent the seasonal sea ice (Lenton et al., 2018).

Lenton et al. (2018) also demonstrated that the process doesn't show a strong sensitivity in seasonality, concerning a homogeneous spatial and temporal application of alkalinization.

Burt et al. (2021) made a recent evaluation of OAE efficiency. They investigated eight regions with different hydrographic regimes, considering merely the open ocean. The eight selected regions are oriented with respect to persistent, large-scale gyre systems: the Subpolar and the Subtropical Atlantic and Pacific gyres; as well as the Indian Ocean and the Southern Ocean. Evaluating the TA increase in all the eight examined regions, the Subpolar North Atlantic (SPNA) and Indian Ocean (IND) regions showed better results. Also, Subtropical North Pacific (STNP) and Subtropical South Pacific (STSP) showed TA surface anomalies greater than the global average at the end of the simulation. The smallest changes occurred in the Subpolar North Atlantic region (SPNA), while the Southern Ocean (SO), Subtropical North (STNA) and South Atlantic (STSA) regions also revealed results worse than the global

average. Figure 2.6 shows total surface alkalinity anomaly time series for the described different regions.

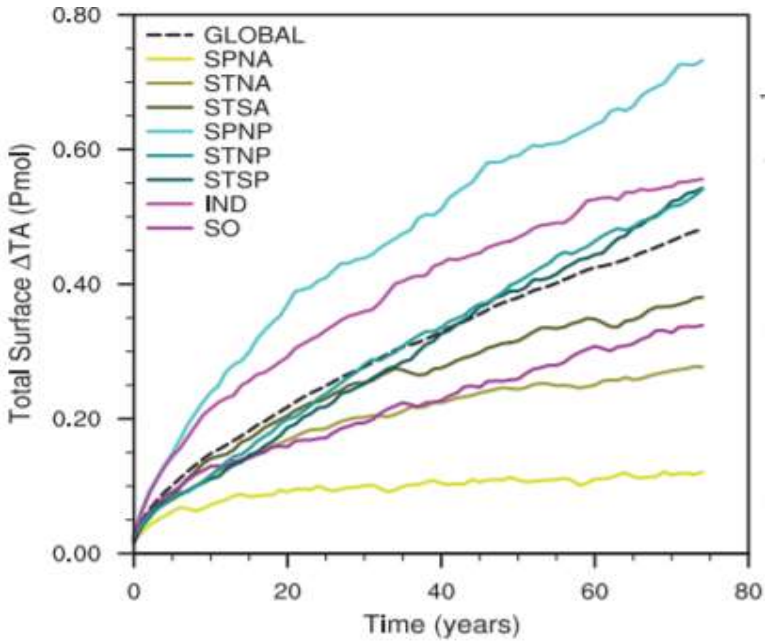

Figure 2.6: Time series of the total surface alkalinity anomaly in an OAE simulation (Burt et al., 2021).

Risk of $CaCO_3$ precipitation in seawater

Another key issue related to the OAE efficiency is the possible calcium carbonate ($CaCO_3$) precipitation, that could occur via three different pathways (Moras et al., 2021):

- heterogeneous precipitation: relying on the presence of existing solid mineral phases in seawater;
- homogeneous precipitation: formation of calcium carbonate crystals from the combination of calcium and carbonate ions when any type of nucleation surfaces is absent;
- pseudo-homogeneous precipitation: quite similar to the homogeneous precipitation but it occurs on nuclei (other than colloids or organic particles).

Independently from the reaction pathway, the $CaCO_3$ precipitation could increase the CO_2 concentration in seawater; the overall reaction (2.6) is well described by Zeebe and Wolf-Gladrow (2003) and involves both calcium and bicarbonate ions.

$$Ca^{2+} + 2HCO_3^- \rightarrow CaCO_3 + CO_2 + H_2O \qquad (2.6)$$

Neglecting such a phenomenon, and assuming a TA addition of 500 μmol kg^{-1} at a global scale, pCO_2 could be lowered by about 92 μatm while increasing the pH level up to 8.61 (Moras et al., 2021). The result is that 1 mole of TA could remove 0.83 moles of atmospheric CO_2, leading to a reduction of 0.7 tCO_2 per ton of source material. However, Moras et al. (2021) stated that the $CaCO_3$ precipitation could significantly lower such values, causing an OAE efficiency decrease ranging between 40-90%. Hence, $CaCO_3$ precipitation has to be strongly avoided. At this purpose, Moras et al. (2021) stated that it is possible to strongly reduce such phenomenon

thanks to different expediencies: increasing the mixing and dilution, equilibrating the seawater to atmospheric CO_2 levels during mineral dissolution, and spreading TA in low rather than high-temperature waters. In particular, an appropriate dilution, according to different TA dosages, has the ability to stop precipitation. The quicker dilution occurs, the less $CaCO_3$ would precipitate. Such dilution could be obtained by the natural seawater mixing and thanks to the use of ships' propellers in the wake of ships.

2.4 SLAKED LIME PRODUCTION AND DISTRIBUTION

Among the different alkaline material suitable for OAE, SL is the principal substance considered in this assessment; alternative alkaline materials will be briefly investigated later.

SL is a white or greyish-white powder with strong basic properties. The traditional pathway for its production, reported in Figure 2.7, starts from limestone ($CaCO_3$) extraction and comminution, followed by its thermal decomposition (calcination) to quicklime (CaO, QL), then QL is slaked (hydrated) to produce SL, and finally SL is distributed.

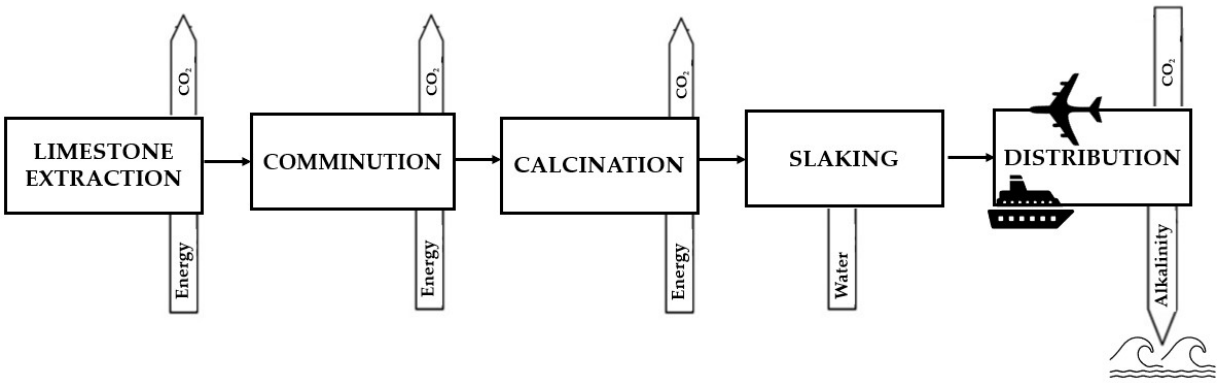

Figure 2.7: Simplified scheme of slaked lime production for OAE (reworked from Renforth et al., 2013).

The supply chain stages are briefly examined in the following section, the main focus is on the principal methods suitable for SL distribution in the oceans.

2.4.1 EXTRACTION AND COMMINUTION

SL production begins from limestone extraction. It is a sedimentary rock mainly composed of carbonate minerals, such as carbonates of calcium and magnesium, but small amounts of impurities such as silica and aluminium may be present.

It is widely distributed, as can be seen in Figure 2.8, covering about 10% of the Earth's land surface; for this reason, its extraction will never be a limiting factor for OAE (Oates, 2008). Blasting or mechanical excavation, depending on its hardness, permit its extraction from the rock through a process termed quarrying. The extracted stone goes under different crushing and grinding steps until the production of a fine powder (comminution phase).

In the OAE aim, the carbonate outcrops of major interests should be the ones near the coast. The transport of carbonates rocks from continental reserves could limit the CO_2 removal efficiency, because of transport consumption and emissions.

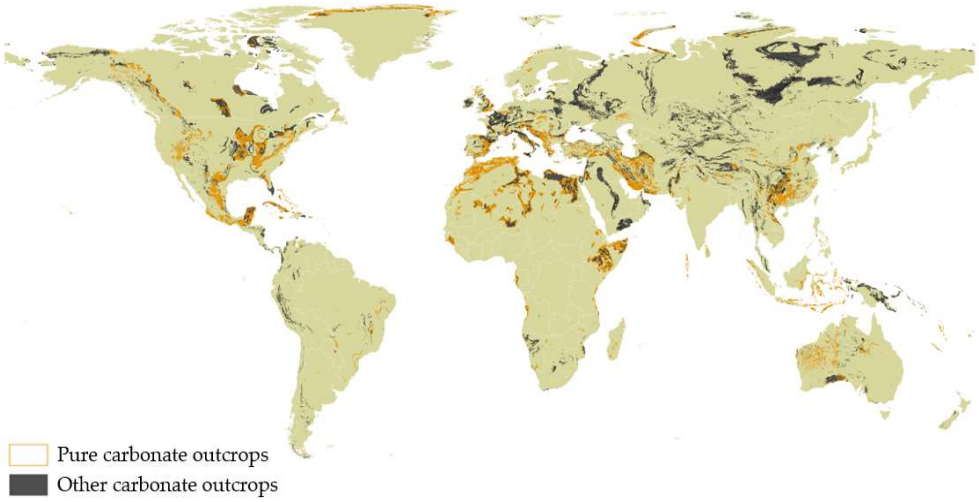

Figure 2.8: Pure carbonate and other carbonate rocks outcrops in the world (Storni et al., 2021).

2.4.2 CALCINATION

Limestone powder undergoes a thermal process termed calcination in which it is heated at around 1,100 °C in a rotary kiln or shaft furnace giving off CO_2 and forming QL (reaction (2.7)).

$$CaCO_3 \rightarrow CaO + CO_2 \uparrow \quad (2.7)$$

The major elements affecting QL quality are (Hassibi, 2009):

- chemical composition of limestone and particle size;
- kiln temperature**:** it should be at least 900 °C in order to ensure good quality of the material;
- residence time of the lime in kiln: it should be sufficient to allow heating to penetrate the limestone particles;
- carbon dioxide concentration in flue gas: there is the necessity to vent it out of the kiln because QL has an affinity to absorb moisture and carbon dioxide itself, and then revert back to limestone (this effect is more pronounced with small particles).

Additionally, process temperature affects material reactivity in further stages, like slaking. Calcination process requires a huge amount of energy, which is estimated to be approximately between 2,910 and 3,492 MJ tQL^{-1} (Renforth et al., 2013).

2.4.3 SLAKING

Then QL is crushed in small fractions and hydrated producing SL powder (reaction (2.8)). There is the necessity to slaking QL in a controlled environment since it is a strong exothermic process, but it is worth noting that the release of heat depends on quality limes.

$$CaO + H_2O \rightarrow Ca(OH)_2 \quad (2.8)$$

The most important factor affecting the slaking process efficiency is the specific surface area of QL particles. The larger the specific surface area of the hydrate, the more surface is available for reaction: therefore, it will be more efficient. The typical specific surface of SL ranges

between 8,000 to 58,000 $cmSL^2\ g^{-1}$. The specific surface is influenced by the following factors (Hassibi, 2009):

- type of limestone: the quality is mainly affected by impurities (magnesium/aluminium oxide);
- slaking temperature: if it is closer to 98 °C the finer the particle sizes and greater the specific surface of particles will be, but when the process temperature is around the boiling point of water, hydrate particles could crystallize and agglomerate forming larger, flat particles with reduced specific surface. In practice, slaking temperatures between 76 to 85 °C are more practical for optimum operation;
- slaking time: it is highly variable depending on the type of lime used, it generally ranges between 2 and 30 minutes;
- water chemistry: the presence of certain chemicals in the slaking water will accelerate or hinder the process;
- air slaking: as stated before it is mainly linked to the conversion of QL to limestone under specific conditions.

SL density is about 2,240 $kg\ m^{-3}$ (Tannenberger and Klein, 2009) and it has a molecular weight of 74.01 $g\ mol^{-1}$; it has a bitter taste and no odour. Particle size distribution is of fundamental importance and could be assessed by laboratory analysis and expressed in terms of percentile of the granulometric distribution. Measurements by an Italian producer (Unicalce, 2021) reported in Figure 2.9, show particle diameters between 4 and 39 μm, with a median mass diameter value of 9 μm and a standard deviation of 7.15.

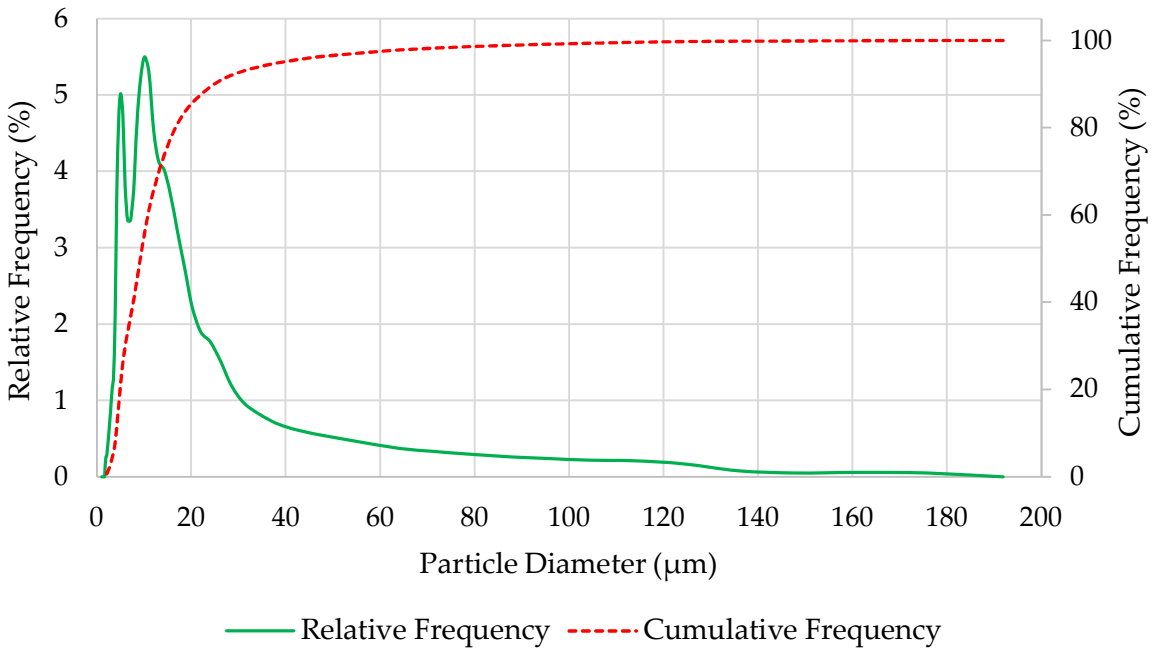

Figure 2.9: Relative and cumulative frequency of SL particles mass distribution.

2.4.4 DISTRIBUTION

Finally, SL could be spread by different methodologies. The most studied configuration in the existing literature is based on the discharge in ships' wake (Köhler et al., 2013; Renforth et al., 2013; Caserini et al., 2021), while the current thesis work investigates other innovative technologies, like aircraft and rainbowing system.

Moreover, each methodology could discharge SL in different physical forms. It could be spread in the form of a powder, or it could be possible to produce a slurry by mixing it with water. This dilute aqueous solution of SL is commonly defined as "limewater". If this solution is saturated, it could be considered pure; in this condition it is a basic substance with a pH of 12.4. When it is added in excess, SL particles remain homogeneously suspended and this liquid is named "milk of lime".

SL spreading in ship's wake happens in the form of milk of lime, prepared on board. It is preferable to obtain milk of lime instead of limewater, because by reducing the water quantity it is possible to maximize the discharge rate while decreasing energy consumption. Even in the case of the rainbowing spreading systems milk of lime is adopted. It is worth noting that too elevated slurry concentrations may cause deposition issues into pipelines.

On the other hand, in the case of aircraft methodology SL is discharged in form of powder due to logistics and energetical issues. Compared to ships, aircraft have a lower transport capacity, so it is required to maximize the SL transported by avoiding unnecessary water.

2.5 CO_2 CONTROL IN SLAKED LIME PRODUCTION

The production of SL is an energy intensive process, resulting in high CO_2 emissions from both mineralogical transformation process and energy used. In particular, the vast majority of the CO_2 emissions occur during the calcination process while the remainder (30-40%) from burning of fossil fuels (Dowling et al., 2014), therefore its capture is a key issue for the OAE technology.

The CO_2 produced quantity is function both of the stone purity and process temperature (Renforth et al., 2013); in particular, the production of 1 tQL entails the emission of around 1.2 tCO_2 (Ochoa George et al., 2010; Sagastume Gutierrez et al., 2012). In a more specific evaluation, about 1 tCO_2 derives only from the calcination phase (OpenLCA, 2021), while a minor portion is related to the extraction, grinding, and transport of raw limestone (18 gCO_2 per kg$CaCO_3$ mined; Kittipongvises, 2017), and the industrial production of almost-pure calcium carbonate (3 kgCO_2 per t$CaCO_3$ produced; OpenLCA, 2021). This makes QL one of the products with the highest specific emissions of CO_2 when compared to other energy intensive industries. Considering all the processes from the mining phase to the grinding of the final product, energy requirement for SL production is usually between 4,000-5,000 MJ per t$Ca(OH)_2$ (Sagastume Gutiérrez et al., 2012).

Therefore, for the upscaling of this technology, it is fundamental to use renewable methods for energy production both in grinding and calcination, and also in the carbonate mining phase: this will improve the CO_2 removal efficiency of the entire system; for instance, the use

of solar power calcining technology would reduce CO_2 production from fossil fuel combustion (Meier et al., 2005; Nikulshina et al., 2006). Additionally, also Carbon Capture and Storage (CCS) could help solving the issue of CO_2 emissions during these processes: it involves the use of technology to collect, concentrate the CO_2 produced, transport, and then store it for a long period in underground or undersea storage (Gale, 2004; Paquay and Zeebe, 2013). CCS would thus allow the usage of fossil fuels with low emissions of GHGs (IPCC, 2005).

CO_2 can be injected into geological storage like deep saline aquifers (onshore below 1 km from the ground or offshore), depleted oil/gas reservoirs, and deep unmineable coal seams, as shown in Figure 2.10. Moreover, the combination of CO_2 storage with Enhanced Oil Recovery (EOR) or, potentially, Enhanced Coal Bed Methane (ECBM) recovery could lead to additional revenues from the oil or gas recovery (IPCC, 2005).

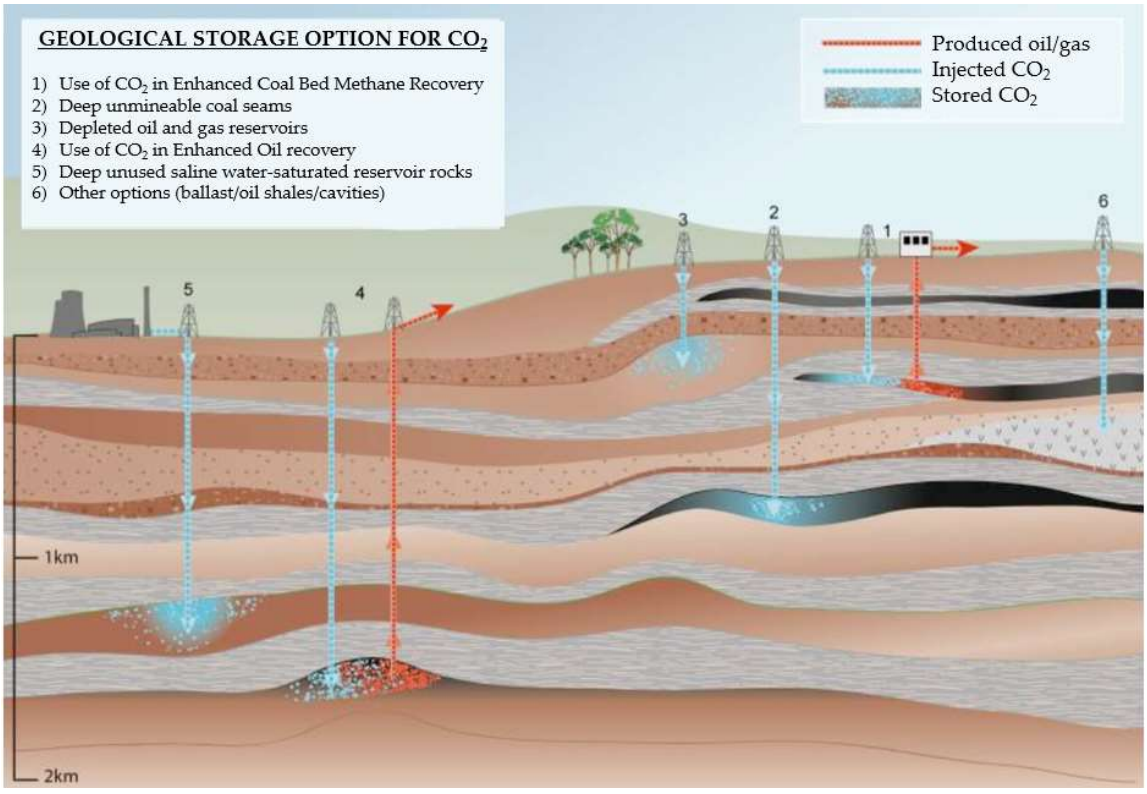

Figure 2.10: Overview of geological storage options (Strogen et al., 2009).

The principal requirement for geological storage is a safe and secure underground disposal site which effectively stores CO_2 for hundreds to thousands of years without contaminating other important natural resources like groundwater, coal, and petroleum (Strogen et al., 2009). Geological formations should have enough millimetre-sized voids or pores with good permeability, in order to allow the CO_2 moving and spreading within the formation, and finally should have an extensive cap rock at the top of the formation to prevent the upwards movement of CO_2 due to buoyancy. Once captured, the CO_2 is compressed, in order to reach the supercritical state at which it has a liquid-like density but flows like a gas. In this physical state, CO_2 density will still be less than water, while the viscosity is typically less than a tenth of the brine resident in the rock (Blunt, 2010).

Storage capacity mainly depends on the geological and petrophysical properties of the geological formation. Different mechanisms operate CO_2 trapping simultaneously and on different time scales; the two main mechanisms are (Ajayi et al., 2019):

- physical trapping: during which carbon dioxide doesn't change its physical nature, provided by both cap rock and capillary forces. It includes structural (hydro stratigraphic) and residual (capillary) trapping in which water tends to wet the surface, leaving the carbon dioxide surrounded by water in pore-space bubbles that cannot escape. It is worth noting that generally, the time period for this kind of trapping is believed to be less than a century (Juanes et al., 2006);
- geochemical trapping: in which carbon dioxide undergoes different geochemical reactions, reacting with the in-situ fluids and host rock. It comprises mineral and solubility trapping. The former directly involves the reactions with minerals (i.e.: transformation of carbon dioxide into calcite) so it strongly depends on rock's composition, while the latter occurs as a result of carbon dioxide dissolution in rock's brine forming a weakly acid solution that on a long-time scale (thousands to millions of years) could react with the host rock forming solid carbonate (Blunt, 2010).

Storage capacity estimation is not a straightforward process due to the different trapping mechanisms taking place, but different studies shown that deep saline aquifer are the most suitable geological storage for CCS because their potential storage is extensive and widely distributed (Blunt, 2010; Michael et al., 2010; Ringrose et al., 2021).

Even though CCS is a viable option for climate change mitigation, the storage phase poses some risks that should be better investigated. The primary and most relevant risk associated with CCS is CO_2 leakage, as a result of:

- abrupt leakage through injection well failure or abandoned wells: this leakage pathway is more plausible in a depleted hydrocarbon reservoir which has been used previously for the commercial production of hydrocarbon dioxides;
- gradual leakage through undetected faults and fractures;
- aquifer over-pressurization that may lead to cracks in the above cap rock or could reactivate faults minerals. (Ajayi et al., 2019).

The risks due to CO_2 leakage fall into two categories: global risks and local risks. The former involves the release of CO_2 that may contribute significantly to climate change while the local hazards may exist for humans, ecosystems, and groundwater (IPCC, 2005).

Additionally, also induced seismicity could be a risk during CO_2 storage phase; it could lead to earthquakes with high magnitude and consequent relevant impacts on the infrastructure. The possibility of the occurrence of a seismic event will be higher if faults are present (Ajayi et al., 2019; Nicol et al., 2011).

Even if the geological storage is currently at the demonstration stage, accurate site selection, characterization and monitoring are needed for successful geological storage (Lane et al., 2021).

Another option could be CO_2 injection into the ocean at great depth, where most of it would remain isolated from the atmosphere for centuries. This could be done via a fixed pipeline or a moving ship, or by depositing it via a pipeline or an offshore platform onto the sea floor at depths below 3 km. On the other hand, ocean storage has not yet been deployed or thoroughly tested and the injection of hundreds of GtCO_2 could produce measurable changes all over the ocean, for instance seawater pH would decrease significantly posing serious problems to marine life (IPCC, 2005).

Finally, Castaño et al. (2021) recently demonstrated a novel aqueous-phase calcination-free process to precipitate SL using industrial alkaline wastes as a feedstock, enhancing also waste utilization. In more detail, this new process presents a specific energy demand that is nearly 44% lower than traditional thermal processes in terms of kJ $kgSL^{-1}$, importantly fixing the need to decarbonize limestone. Hence this new process could allow the production of a truly CO_2-negative material.

2.6 SIDE EFFECTS OF SLAKED LIME

The ecological implications of marine organisms due to OAE are not yet fully understood. For the estimation of the environmental side effects of this technology it is crucial the evaluation of the localized temporary pH spikes due to SL particles dissolution. Excessive local alkalinity may be ecotoxic and detrimental, especially for the ecologically sensitive sea surface microlayer (SML) causing harmful effects on any living organism (Locke et al., 2009). Moreover, open ocean is characterized by the presence of euphotic zones that host a high biodiversity of marine species, which could be considered as a highly sensitive layer (Costello and Chaudhary, 2017). However, an adequate increase of pH on a large scale could apport large benefits on the oceans' ecosystems affected by ocean acidification.

Additionally, an investigation on SL human toxicity allows to basically understand the principal side effects in case of human contact.

2.6.1 SIDE EFFECTS ON BIOLOGY

The potential environmental effects of the OAE at local scale depend on various factors; the disposal depth and the spatial scale, the type of ecosystem involved (coastal or pelagic), and the pH variation in the specific site. Such impact is dependent on the type of discharge, and also on the mineral composition of the seawater (Renforth and Henderson, 2017). An ocean alkalinity increase could positively influence the saturation state of carbonate minerals. These minerals are essential for carbonate-producing organisms, which live in pelagic ecosystems (coccolithophorids and foraminifera) or in coral reefs. Otherwise, excessive alkalinization could disrupt the delicate acid-base balance of some marine organisms; pH values outside the range of 7.0 to 8.5 for a sufficiently high time can preclude the growth of some species (Cripps et al., 2013). Phytoplankton is the vegetal ocean organism more affected by alkalinity addition, because of the photosynthesis inhibition. Consequently, the alteration of phytoplankton's function and structure has important implications for the whole marine ecosystem (Henderson et al., 2008).

However, it is unknown if the time scale of the local pH increase is long enough to cause such problems: deleterious effects related to pH peaks on short-time exposure should be better investigated. Literature studies assessed the biological impact of elevated pH levels on marine species, but these studies refer to high exposure periods. For instance, Hansen et al. (2017) defined the effects of elevated pH on six copepods species: five species out of six showed no mortality effects for pH level until 9.5, considering an exposure period of 24 h. Only *Oithona similis* revealed mortality effects, which appear for a pH level of 8.73. Furthermore, tests on *Sinonovacula constricta* (Maoxiao et al., 2018) demonstrated no acute toxicity effects for pH below 9.5 during exposures of 48 h, but they showed large mortality when the pH reaches the 10.5 level, even for 24 h of exposure.

SL concentrations that cause ecotoxicity in water are available (Locke et al., 2009). For sand shrimp (*Crangon septemspinosa*) the Lethal Concentration of half population for SL exposure for 96 h (96h-LC50) is 158 mg L^{-1} and the No Observed Adverse Effect Concentration (NOAEC) is 50 mg L^{-1}, while for threespine stickleback (*Gasterosteus aculeatus*) 96h-LC50 is 457 mg L^{-1} and NOAEC is 100 mg L^{-1}. Table 2.1 shows the different ecotoxicity levels for SL in seawater; these values are environmentally conservative because they are based on 96 h of exposure, while actually, dissolution lasts only a few minutes (Caserini et al., 2021). On the other hand, SL does not show bioaccumulation effect or food chain concentration toxicity (Lhoist North America, 2008).

Table 2.1: Ecotoxicity levels for SL in seawater (Locke et al., 2009).

Substance	Species Name		u.m.	Parameter	Value
$Ca(OH)_2$	Sand shrimp	*Crangon septemspinosa*	mg L^{-1}	96h-LC50	158
				NOAEC	50
	Threespine stickleback	*Gasterosteus aculeatus*	mg L^{-1}	96h-LC50	457
				NOAEC	100

According to the different methodologies of discharge, it is worth noting that also the SML biology could be affected. Even though a ship discharge should avoid this interference releasing SL not actually on the surface, could pose some problem for a certain type of disposal (for instance, aircraft or rainbowing discharge). The SML is the boundary interface between the atmosphere and the ocean. Its properties make it acts differently from underlying water, because of peculiar physicochemical behaviour and biology. It is a 1 mm laminar layer, free of turbulence, affecting the gaseous exchange of oceans with the atmosphere, and exerting short-term and long-term impacts on different Earth system processes like biogeochemical cycles (Cunliffe et al., 2013; Baker et al., 2021). It is very rich in marine microorganisms and strongly sensitive to pH variations (Engel et al., 2017; Wurl et al., 2017; Whitney et al., 2021). It contains amino acids, carbohydrates, fatty acids, phenols and also high concentration of bacteria, viruses, toxic metals, and a lot of pollutants that stop in this zone and don't enter the ocean so that concentration of pollutant is higher in SML compared to underlying water. In addition, the SML provides a habitat for a biota, including the larvae of many commercial fishery species (Hardy, 1982; Wurl and Obbard, 2004).

The impact on the surface ocean ecosystem could be very low in terms of SL toxic concentration or pH level, but further studies are needed to better understand SML effects in shorter exposure, including average alkalinity concentration, concentration in the immediate vicinity of the particles, and especially with the mechanical action of the surface impact. SL maximum addition rate is strongly limited by ecological considerations.

2.6.2 SIDE EFFECTS ON HUMANS

SL is also toxic for humans through inhalation, skin, or eye contact. It is tissue corrosive and may lead to corrosive chemical burns (Clayton and Clayton, 1981; Grant, 1986). The effects are proportional to the duration and degree of exposure (NLM, 1992). Chronic inhalation of SL causes pneumonia and bronchitis, and a prolonged skin contact could also induce dermatitis (Parmeggiani, 1983). It is fundamental to avoid human contact; the American Conference of Governmental Industrial Hygienists (ACGIH) has assigned a SL threshold limit value of 5 mg m^{-3} for an 8-h workday and a 40-h workweek, based on the risk of irritation associated with exposure to SL (HHS, 1995). An exposure to 2.5 mg m^{-3} for 30 min results in nasal irritation, while additional studies report a NOAEC value of 2 mg m^{-3} for eyes, nose and throat irritation following a 20 min exposure (Safe Work Australia, 2019).

2.7 ALTERNATIVE ALKALINE MATERIALS FOR OCEAN ALKALINIZATION

In past times, some researchers and scientists studied different suitable alkaline materials for OAE. In particular, Kheshgi (1995) proposed two different substances: these two materials are soda ash (Na_2CO_3) and calcium carbonate ($CaCO_3$). Other studies (Köhler et al., 2013; Renforth and Kruger, 2013) examined the possibility of using forsterite-rich olivine (Mg_2SiO_4). Moreover, quicklime (an intermediate product in the SL production process) suitability is briefly explored.

Soda ash

Soda ash (sodium carbonate, Na_2CO_3) could be a proper material for the OAE. It is readily soluble in water, and from one mole of soda ash, two theoretical mole equivalents of TA are spread into the ocean system. The largest reservoirs of this chemical are in Wyoming (U.S.A.). However, the abundance of this material in the Earth's crust is very poor; the entire estimated quantity of Na_2CO_3 could offset only one year's emissions from fossil fuels combustion at the current rate (Kheshgi, 1995).

Calcium carbonate

One way to obtain the ocean's alkalinization is to discharge calcium carbonate. $CaCO_3$ will so react with water and CO_2, following reaction (1.10). Every mole of calcium carbonate should remove one mole of CO_2, but possible collateral reactions reduce the efficiency to 40-70%. However, this method is not so effective in carbon removal, because the $CaCO_3$ itself increases the presence of carbon in water.

Even though calcium carbonate has been used in the past for freshwater liming, its use is not very suitable for OAE. The Orta Lake liming employed a $CaCO_3$ slurry discharge with a minimal part of magnesium carbonate ($MgCO_3$). The slurry injection took place in the deepest layers because otherwise such chemical tends to stay on the surface. However, it was possible to practice this type of discharge because the water life was very compromised, with a pH level lower than 3.9: in the twenties, many investigations assured that there was no more evidence of living organisms in that ecosystem (Monti, 1930).

The discharge of $CaCO_3$ in a seawater ecosystem could pose indeed biological problems. The main issue is that $CaCO_3$ is not soluble in ocean surface water (Harvey, 2008) because seawater is generally supersaturated with respect to $CaCO_3$ especially near the surface, as described in Chapter 1.4, and so its dissolution is too slow (Zeebe and Wolf-Gladrow, 2003). This chemical does not dissociate in a short time, so it tends to accumulate following more discharges. As a result, it increases water turbidity, blocking the filtration of light rays in the underlying water layers. Consequently, this material could damage oceans' ecosystems slowing down photosynthesis: this deleterious situation could affect many marine organisms. Therefore, the biological pump efficiency, which naturally removes CO_2, is reduced.

This peculiar effect, negligible in a biologically inert water mass, is yet significant in an ocean ecosystem. Nevertheless, the direct toxicity effects of this chemical are not so consistent. It causes moderate-to-severe irritation in contact with the tissues of animals, especially the eyes; skin contact entails only moderate irritation (NIOSH, 1997). The fish exposure (tests on *Oncorhynchus mykiss*, rainbow trout) in saturated $CaCO_3$ solution for a 96-hour period does not show any mortal or sub-lethal effect. Similarly, experiments on the aquatic invertebrate *Daphnia magna* were taken in the same conditions for a period of 48 h: no acute or lethal toxic effects were found. Different is the situation for algae and cyanobacteria: studies on a green alga (*Desmodesmus subspicatus*) demonstrated that the 72h-NOAEC is 14 mg L^{-1} (ECHA, 2021).

As well, toxic effects on humans are examined briefly. $CaCO_3$ dust is a physical irritant of the eyes, nose, mucous membranes, and skin. Skin contact generates only a local and moderate degree of irritation, while eye contact causes redness, pain, and inflammation (NLM, 1991). ACGIH has assigned a $CaCO_3$ threshold limit value of 10 mg m^{-3} for an 8-hour workday and a 40-hour workweek (HHS, 1995).

Olivine

Olivine is a material rich in forsterite (Mg_2SiO_4). Köhler et al. (2013) evaluated its efficiency in a direct discharge for the OAE. The dissolution of this substance increases TA with an olivine/alkalinity molar ratio of 1:4. However, there is a release of silicon; such Si increases in the ocean would lead to a significant fertilization effect. Furthermore, the presence of iron (Fe) in olivine may fertilize biological activity.

Instead, Renforth and Kruger (2013) investigated the possibility of using forsterite-rich olivine for a coupled mineral carbonation OAE process. Ground olivine could be used to produce magnesite ($MgCO_3$) and silica (SiO_2) in proper carbonation reactors. The magnesite obtained

could be used subsequently to produce brucite ($Mg(OH)_2$) through a slaking process. The overall process reactions are reported below (reactions from (2.9) to (2.11)).

$$Carbonation:\ Mg_2SiO_4 + 2CO_2 \rightarrow 2MgCO_3 + SiO_2 \quad (2.9)$$

$$Slaking:\ 2MgCO_3 + 2H_2O \rightarrow 2Mg(OH)_2 + 2CO_2 \quad (2.10)$$

$$Liming:\ 2Mg(OH)_2 + 4CO_2 \rightarrow 2Mg^+ + 4HCO_3^- \quad (2.11)$$

The CO_2 emissions from the decomposition of $MgCO_3$ in $Mg(OH)_2$ are recycled in the reactors to carbonate forsterite in magnesite. Furthermore, $MgCO_3$ decarbonates at a lower temperature than $CaCO_3$, saving energy (however, saved energy is significantly lowered due to water evaporation in the kiln and to olivine grinding).

This system could minimize constraints on plant location while decreasing the overall cost by 60-80%. However, there are no in-depth studies investigating the efficacy of $Mg(OH)_2$ in increasing TA, and its biology impact. The presence of Fe and Si impurities could be a significant problem, as mentioned above.

Quicklime

As stated before, it is also possible use QL rather than SL, but different literature studies show that it could cause several deleterious effects both on the ecosystem and on human health. Its usage should be strongly avoided.

In particular, QL interaction with water releases heat causing serious injuries to marine organisms, including hypoxia effects (El-Mansy, 2020). The threshold value 96h-LC50 for the European carp (*Cyprinus carpio*) is 1.07 mg L^{-1} (Sigma-Aldrich, 2014).

Additionally, significant health safety issues for humans exist; QL is highly corrosive, and severely irritant to eyes, skin, and mucosa (WHO, 2017). It is not listed as carcinogen, but it may contain trace of crystalline silica, which has been classified as carcinogenic to humans when inhaled as quartz or as cristobalite (Lhoist North America, 2012). It is therefore relevant to avoid human contact with QL; the ACGIH sets a limit for the airborne exposure over an 8-hour work shift at 2 mg m^{-3} (NJDHSS, 2003).

Furthermore, it is advisable to make the slaking reaction (2.8) happen in a controlled environment and not directly in seawater, because of its exothermal properties. Marine ecosystems are therefore preserved, and in addition, it is possible to gain energy from such a situation. The installation of heat recovery plants where slaking processes take place could improve the environmental efficacy of the OAE, combining many positive effects; 1 kg of almost pure QL could generate approximately 814 kJ in the form of heat (Harper, 1934).

At the end of this brief investigation, SL appears to be the best suitable alkaline material for OAE because it has a better CO_2 removal efficiency and also minor environmental side effects.

3. DISCHARGE VIA SHIPS

One of the most analysed types of discharge for OAE, is the use of vessels. In literature, many studies focused on the SL discharge in the ships' wake (Köhler et al., 2013; Renforth et al., 2013; Caserini et al., 2021). In this regard, these previous studies assessed the great potentiality of the methodology, but on the other hand, they also show that CO_2 removed is strictly related to several variables, like the number of vessels and their load, the travelled distance, the speed during the discharge, and the discharging rate. It is worth noting that the discharge rate mainly affects SL concentration in seawater and the duration of the process. As expected, a high discharge rate implies high SL concentration, and also high pH level due to the release of hydroxyl ions during the dissolution process; these two factors may be ecotoxic and detrimental for the marine environment, as already investigated in Chapter 2.6.1.

The dispersion of SL in ship's wake could provide many positive effects; both hull passage into the water and the agitation created by the propellers guarantee fast mixing, increasing the OAE efficiency. On the other hand, this configuration could have a minor number of environmental issues since the sea surface microlayer (SML) is not directly involved because the discharge takes place below the water surface.

In the following chapters, basing on existing literature, three main discharging scenarios are evaluated, considering both emissions and costs, to better understand the potential and the feasibility of this shedding configuration for OAE.

3.1 LITERATURE STUDIES ON OAE VIA SHIPS

The aim of this chapter is to briefly investigate literature information and data on OAE via ships.

According to Renforth et al. (2013), 101 dedicated bulk carriers (with a 300,000 deadweight tonnage, dwt) could be sufficient to spread 1 Gt yr^{-1}, assuming an outflow of 1 tSL s^{-1}. The mentioned study assumed a bulk carrier discharge time of 3.5 days, adding time for loading and return to port.

A portfolio of different scenarios could be analysed. Use existing ships could be the less impactful choice, assigning a fraction of their load to the pulverized SL storage, because for logistical reasons ships for goods transportation do not sail fully loaded (Narula, 2019). At this purpose, Caserini et al. (2021), hypothesized the possibility to use 15% of the deadweight cargo capacity (DWCC) without compromising the normal business of the vessel, since it corresponds to the space in the hold. The problem in this scenario could be that fixed routes are given, without any possible optimization (for instance analysing adequate currents, pH levels, or temperature). Another option could be to use a new dedicated fleet, purchased or built for the purpose; in this scenario it is possible to use appropriate vessels, driven in optimal routes discharging bigger SL quantities in the most suitable areas.

Caserini et al. (2021) assessed, according to IMO data for bulk carriers and container ships, a potential global maximum discharge of 1.7-4.0 GtSL yr^{-1}. Focusing on the Mediterranean Sea,

the mentioned study assessed that in such a close basin is possible to discharge about 186 MtSL yr^{-1}. The physical characteristics of a semi-enclosed basin like the Mediterranean Sea, with currents driving wide circulation patterns, lead to an efficient distribution of SL reducing uncontrolled dispersal into confining waters and also it demonstrates large physical and chemical variations due to global warming and acidification. Moreover, this region is an area of anthropogenic increase in carbon uptake; it is so identified as a climate change hotspot (IPCC, 2013).

Furthermore, in literature are also present some studies regarding ships energy consumptions. The energy demand for SL discharging via ships is mainly related to its size and method of propulsion. Renforth et al. (2013) evaluated the fuel energy costs that are approximately equal to 100 MJ t^{-1} of material added to the ocean; additionally, 8 MJ t^{-1} for electrical energy and 19 MJ t^{-1} for fuel energy for dockside operations are needed.

3.2 DISCHARGING SCENARIOS IN SHIPS' WAKE

SL discharging in ships' wake could occur according to different spreading scenarios, that are here evaluated basing on the previous study made by Caserini et al. (2021).

3.2.1 EXISTING SHIPS

This scenario assumes to dedicate a portion of cargo vessels capacity, normally navigating in the oceans, to SL transport. This could obviously cause competition in the shipping of goods; otherwise, revenues could be obtained by SL discharging: for instance, the gain of carbon credits thanks to CO_2 removal.

Even if they represent solely 40% of the total vessel number, cargo (like bulk carriers, container, general cargo) are the most suitable vessels for SL discharging; a graphical representation of the different ships is given in Figure 3.1.

Figure 3.1: Scheme of two different type of vessels: container ship and bulk carrier.

Thanks to their structure, only bulk carriers are immediately suitable for SL discharge, so they would not need many modifications. Instead, container ships could be suitable after few changes in their structures; they would necessitate appropriate tanks and pumping systems. Nevertheless, more dedicated infrastructures should be installed at calling ports.

Despite these two categories represent less than half of the vessels' number, they are responsible for 53% of total active tonnage. In a more detailed analysis, bulk carriers and container ships sail for at least half of a year (respectively 181 and 218 days) covering 70% of the total distance travelled by vessels worldwide. They are particularly appropriate also for logistic reasons (Panarello, 2020). The total fleet analysed is formed of 32,015 cargos, as shown in Table 3.1.

Table 3.1: Main characteristics of the existing cargo fleet (reworked from Caserini et al., 2021).

Ship type	Total fleet size	Active ships observed	Average days at sea	Distance covered	
	-	-	d yr^{-1}	Mkm yr^{-1}	%
Bulk carrier	10,397	9,286	181	862	20
Container	5,132	4,855	218	688	16
General cargo	16,486	9,433	165	675	15

The quantity of SL transported is strictly related to the tonnage of the vessels and to the frequency of reloading, which plays a key role in determining OAE potential. Averagely bulk carriers and container ships, respectively, make one and between two and four intermediate stops (MarineTraffic, 2020).

3.2.2 NEW DEDICATED SHIPS

As mentioned in Chapter 3.1, a different chance is to build new dedicated ships. Even if new dedicated vessels could have higher costs, among the true advantages it is worth noting that they could have wider operational flexibility because they could be designed, built, and managed with more efficacy and efficiency.

One of the main advantages is that a dedicated vessel is not forced to follow fixed routes while operating its standard own business. This fact could lead it to be driven along peculiar tracks, looking for the best proper locations to discharge SL. Spread in downwelling currents is surely avoided, and even regions where possible sensible marine life is present (while existing ships could have to occasionally stop their discharge to avoid these possible problems). To select an optimal route must be considered not only the chance to increase the CO_2 removal, but also the counteract to ocean acidification.

It could be possible to implement an adequate discharge method, but also to install an efficient water pumping system (to create a SL slurry) without space-saving problems. The possibility to choose the location and to dedicate all the naval systems to the purpose, may lead to the chance to significantly increase the discharge rate from each vessel.

Caserini et al. (2021) assumed to dedicate the 85% of the average tonnage for SL storage, maximizing the quantity of such chemical carried simultaneously. By incorporating this method with the existing ships scenario, it is possible to increase widely the yearly discharge rate of SL.

The construction of a new dedicated fleet could appear as a monumental task. Caserini et al. (2021) hypothesized the realization of a fleet composed of 1,000 dedicated ships, with an

average dwt of 75,000, to SL shedding in the Mediterranean basin, spreading 1.3 GtSL yr^{-1} to remove about 1.1 GtCO_2 yr^{-1} from the atmosphere (same efficiency from Keller et al., 2014). However, it is worth noting that a quarter of existing registered cargo ships is not active (about 8,000 vessels), and so the idea to create a dedicated fleet is not so unaffordable.

3.3 SHIPS DISCHARGING SCENARIOS: ASSESSMENT AND RESULTS

Mainly basing on the Caserini et al. (2021) assessment, an investigation of different scenarios allows to better comprehend the potential of SL discharging via ships.

Caserini et al. (2021) work develops different scenarios by combining various parameters such as fleet used, vessel type, and the number of intermediate reloads (merely in the case of existing fleet). In more details, for this later parameter, single load and multiple loads are analysed. The former considers SL loading only at the departure and arrival ports and so the discharge rate depends merely upon the tonnage of the vessels and the travelled distance; in the latter, intermediate stops could allow more SL loadings, thus increasing the discharge potential. In particular, one intermediate stop for bulk carriers and two intermediate stops for container ships have been assumed.

In sight of this, three different scenarios have been assessed:

1. existing ships without intermediate stops;
2. existing ships with intermediate stops;
3. new dedicated fleet.

For the reasons mentioned in the previous chapter, the case of existing vessels involves bulk carriers and container ships, while the new dedicated fleet considers only bulk carriers because more suitable for a slurry storage.

IMO database and the Emission Database for Global Atmospheric Research (EDGAR) provide data like vessel tonnage, distance travelled during a route, average cruising speed and average CO_2 emission factors (EFs) (Caserini et al., 2021). The existing scenario considers a travelled distance and a typical vessel speed that are average values of the current global fleet. Instead, the travelled distance in the dedicated scenario is a result of a set of assumptions: a cruising speed of 25 km h^{-1} and a discharge rate of 50 kg s^{-1}; this last assumption has been made to compare these chapter's results with Caserini et al. (2021) study, which assumed such rate as conservative to limit biological problems. Such discharge rate allows obtaining a discharge distance similar to the previous one described in the existing ships' scenario. This similarity leads to a better comparison between the intended scenarios.

Table 3.2 reports the main parameters adopted for the different fleets.

Table 3.2: Main parameters of the different fleets (reworked from Caserini et al., 2021).

Ship type	Fleet type	Vessel tonnage	% tonnage for SL	Distance travelled	Average speed	Average EF
		dwt	%	km	km h^{-1}	kgCO_2 km^{-1}
Bulk carrier	Existing	75,000	13	6,300	21.4	193
	Dedicated		85	8,854	25.0	
Container	Existing	45,000	13	8,900	27.4	299

The information about the travelled distance and the number of the intermediate stops during a route, allow to evaluate the sea-leg distance travelled by bulk carriers and container ships in each scenario. In more details, this parameter represents the navigation length between each stop. Moreover, knowing the SL tonnage and the average cruising speed it is also possible to appraise the SL discharge rate, in terms of kgSL s^{-1}. The scenario with intermediate stops assumes that the SL tonnage is completely consumed in a sea-leg distance, thus implying a complete reload during the stop (Caserini et al., 2021). For existing ships SL discharge rate ranges between 4.9 and 18 kgSL s^{-1}. Table 3.3 shows all these parameters. Also, the duration of the discharging trip in each scenario is reported; knowing the transported SL mass by each vessel and the discharge rate it is possible to calculate this later parameter.

Table 3.3: Number of intermediate stops, sea-leg distance, and discharge rate for every implemented scenario (reworked from Caserini et al., 2021).

Scenario	Ship type	Intermediate stops	Sea-leg distance	Discharge rate	Discharging duration
		-	km	kgSL s^{-1}	d $trip^{-1}$
1	Bulk carrier	0	6,300	9.0	12.3
	Container	0	8,900	4.9	13.5
2	Bulk carrier	1	3,150	18.0	6.1
	Container	2	2,967	14.7	4.5
3	Bulk carrier	0	8,854	50.0	14.8

It is worth noting that in the dedicated ships scenario, the discharge parameters could be more flexible. The discharge rate could certainly be higher, but side effects on marine biology are not well known, and therefore a conservative value has been chosen. Additionally, further calculations aim to assess the yearly number of trips, considering the average days at sea (reported in Table 3.1) and the duration of a single discharging trip (reported in Table 3.3). In the case of dedicated ships, assuming that about 55 days are devoted to loading and maintenance operations, 310 days yr^{-1} at sea per vessel has been assessed (Caserini et al., 2021).

3.3.1 CO_2 EMISSION ASSESSMENT

To investigate the viability of this discharging configuration, each scenario should include an evaluation of CO_2 emissions. It is important to emphasise that the CO_2 emissions due to existing ships (scenarios 1 and 2) are apparent since ships would already travel for goods transportation.

Emissions in the dedicated ships scenario (scenario 3) are evaluated knowing proper EFs, subsequently described.

On the other hand, in the case of existing ships, SL transport emissions account only for a small fraction of the total travelling emissions (such portion of emissions is considered in scenarios 1 and 2), which are calculated throughout the previously cited EFs. Literature suggests that a percentage variation increase in total tonnage causes an emission increase corresponding to 70% of this increment, only if such tonnage variation is kept under a 100% value (Arpav, 2013; EMEP/EEA, 2019). As a result, emissions related to SL transport in existing ships scenarios account for the 13% of the total navigation emissions multiplied by 0.7 (for a total of 0.09), since a 13% value corresponds to the tonnage fraction dedicated to SL storage.

As previously mentioned in Chapter 3.3, EFs shown in Table 3.2 are obtained from EDGAR database, which contains emissions inventories both of GHGs and air pollutants. EDGAR is a collaborative project carried out by the Joint Research Center (JRC) and the PBL Netherlands Environmental Assessment Agency (Crippa et al., 2020). The knowledge of the global ship traffic fuel consumption allows calculating ships' EFs, throughout a spatial disaggregation thanks to Long Range Identification and Tracking (LRIT) data signals (Alessandrini et al., 2017): Figure 3.2 reports an example. EFs are considered identical in all the vessels of the same category. This study considers EDGAR data referred to the year 2018 analysis (EDGAR, 2018), getting the previously mentioned 193 and 299 kgCO_2 km^{-1} EFs for bulk carriers and container ships respectively (Table 3.2).

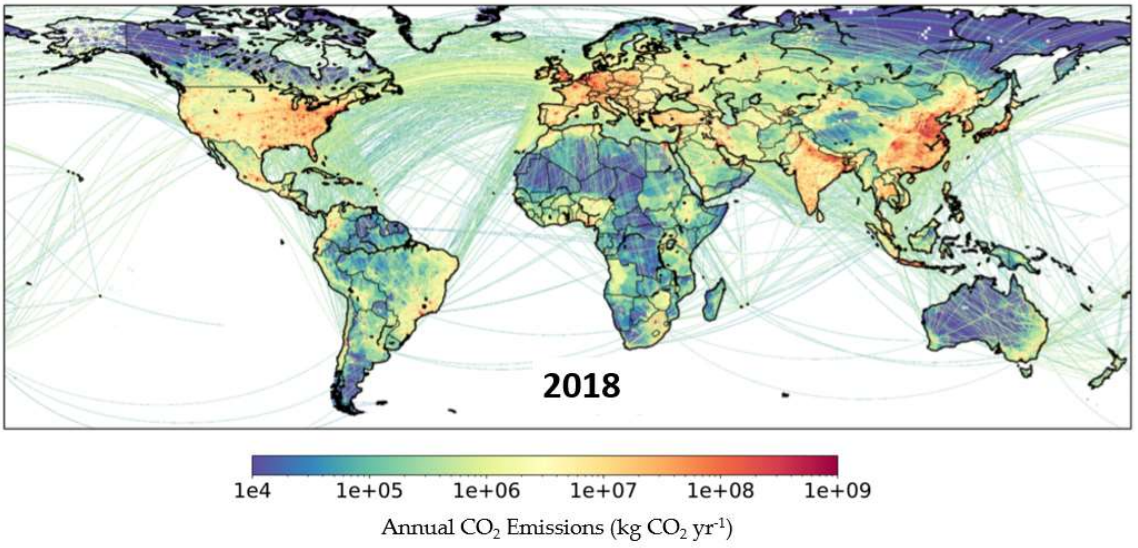

Figure 3.2: Annual CO_2 emissions (in term of kgCO_2 yr^{-1}) in 2018 due to shipping (Jones et al., 2021).

Total emissions in each scenario are calculated multiplying EFs by the total discharging distance travelled during one year of spreading, thanks to the following formula (3.1).

$$E_{CO_2} = EF_{ship}\, d \tag{3.1}$$

where:

E_{CO_2}: total emissions [gCO_2 yr^{-1}];
EF_{ship}: emission factor of the vessel [gCO_2 km^{-1}], reported in Table 3.2;

d: travelled distance [km yr^{-1}], reported in Table 3.3.

These emissions shall be subtracted from the theoretical amount of CO_2 removed via OAE to obtain the net amount of CO_2 actually removed. First of all, the yearly SL mass discharged by each ship is calculated as the ratio between the total SL mass discharge and the discharge duration (formula (3.2)). In more detail, this theoretical amount of CO_2 removed can be calculated by multiplying the total SL mass discharged yearly by the specific theoretical removal rate (formula (3.3)), as described in Chapters 2.2 and 2.3.

$$M_{SL,y} = M_{SL} \frac{365}{d_d} \tag{3.2}$$

where:

$M_{SL,y}$: yearly SL mass discharged [tSL yr^{-1}];
M_{SL}: total SL mass transported by each vessel [tSL];
d_d: discharge duration [yr].

$$CO_{2,th} = M_{SL,y}\ \delta_{th} \tag{3.3}$$

where:

$CO_{2,th}$: theoretical amount of CO_2 removed [tCO_2 yr^{-1}];
δ_{th}: theoretical CO_2 removed per SL unit [tCO_2 tSL^{-1}], assumed 0.83 tCO_2 tSL^{-1} as previously explained in Chapter 2.3.

Net CO_2 removed per SL unit is evaluated (δ) (formula (3.4)), and it is compared to the theoretical CO_2 removal rate (δ_{th}) getting the penalty of this methodology (formula (3.5)). So, penalty permits to compare the CO_2 removal with an ideal scenario without transport emissions where the CO_2 removed is equal to the maximum value obtainable.

$$\delta = \frac{CO_{2,th} - E_{CO_2}}{M_{SL,y}} \tag{3.4}$$

$$\eta_p = 1 - \frac{\delta}{\delta_{th}} \tag{3.5}$$

where:

δ: net CO_2 removed per SL unit [tCO_2 tSL^{-1}];
η_p: penalty [-].

All these results are reported in Table 3.4.

Table 3.4: Main results of the assessment of the discharging configuration in ship's wake, in terms of theoretical CO_2 removed, net CO_2 removed, CO_2 removed per SL unit discharged and penalty.

	Scenario	1	2	3	Reference
Total SL discharged, $M_{SL,y}$	GtSL yr^{-1}	1.78	4.00	1.34	Formula (3.2)
Theoretical CO_2 removed, $CO_{2,th}$	GtCO_2 yr^{-1}	1.48	3.33	1.11	Formula (3.3)
	tCO_2 $vessel^{-1}$ $trip^{-1}$	6,820	6,510	53,068	
Emitted CO_2, E_{CO_2}	GtCO_2 yr^{-1}	0.03	0.03	0.04	Formula (3.1)
	tCO_2 $vessel^{-1}$ $trip^{-1}$	155	155	1,709	
Net CO_2 removed	GtCO_2 yr^{-1}	1.45	3.30	1.08	Formula (3.4)
	tCO_2 $vessel^{-1}$ $trip^{-1}$	6,665	15,196	51,359	
Net CO_2 removed/SL discharged, δ	tCO_2 tSL^{-1}	0.81	0.82	0.81	Formula (3.4)
Penalty, η_p	%	2.27	1.01	3.22	Formula (3.5)

It is easily notable that second scenario's penalty is minor that the others because much more SL could be discharged thanks to the intermediate reloading, even if the total travelled distance by the entire fleet remains always the same. On the other hand, logistic issues (i.e.: additional time needed for loading, lime manufacturing infrastructure) might narrow this opportunity.

3.3.2 PRELIMINARY COST ASSESSMENT

For cost evaluation, it is important to distinguish between the operating (Opex) and capital (Capex) expenditures. Opex is defined as a continuous cost for running a system or a business, while Capex is the expense of providing durable parts for a product or system. The following cost estimation is based on the methodology adopted in the study by Caserini et al. (2019), revising it to the scenarios previously described.

Opex evaluation

Opex considers all the time-dependent expenditures of the system. Therefore, total Opex increases according to the discharge duration: as a consequence, it decreases with the increment of vessel speed and discharge rate (especially in the case of dedicated ships scenario). Opex depends on various factors. The principal operating costs are crew salaries, fuel consumption, eventual maintenance or repairs, taxes related to the shipping duration and harbour fees, insurance and administration costs, cargo handling, and ground operations in port (Polo, 2012).

Literature reports daily costs for various types of ships, mainly characterized by different tonnages. According to the evaluated scenarios, this assessment considers vessels with 75,000 and 45,000 dwt. A typical average daily cost for a 75,000 dwt vessel could be 14,750 \$ d^{-1}, while a 45,000 dwt vessel cost could range between 10,000 and 12,750 \$ d^{-1} (Vasileiou, 2018); in this last case a value of 11,500 \$ d^{-1} is evaluated. The cost estimation considers an exchange rate of 1.19 \$ $€^{-1}$ (Morningstar, 6th September 2021). The total shipping Opex is calculated as the product between the average daily costs and the discharge duration; consequently, this value

is divided by the tonnage of transported SL to find the shipping Opex per ton of SL, and then it is divided by the specific CO_2 removed per SL mass δ to find the cost per CO_2 removed. The equation (3.6) allows calculating the shipping Opex per unit of transported mass.

$$C_{opex,s} = \frac{c_d\ t}{M_{SL}\ \delta} \tag{3.6}$$

where:

$C_{opex,s}$: total shipping Opex [€ tCO_2^{-1}];
c_d: average daily shipping cost [€ d^{-1}];
t: navigation duration [d].

It is worth noting that the existing ships scenario considers average values and takes into account only active vessels. The total shipping Opex (equal to 2.9 € tSL^{-1}) permits obtaining a proximate Opex evaluation in existing ships scenarios. Considering the quantity of transported SL, such costs has been obtained multiplying the transported mass unit cost by the SL quantity, since it is the lack of revenue for the transportation of other goods.

Considering the Opex evaluation, Caserini et al. (2019) supposed to install suction pumps with 24 MW power and capacity 3600 t h^{-1}. It is possible to calculate the energy needed for SL discharging by multiplying the discharging time (reported in Table 3.3) and the pump's power.

An evaluation of the pumping system fuel consumption is necessary. The lower heating value (LHV) of HFO combustible is about 40.4 MJ kg^{-1} (Bengtsson et al., 2011); considering that 1 kWh is equal to 3.6 MJ, it is possible to assess that the intended LHV is 11.2 kWh kg^{-1}. It is also important to determine the effective pump power; at this purpose a pump efficiency of 0.70 has been assumed (Stoffel, 2015). To evaluate the fuel cost per trip, the assessment of HFO cost is fundamental: the chosen fuel price is 620 $ t^{-1} (Ship & Bunker, 27th October 2021). Knowing the energy consumption, therefore, it is possible to evaluate the fuel usage and its price per each discharging trip (formula (3.7)). The total pumping Opex is found as the product between the energy cost and the total energy requirement (3.8); as done before, it is divided by the SL tonnage transported, and then by the specific CO_2 removed per SL mass.

$$c_{fuel} = \frac{t_p\ P_p}{\eta\ LHV} \tag{3.7}$$

where:

c_{fuel}: fuel consumption [kg];
t_p: pumping time [h];
P_p: pump power [kW];
η: pump efficiency [-];
LHV: lower heating value [kWh kg^{-1}].

$$C_{opex,p} = \frac{c_{fuel}\ c_f}{M_{SL}\ \delta} \tag{3.8}$$

where:

$C_{opex,p}$: total pumping Opex [€ tCO_2^{-1}];
c_f: specific fuel price [€ kg^{-1}].

Total Opex costs per unit of CO_2 removed are calculated as the sum of the shipping Opex and the pumping Opex (formula (3.9)).

$$C_{opex} = C_{opex,s} + C_{opex,p} \quad (3.9)$$

Capex evaluation

Capex is generally split into two parts; bare erected costs, which include the cost of process equipment and needed infrastructures, and contingencies. Dedicated ships scenario considers the costs of vessels and infrastructures for the SL discharge, while existing ships scenarios evaluate only infrastructures prices. It is worth noting that eventual rates of interests are neglected because they are compensated by the savings from adaptation of existing ships.

The dedicated ship scenario evaluates Capex considering even vessels' cost. This case considers a Panamax vessel, since it is a bulk carrier type with a similar cargo capacity to the analysed vessels; a price of €25,000,000 has been assumed (Kretschmann et al., 2017) for a lifespan of 25 years (Hua et al., 2018). It is worth remembering that existing ships or inactive vessels could be used to build new vessels for the dedicated fleet, Capex related to ships' price could be significantly lower. So, to calculate ships capital cost for each trip, it is necessary to divide vessels' price by their lifespan and by the number of their yearly trips.

Moreover, this study aims to examine only the discharge systems, so it neglects SL production costs. In each scenario, the fixed costs evaluated are related to engines and pumps for water suction and SL discharge, pipes and distribution lines, and dedicated tanks. A 10% contingencies value on the total Capex is added. Furthermore, these infrastructures are associated with a 25 years lifespan. Table 3.5 reports the costs of these infrastructures, as reported by Caserini et al. (2019).

Table 3.5: Ship conditioning Capex for a bulk carrier with a dwt of 75,000 (Caserini et al., 2019).

Parameter	u.m.	Value
Engine, pump, accessories	$	16,250,000
Distribution lines	$	3,250,000
Discharge pipes	$	2,437,000
Tank improvement	$	2,275,000
Control	$	812,500
Contingencies	$	1,755,000
Total	$	26,780,000
Lifespan	yr	25
Yearly total Capex	$ yr^{-1}	1,071,200

Comparing these costs to the actual capacity of the ships of the analysed scenarios, Capex per ton of SL transported is calculated. The specific total Capex cost per unit of CO_2 removed has been obtained dividing the cost per unit of discharged SL by the CO_2 removed per unit of spread SL, δ.

Total costs

Total costs are calculated as the sum of Opex and Capex costs for each analysed scenario and reported in Table 3.6. Additionally, Figure 3.3 provides a graphical analysis of the costs.

Table 3.6: Assessment of the operative, capital, and total costs for discharging via ships.

	Scenario	**1**	**2**	**3**
Total Opex	€ vessel^{-1} trip^{-1}	27,476	61,513	211,155
	€ tCO_2^{-1}	4.09	4.04	4.11
Shipping Opex	€ tCO_2^{-1}	3.53	3.48	3.56
Pumping Opex	€ tCO_2^{-1}	0.57	0.56	0.55
Total Capex	€ vessel^{-1} trip^{-1}	31,325	32,227	90,484
	€ tCO_2^{-1}	4.67	2.02	1.76
Conditioning Capex	€ tCO_2^{-1}	4.67	2.02	0.83
Vessel Capex	€ tCO_2^{-1}	-	-	0.93
Total costs	€ vessel^{-1} trip^{-1}	58,801	93,739	301,639
	€ tCO_2^{-1}	8.76	6.06	5.87

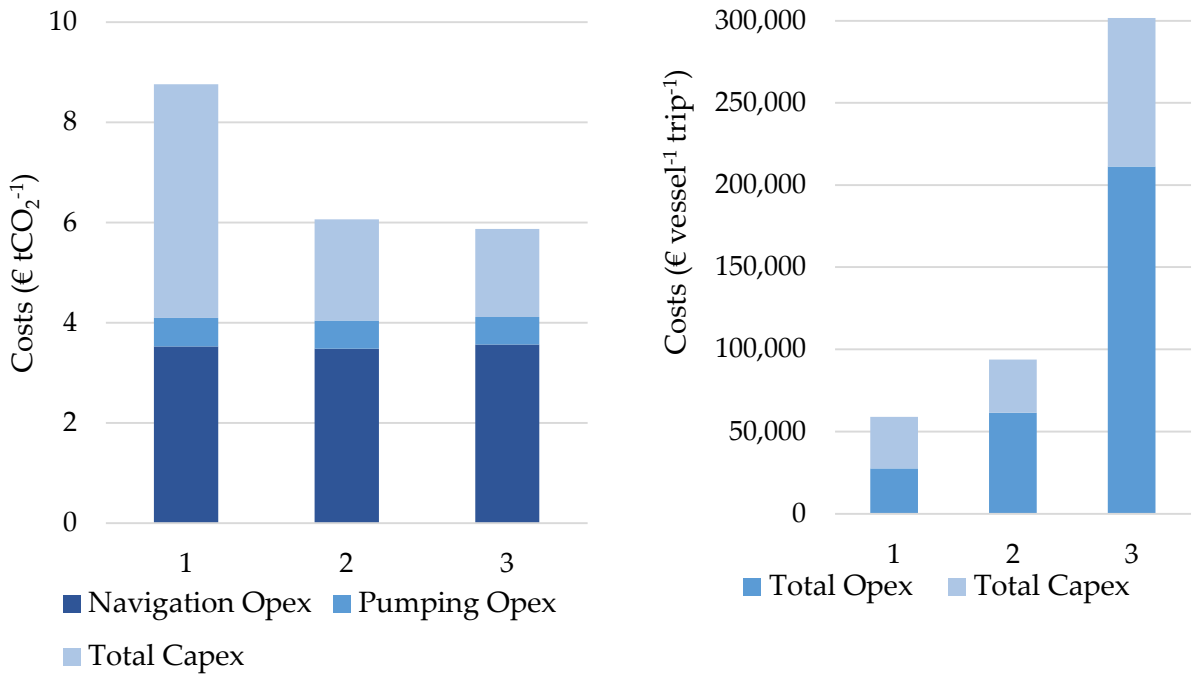

Figure 3.3: Graphical analysis of the total costs for each analysed scenario in terms of € tCO_2^{-1} (left) and also in terms of € vessel^{-1} trip^{-1} (right).

It is worth noting that the Capex costs are the main voice in determining total costs for the existing ships scenarios. The specific Capex per unit of CO_2 removed is bigger for existing ships rather than dedicated ships; this is mainly due to the fact that dedicated ships could transport much more SL than the vessels in other scenarios. On the other hand, the Capex per trip for each vessel in the dedicated ships scenario is higher than the other two with existing ships because of the vessels' capital cost since they should be bought. Total Opex per trip is higher in the case of dedicated ships because it is a function of the transported and discharged SL amount.

4. DISCHARGE VIA RAINBOWING

The following chapter investigates a new kind of marine vessels for SL shedding: a particular type of hydraulic dredger, the so-called Trailing Suction Hopper Dredger (TSHD). Hydraulic dredgers comprehend a list of structures that make use of centrifugal pumps for the transport process of dredged materials. A wide variety of maritime construction and maintenance - projects usually operating in the upholding of ports, conventionally utilize them. Moreover, they are used to remove sand and even to transport it during land reclamation plans, mixing it with water (IADC, 2014).

An investigation examines the rainbowing pumping and discharging systems in order to take into consideration their installation on conventional ships. In light of this, the assessed scenario involves the installation of rainbowing systems on conventional ships for good transportation like bulk carriers. Later, two alternative scenarios are briefly examined; the former is built up by installing multiple rainbowing outlets on the same vessel, while the latter it is built by coupling the rainbowing discharge with the shedding in ship's wake with the aim to maximize the discharge rate.

Additionally, further analyses investigate the discharge phase with the aim to better understand the area involved during the discharging phase and consequently the related impacts on marine biology both in terms of ecotoxicity and mechanical stress.

4.1 TSHDs CHARACTERISTICS

The main aim of this chapter is to investigate the possibility to install the rainbowing system and the suction system typical of a TSHDs on a bulk carrier for SL spreading. The vessel hold stores the SL powder, and when arrived at proper location, water is pumped into the ship and mixed with SL, creating a slurry; the suction system operates in a similar way compared to a traditional dredger but pumping only seawater and not sand or other materials. Later, a discharge system unloads the mixture on the ocean's surface. At this purpose, an evaluation of the TSHDs characteristics is carried out.

TSHDs are self-propelled naval vessels, containing a hopper or hold. Mainly used to dredge sand, they can also operate with other materials, such as clay or gravel. They are equipped with one or more suction pipes with a special dredging head; a high-pressure circulation system for water equips the last stretch of the dredging head. Suction pipes are underwater, and they aim to suck up materials while the ship is moving; this mixture of sand and water is then moved to the hopper.

A TSHD must have an overflow system to remove excess water. Besides, they don't need any type of anchorage system during dredging operation, which can be an obstacle for passing ships. Since TSHDs are self-propelled, they can carry dredged materials over long distances. TSHDs are the only dredgers able to operate offshore, in bad weather conditions. Rough seas and strong winds don't affect substantially the activity of these vessels; only winds over 35 knots (about 65 km h^{-1}) could influence the working performance of such ships. A loaded vessel moves to the placement site, where the slurry discharge occurs in many possible

methods. The easiest way is the hatches opening on the bottom of the vessel, and so the material is deposited. Otherwise, an alternative is to use submerged, or floating pipelines to pump ashore the slurry. The last possibility is the usage of heavy-duty pumps, which eject the material into the air forming an arc, during a process called "rainbowing", as represented in Figure 4.1.

Figure 4.1: TSHD during rainbowing process.

A rainbowing technique is traditionally practiced pumping a sand slurry and depositing it at the reclamation site: heavy duty pumps spray the mixture over the vessel's bow into the air, forming an arc in the sky which looks like a rainbow: for this reason, this method is called rainbowing. Various reasons support this discharging configuration. Generally, it is the best way to discharge huge quantities of materials in shallow waters; additionally, it is the most economical depositing method in dredging because it avoids the usage of pipelines, boosters, or landlines (IADC, 2014).

The chance to utilize the rainbowing in the SL discharging methodology is feasible because of the large flexibility of this system. They can actually operate with a large variety of materials: gravel, sands, silts, or even clays. As described in Chapter 2.4.3, SL particles dimensions usually range between 4 and 39 μm (Unicalce, 2021), which is included in the silt size class, generally considered between 2 and 50 μm (Moorberg and Crouse, 2021). TSHDs could be appropriate because they can work in a great variety of meteorological conditions, from calm waters to turbulent situations with more active weather and waves.

4.2 RAINBOWING DISCHARGE EFFICIENCY

One of the main advantages of the rainbowing methodology applied in the OAE is that it involves a SL slurry spreading right over the sea surface in a large impact area.

Different factors influence the flow rate of a TSHD when rainbowing; an examination of the nozzles characteristics is fundamental: especially their diameter, shape, and their height in relation to the waterline. The angle of the nozzle is one of the main characteristics of the discharge. In the past, a 45° angle was common, but nowadays a 30° angle is generally adopted. Studies demonstrated that in this technique, such an angle allows for better sediment

loss control (Wang et al., 2018). The nozzle diameter plays a key role: a small nozzle implies a low output production, but it projects the slurry over high distances.

The assessment feasibility of this discharge type must consider many factors. The consumption of the rainbowing pump must be sufficiently low, but it has to be powerful enough to spread the slurry on a long-range. Even the fuel consumption of the suction system must be evaluated: in any case, a vessel loaded at the departure with a slurry, and not a powder, would have a great penalty in SL discharge potential. The impact area must be adequately wide because it aims to minimize the load per unit area, to reduce surface concentration and the pH spike. The nebulization during the discharge aids to achieve a great dispersion of the material, because winds could transport small slurry droplets before the settling.

However, it is worth noting that an additional reaction could occur during the rainbowing trajectory. SL particles could react in the atmosphere with CO_2 by forming calcium carbonate and water. This reaction is known as carbonatation and is still suitable to remove CO_2 from the atmosphere. Nevertheless, the carbon removal efficiency of this reaction is much lower than a typical OAE process. In fact, only one theoretical mole of CO_2 is removed by one mole of SL, as can be seen from reaction (4.1), compared to the two removed moles considering an ocean liming approach (equations (2.4) and (2.5)). The occurrence of this phenomenon could slightly reduce the overall efficiency.

$$Ca(OH)_2 + CO_2 \rightarrow CaCO_3 + H_2O \tag{4.1}$$

4.3 RAINBOWING DISCHARGING PARAMETERS

TSHDs could differ widely in dimensions and discharging parameters (i.e.: flow rate, rainbowing distance, installed power). For instance, one of the largest TSHD produced (the "Cristobal Colòn", built by the Jan De Nul company in 2009) has a capability of 46,000 m^3, a length of 223 m, and its deadweight is 78,500 t. Its sailing velocity is about 18 knots (about 33 km h^{-1}) thanks to a propulsion power of 2×19,200 kW. The power of the suction system is 2×6,500 kW, while the discharging pump operates at a 16,000 kW power (Indar, 2021).

The TSHDs flow rate is significantly high: generally, it ranges between 200 and 10,000 $m^3\ h^{-1}$ (ISPRA, 2017). It is also important to assess the discharging system power installed, in order to evaluate the consumption of this discharge methodology. This power is obviously very variable, because it depends on the material outflow and the rainbowing distance reached. The smallest TSHDs, with a hopper volume between 3,000 and 7,500 m^3, usually have an installed discharging power that ranges between 2,000 and 4,000 kW. Quite larger TSHDs, with a capacity of 10,000-15,000 m^3, generally have a 7,500-9,000 kW powered spreading system. TSHDs with the higher hopper volume, more than 20,000 m^3, have usually discharging system with a power of 14,000-16,000 kW (Jan De Nul, 2021). The relation between pump power and flow rate is reported by the formulation (4.2).

$$P_p = \frac{\gamma_w\ Q_s\ H}{\eta} \tag{4.2}$$

where:

P_p: pumping power [W];
γ_w: seawater specific weight [N m^{-3}];
Q_s: slaked lime slurry discharge rate [m^3 s^{-1}];
H: pump total head [m];
η: pump efficiency [-].

The rainbowing distance is a fundamental characteristic in the evaluation of the SL discharge feasibility by TSHDs. Usually, it is about tens of meters, ranging between 40 and 100 m. However, the most powerful vessels could reach higher distances; for instance, modern jumbo trailers can spray the slurry reaching 150-160 m.

Table 4.1 summarizes all these described parameters.

Table 4.1: Typical ranges of TSHDs parameters (ISPRA, 2017; Indar, 2021; Jan De Nul, 2021).

Parameter	**u.m.**	**Range**
Hopper volume	m^3	3,000 - 46,000
Discharge flow rate	m^3 h^{-1}	200 - 10,000
Installed power	kW	2,000 - 16,000
Rainbowing distance	m	40 - 160

The slurry imprint is clearly not well defined, because droplets fall from all the water mixture arc: wind turbulence maximizes this dispersion. During a rainbowing discharge, the slurry outflow falling boundary on the sea surface has an elliptical shape. This ellipsis could be generally approximated as a circle; such a circle usually has a diameter b that accounts for about the 20% of the total rainbowing distance l (Wang et al., 2018). This causes a triangular imprint with a higher concentration of slurry in a circular boundary at the end of the rainbowing distance. As stated in the previous chapter, the spray angle with respect to the water surface α_h that maximizes rainbowing distance is about 40-45°; however, TSHDs usually discharge with a 30-35° angle, because literature studies evaluated that a 40-45° angle creates craters on the seafloor. Since the current study aims to minimize the SL load on the surface in order to avoid environmental and biological issues, it is important to guarantee a larger impact area, maximizing the rainbowing distance. The angle is considered 40-45°, and this value ensures a more circular impact area.

Since the basis of the triangular imprint is about 20% of the rainbowing distance (formula (4.3)), after simple trigonometric assumptions, it is possible to state that the longitudinal discharge angle α_l (transversal to the main movement direction of the ship) is about 11.5°.

$$b = \frac{l}{5} \tag{4.3}$$

where:

b: basis of the triangular imprint [m];
l: rainbowing distance [m].

Assuming a semi-circular slurry trajectory with a 100 m diameter (which corresponds to efficient rainbowing systems in circulation (Indar, 2021)), the rainbowing arc apex h is calculated at about 50 m from the seawater surface thanks to the following formula (4.4); this assumption is made for the sake of simplicity, neglecting any possible wind interferences.

$$h = \frac{l}{2} \tag{4.4}$$

where:

h: rainbowing arc apex [m].

Figure 4.2 provides a qualitative diagram of the discharging process.

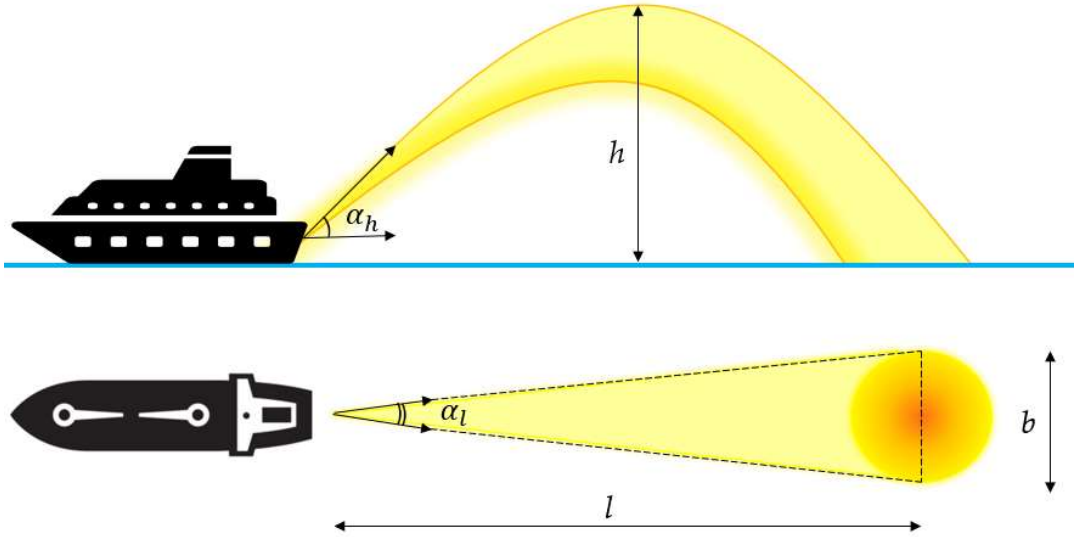

Figure 4.2: Qualitative diagram explaining the area covered by SL slurry during rainbowing showing the spray angle with respect to the water surface and longitudinal angle (vessel not in scale).

4.4 DISCHARGING SCENARIO VIA RAINBOWING FROM TYPICAL VESSELS

The present evaluation builds a discharging scenario supposing to apply the water suction and discharging devices to a typical naval vessel as general bulk carriers or container ships, considering the cargo capacity of such vessels instead of a classical hopper volume. This assumption maximizes the transported SL, comparing this discharge method to the discharge in the ship's wake, already discussed in Chapter 3.3. The current chapter assumes to consider only bulk carriers, fully loaded with SL: ship's capacity is so maximized.

Therefore, in the analysed system there are many differences if compared to a typical TSHD. The main dissimilarity is the absence of the dredging system because there is no need for suction sand or other materials in the cargo hold. Drag head components are thus avoided, as well as complex suction arm and long suction pipelines originally aimed to transport the sand

mixture from the seabed to the ship. A simple hydraulic suction device replaces this structure to pump water on the vessel. This latter appliance is however included also in a classic TSHD, which has to transport a mixture of sand and water, in form of a slurry.

A dedicated space in the hold allows the pumped water mixing with SL, to obtain a slurry with a suitable calcium hydroxide concentration. Then, adequate mixture pipelines transport this slurry toward the rainbowing device. Another space in the ship must include the pumps' room, which aims to aspire water and to eject the SL slurry through the rainbowing system (Boskalis, 2012).

A rainbowing device must be therefore installed at the vessel's stern. The installed power is the main parameter that affects the discharging distance. Other important characteristics of this system are the injection angle and the diameter of the nozzles (Wang et al., 2018).

4.5 ANALYSIS OF DISCHARGE PHASE

The present chapter focuses on the study of the discharged water jet behaviour to understand the impacts and side effects on the organisms present in seawater, especially in the SML. In particular, it is crucial to assesses the sinking depth of the rainbowing jet below the water surface and consequently a deep investigation of the imprinting area and volume is required.

Additionally, the analysis of the discharging phase is helpful to better investigate the biological issues mainly linked to ecotoxicity due to SL dissolution in seawater.

4.5.1 ANALYSIS OF THE SINKING DEPTH OF THE RABOWING JET

In order to analyse the sinking depth of the rainbowing jet, some simple experiments have been carried out to basically understand and comprehends the physical phenomenon taking place and the volume of water involved. However, since this is a preliminary analysis, it does not consider the intensity of the jet that could be quite different from the rainbowing spreading scenario.

For this purpose, the experiments involved the creation of different slurries with similar characteristics (i.e.: orange juice with salt or water and tomato sauce) and subsequently discharged to understand how deep the mixture develops below the water surface; in addition, to better investigate the behaviour of SML and how it is involved during the discharging, it has been recreated thanks to the use of a floating powder (i.e.: pepper, coffee powder) or oil so that it was placed at the interface between air and water. In this way it is easy to note how much it is affected by the discharging phase.

It is important to underline that these simple experiments have been carried out creating slurries with a density difference that is comparable to the ones of the slurry discharged. In particular, the discharged slurry has been produced by adding a quantity of table salt ($NaCl$) to obtain a 1.14 kg L^{-1} density mix; this density differs by 0.12 kg L^{-1} compared to freshwater, that is the same divergence between seawater density ρ_w and a SL slurry at a 10% concentration.

Figure 4.3 shows different spreading tests conducted at different discharging heights. In the first figure the slurry used is made by mixing water with tomato sauce and SML is recreated thanks to an oil layer; in the last two photos orange juice and salt are mixed while SML is recreated with coffee powder.

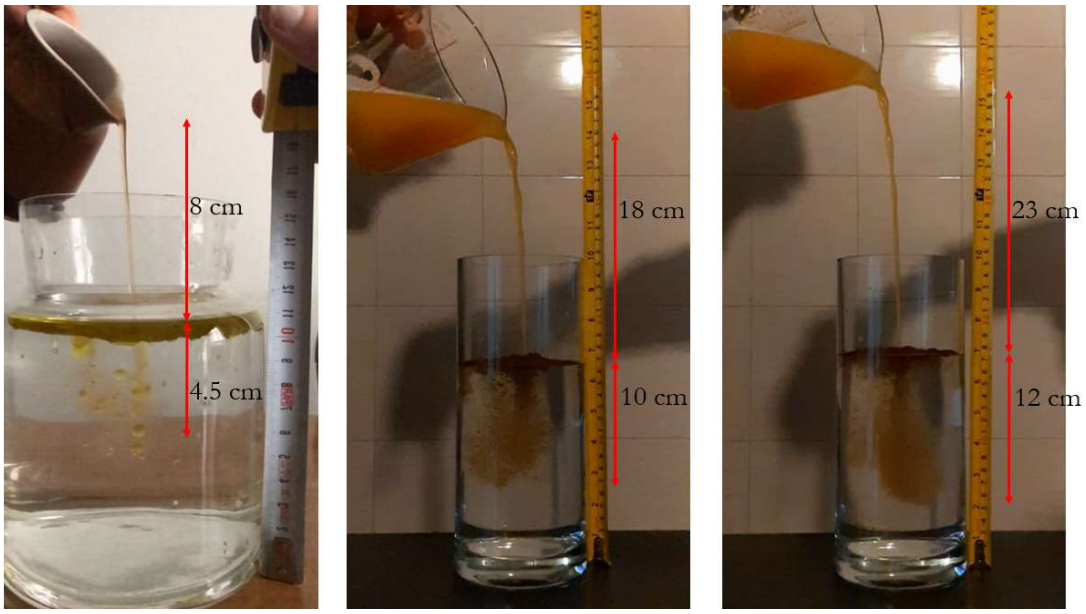

Figure 4.3: Different experiments showing that the sinking depth is almost equal to half the discharging height.

This analysis shows that the jet sinks about half the maximum discharge height; in this regard, knowing the height of the apex of the flow h, a maximum sinking depth equal to half height has been calculated thanks to the formula (4.5). Figure 4.4 reports a qualitative graphical scheme.

$$z = \frac{h}{2} \tag{4.5}$$

where:

z: sinking depth [m].

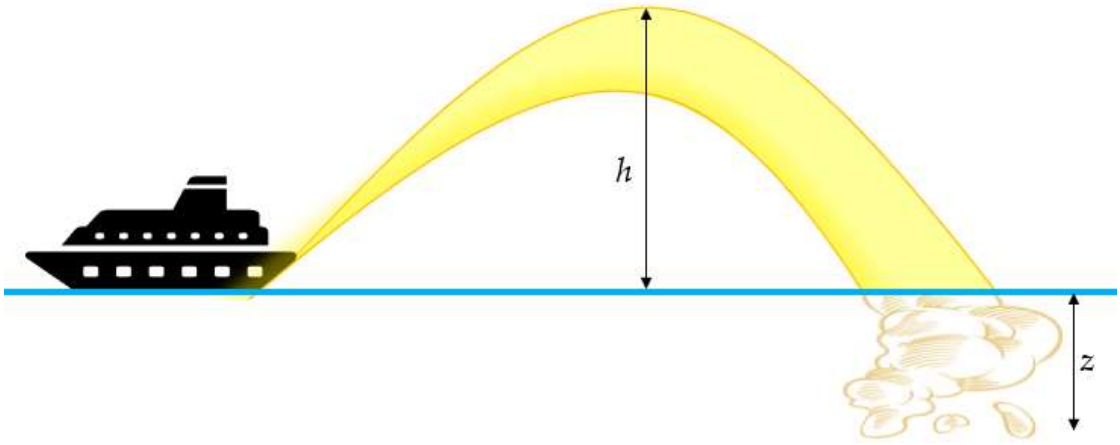

Figure 4.4: Qualitative diagram explaining the jet sinking below water surface (vessel not in scale).

The experiments show that the simulated SML is highly involved in jet sinking process, but different behaviours occur according to its different composition. When it is recreated as a powder (like coffee), the water jet drags downwards only few SML particles, while the major part stays right under the surface; differently, a liquid SML (as the case of the oil layer) is more involved in this phenomenon as it sinks reaching the same depth of the slurry jet. Nevertheless, a rainbowing jet fractionates more in the atmosphere, and so its mechanical impact on the surface could be less significant than simulated. However, it is possible to assess that the SML perturbation is quite high due to the rainbowing jet mechanical action, but future fluid dynamic studies should better assess diffusion.

4.5.2 ANALYSIS OF THE IMPRINTING AREA AND VOLUME

This discharging method could pose some problems to marine environment, especially to SML. The major problems are given by the mechanical impact of the slurry jet over the sea surface and also if SL concentrations are higher than ecotoxic threshold. For this main reason a rough assessment of the SL load per unit area is carried out.

A sequence of geometrical assumptions is necessary to evaluate the impact on the sea surface. As described in Chapter 4.3 and graphically in Figure 4.2, the rainbowing imprint area is a circle with a 20 m diameter; but the discharged SL is not homogenously distributed in this circular imprint area. The majority of SL impacts the proximity of the imprint circumference centre, likely spread as a normal distribution. Nevertheless, according to Wang et al. (2018), it is possible to assess that the principal impact zone is not located exactly in the centre of the circular imprint area but slightly shifted toward the ejection point. Thanks to the qualitative representations made by Wang et al. (2018), it has been assessed that the centre line impact is located approximately at a quarter of the distance between the inner and the outer boundary, as Figure 4.5 shows. The distance between these two centres represents a sort of eccentricity and can be calculated thanks to the following formula (4.6).

$$e = \frac{b}{4} \tag{4.6}$$

where:

e: eccentricity of the rainbowing imprint area [m];
b: basis of the triangular imprint [m].

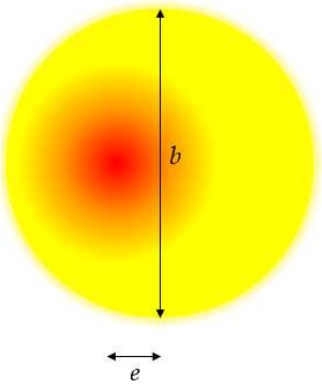

Figure 4.5: Qualitative diagram explaining the total impact area (yellow) and the principal imprint area (red).

As a result, the majority of SL impacts the surface water on a narrower strip if compared to the ideal length of 20 m. For the sake of simplicity, in order to calculate the SL load per unit area, the impact distribution adopts an equilateral triangular shape. By subdividing such distribution into N different sections, the percentage load f_i for each section has been obtained, as Figure 4.6 shows.

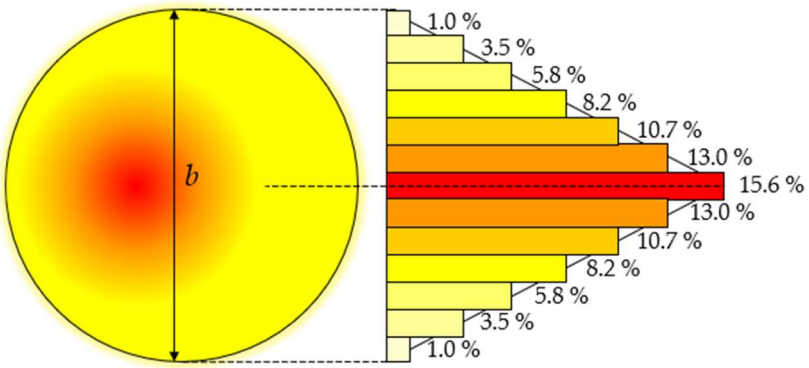

Figure 4.6: Diagram showing the SL percentage distribution over the total imprinting area.

The SL load per unit area, in terms of kgSL m^{-2}, is calculated considering that the entire SL tonnage is discharged in a linear trajectory long as the entire discharge distance d and with a width b of 20 m, as Figure 4.7 qualitative explains. The SL load per unit area for each stripe is calculated thanks to the following formula (4.7).

Thirteen stripes equally divide the width of the impact area, and so SL tonnage M_{SL} is discharged on each stripe as a function of the percentage distribution f_i, shown previously in Figure 4.7.

$$L_i = \frac{M_{SL}\, f_i}{\frac{d\, b}{N}} \tag{4.7}$$

where:

L_i: SL load per unit area [kgSL m^{-2}];
M_{SL}: SL total transported mass [kgSL];
f_i: percentage distribution [-];
d: travelled distance per trip [m];
N: number of stripes [-], assumed 13.

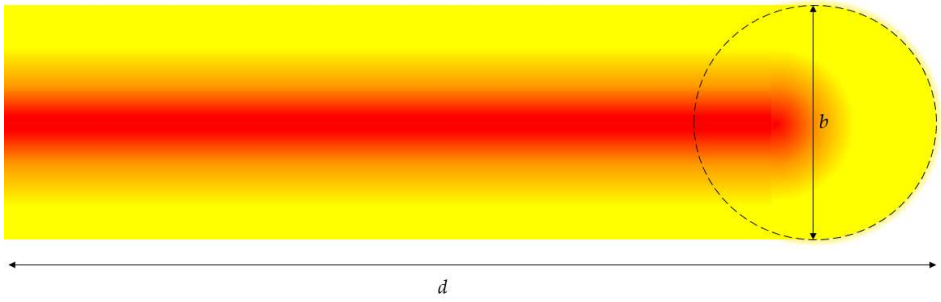

Figure 4.7: Qualitative diagram showing the linear trajectory during SL discharge.

Figure 4.8 presents SL load per unit area L_i; as expected it reaches the maximum value (0.73 kgSL m^{-2}) in the central stripe and decreases toward the boundaries.

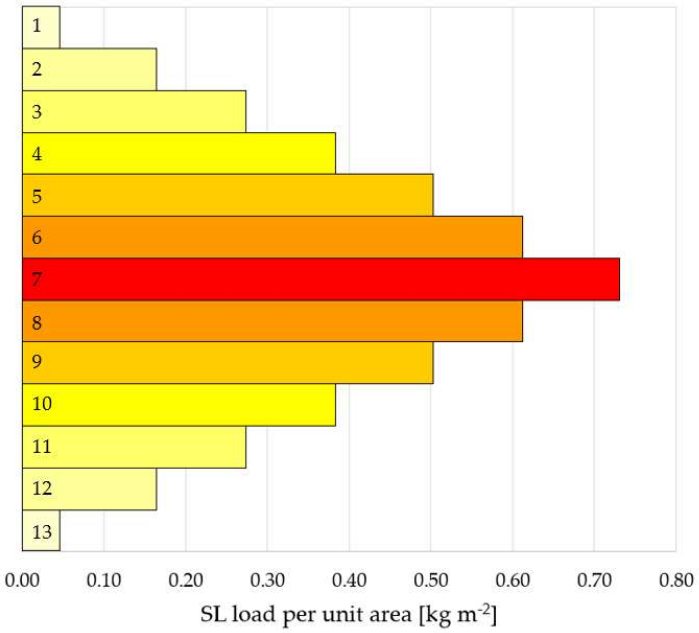

Figure 4.8: Specific SL load, in terms of kgSL m^{-2}, per each fraction of the total rainbowing discharging area. The number in each stripe indicates the stripe's number.

In order to evaluate the maximum SL concentration in water, it is necessary to assess the water volume involved during the particles' sinking (formula (4.8)). As done before, N different fractions (denoted by V_N) divide this total volume (formula (4.9)). The knowledge of the impact area and the depth z reached by the rainbowing jet allow the evaluation of this volume.

$$V = V_N \, N \tag{4.8}$$

$$V_N = d \frac{b}{N} \, z \tag{4.9}$$

where:

V: water volume involved during the sinking phase [m^3];
V_N: water volume per each stripe involved during the sinking phase [m^3];
z: sinking depth [m].

It is possible to calculate the SL concentration in seawater for each stripe by multiplying the total SL mass M_{SL} by its related fraction f_i, dividing by the water volume V_N involved during the sinking phase for each stripe (formula (4.10)).

$$c_{SL,i} = \frac{M_{SL} \, f_i}{V_N} \tag{4.10}$$

where:

$c_{SL,i}$: SL concentration in seawater [mg L^{-1}];

Table 4.2 reports SL load per unit area and SL concentration in seawater; it is worth noting that the maximum load is reached in the central stripe.

Table 4.2: SL load and concentration in seawater for each stripe.

#Stripe	Distribution f_i	SL load	SL concentration
	%	kgSL m^{-2}	mgSL L^{-1}
1 – 13	1.0	0.05	1.82
2 – 12	3.5	0.16	6.55
3 – 11	5.8	0.27	10.92
4 – 10	8.2	0.38	15.29
5 – 9	10.7	0.50	20.03
6 – 8	13.0	0.61	24.40
7	15.6	0.73	29.13

Knowing the SL concentration in seawater and the water volume involved during discharging, it is possible to examine the possible ecotoxic impacts on biology (the ecotoxic levels are reported in Table 2.1); these evaluations neglect possible reactions and water turbulence, thus providing conservative and probably too high concentration values compared to a real situation.

Maximum SL concentration in seawater accounts to 29.1 mg L^{-1}, so ecotoxic problems are at least avoided because the minor NOAEC considered accounts to 50 mg L^{-1} (96 h of exposure for sand shrimp). Since this value is the result of a series of strong assumptions (the sinking depth, the rainbowing distance and the related imprint area, the SL distribution in the imprint area), the sinking depth which could provide biological issues has been found. In particular, it is possible to state that assuming a sinking depth of 14.5 m instead of 25 m, would provide a SL concentration of 50.2 mg L^{-1}, slightly higher than the minor NOAEC considered, the one of sand shrimp (it is worth remembering that NOAEC values are defined for exposure time of 96-h). In this regard, more careful and detailed studies about the described sinking depths are necessary. Nowadays such investigations are not available in scientific literature, because usually TSHDs are used to deposit inert materials on the seafloor.

Moreover, in addition to ecotoxic problems, the discharge phase could pose some issues for the organisms present in the SML. In this regard, as anticipated in Chapter 4.6.1, laboratory experiments have shown that, especially the first layer of water, undergoes an intrinsic mixing due to the impact of the rainbowing jet over the surface; it is easy to understand that the main issues for SML are mainly linked to the mechanical impact of the jet and the consequent turbulence.

4.6 RAINBOWING DISCHARGING SCENARIO: ASSESSMENT AND RESULTS

As already explain in the previously chapters, the present study supposes to install a rainbowing system (discharging and suction pumps) on a bulk carrier, due to its big transport capacity. The main parameters (SL capacity, average cruising speed, SL discharge rate, and

navigation EF) are analogous to the ones adopted in the previous assessment of the new dedicated fleet, reported in Table 3.2 and in Table 3.3.

This study assumes a SL discharge rate of 50 kgSL s^{-1} to evaluate the characteristics of the rainbowing system, in accordance with the discharge rate evaluated in the ships' wake scenario in Chapter 3.3. Knowing the SL tonnage, it is possible to determine the distance and duration of the entire discharging trip, as previously described in Chapter 3.3.

However, flow rate could be modified in various ranges. If proven that considering the same flow rate, the rainbowing methodology could allow lower SL concentration if compared to the ship's wake discharge, this parameter could be significantly increased.

The slurry concentration c_s is a fundamental parameter because it could cause problems in the pipelines and nozzles. An excessive concentration could induce SL particles deposition in the pipes, reducing the quantity of emitted SL and posing possible clogging issues; additionally, it could block some rainbowing nozzles, interfering with the spray formation. Knowing that a TSHD normally works with a slurry concentration ranging between 0.05 and 0.2 kg kg^{-1} (ISPRA, 2017), so a value of 0.11 kgSL kg^{-1} has been chosen. The chosen concentration is conservative, but it is possible to increase it after accurate studies; it is worth noting that in this scenario the slurry concentration could be greater than the one adopted in ships scenario. Higher concentrations could allow a greater overall process efficiency at a generic time scale, assuming the same flow rate; moreover, higher concentrations mean less water usage, and therefore less required energy to pump water. The slurry density is later obtained, as a function of concentration, thanks to the following formula (4.11).

$$\rho_s = \left(\frac{c_s}{\rho_p} + \frac{1 - c_s}{\rho_w} \right)^{-1} \tag{4.11}$$

where:

ρ_s: slaked lime slurry density [kg m^{-3}];
c_s: slurry concentration [kgSL $kgslurry^{-1}$];
ρ_p: SL particle density [kgSL m^{-3}];
ρ_w: seawater density [kg m^{-3}]; assumed 1,024.75 kg m^{-3} (Kaye and Laby, 1995).

The result is a slurry flow rate (formula (4.12)) which allows calculating the seawater flow rate needed to make the SL mixture, as the difference between the rainbowing flow rate and SL discharge rate (formula (4.13)).

$$Q_s = \frac{Q_{SL}}{c_s \, \rho_s} \tag{4.12}$$

$$Q_w = Q_s - \frac{Q_{SL}}{\rho_s} \tag{4.13}$$

where:

Q_s: slaked lime slurry flow rate [m^3 s^{-1}];

Q_{SL}: slaked lime discharge rate [kg SL s^{-1}];
Q_w: water pumping [m^3 s^{-1}].

As a result, knowing the SL quantity transported, it is possible to evaluate the time needed for SL discharging t as the ratio between the total SL mass transported M_{SL} and the discharging rate Q_{SL} as shown in formula (4.14); consequently, the travelled distance per trip is calculated as the product between the discharging time t and the average cruise speed (formula (4.15)).

$$t = \frac{M_{SL}}{Q_{SL}} \tag{4.14}$$

$$d = t\ v \tag{4.15}$$

where:

t: discharging time [s];
d: travelled distance per trip [km];
v: vessel cruise speed [km s^{-1}].

Likewise, an analysis of the discharging and water suction systems is necessary to evaluate the carbon footprint of this shedding methodology. The evaluation of the consumption of the water suction system considers typical dredging pumps, without the extraction of sand or other materials. Power of discharging and hydraulic pumps are known from the manufacturers' catalogues; consequently, assuming an efficiency pump value of about 70%, it is possible to determine the effectivity power of both pumps. A group of technical catalogues (Jan De Nul, 2021) allows the assessment of many discharging system parameters, including the discharging system installed power and their flow rate, as can be seen in Chapter 4.3. Since the pump power is a linear function of the flow rate, the current installed power is obtained by multiplying the catalogues' power for similar rainbowing distances by the ratio between the different flow rates. Such comparison has been carried out examining the "Cristobal Colòn" TSHD catalogue by the Jan De Nul company, which could spray the slurry for a 100-150 m rainbowing distance. Such vessel has an installed power of 16,000 kW, for a discharging flow rate of 15,000 m^3 h^{-1}. The result of this calculation is the estimate of a 1,609 kW installed discharging power on a bulk carrier with a SL flow rate of 50 kgSL s^{-1}, corresponding to a slurry flow rate of 1,500 m^3 h^{-1}. Similarly, dredging systems catalogues have been analysed to assume the installed power of the water suction system. Comparing information found on hydraulic pumps technical specifications (Dragflow, 2021) with the described scenario, an installed power of 377 kW has been assumed for the water suction device, related to a water flow rate of about 1,400 m^3 h^{-1}. This comparison considered a similar flow rate suction pump: the hydraulic pump HY600 by Dragflow company, suitable for a 1,500 m^3 h^{-1} water flow rate.

Table 4.3 reports the assumptions made during the assessment, while Table 4.4 reports the main results.

Table 4.3: Main parameters assumed for rainbowing assessment thanks to literature available data.

Parameter	u.m.	Value
Slaked lime mass transported, M_{SL}	tSL vessel^{-1}	63,750
Slurry concentration, c_s	kgSL kgslurry^{-1}	0.11
SL discharge rate, Q_{SL}	kg s^{-1}	50
Average cruise speed, v	km h^{-1}	25
Discharging power	kW	1,609
Suction power	kW	377
Pump efficiency	%	70

Table 4.4: Main parameters calculated during rainbowing assessment.

Parameter	u.m.	Value	Reference
Slurry density, ρ_s	kg m^{-3}	1,085	Formula (4.5)
Slurry discharge rate, Q_s	m^3 h^{-1}	1,508	Formula (4.6)
Water pumping, Q_w	m^3 h^{-1}	1,428	Formula (4.7)
Discharge time, t	d	14.8	Formula (4.8)
Distance per trip, d	km	8,855	Formula (4.9)

All described parameters are in accordance with the ships' scenario. However, they could vary to increase the distribution rate. For instance, it is possible to triple the slurry concentration without exceeding the normal operating range of a rainbowing dredger. An increase in the slurry concentration would generate actually a higher discharging rate.

4.6.1 CO_2 EMISSIONS ASSESSMENT

The CO_2 emissions should be evaluated as the sum of the navigation's emissions and pump's emissions. The EF used for ship's movements evaluation is known from the previous assessment (193 kgCO_2 km^{-1}) while an investigation of the system fuel consumption is necessary for determining pump's emissions. The most common fuel used in naval vessels is the heavy fuel oil (HFO), a residual fuel from crude oil refineries.

It is also important to determine the effective pump power of both the discharging and water suction system; at this purpose, as already specified previously in Chapter 3.3.2, a pump efficiency of 0.70 has been assumed (Stoffel, 2015).

The following formula allows calculating the total discharge CO_2 emissions, thanks to the following formula (4.16).

$$E_{CO_2} = EF_{ship}\, d + EF_{HFO}\, t \left(P_{eff,suction} + P_{eff,disc}\right) \tag{4.16}$$

where:

E_{CO_2}: total emissions [gCO_2 yr^{-1}];
EF_{ship}: emission factor of the navigation [kgCO_2 km^{-1}];
d: travelled distance [km yr^{-1}];
EF_{HFO}: emission factor of the heavy fuel oil (HFO) [kgCO_2 kWh^{-1}], assumed equal to 0.28 kgCO_2 kWh^{-1} (Ramphull and Surroop, 2017);

t: discharging duration [h yr^{-1}];
$P_{eff,suction}$ and $P_{eff,disc}$: effective power of the discharging and water suction system [kW].

Even in this case, like done previously in ship's assessment in Chapter 3.3.1, the theoretical amount of CO_2 removed ($CO_{2,th}$) is calculated as the product between yearly discharged SL ($M_{SL,y}$) and the theoretical CO_2 removed per SL unit (δ_{th}) (formula (3.3)). Later, the CO_2 emissions E_{CO_2} are subtracted from the theoretical amount of CO_2 removed $CO_{2,th}$ to obtain the net amount of CO_2 per unit of SL discharged actually removed δ (formula (3.4)). Finally, it is compared to the ideal carbon removal rate getting the penalty η_p of this spreading configuration via the formula (3.5). Table 4.5 reports the main results of this assessment.

Table 4.5: Main results of rainbowing assessment, in terms of total navigation and pumping emissions, theoretical CO_2 removed (also per unit of SL discharged), and penalty.

Parameter	u.m.	Value	Reference
Total navigation emission, E_{CO_2}	tCO_2 vessel^{-1} trip^{-1}	1,709	Formula (4.16)
Total pumping emission	tCO_2 vessel^{-1} trip^{-1}	138	
Theoretical CO_2 removed, $CO_{2,th}$	tCO_2 vessel^{-1} trip^{-1}	53,068	Formula (3.3)
Net CO_2 removed/SL discharged, δ	tCO_2 tSL^{-1}	0.80	Formula (3.4)
Penalty, η_p	%	3.48	Formula (3.5)

It is it worth noting that the penalty is only slightly higher than the dedicated fleet scenario (3.22%), reported previously in Chapter 3.3.1; this is due to the very low consumption of the pumping system, not comparable to the navigation emissions.

4.6.2 PRELIMINARY COST ASSESSMENT

The following cost evaluation aims to assess Opex and Capex expenditures. In particular, rainbowing discharging scenario is based on the structural modification of bulk carriers, so even in this case Caserini et al. (2019) results are taken into consideration as done for cost assessment in ship's wake discharging configuration (previously described in Chapter 3.3.2).

Opex evaluation

The total Opex costs are given by the sum of transportation costs, pumping costs and fuel cost of the pumping system for rainbowing discharging, related to the energy usage in the discharging and suction system.

It is worth noting that transportation and pumping costs are evaluated like done before; more precisely, the shipping Opex is the same as in the dedicated ships scenario, while pumping Opex is bigger than before because pump's energy consumption is higher in this case.

An evaluation of the pumping system consumption is indeed required; the adopted methodology is the same as the one used for ships cost assessment in Chapter 3.3.2.

Capex evaluation

In this assessment, Capex expenditure is equal to sum of the fixed costs (evaluated previously in dedicated ship scenario in Chapter 3.3.2, mainly linked to engines, pipes, and vessels price)

and the pumps fixed costs. Specifically, according to sellers' catalogues, centrifugal pump cost for the evaluated flow rate (1,508 m^3 h^{-1}) is approximately estimated around €60,000 (Stuart Pumps LTD, 2021). This preliminary cost evaluation does not consider any interest rate.

Total costs

Total costs evaluation is made by summing Opex and Capex expenditures; specifically, they are evaluated in terms of € tCO_2^{-1}, as described in Chapter 3.3.2.

Table 4.6 and Figure 4.9 report the principal results.

Table 4.6: Assessment of the operative, capital, and total costs for discharging via rainbowing.

Parameter	u.m.	Value
Total Opex	€ vessel^{-1} trip^{-1}	229,728
	€ tCO_2^{-1}	4.49
Shipping Opex	€ tCO_2^{-1}	3.57
Discharging Opex	€ tCO_2^{-1}	0.36
Pumping Opex	€ tCO_2^{-1}	0.55
Total Capex	€ vessel^{-1} trip^{-1}	90,695
	€ tCO_2^{-1}	1.77
Total costs	€ vessel^{-1} trip^{-1}	320,422
	€ tCO_2^{-1}	6.26

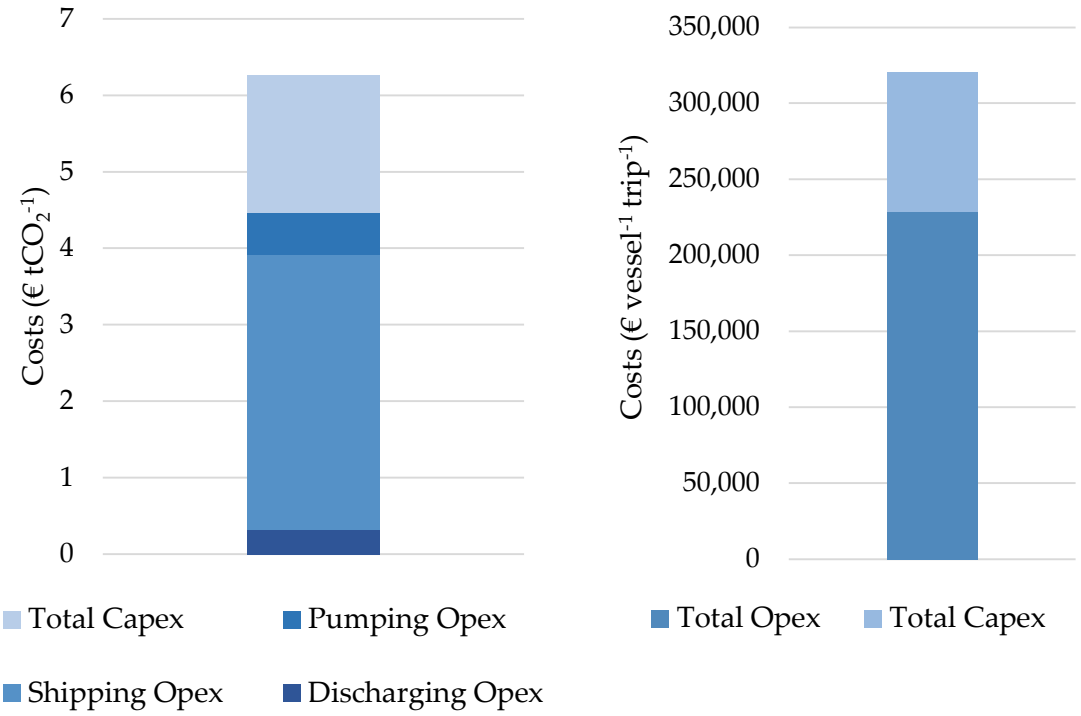

Figure 4.9: Graphical analysis of the total costs for rainbowing system in terms of € tCO_2^{-1} (left) and also in terms of € vessel^{-1} trip^{-1} (right).

It is worth noting that, in this configuration, total costs are a little bit higher than for dedicated ships (as described in Chapter 3.3.2) because there is the additional term related to fuel usage by pumps.

4.7 ALTERNATIVE DISCHARGING METHODS

This chapter aims to investigate alternative scenarios for SL shedding via rainbowing, also combining this new innovative practice with the conventional discharge in ship's wake.

Multiple rainbowing discharge system

A structural change could be helpful to realize a vessel with multiple outlets, thus increasing the OAE potential. However, this possibility should be examined in detail in order to avoid possible overlapping between areas covered by rainbowing and so minimizing the potential side effects of marine biology.

This brief chapter aims to investigate the possible advantages of a multiple rainbowing discharge. In this way, one or more suction systems should provide water to multiple discharging pumps. These discharging pumps should be positioned on different sides of the ship maximizing the available space, but on the other hand, avoiding possible overlapping between imprint areas, so minimizing possible issues on SML and marine biology. For instance, a vessel could be equipped with ten discharging pumps Figure 4.10 shows: two placed at the ship's stern and the other eight systems at its sides. This number of rainbowing systems has been chosen after the knowledge of the dimensions of a generic bulk carrier (for example a Panamax vessel type, whose main sizes are: a length of 294 m and a beam of 32 m (Morrison, 2012)).

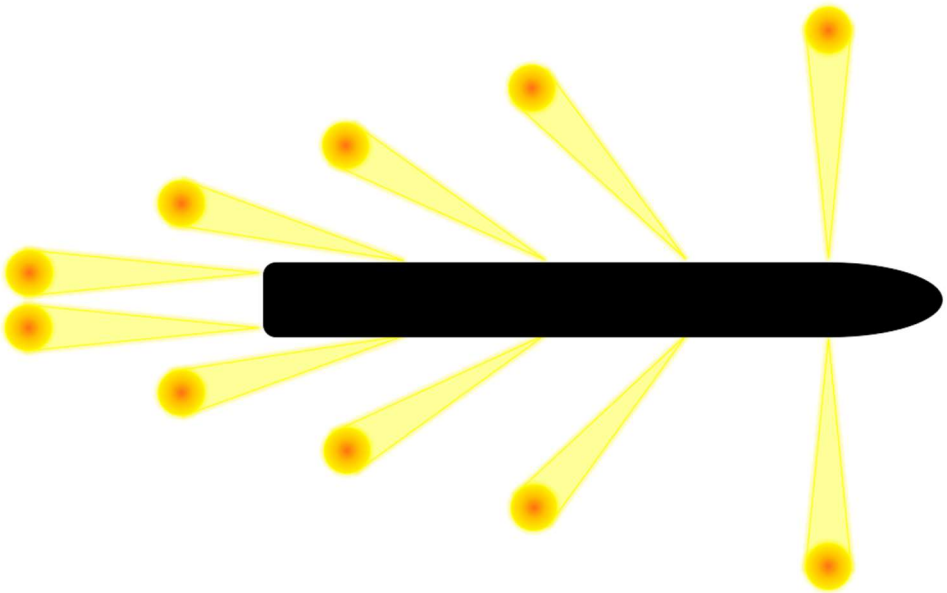

Figure 4.10: Diagram of a multiple discharging rainbowing system (Panamax vessel in scale).

One of the main advantages of this methodology is that the vessel could discharge more SL in a minor duration. For instance, all the rainbowing systems could operate with a rate of 50

kgSL s^{-1}, tripling the vessel discharge potentiality but without increasing the possible effects on the ocean's biology related to SL concentration, because it remains the same as the previous scenario. In this way, the ship could discharge ten time the quantity of SL in the same discharging distance as the base scenario. Clearly, more frequent stops are required to reload the vessel but on the other hand, this methodology increases OAE efficiency.

Furthermore, the rising SL spreading rate counterbalances the increasing energy consumption for the discharging systems. The increase in such a discharge rate further amortises navigation emissions. Table 4.7 reports the main results of the assessment.

Table 4.7: Main parameters in the assessment of multiple rainbowing discharge system with 10 outlets.

Parameter	**u.m.**	**Value**
Nr. of outlets	-	10
Total pumping emission	tCO_2 trip^{-1}	1387
Tot CO_2 removed/SL discharged	tCO_2 tSL^{-1}	0.83
Penalty	%	0.58
Total Opex	€ tCO_2^{-1}	1.23
Shipping Opex	€ tCO_2^{-1}	0.35
Discharging Opex	€ tCO_2^{-1}	0.35
Pumping Opex	€ tCO_2^{-1}	0.54
Total Capex	€ tCO_2^{-1}	0.91
Total Costs	€ tCO_2^{-1}	2.14

It is worth noting that, since a general bulk carrier has a breadth dimension that ranges between 30 m up to 50 m or more (Shu and Moan, 2011; Minchev et al., 2013), it is possible to install up to three rainbowing systems at the vessel's stern, without causing overlapping between the imprint areas. This could allow increasing the number of discharging pumps without posing additional biological issues.

Also, it is possible to develop a more conservative scenario, if proven that the previously described scenarios cause a too elevated biological impact. There is the opportunity to subdivide the overall flow rate of 50 kg s^{-1} from all the rainbowing systems, further reducing the concentration in seawater. In the case of ten rainbowing systems, all the spraying pumps have a flow rate of 5 kg s^{-1}, allowing a maximum seawater SL concentration of 2.91 mg L^{-1}, ten times lower than the main scenario.

5. DISCHARGE VIA AIRCRAFT

This chapter evaluates the potential of the OAE technology using aircraft to discharge SL into seawater. This study aims mainly to conduct a viability analysis of ocean SL dispersion through aircraft: an assessment of different discharging scenarios allows to evaluate pros and cons of such a methodology, approximately estimating even the economic feasibility. In addition, a further investigation permits the discussion of potential environmental impacts related to pH change and risks for human populations linked to SL contact and inhalation

5.1 AIRCRAFT LIMING HISTORY

In past times, this practice allowed to counteract the water pH changes generated by acid rain; in this way, this application has led to the return of fish life and was an example of success in lake restoration (Klapper, 2003). Moreover, the aircraft usage sometimes enabled the recovery of acidified ponds and lakes, as shown in Figure 5.1. The aircraft spreading of alkaline materials, especially calcium carbonate powder, occurred particularly in Sweden, Norway, Canada, and the USA (Olem, 1991).

This technology supported the recovery of both lakes/watersheds and even forest soils. Indeed, also forest soils suffer from acidification by polluted precipitation, and the air discharge of alkaline materials has been successfully applied several times. The application of liming materials in freshwater by aircraft may be efficient and cost-effective especially for remote situations, but it is generally less accurate than other discharge methodologies because of the manoeuvrability of the plane. Air discharge applications may be more suitable for areas with limited road access and not far from an airport. Even though this technique has a limited diffusion in surface waters neutralization, commercial equipment is available thanks to firefighting applications and agricultural chemicals spreading. A storage system and a simple dispersal mechanism must equip the plane. When a slurry is employed, chemical dispersants must be added to avoid limestone deposition during the transport and to obtain a more concentrated slurry (Olem, 1991).

Figure 5.1: Example of limestone application by firefighting aircraft during a lake liming operation (Olem, 1991).

Olivine and limestone discharges helped to recover many watersheds and wetlands in Sweden since the late '70 (Fraser and Britt, 1982). In Norway, the first case of air discharge

happened in 1983 (Rosseland and Hindar, 1988), while the first reported liming of a watershed in the U.S.A. was in 1989, in the Woods Lake, by spreading pelletized limestone (Boutacoff, 1990). In the Adirondack region of New York, liming operations were undertaken to neutralize small remote lakes, by the usage of small fixed-wing aircraft designed for discharge agricultural fertilizers (Gloss and Schofield, 1989). Other successful examples of aerial recovery were the applications of powdered limestone in Ontario, Canada (Booth et al., 1985), managed by the use of a twin-engined amphibious plane designed for forest fire control operations.

5.2 TYPES OF AIRCRAFT

The evaluations in this chapter analysed OAE feasibility via aircraft considering three different airplanes that are substantially dissimilar in terms of characteristics and dimensions. Various peculiarities reflect the divergences regarding costs and emissions. Not all the aircraft examined are actually able to discharge material during the flight. The assumption made is to consider a range of cargo airplanes, assuming the possibility to equip them with a discharge system (similar to firefighting aircraft). Aircraft examined are bigger than the ones generally used for lake liming; that's because the SL quantity to discharge is much wider. For this reason, a conventional firefighting plane and two large freighters are considered, differently for lake and watershed liming, generally using small fixed-wing firefighters and agricultural fertilization purposed aircraft.

The first aircraft considered is the Antonov AN-32P (AN32), shown in Figure 5.2. It is a turboprop twin-engined Ukrainian military transport aircraft. Also known as "Fire killer", it is widely used as a firefighting aircraft. Produced since 1982, it was designed to fly easily in adverse weather conditions. With a 29.2 m wingspan and a length of 23.78 m, it is the smallest and lightest aircraft evaluated, carrying about 8 ton of payload. Its typical cruise altitude is 4-8 km if used as a cargo plane, while during firefighting flies it discharges liquids or powder from a standard height of 40-50 m above the ground. The average cruise speed is about 460 km h^{-1} (Antonov, 2021).

Figure 5.2: Antonov AN-32P.

The second aircraft evaluated is the Boeing 737-700C (B737), displayed in Figure 5.3. It is part of the airplane series "Boeing 737 Next Generation": this typology of aircraft comprehends all the models from Boeing 737-600 to 737-900. Produced in the United States since 1996, it is a

narrow-body aircraft powered by two jet engines. The letter "C" of the Boeing 737-700C stands for "Convertible": this aircraft is indeed an airliner, but the seats can be easily removed in order to convert it into a cargo aircraft. Its characteristics are intermediate between the two other evaluated aircraft. Its length is 30.53 m while the wingspan is 34.32 m. The payload is more than two times the AN32, shipping about 18.8 ton. It usually flies at an altitude between 5-12 km. When analysing cargo aircraft, to assess adequate flying speed, has been chosen the typical velocity of discharging-type aircraft (in the specific firefighting aircraft) with similar characteristics in terms of size and payload. For these reasons, a cruise speed of 612 km h^{-1} for the B737 is considered (Cal Fire, 2019).

Figure 5.3: Boeing 737-700C.

The last airplane evaluated is the McDonnell Douglas MD-11 (MD11), shown in Figure 5.4. It is an American tri-jet wide-body aircraft, produced firstly in 1988 by McDonnell Douglas and later by Boeing. It is the largest and heaviest aircraft evaluated. It was born as an airliner, but then also some freighters were built. However, the largest quantity of MD11 cargo is made of converted passenger aircraft: nowadays it is no longer used as an airliner. Its length is 61.20 m while the wingspan is 51.97 m. The cargo capacity is elevated, it is able to carry about 82.2 ton of payload. The cruise speed has been assessed in the same way as the B737, obtaining a value of 781 km h^{-1} (Cal Fire, 2019).

Figure 5.4: McDonnell Douglas MD-11.

As assessed by Olem (1991), it is quite simple to convert a general airplane into a spreading aircraft. Storage bays or tanks are clearly already present in cargo planes, while a simple

dispersal system is necessary. This discharging system should be able to spread at different flows, according to the various scenarios.

Table 5.1 reports the principal aircraft characteristics assumed in this specific assessment.

Table 5.1: Principal aircraft characteristics.

Parameter	u.m.	Antonov AN-32P	Boeing 737-700C	McDonnell MD-11
Deadweight	t	17	29	128
Payload	t	8.0	18.8	82.2
Length	m	23.78	30.53	61.20
Average cruise speed	km h^{-1}	460	612	781
Typical cruise altitude	km	4 - 8	5 - 12	5 - 12
Motors	-	2	2	3
Engine type	-	Turboprop	Turbofan	Turbofan

The dedicated chapter considers typical cruise speeds for firefighting aircraft. However, the velocity during the discharge in fire control operations could be very variable, also much less intense. Flight speeds examined are not too low, as the aim is to minimize the impact on the sea surface.

5.3 AIRCRAFT ASSESSMENT FOR SLAKED LIME DISCHARGING

In order to evaluate the environmental impact of this type of discharge, a simple model is built. Evaluating aircraft emissions, especially from the fuel burnt, is the first fundamental aspect. Furthermore, the fate of falling SL particles on the ocean surface is a key analysed issue. It is important to remember that all these characteristics are constrained to the flight and discharge parameters.

5.3.1 AIRCRAFT CO_2 EMISSIONS

Aircraft emit gases and particles directly into the upper troposphere and lower stratosphere, impacting on atmospheric composition; these gases and particles modify the concentration of atmospheric GHGs and cause a penalty in their removal. In particular, the principal emissions include CO_2, carbon monoxide (CO), water vapour (H_2O), nitric oxides (NO_x), sulphur oxides (SO_x) and soot.

Net emissions, defined as the difference between the gross emissions of the process and the carbon removal from OAE, must be negative for process efficacy and substantially negative for cost-effectiveness.

After defining the different aircraft types, it is crucial to evaluate their CO_2 emissions, which are different in each part of the journey of an aircraft. The International Civil Aviation Organisation (ICAO) divides flights into the Landing and Take-Off cycle (LTO), under about 914 m (3000 ft) and the Climb/Cruise/Descent cycle (CCD) over 3000 ft, as shown in Figure 5.5.

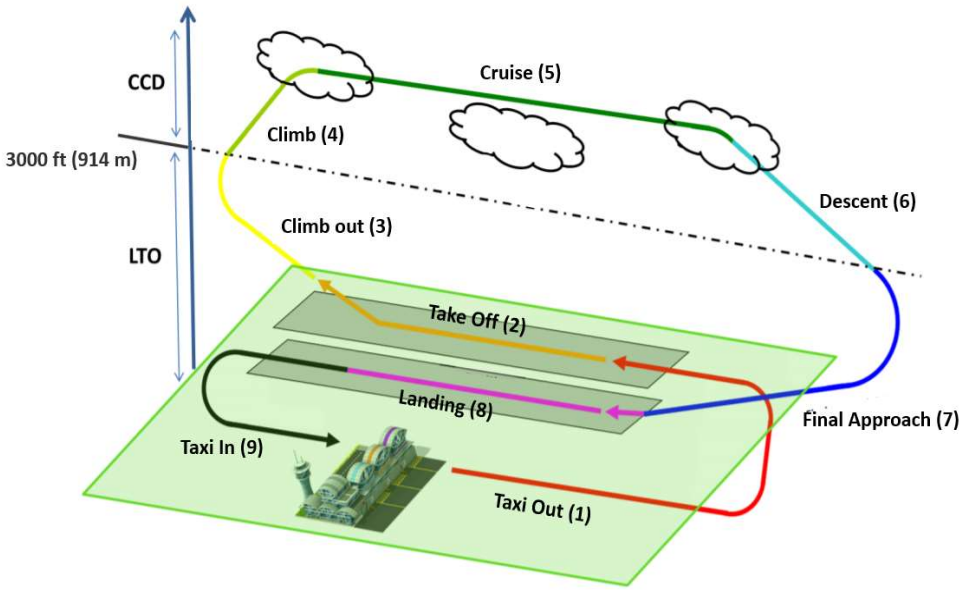

Figure 5.5: Aviation activities phases (ICAO, 2019).

Aircraft characteristics and airport configuration determine the LTO cycle duration; it includes 5 phases:

1. taxi-out: controlled ground movement between parking stand and runway take-off point;
2. take-off: takes place partly on the ground and partly in flight, at maximum engine thrust, and includes the movement of the aircraft from the moment it starts to accelerate on the runway at the time when it develops lift and then sustenance in flight;
3. climb-out: ascent to 3000 ft (914 m);
4. final approach: landing phase, from 3000 ft altitude to the ground;
5. landing and taxi-in: from ground contact to the parking stand.

Each LTO phase is associated with a specific typology and quantity of pollutants. Variations of engine thrust imply all these possible differences. During take-off and climb-out, NO_x and particulate matter emissions are prevalent; rather, during ground phases are prevalent CO and hydrocarbons emissions. During taxi-out and take-off phases, engines operate at 100% of their potential. ICAO provides average durations for each LTO stage, based on measurements made on several engine types: taxi-out and take-off last about 0.7 min. In the climb-out phase, engines usage decrease to 85%, for an average duration of 2.2 min. After the CCD, the final approach begins; it lasts 4 min with 30% of the available thrust. The landing and taxi-in phase is the longest stage of the LTO cycle: its duration is about 26 min, and the thrust is at the minimum, with an average value of 7% (ICAO, 2017).

The CCD cycle includes three operations (climb, cruise, and descent), over 914 m (3000 ft); it is usually the longest part of a journey.

The guidebook of the European Monitoring and Evaluation Programme/European Environment Agency (EMEP/EEA, 2019) allows obtaining CO_2 EFs of the LTO and the CCD cycles. EFs from fuel consumption in the LTO and CCD cycle derive from the

EUROCONTROL's Base of Aircraft Data (BADA), the international reference for aircraft performance modelling, and from the ICAO Aircraft Engine Emissions Databank (AEED), which provides fuel consumption for a very large number of aircraft engines.

EFs of the LTO cycle depends solely on the type of aircraft considered and they are given in terms of CO_2 emitted per cycle. On the other hand, CCD cycle emissions depend on stage length and cruise altitude: the EMEP/EEA inventory provides the quantity of CO_2 emitted for various stage lengths and altitudes, permitting the estimation of the CCD cycle EFs, expressing them in terms of emitted CO_2 per travelled km. The knowledge of the dependence between emissions and altitude is fundamental because air density, which decreases with height, strongly affects the EFs. Default stage lengths are defined by EMEP/EEA basing on the main travelled pathways by each plane; a graphical representation is reported in Figure 5.6. Every stage length, which includes the climb phase, is associated with a characteristic cruise altitude.

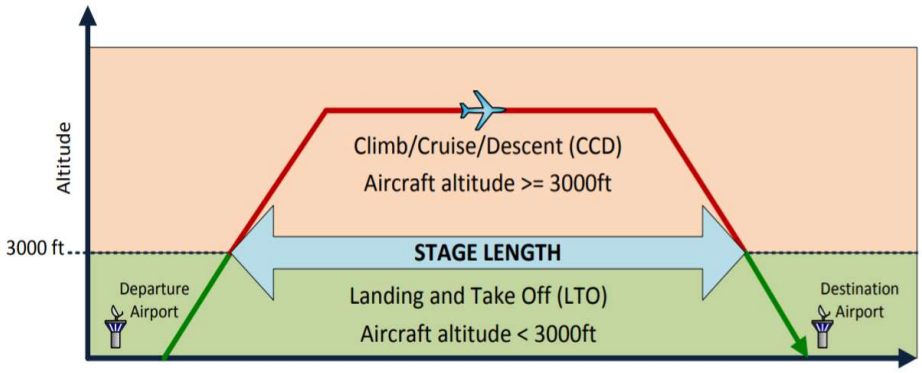

Figure 5.6: Scheme of the stage length (EUROCONTROL, 2016).

Since the EMEP/EEA inventory includes few flying heights, whereas different discharging scenarios consider different altitudes defined in more detail later, it is necessary to assume an exponential decrease of CCD fuel consumption with altitude (Turgut and Rosen, 2011), because of decreasing air density. An exponential interpolation of the available data allows obtaining EFs for not given altitudes.

Since stage lengths in the EMEP/EEA inventory are relative to cruise lengths of hundreds of kilometres or more (from about 200 km to 14,000 km), the CCD EFs obtained are considered representative specifically only of the cruise phase, because the climb and descent phases usually last few minutes compared to the entire CCD cycle. For the assessment of the emissions of the climb and the descent phase it is crucial to estimate the climb rate; literature data suggest a value of 1,500 ft min^{-1} (about 457 m min^{-1}), (Deutsche Flugsicherung DFS, 2014). Fuel consumption for a 73,900 kg aircraft (Airbus A320) flying crosswind is 93 kg fuel min^{-1} during the climb phase (Zhang et al., 2019) and 6.7 kg fuel min^{-1} during the descent phase (Şahin and Ağayeva, 2018), which are approximatively constant during these phases without altitude dependence. Assuming a linear increase of consumption with the aircraft weight, climb and descent EFs are estimated for each aircraft, considering a carbon intensity of fuel for aviation of 3.15 kgCO_2 per kg of fuel (Graver et al., 2020).

Since the cruise and descent EFs are calculated in terms of the mass of CO_2 min^{-1}, climb and descent durations need to be evaluated for each aircraft type. They are calculated as the ratio between the CCD height (defined as the total flying height minus the LTO height, that is approximately 1 km) and the climb rate.

The following formula (5.1) allows calculating the total discharge CO_2 emissions.

$$E_{CO_2} = E_{LTO} + EF_{cruise}\, d + (EF_{climb} + EF_{descent})\, t \tag{5.1}$$

where:

E_{CO_2}: total CO_2 emission [gCO_2];
E_{LTO}: total mass of emitted CO_2 during the LTO cycle [gCO_2];
EF_{cruise}: emission factor of the cruise phase [gCO_2 km^{-1}];
d: travelled distance during the cruise phase [km];
EF_{climb} and $EF_{descent}$: emission factor of the climb and descent phase [gCO_2 min^{-1}];
t: duration of the climb and descent phase [min].

It is worth noting that for flying heights below 1 km, since the LTO cycle comprehends a climb-out phase until about 1 km of altitude, the total CO_2 emissions are assessed as the LTO cycle emissions minus the climb emissions to reach 1 km from the intended altitude, plus the cruise emissions.

This assessment neglects emissions deriving from the supply chain because they are independent of the discharging method. Once the SL payload of each aircraft type is known, net CO_2 removal for any flight can be evaluated from the difference between the CO_2 removal derived from SL spreading and CO_2 emission from fuel consumption.

Basing on the method used in Chapter 3.3.1 for emissions assessment, the theoretical amount of CO_2 removed, $CO_{2,th}$, is assessed thanks to the formula (3.3); in this way it is possible to evaluate the net amount of CO_2 actually removed, δ (formula (3.4)). Finally, it is compared to the ideal carbon removal rate getting the penalty, η_p, thanks to the formula (3.5).

5.3.2 DYNAMIC OF PARTICLES SETTLING IN AIR

Once the discharge begins, SL particles fall in a cloud of dust. Each particle has a particular dimension, and those which belong to the same size class act similarly. Particles of the same size fall with the same settling speed, and the result is a fractionation of the various particles while reaching the ocean surface. After that, they impact the first aquatic layer and start to dissolve, increasing the surface pH value for a while.

Each particle has a specific sedimentation velocity in air, which is related to its size. The powder trajectory is then linked with the wind speed and direction because wind is the main factor influencing the track of a falling particle in the atmosphere.

Under the assumption of particles with a spherical shape, the settling speed in air is calculated throughout Stokes' equation (5.2), reported below:

$$v_{TS} = \frac{\rho_p \, g \, d_p^2}{18 \, \mu_f} \tag{5.2}$$

where:

v_{TS}: settling velocity [m s^{-1}];
ρ_p: SL particle density [kg m^{-3}];
g: gravitational acceleration [m s^{-2}];
d_p: particle diameter [m];
μ_f: air viscosity [Pa s], assumed 1.76 10^{-5} Pa s at 1 km of height (Çengel, 1998).

Such an examination considers the variation of air viscosity as a minor effect, so this modelling neglects it.

Terminal sedimentation velocity in the air determines approximate settling distances from the discharge point along the wind direction (the wind vector would ideally cross the travelling direction of the aircraft); Figure 5.7 provides a qualitative diagram of the discharge process. This study offers a simple settling model, ignoring turbulence, clouds, and precipitation, and also, as stated previously, considering only a stable wind vector orthogonal to aircraft travel. Predicting aeolian transport of SL particles allows flight plans that avoid terrestrial settling, which could interfere with ecosystems or human activities or raise political problems if different States are in involved to those carrying out the operations.

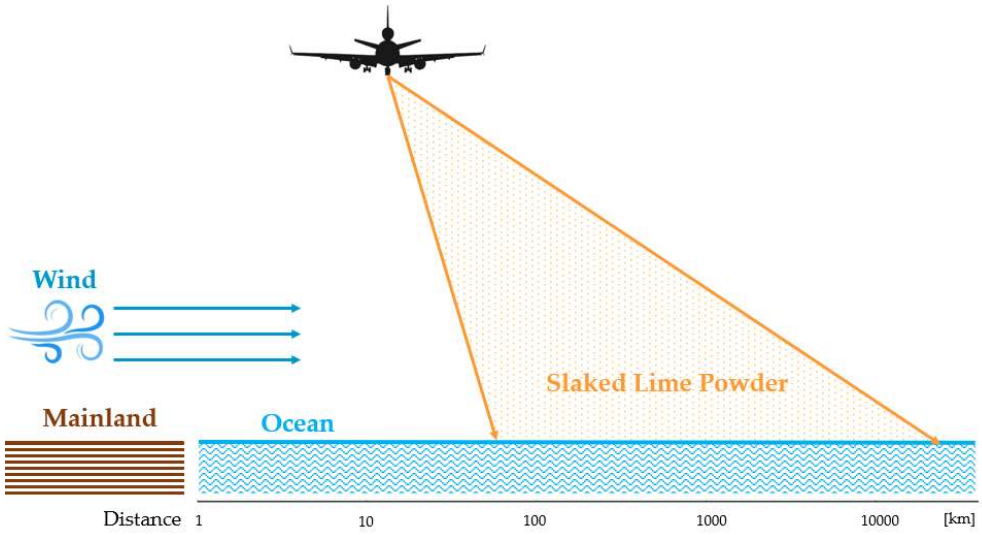

Figure 5.7: Qualitative diagram of aeolian transport of SL particles (not in scale).

Due to different settling speeds, crosswinds allow aeolian payload fractionation by particle size, thus greatly improving distribution when compared to a hypothetical monodisperse payload; small particles are carried on the breeze like pollen while large ones fall like sand grains. It is worth noting that particles under the 50-percentile could act as the so-called PM10 because their diameter is smaller than 10 μm. This size class is of great interest because winds could transport it for a very long distance if discharged by high altitude, and it could be a particular human health issue if settling in a not desirable location.

5.3.3 DYNAMIC OF PARTICLES SETTLING IN WATER

To evaluate the concentration of dissolved SL in water, complex modelling is necessary. The current section carries out a simplified analysis to assess the order of magnitude of SL concentration in seawater obtained by the discharge. A simplified evaluation assumes full particles wetting without air bubbles adhesion, spherical shapes, and instant penetration without surface tension. Furthermore, this approach does not consider other mechanisms such as surface tension forces in the surface layer (Nave, 2002) or particle clumping (McNamara and Young, 1991). Rain and clouds have a substantial effect on particle settling, as they allow the particles to dissolve fully or partially into rain and cloud droplets. This may influence cloud droplets number concentration and resultant precipitation and/or albedo; these effects are beyond the scope of this study.

Particles are supposed to sink immediately after encountering the sea surface. Immediately later, SL molecules begin to dissolve. In the simple model offered, the particles are assumed to distribute homogeneously in the water volume involved while completing the dissolution.

Under these assumptions, Stokes' equation (5.3) gives particle speed settling into seawater.

$$v_{TS} = \frac{(\rho_p - \rho_w) g \, d_p^2}{18 \, \mu_w} \tag{5.3}$$

where:

v_{TS}: settling velocity of the particle in water [m s^{-1}];
μ_w: seawater viscosity [Pa s], assumed 1.08 10^{-3} Pa s (Leyendekkers, 1979).

After settling speed is obtained, the assessment of the water volume in which the SL completely dissolves, giving a pH peak, requires a dissolution time. Data from literature suggest that dissolution last a maximum of few minutes (Caserini et al., 2021); conservatively, this section considers a time of 30 s, but further studies are necessary to establish the effect of particle size. Concentration values calculated could be compared to the NOAEC concentration limits. This rough comparison to analyse the maximum possible concentration is a preliminary evaluation as there is no literature on toxicity in the short period (the LC50 concentration and the NOAEC level from literature are based on an exposure period of 96-hour).

Overlapping of the discharge area on subsequent flights could not be excluded, but it is assumed that daily vertical mixing in the surface ocean layer avoids concentration spikes due to the sum of loads coming from subsequent discharges.

5.3.4 DISCHARGE SCENARIOS

To evaluate the impact of various flying characteristics on discharge efficiency, a set of parameters should be considered, analysing the effect of their variation. The following assessment of 18 scenarios requires different aircrafts types, discharge heights, discharge durations, and daily time available for discharge depending on meteorological conditions (i.e.: wind speed and direction).

Discharge altitude

Assessing optimal discharge altitude is challenging: increasing altitude leads to wider dispersion since smaller particles may travel vast distances, but this complicates the prediction of impact sites due to turbulence, entrainment in clouds, and changing winds. According to the Federal Aviation Administration (FAA), it is mandatory to fly above an altitude of 1,000 ft (about 300 m) over congested areas, while in other cases it is possible to fly at an altitude of 500 ft (about 150 m); no restrictions are given for the open water surfaces (FAA, 2021). Three discharge altitudes are considered: 0.2 km, 1 km, and 5 km.

Discharge duration

Discharge is assumed to begin after the climb phase, during the entire cruise phase. Three discharge durations (1 min, 20 min, and 40 min) have been considered, that correspond to minimum-maximum discharge ratio of 3-133 kg s^{-1} for the Antonov AN-32P, 8-313 kg s^{-1} for Boeing 737-700C and 34-1,367 kg s^{-1} for McDonnell Douglas MD-11. As suggested by the National Fire Protection Association (NFPA), discharging aircrafts have a pumping-out system with a minimal nominal flow for dry chemicals between 2-10 kg s^{-1} (NFPA, 2015) for small aircraft, which could be more than 80 kg s^{-1} for larger firefighting aircraft (tank capacity more than 6 m^3).

It is worth noting that the 1 min discharge scenario represents a near-instantaneous discharge limit case, minimising CO_2 emissions, whose technical feasibility should be investigated.

Total mission duration

Total mission duration plays a key role in this specific feasibility analysis. It considers both phases taking place on the ground and in air, so it is the sum the ground handling time, the ground LTO phases and the flying time.

Literature offers ground handling times for each aircraft type (ICAO, 2019): loading, fuelling and supervision (routine and pre-flight engineering inspection). Since a typical ground handling time is about 1 hour (Popova et al., 2015), this study assumes a very efficient optimisation: suggested ground handling time for the AN32 is assumed to be 20 min; for the B737, 30 min; and for the MD11, 50 min.

In more details, the ground LTO phases are taxi-out, take-off, landing, and taxi-in; they all last about 27 min according to ICAO definitions (Nowak et al., 2018), while the total flight time varies according to each assessed scenario. In particular, total flight time includes both flying LTO phases (climb-out and final approach) and CCD phase; flying LTO phases durations are respectively 2.2 and 4 min, according to the averaged time measured by ICAO to include each engine type. On the other hand, in the 200 m discharge scenario these phases last 0.4 and 0.8 minutes, due to the fact that aircraft does not reach 1 km altitude.

Given a fixed CO_2 removal goal, the information on total mission duration allows calculation of sorties per day and fleet size.

Under the hypothesis of beginning the discharge during the cruise phase, SL discharge starts at different distances from the point of departure, depending on the duration of climb-out and climb phases. It increases with discharging altitude and aircraft size, because of airspeed differences. Additionally, the total no-discharging flying distance can be evaluated as the sum of the travelled distance during the LTO cycle (that counts climb-out and final approach phases) and travelled distance during the climb and descent phase; it depends both on aircraft size and discharging altitude. All these calculations are reported in Table 5.2.

Table 5.2: Flying distance of no-discharging from the departure point and distance from the departure point at which the discharge begins.

	No-discharging flying distance			**Distance of discharge beginning**		
	km			km		
Discharge altitude	0.2 km	1 km	5 km	0.2 km	1 km	5 km
Antonov AN-32P	10	48	182	3	17	84
Boeing 737-700C	13	63	242	4	22	112
McDonnell MD-11	16	81	308	6	29	143

Once the climb is completed, the cruise phase begins and so discharging takes place; aircraft fly perpendicular to the average wind direction. Discharge takes place during the entire route, terminating close to the departure point. The return leg is considered along a different track to limit overlapping.

5.3.5 METEOROLOGICAL PARAMETERS: WIND SPEED AND DIRECTION

Falling SL particles encounter different wind speeds during descent. Wind speed appears to increase parabolically below a few hundred meters, while it increases linearly at higher altitudes (Justus and Mikhail, 1976), as also shown in the diagrams in Figure 5.8. Wind speeds considered for the calculations are taken as the arithmetic average between the ground and the discharging altitude values.

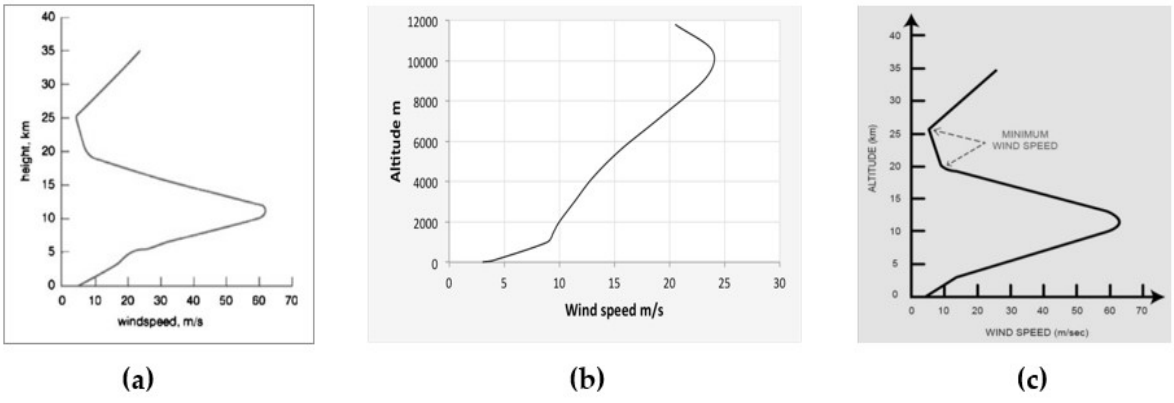

Figure 5.8: Example of different profiles of average wind speed in the atmosphere. In figure (a) it is reported a profile of global average wind speed (Boccia et al., 2007), in figure (b) it is reported the profile of average wind speed in Netherlands (Becker, 2017), while in figure (c) it is reported the average wind speed in Iraq (Hasan, 2018).

Based on observations and modelling results of the US National Weather Service and the European Centre for Medium-Range Weather Forecasts (ECMWF) it is possible to estimate

wind speed at different altitudes. Wind speeds in the troposphere increases with altitude (Boccia et al., 2007): at 0.2 km altitude, generally varies between 2.5 and 8.5 m s^{-1}, at 1 km altitude it is generally between 5.5 and 10 m s^{-1} while at 5 km it is usually between 14 m s^{-1} and 28 m s^{-1}. Typical ground wind speed in coastal areas usually varies between 1.5 and 5.5 m s^{-1}.

Even if average values for wind speed are given, coastal winds are subjected to a large variation, especially regarding their direction. Onshore/offshore winds could be subjected to a particular diurnal pattern, where the wind blows toward the land during the day and toward the sea at night (Cleveland, 2004). When manifesting, this sea breeze effect could pose problems about choosing the area where to discharge SL, because of this possible wind dragging particles toward the land. Moreover, many factors affect nearshore winds, such as orography, coastline shape, and air-sea interaction. These characteristics may lead to a wind weakening close to the coast, the so-called wind drop-off (Renault et al., 2016). All these peculiarities of the nearshore wind, result in a difficult prediction in speed and direction.

Local wind conditions constrain the discharge since terrestrial deposition should be avoided. This study considers two different scenarios, where optimal conditions (i.e.: seaward wind) occur 50% and 75% of the time, so discharging times of 4,380 h yr^{-1} and 6,570 h yr^{-1} are taken into account. Areas where sufficiently suitable conditions occur less than half the available time, should be avoided.

Since the aim is to evaluate peak concentrations of SL in water, this assessment evaluates the lowest literature wind speed, under the assumption of linear increase of speed with altitude (because discharge occurs at elevated altitudes and so settling pattern is affected by wind speed encountered during the descent) with a gradient of 7.5 km h^{-1} km^{-1} (about 2 m s^{-1} km^{-1}) to guarantee the evaluation of the maximum concentrations that could occur. Thus, for discharge at 0.2 km altitude, an arithmetic mean wind speed between the discharge altitude and the ocean surface is 3.7 m s^{-1}, while the 1 km and 5 km altitude scenarios use average wind speeds of 4.5 m s^{-1} and 8.7 m s^{-1}.

The wind profile and the length of the discharge path leads to the determination of the area affected by SL deposition. A rectangular area is dusted; one side is the discharging distance, and the other is the maximum drift distance of the particles. Figure 5.9 offers a qualitative diagram.

The dusted area is rectangular under the assumption of no air turbulence, considering only a wind direction perpendicular to the flight. This hypothesis leads to the calculation of the maximum load per unit area on the ocean surface. Larger particles would settle near the aircraft track, while the smallest would be transported for a wide distance, resulting in small loads but covering a vast surface. The hypothesis of no wind speed has been neglected, because quite unrealistic and because only regions with suitable meteorologic conditions should be dedicated to this technology.

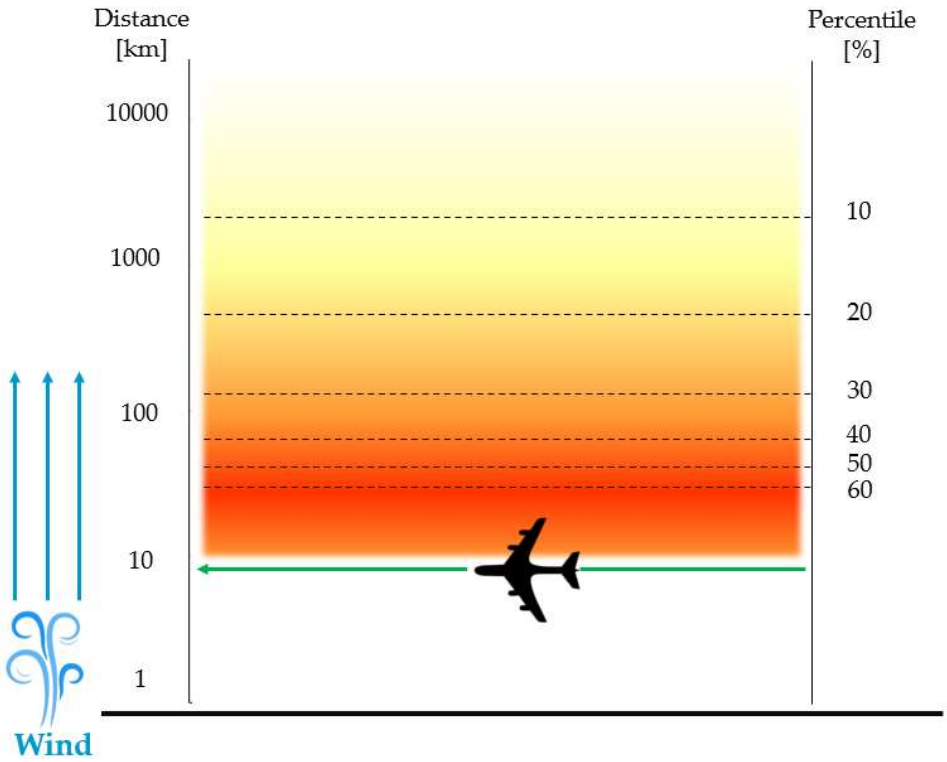

Figure 5.9: Qualitative diagram explaining the dusted area covered by SL particles both in terms of travelled distance and of percentile (not in scale).

5.4 RESULTS OF AIRCRAFT ASSESSMENT FOR SLAKED LIME DISCHARGING

Calculations are made for each scenario described in Chapter 5.3.4. The following section shows and discusses the results.

5.4.1 FATE AND TRANSPORT OF SLAKED LIME PARTICLES

For each particle size class sedimentation speed in air, settling time, and so travelled distance from the point of release is calculated, as reported in Table 5.3; it is worth noting that the last two parameters depend also on the discharging altitude. Moreover, knowing the travelled distance it is possible to evaluate the total dusted area; it is important to underline that the minimum drift distance of particles is negligible with the respect to the total distance, and so it has been ignored for the calculation of the total dusted area. Consequently, a new parameter termed "covered area" is calculated: it represents the fraction (in terms of percentage) of the total dusted area covered by the SL particles of that specific size class.

This simple model used ignores possible uplift, yet smaller SL grains could travel thousands of kilometres. For instance, assuming a discharging height of 1 km, particles under the median value, classified as to the PM10, remain suspended for at least long time, ranging from 2 days till 10 days, and reach for instance from 800 km to at least 4,000 km.

Table 5.3: Evaluation of terminal sedimentation velocity in air and settling time, travelled distances and covered area for each particle size.

Percentile	Diameter μm	Settling velocity m s^{-1}	Settling time h			Travelled distance km			Covered Area %
			Discharge altitude km			Discharge altitude km			
			0.2	1	5	0.2	1	5	
10	4.09	0.0012	48	238	1,190	631	3,868	37,193	31.2
20	4.93	0.0017	33	164	819	434	2,662	25,598	22.5
30	6.01	0.0025	22	110	551	292	1,791	17,225	18.2
40	7.71	0.0041	13	67	335	178	1,089	10,466	8.5
50	9.22	0.0059	9	47	234	124	761	7,319	5.4
60	10.81	0.0081	7	34	170	90	554	5,324	4.7
70	13.16	0.0120	5	23	115	61	374	3,592	3.6
80	16.65	0.0192	3	14	72	38	233	2,244	3.3
90	24.86	0.0429	1	6	32	17	105	1,007	1.6
95	38.99	0.1054	1	3	13	7	43	409	1.1

Additionally, following results show the peak SL load per m^2 of ocean surface, and they are reported in Table 5.4 for the three discharge heights and the three discharge times.

Table 5.4: Maximum SL load per unit area in different scenarios, related to a single discharged load.

		Maximum SL load mgSL m^{-2}		
Altitude	**Time**	Antonov AN-32	Boeing 737-700C	McDonnell MD-11
0.2 km	1 min	10.1	17.8	61.0
	20 min	0.51	0.89	3.05
	40 min	0.25	0.45	1.52
1 km	1 min	1.65	2.91	9.95
	20 min	0.08	0.15	0.50
	40 min	0.04	0.07	0.25
5 km	1 min	0.17	0.30	1.03
	20 min	0.01	0.02	0.05
	40 min	0.00	0.01	0.03

5.4.2 MAXIMUM SLAKED LIME CONCENTRATION IN SEAWATER

To roughly evaluate SL concentration in water caused by the SL load, calculation of sedimentation velocity in seawater and resultant depth of complete dissolution is necessary. Table 5.5 reports terminal sedimentation velocity in seawater for each percentile of the granulometric distribution.

Table 5.5: Terminal sedimentation velocity and sinking depth in seawater for each particle size.

Percentile	Diameter	Terminal sedimentation velocity	Sinking depth
	μm	cm s^{-1}	cm
10	4.09	0.12	0.03
20	4.93	0.17	0.05
30	6.01	0.25	0.07
40	7.71	0.41	0.11
50	9.22	0.59	0.16
60	10.81	0.81	0.22
70	13.16	1.20	0.33
80	16.65	1.92	0.52
90	24.86	4.29	1.17
95	38.99	10.54	2.87

Using calculations from paragraph 5.3.3, considering the mass median diameter of 9 μm, a sedimentation speed in water of 0.59 cm s^{-1} has been found; as a result, particles sink 1.6 mm into oceans before complete dissolution. Experimental studies are crucial to analyse how the peak load varies according to the different particle size; big particles sink further, but they land in a narrower strip increasing their concentration. SL maximum concentrations obtained for each discharge scenario are reported in Table 5.6; specifically, they have been evaluated knowing maximum SL load per unit area (reported in Table 5.4) and the sinking depth.

Table 5.6: Evaluation of maximum concentration in seawater of SL per unit volume in each assessed scenario.

		Maximum SL concentration in seawater mgSL L^{-1}		
Altitude	**Time**	Antonov AN-32	Boeing 737-700C	McDonnell MD-11
0.2 km	1 min	13.5	23.8	81.3
	20 min	0.67	1.19	4.07
	40 min	0.34	0.59	2.03
1 km	1 min	2.20	3.88	13.3
	20 min	0.11	0.19	0.66
	40 min	0.05	0.10	0.33
5 km	1 min	0.23	0.40	1.38
	20 min	0.01	0.02	0.07
	40 min	0.01	0.01	0.03

As can be seen, only the case of a nearly instant discharge scenario with MD11 flying at 0.20 km from the ground does not respect the sand shrimp's NOAEC (50 mg L^{-1}), but the other implemented scenarios largely respect it. On the other hand, the threespine stickleback's NOAEC (100 mg L^{-1}) is always respected. It is worth remembering that such evaluation is made under a conservative assumption, since the mentioned NOAEC values are referred to a 96-hour exposure period. Moreover, the sinking depth related to the postulated time of

settling before dissolution, is a key hypothesis. However, even assuming more restrictive sinking times, each scenario until at least a 25 s dissolution time respects the threespine stickleback's NOAEC. Furthermore, if excluding MD11 scenario, the lowest NOAEC considered (50 mg L^{-1}) is ever respected even in the case of a 14 s dissolution time.

However, biological issues related to organisms inhabiting the atmosphere (i.e.: sea birds, insects) could be better investigated in future works.

In a multitrack analysis, where several sorties follow the same route, it is notable that horizonal surface ocean currents are ten times smaller than the related wind speed (Kelly et al., 2001). It is impossible to avoid track overlapping, because of the extended drift distances. However, a key role is played by dissolution time, which is not more than a few minutes thanks to the high vertical settling (Caserini et al., 2021). Assuming a large conservative environmental dissolution time of 3 minutes and considering the fastest aeroplane analysed (MD11 cruise speed: 781 km h^{-1}, Table 5.1), following aeroplanes should fly about 40 km behind to avoid unacceptably increasing SL concentration.

5.4.3 CO_2 EMISSIONS FROM DIFFERENT SCENARIOS

As stated before, the duration of the cruise varies according to each scenario, while climb and descent duration depends merely upon the flying altitude; in more detail, for 0.2 km and 1 km flying height these phases last 0 min (this because the LTO cycle reaches about 1 km), and for 5 km last 8.7 min.

Table 5.7 reports for each aircraft: cruise EFs that have been estimated for defined discharging altitudes in terms of kgCO_2 km^{-1} while the total emissions of the LTO cycle and the EFs for the climb and descent phases, in terms of kgCO_2 min^{-1}. Knowing the EFs of each phase it is possible to assess the total CO_2 emissions in each implemented scenario, thanks to the formula (5.1).

Table 5.7: Emissions of the LTO cycle and emission factor for every phase of the CCD cycle, for each aircraft type.

	Cruise EFs kgCO_2 km^{-1}			**Climb EFs**	**Descent EFs**	**LTO cycle emissions**
	Discharge altitude km			kgCO_2 min^{-1}	kgCO_2 min^{-1}	kgCO_2 $cycle^{-1}$
	0.2	1	5			
AN32	13.53	12.59	8.78	98.6	7.1	1,141
B737	17.89	17.06	13.42	192.6	13.8	2,598
MD11	47.04	45.56	38.82	838.3	59.9	8,278

Considering a goal of removing 1 GtCO_2 yr^{-1} through OAE, fleet size, CO_2 emissions, CO_2 removed per unit of SL discharged, and CO_2 penalty for every implemented scenario (resulting from the combination of aircraft type, discharge height and duration) are calculated, in the case of discharging for 50% or 75% of the time. These results are reported in Table 5.8 and in Table 5.9.

Net negative emissions are achieved, but the air distribution penalty is significant, between 10.6% and 76.5%. The penalty decreases as payload increases, due to lower drag losses.

Table 5.8: Mission duration, number of planes and daily trips, net CO_2 emissions, CO_2 removed per unit of slaked lime discharged, CO_2 penalty, per different aircraft type discharge duration and height. Discharge for 50% and 75% of the time.

Discharge altitude	Yearly discharging time		50%								
	Discharge time		1 min			20 min			40 min		
	Aircraft		AN32	B737	MD11	AN32	B737	MD11	AN32	B737	MD11
0.2 km	Mission duration	h	49	59	79	68	78	98	88	98	118
	Nr. of daily trips	trip (d plane)$^{-1}$	15	12	9	11	9	7	8	7	6
	Nr of planes	-	28135	14404	4417	38992	19024	5476	50420	23887	6591
	Net CO_2 emissions	$GtCO_2\ y^{-1}$	-0.84	-0.85	-0.89	-0.55	-0.63	-0.72	-0.24	-0.39	-0.54
	CO_2 rem. / SL disch.	$kgCO_2\ kgSL^{-1}$	0.70	0.70	0.74	0.46	0.52	0.60	0.20	0.33	0.45
	CO_2 penalty	%	16	15	11	45	37	28	76	61	46
1 km	Mission duration	h	54	64	84	73	83	103	93	103	123
	Nr of daily trips	trip (d plane)$^{-1}$	13	11	9	10	9	7	8	7	6
	Nr of planes	-	30970	15610	4694	41826	20230	5753	53254	25093	6868
	Net CO_2 emissions	$GtCO_2\ y^{-1}$	-0.81	-0.82	-0.87	-0.54	-0.61	-0.70	-0.25	-0.39	-0.53
	CO_2 rem. / SL disch	$kgCO_2\ kgSL^{-1}$	0.68	0.68	0.72	0.45	0.51	0.59	0.21	0.32	0.44
	CO_2 penalty	%	19	18	13	46	39	30	75	61	47
5 km	Mission duration	h	72	82	102	91	101	121	111	121	141
	Nr of daily trips	trip (d plane)$^{-1}$	10	9	7	8	7	6	7	6	5
	Nr of planes	-	40968	19865	5669	51824	24484	6728	63252	29347	7843
	Net CO_2 emissions	$GtCO_2\ y^{-1}$	-0.68	-0.71	-0.76	-0.49	-0.54	-0.62	-0.29	-0.37	-0.47
	CO_2 rem. / SL disch	$kgCO_2\ kgSL^{-1}$	0.57	0.59	0.63	0.41	0.45	0.51	0.24	0.31	0.39
	CO_2 penalty	%	32	29	24	51	46	38	71	63	53

Discharge altitude	Yearly discharging time		75%								
	Discharge time		1 min			20 min			40 min		
	Aircraft		AN32	B737	MD11	AN32	B737	MD11	AN32	B737	MD11
0.2 km	Mission duration	h	49	59	79	68	78	98	88	98	118
	Nr. of daily trips	trip (d plane)$^{-1}$	22	18	14	16	14	11	12	11	9
	Nr of planes	-	18757	9603	2945	25995	12683	3651	33613	15924	4394
	Net CO_2 emissions	$GtCO_2\ y^{-1}$	-0.84	-0.85	-0.89	-0.55	-0.63	-0.72	-0.24	-0.39	-0.54
	CO_2 rem. / SL disch.	$kgCO_2\ kgSL^{-1}$	0.70	0.70	0.74	0.46	0.52	0.60	0.20	0.33	0.45
	CO_2 penalty	%	16	15	11	45	38	28	77	61	46
1 km	Mission duration	h	54	64	84	73	83	103	93	103	123
	Nr of daily trips	trip (d plane)$^{-1}$	20	17	13	15	13	10	12	10	9
	Nr of planes	-	20646	10407	3129	27884	13487	3835	35503	16728	4579
	Net CO_2 emissions	$GtCO_2\ y^{-1}$	-0.81	-0.82	-0.87	-0.54	-0.61	-0.70	-0.25	-0.39	-0.53
	CO_2 rem. / SL disch	$kgCO_2\ kgSL^{-1}$	0.68	0.68	0.72	0.45	0.51	0.59	0.21	0.32	0.44
	CO_2 penalty	%	19	18	13	46	39	30	75	61	47
5 km	Mission duration	h	72	82	102	91	101	121	111	121	141
	Nr of daily trips	trip (d plane)$^{-1}$	15	13	11	12	11	9	10	9	8
	Nr of planes	-	27312	13243	3779	34549	16323	4486	42168	19565	5229
	Net CO_2 emissions	$GtCO_2\ y^{-1}$	-0.68	-0.71	-0.76	-0.49	-0.54	-0.62	-0.29	-0.37	-0.47
	CO_2 rem. / SL disch	$kgCO_2\ kgSL^{-1}$	0.57	0.59	0.63	0.41	0.45	0.51	0.24	0.31	0.39
	CO_2 penalty	%	32	29	24	51	46	38	71	63	53

Fuel consumption, and thus CO_2 emissions, is mainly related to flight height and distance. Specific CO_2 emissions generally increase with altitude because the climb phase emissions are too elevated and they have a higher impact over short flight durations; it is worth noting that while for the 1 and 20 min discharge scenarios the specific CO_2 removed increases as the altitude decreases, it is the opposite in the 40 min scenario; that is because for long tracks the climb emissions become less impacting than cruise emissions, which decrease with the altitude. Moreover, net emissions decrease with the aircraft size, due to the high SL load discharged which compensate the released CO_2.

5.4.4 PRELIMINARY COST ASSESSMENT

A preliminary costs assessment considers approximate Opex and Capex costs. Following cost estimations take into account the previously adopted exchange rate of 1.19 \$ €$^{-1}$ (Morningstar, 6th September 2021).

Opex evaluation

Fuel cost derives from fuel consumption, assessed from CO_2 emissions and average fuel costs: it has been considered 80.53 \$ bbl^{-1} (IATA, 2021), which is equal to about 0.51 \$ L^{-1}.

Literature data for Europe allow the assessment of a total operating cost (including fuel and oil, maintenance, landing fees, navigation fees, handling fees and crew expenses) of about €0.80 per available ton of load per km (€ ATK^{-1}), (Infras, 2006). Generally, the fuel cost accounts for 30-70% of the overall operating cost, and the consequent hourly Opex is \$11,000-12,500 for the larger wide-bodied aircraft versus \$7,000-10,000 for medium wide-bodied aircraft and \$3,000-4,250 for the narrow-bodied aircraft (World Bank, 2007).

Capex evaluation

Aircraft prices allow the calculation of the Capex in each scenario; that's because of the different existing fleets and the number of vehicles needed for the discharge. While in the ships' case, the number of existing cargo vessels could be sufficient to supply the OAE request, different is the aircraft situation. A brief analysis of the global current aircraft fleet is therefore carried out before the cost evaluation.

The active fleet in 2021 appears to be slightly less than 24,000 aircraft in total. This number is affected by the global pandemic that occurred in 2020 since such fleet has decreased by about 15%, if compared to January 2020. Before the COVID-19 pandemic, there were about 28,000 active aircraft, while nowadays, more than 4,000 aircraft are stored, waiting to be recalled or retired early. Widebodies compose a large part of this inactive fleet, and their operating number is not expected to recover the pre-COVID levels until 2024. However, narrowbody aircraft mainly compose the global fleet, representing more than 50% of the total fleet. Of predominant interest in this study is the size of the cargo fleet; currently, the number of cargo aircraft stands for 9% of the total fleet, and this percentage value is not expected to grow through the next decade. Estimates provide that in 2031 there will be 36,000 total aircraft, but nearly 34,000 will fly passengers. According to 2020 values, there are about 2,500 active cargo aircraft, and the large part is composed of widebodies (Cooper et al., 2021).

The various size of existing cargo aircraft has not been considered in the previous brief evaluation, because it is a minor issue if compared to the small cargo fleet size. The most optimistic scenario which is recognizable in table 5.9 (MD11 discharge from 0.2 km, during a 1 min cruising time), provides the requirement of a fleet composed of 2,945 aircraft. This value is slightly over the total current cargo fleet, but this gap becomes enormous considering other scenarios. The obtained fleet size varies from 2,945 to 7,843 considering the various MD11 scenarios, while it ranges between 9,603 and 129,437 in the case of B737. AN32's needed fleet is sensibly higher, never less than 18,757 aircraft. However, the latter situation is different since AN32 is not a cargo aircraft, but a firefighting or military plane.

The result of this consideration is that no cargo aircraft are currently available for OAE, neither active nor inactive, and so the needed fleet should be almost entirely built for the purpose. For this reason, Capex is evaluated considering the aircraft prices, but the realization of such a fleet appears as a monumental task.

Capital cost is assessed considering the aircraft cost and average lifetime. The average cost of a single Antonov AN-32P is about €6.72 mln (Karnozov, 2007), while the cost of a Boeing 737-700 is €72.2 mln (Boeing, 2018) and a McDonnell-Douglas MD-11 costs about €117.6 mln (Forecast International, 2003). Aircraft costs could be very variable, and above all, they don't increase linearly according to the payload.

For Capex evaluation, it is important to assess the average aircraft lifetime. United States Department of Transportation databases (USDT) estimates an average lifetime of the Boeing 737-700 of about 25 years, and of the McDonnell Douglas MD-11 of about 28 years (Bureau of Transportation Statistics, 2019), while other studies suggest that the average lifetime for the Antonov AN-32P is about 15 years (Airforce Technology, 2019). The yearly Capex has been obtained simply by dividing the total cost for the average lifetime. This study neglected every type of rate of interest.

Total cost

The sum of operating costs and capital costs allows the calculation of the total costs. Only the discharging cost has been evaluated, so the SL supply chain cost has been neglected.

Total cost per ton of CO_2 removed varies between a minimum of 30 € tCO_2^{-1} and a maximum of 1,846 € tCO_2^{-1}; the costs per ton of CO_2 removed for short distances (discharge duration: 1 min and 20 min) are lower for smaller aircraft, because of Opex increases with aircraft size (fuel consumption is much higher, especially during LTO and climb phase). On the other hand, for longer duration scenarios (discharge duration: 40 min), the costs are higher for smaller aircraft, because the increasing number of emissions due to the cruise phase are not compensated by the low amount of SL discharged: the climb and descent phases emissions (which are lower for smaller aircrafts) become less important over long distances. Instead, the specific cost does not show a linear proportion between the bigger airplanes (B737 and MD11); that is related to Capex evaluation: while the Opex increases with the size, the Capex does not vary linearly according to the payload (a huge significance is given by the MD11 fleet size, much smaller than the others). Total costs estimations are reported in Table 5.9.

Table 5.9: Assessment of the operative, capital, and total costs for discharging via aircraft.

Discharge altitude	Discharge time		1 min			20 min			40 min		
			AN32	B737	MD11	AN32	B737	MD11	AN32	B737	MD11
0.2 km	Opex per trip	€ trip^{-1}	110	344	1,913	1,042	3,258	18,137	2,024	6,327	35,215
	Opex per year	bn € yr^{-1}	17	22	28	156	208	266	304	404	516
	Capex per year	bn € yr^{-1}	8	28	12	12	37	15	15	46	18
	Total cost per year	bn € yr^{-1}	25	50	40	168	245	281	319	450	534
	Cost per rem. CO_2	€ tCO_2^{-1}	30	59	45	308	392	388	1357	1148	982
1 km	Opex per trip	€ trip^{-1}	353	1,105	6,148	1,286	4,019	22,372	2,267	7,087	39,450
	Opex per year	bn € yr^{-1}	53	71	90	193	257	328	340	453	578
	Capex per year	bn € yr^{-1}	9	30	13	12	39	16	16	48	19
	Total cost per year	bn € yr^{-1}	62	101	103	206	296	344	356	501	597
	Cost per rem. CO_2	€ tCO_2^{-1}	77	122	119	381	484	488	1,432	1,288	1,124
5 km	Opex per trip	€ trip^{-1}	1,212	3,789	21,089	2144	6,704	37,313	3,125	9,772	54,391
	Opex per year	bn € yr^{-1}	182	242	309	322	428	547	469	624	797
	Capex per year	bn € yr^{-1}	12	38	16	15	47	19	19	57	22
	Total cost per year	bn € yr^{-1}	194	280	325	337	476	565	488	681	829
	Cost per rem. CO_2	€ tCO_2^{-1}	286	395	430	692	875	919	1,710	1,846	1,751

The high cost of SL discharge by aircraft is dominated by Opex, principally fuel. Although a near-instant discharge could reduce costs, SL discharge by ships remain very much cheaper. The Opex increases as the aircraft payload increases because of the fuel usage due to the weight. However, the cost per unit of CO_2 removed acts differently: smaller aircraft have minor climb emissions, and so they are convenient over shorter tracks. Larger aircraft are better when the cruise phase lasts longer (at least 40 min, where the cruise phase has a higher significance comparing it with the LTO and climb phase), because they can compensate the cruise emissions with a large SL payload needing a smaller fleet. Moreover, Capex varies significantly, and this variation is not linear according to aircraft payload: in fact, a larger aircraft has a higher cost, but the fleet size needed will be smaller. For this reason, also the specific cost does not show a linear proportion between the bigger aeroplanes as investigated before.

5.4.5 FINAL EVALUATION OF AIRCRAFT DISCHARGE SYSTEM

Issues related to SL shedding via aircraft should be better analysed. One of the predominant problems is given by the smallest particles that remains suspended into the atmosphere and may become Cloud Condensation Nuclei (CCN). Cloud dilution may reduce peak ocean alkalinity, but it is complex to predict the fate of these small particles. Winds could transport them as clouds far from the intended settling area, possibly over land, before precipitation. In addition, the finest SL particles that remain suspended in the atmosphere layer over the ocean surface (so-called Marine Atmospheric Boundary Layer, MABL) could act as CCN improving the albedo of marine clouds and increasing the reflection of solar radiation from the Earth-atmosphere system (Alterskjær and Kristjánsson, 2013).

Moreover, the assessment shows that it is not always convenient to discharge at elevated altitudes for short time due to the decrease with height of air viscosity and density (Çengel, 1998), because climb phase and LTO cycle emissions have a bigger impact over short

discharging length. This can be seen also from the penalties obtained from the assessment, reported in Figure 5.10. The penalty increases as the discharging time, discharging height and aircraft size increase.

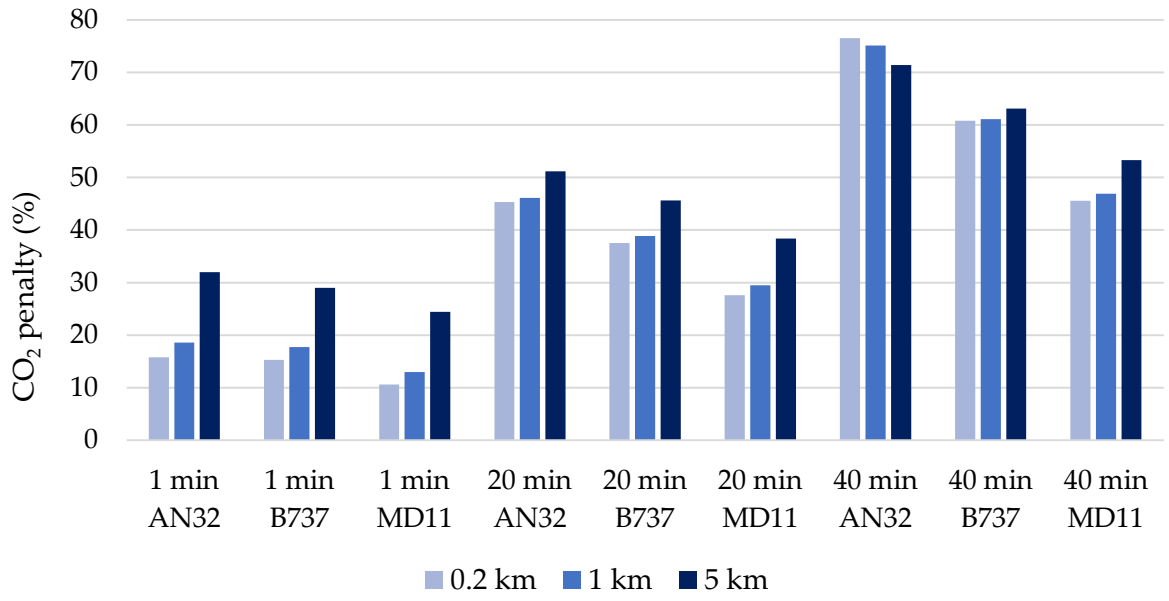

Figure 5.10: CO_2 penalty for each type of aircraft for different discharging height and duration.

However, if the discharge lasts longer, the SL discharge at high altitude would become convenient. On the other hand, even though the assessment shows that is more convenient (in terms of penalty, and costs) to discharge at low altitude, it is worth noting that it is not always suitable to fly for a long time at these heights because of the risks liked to the significant and uncomfortable turbulence. Furthermore, extreme weather could pose some problems; in rough seas, sea spray could interfere with the engine functionality, and also the presence of fog could limit visibility. For these main reasons, the discharge should be very fast in order to reduce the risks. Similar altitudes are typical of firefighting aircraft (usually about 100 m), which fly for short periods allowing swift discharge.

SL discharge should be limited to areas without maritime traffic for a huge space, since the settling distance for the median diameter in the different scenarios varies from 130 km to 7,500 km. Careful meteorology (especially wind direction) is necessary, to avoid the sedimentation of particles in inhabited or trafficked areas. The elevated distances travelled by the smallest particles, due to the wind speed, avoid the possibilities of discharging SL at too much elevated quotes: the distance covered by the 10-percentile particles from a 5 km discharging altitude (about 40,000 km) is almost equal to the circumference of the planet, and so it is impossible to determine the fate of these particles using a simple model. Realistically, they could settle anywhere on the Earth.

Costs of SL aircraft distribution is substantial, one order of magnitude higher than the cost of discharging technology using ships (Renforth et al., 2013; Caserini et al., 2019). Further development could lead to lowering costs, for example, by using renewable energy aircraft (i.e.: electric aircraft) with large payload (with reduced environmental impact), but the energy

penalty linked to flying at high altitude could remain a constrain for this technology. Another option could be relying on wind distribution; aircraft could avoid long routes by flying short sorties, leading the lime to be transported principally by the wind. This option requires a seaward wind, mandating accurate meteorology forecasts.

A preliminary analysis of the suitable airports all over the world is carried out. Airports used should be not far away from the coast (minimising transfer distance), located where maritime traffic is minimal, and be far from population centres which may be affected by wind drift. Further, they must be located far from marine downwelling regions created by the thermohaline circulation, which will reduce the long-term contact between the alkaline material and the atmosphere and should also be near sources of alkaline material to minimise terrestrial transport distances to the airports. Table 5.11 reports some airports that have been analysed as a preliminary overview of some areas where the meteorological condition and the maritime traffic intensity could be optimal for the intended purpose, moreover, Figure 5.10 shows airport location.

The areas where both marine traffic and circulation conditions seem to be optimal are the following:

- Southern and South Atlantic Ocean below South America;
- Oceania, especially islands in the Pacific Ocean;
- Southern Ocean below South Africa;
- North Atlantic Ocean along the north-western coast of Europe;
- North Pacific Ocean along the north-western coast of Canada and Alaska.

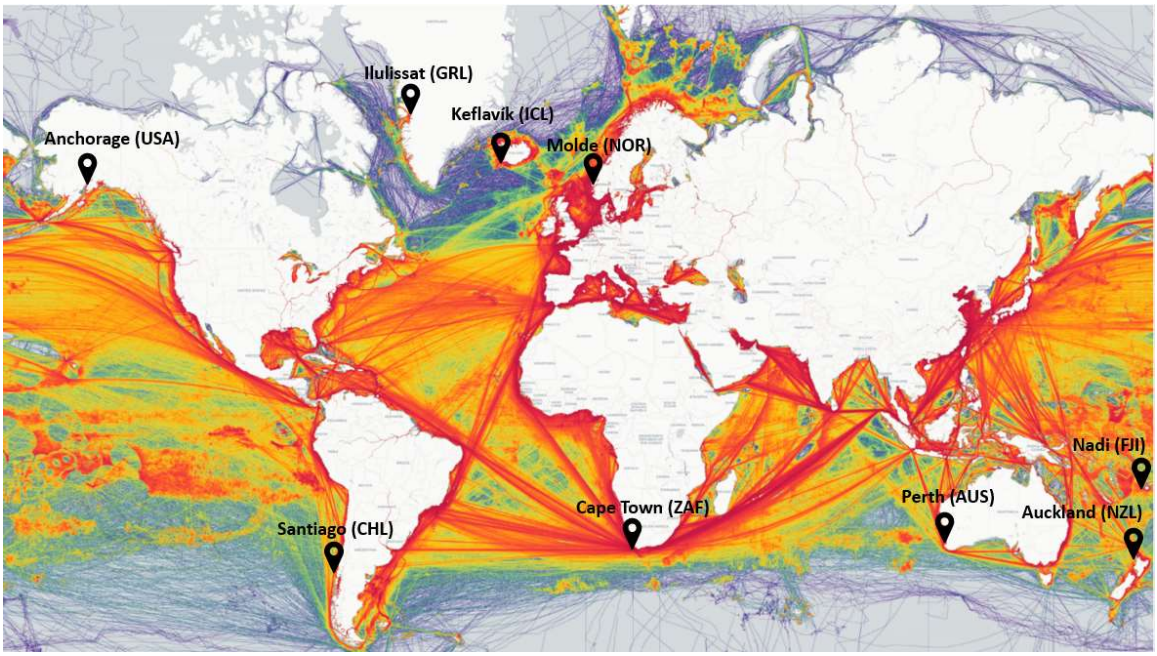

Figure 5.11: Possible suitable airports for departure. The map also reports the density of global shipping in 2020, in order to have a preliminary idea of the most congested areas that should be avoided (reworked from MarineTraffic, 2020).

Table 5.10: Analysed airports all over the world for aircraft departures.

IATA Code	Airport Name	Location
ANC	Ted Stevens Anchorage International Airport	Anchorage, Alaska, USA
AKL	Auckland Airport	Auckland, New Zealand
CPT	Cape Town International Airport	Cape Town, South Africa
JAV	Ilulissat Airport	Ilulissat, Greenland
KEF	Keflavík International Airport	Keflavík, Iceland
MOL	Molde Airport	Molde, Norway
NAN	Nadi International Airport	Nadi, Fiji
PER	Perth Airport	Perth, Western Australia
SCL	Comodoro Arturo Merino Benitez International Airport	Santiago, Chile

5.4.6 ALTERNATIVE DISCHARGING METHODS

This chapter aims to briefly investigate alternative SL discharging methods relying both on dry and wet technologies, but also possible way to spread even QL, reducing its related side effects.

Vessels as aircraft support base

Alternatively, ships transporting SL powder could support the use of seaplanes, avoiding the return route to the airport to load the aircraft. Carriers could transport alternative small aircraft. In this way, the airport location should not constrain the aircraft route planning, and there is also the chance to avoid trafficked areas near the coast, minimizing the risk of land settling or other types of human interferences. This possibility is related to the cargo capacity of dedicated vessels, much larger than the air freighters' load. For instance, considering a bulk carrier with a 75,000 dwt and an Antonov AN-32P aircraft, which could carry about 8 tSL, a single vessel could restock such a plane more than 9,000 times. This value could be lower because of the needing to transport the aircraft fuel. Moreover, many aircraft could fly simultaneously along different routes from the vessel, maximizing the process efficiency but without increasing the SL load per unit area. This technique could be better using small aircraft, because they must be very manoeuvrable and easy to be stationed on or near the vessel for refuel and reload operations, maybe with the help of dedicated aircraft carriers cruising alongside the cargo ship.

Slaked lime slurry discharge via aircraft

If the problem of particles settling too far from the aircraft route is a huge obstacle, causing many consequences including land deposition, the possibility to discharge SL in a different form could be interesting. Spreading a SL slurry would reduce the excessive wind transportation, leading to more controlled particles settling. However, huge obstacles are present, because the SL transport capacity would be lowered, as a consequence of the water portion in the milk of lime. Furthermore, the impact of slurry droplets in higher concentrations could pose problems on the SML, due to the mechanical impact, and even increasing SL load on the surface. By this type of spreading, an adequate nebulization of the

discharged slurry droplets could increase the efficiency, but it must be a compromise between the abovementioned properties.

Slaked lime dispersion driven by winds

Alternative methodologies based on dry deposition could be investigated to exploit SL dispersion driven by winds. Towers, tethered balloons, or cannons could be located on windy coasts: this solution could however cause problems because of the sea breeze effect. These could also locate on ships or buoys, right in the middle of the ocean, or still sufficiently far from the coast, according to meteorological conditions. The advantages of positioning such discharge methods in the middle of the ocean are various: interferences with human activities are minimized, and winds are more predictable if compared to nearshore breezes. Otherwise, a great obstacle is related to material transportation in such remote areas, which could pose energetic limitations.

Quicklime wet deposition

Another option could be deliberate wet deposition. QL particles can be dropped into clouds: these particles are very hygroscopic and so they could act as CCN, or dissolve quickly into existing cloud droplets (Kecorius et al., 2019). Clouds could transport the resulting solution, which is dissolved in them before being discharged as precipitation. While dilution takes place, QL is in contact with water and so slaking process could occur. During this hydration QL reacts forming SL, reducing the possible negative effects on biology impacting the ocean surface.

Free-floating particles impact the direct radiative effect due to their extreme surface area. At altitude, the presence of these particles drying the atmosphere, in clean saturated air, will cause precipitations from cirrus clouds, ultimately reducing homogeneous nucleation, inducing Cirrus Cloud Thinning (CCT) (Liu and Shi, 2021). Cirrus clouds have a key role in climate warming blocking Earth's outgoing longwave radiation (Muri et al., 2014). Cirrus cloud modification may reduce global temperature (Gasparini et al., 2020). The dissolution into cirrus cloud droplets will dilute QL before its impact on the ocean surface. These droplets may have a second dilution in boundary layer clouds. During a typical 1-inch rainstorm, an average water quantity of 103 m^3 is related per 4,000 m^2 (USGS, 1988), and so it is possible to discharge about 5.15 tSL in the clouds per acre before reaching the NOAEC level (considering the 50 mg L^{-1} sand shrimp NOAEC), thanks to the dilution effect, thus not considering a second dilution by the ocean surface. This type of wet deposition will also reduce the negative effects of QL on ecosystems.

6. PHYSICAL MODEL OF SLAKED LIME DISCHARGE AT SEA

The main process under study is SL dissolution in seawater, a process during which both particle diameter and surface area decrease. In past times, many literature studies analysed this phenomenon implementing various physical models (Johannsen and Rademacher, 1999; Bernard, 2000), but this must be adequate to the process with a suitable physical mathematical procedure. To do this, literature allowed the investigation of appropriate models, while experimental studies have been carried out. This analysis aims to identify the best dissolution model and then implement it in MATLAB.

Later, it is also on-topic to preliminary assess the evolution of pH level reached after SL discharge, to better understand the maximum spikes and its resulting side effects on the marine environment and biology. A fluid dynamic model is necessary to carry out this evaluation, comprising turbulence modelling and involving the SL dissolution MATLAB code.

6.1 EXPERIMENTAL STUDIES ON SLAKED LIME BEHAVIOUR IN SEAWATER

For the realization of a physical model for the description of SL behaviour in seawater, laboratory experiments are necessary. All the laboratory experiments described in the following chapters are the results of Colombo and Crisanto's (2021) Master's degree thesis.

Colombo and Crisanto (2021) made laboratory experiments for studying SL dissolution. They poured various SL amounts in beakers under stirring containing artificial seawater. Parameters, like pH and conductivity, are measured using appropriate sensors. Moreover, additional measurements are made to quantify the alkalinity and solid residues after filtration of the solutions.

In this regard, the Roy et al. (1993) recipe allowed producing synthetic seawater in the laboratory, as reported in Table 6.1; this recipe solely considers the major five salts, it has a salinity S of 35 g kg^{-1}, and a synthetic seawater density ρ_w of 1,024.75 kg m^{-3}.

Table 6.1: Artificial seawater composition in terms of mole of salt per kg of solution (Roy et al., 1993).

Salt		**Molality**
		mol kg^{-1}
Sodium chloride	$NaCl$	0.413
Sodium sulphate	Na_2SO_4	0.028
Potassium chloride	KCl	0.010
Magnesium chloride	$MgCL_2$	0.053
Calcium chloride	$CaCl_2$	0.010

All tests are carried out in 2 L beakers usually using one litre of seawater solution, agitated thanks to a magnetic or a mechanical stirrer to guarantee an adequate and homogenous

mixing. A known quantity of SL is added in seawater either as a slurry or as a powder. Poured SL concentration varies between 0.2-8 gSL L^{-1}, in more details the following concentration, in terms of gSL L^{-1}, values have been adopted: 0.2, 0.4, 0.8, 2, 4, and 8 gSL L^{-1}.

Thanks to a pH-meter and a conductivity-meter, it was possible to measure pH and conductivity every second. Measurements are taken at about 5 cm from the water surface.

The electrical conductivity of the solution is a measure of water's capability to pass electrical flow, directly related to ions concentration into water. It depends strongly on temperature, so the measured values require a temperature-dependent correction and conversion to the standard temperature of 25 °C, as shown in formula (6.1). For the solution under study, the conductivity increases 2% each Celsius degree higher than 25 °C (Down and Lehr, 2004).

$$\sigma_{25} = \sigma_T[1 + \alpha_T\,(25 - T)] \tag{6.1}$$

where:

σ_{25}: seawater conductivity at 25 °C [μS cm^{-1}];
σ_T: seawater conductivity at temperature T of measurement [μS cm^{-1}];
α_T: temperature coefficient of variation [-], assumed 0.02 (Down and Lehr, 2004);
T: seawater temperature of measurement [°C].

These experiments have been carried out firstly at an ambient temperature of about 22 °C. To recreate the different oceans' conditions all over the world, some additional analyses are made for different temperatures (ranging between 5°C and 25°C) and salinity (ranging between 10 g kg^{-1} and 40 g kg^{-1}).

It is important to underline that these experiments have some measurement limitations that should be discussed in more detail, related to the assessments of calcium ions concentration and alkalinity. These parameters could be useful because they allow evaluating the quantity of SL that dissolves. One of the main limitations is due to titrations tests done during the initial experiments to assess how much SL dissolves in seawater. The titration method calculates the solution's alkalinity by adding a strong acid and evaluating the pH variation. The addition of acid enhances SL dissociation in the laboratory experiment, so it is not a reliable method for estimating the quantity of dissociated SL because it generally overrates this calculation. Subsequent analyses have been carried out filtrating the solution, with a significantly lower quantitative of undissolved SL. However, such measurements are not continuous, causing not perfectly reliable results. Furthermore, some technical problems occurred to the probe devoted to the measurements of calcium ions, making it impossible to evaluate the increase of such ions during SL dissolution. For these reasons, pH and conductivity results are more reliable than the calcium ions and alkalinity measurements.

Further analyses are necessary to understand the characteristics of the artificial seawater used in laboratory experiments. First of all, an investigation of the ionic compositions of the intended seawater, shown in Table 6.2, allowed examining additional properties of such water (i.e.: total alkalinity). This simple ionic study is performed assuming the complete dissolution of the salt dosed according to the Roy et al. (1993) recipe.

Table 6.2: Ionic composition of the artificial seawater.

Ionic species	Concentration		Molecular weight
	g L^{-1}	mol kg^{-1}	g mol^{-1}
Na^+	11.00	0.47	23.0
Cl^-	19.85	0.55	35.5
SO_4^{2-}	2.77	0.03	96.1
K^+	0.41	0.01	39.1
Mg^{2+}	1.31	0.05	24.3
Ca^{2+}	0.42	0.01	40.1

The ionic analysis in Figure 6.1 shows that the main component is chlorine ion (56%), followed by sodium ion (31%); other ions range between the 1% and 8%.

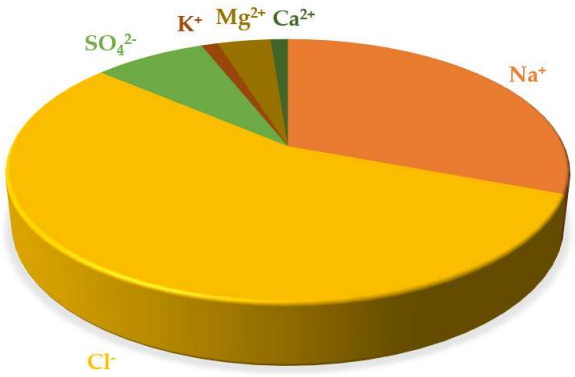

Figure 6.1: Ionic analysis of artificial seawater, in terms of percentage.

Following this analysis, it is possible to examine the initial TA of such a water sample. Two different ways could express the TA evaluation, either in moles per kg of solution or equivalent mg of $CaCO_3$ per litre of solution. In both situations, TA is calculated as the difference between conservative cations and anions, as described in Chapter 2.1, taking into consideration the valence of each ion. The result is that the concentration of cations is the same as the anions, and equal to 0.61 mol kg^{-1}. The consequence is that this water has low TA, and so it has low buffer capacity, as graphically shown in Figure 6.2. Laboratory experiments confirmed that the starting alkalinity was very low, under the instrument sensitivity of 30 mg $CaCO_3$ L^{-1}.

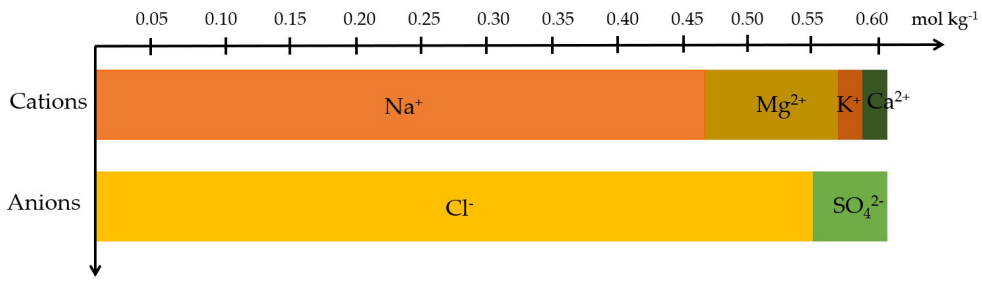

Figure 6.2: TA analysis of artificial seawater used in laboratory experiments. It is worth noting that the sum of all cations is equal to the sum of all anions, so it has no buffer capacity.

6.2 NATURAL SEAWATER CHARACTERISTICS

In order to obtain the results of the intended model in a real situation it is fundamental to investigate and understand the characteristics and peculiarities of natural seawater.

Following results and calculations assumed the global oceans' average conditions, which contains more ionic species than synthetic seawater. In addition to the major constituent salts already considered in artificial seawater, the real one contains also numerous minor elements, in terms of parts per million or per billion, like radionucleotides, organic compounds, and metals. These minor constituents represent numerous substances, but together they make up less than 1% of the ions in the seawater; at this purpose the major ions in seawater comprise over 99% of the total salinity, this implies that changes in abundance of the minor constituents have little effect on overall salinity (Webb, 2019). So, on average the seawater's natural salinity is assumed equals to 35 g kg^{-1}, the same characterizing synthetic seawater.

It is also relevant to examine the ocean temperature. This specific study investigates only SST because sea surface it is main ocean's part involved in SL spreading and dissolution. SST varies with latitude due to the variation of the angle of incoming solar radiation. At low latitudes, near the equator, the surface receives all year direct overhead sunlight warming shallow waters, while at high latitudes ocean waters receive less sunlight. So, the ocean surface can vary in temperature from a warm 30°C in the tropics to a very cold -2°C near the poles; it is worth noting that at equivalent latitudes, water on the eastern side of the ocean basins is colder than the water on the western side. In some areas, this surface temperature is relatively stable while in others, it seasonally fluctuates (Webb, 2019; Earle, 2019).

Temperature variation has great effects on seawater density ρ_w and viscosity μ_w: they both decrease as SST increases. In particular, global surface density ρ_w ranges between 1020 and 1028 kg m^{-3}, while viscosity μ_w ranges between 1.84 10^{-3} and 8.61 10^{-4} Pa s (ITTC, 2011).

For these reasons, the first analyses (aiming to validate the MATLAB code described in Chapter 6.3.5) consider three different temperatures T, and consequently seawater density ρ_w and viscosity μ_w: 15 °C is a representative SST in ocean areas at a latitude of about 40° N and 40° S, 22 °C as an indicator of the tropics' SST (and, moreover, it is the temperature of the synthetic seawater samples) and finally 25 °C for the equatorial zone. Maps showing sea-surface temperature and density are reported in Figure 6.3.

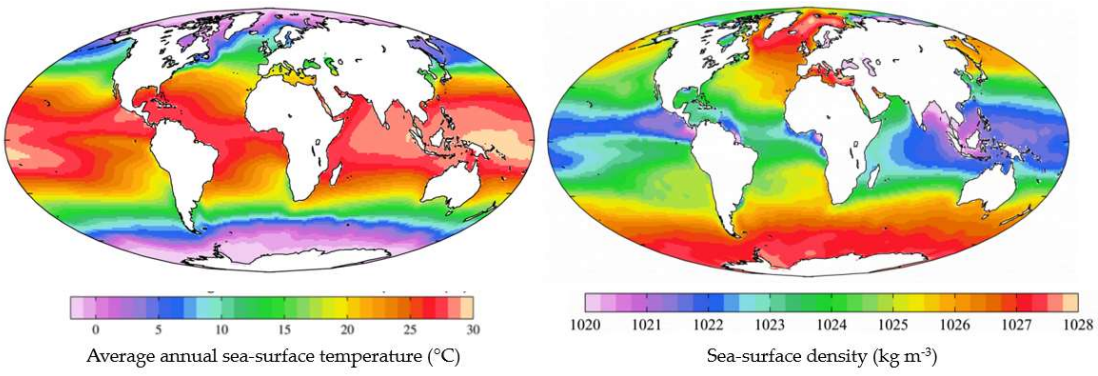

Figure 6.3: Maps of average annual sea-surface temperature (left) and density (right) (Webb, 2019).

The first fundamental parameter to be assessed is the seawater pH. Although pH is decreasing in the last years due to climate change, a typical value of 8.2 is considered (Wolf-Gladrow et al., 2007). According to that, the concentration of H^+ ions and then OH^- concentration is calculated. To do this evaluation, the assumption about the ionic product for seawater K_w^* is necessary (formula (6.2)), which links the concentration of H^+ and OH^- ions.

$$[OH^-] = \frac{K_w^*}{[H^+]} \tag{6.2}$$

where:

K_w^*: ionic product for seawater [mol^2 kg^{-2}].

K_w^* is strongly dependent on the temperature. Constant values are available in literature for various temperatures; for instance, Wolf-Gladrow et al. (2007) suggest a pK_w^* of 13.2 at 25°C. However, when needed, equations are available in literature to fix these constant values according to temperature and salinity. Following equation (6.3) is considered for K_w^* calculation, expressed in terms of mol^2 kg^{-2}, as a function of temperature T and salinity S (Dickson and Goyet, 1994).

$$ln(K_w^*) = 148.96502 - \frac{13847}{T} - 23.651\, ln(T) + \\ + \left(\frac{118.67}{T} - 5.977 + 1.0495\, ln(T)\right)\sqrt{S} - 0.01615\, S \tag{6.3}$$

where:

T: seawater temperature [K];
S: seawater practical salinity [g kg^{-1}].

Previous literature studies (Wolf-Gladrow et al., 2007) assessed the DIC value: even this value depends on the temperature because strictly correlated with the partial pressure of CO_2 in the atmosphere.

Table 6.3 reports the main parameters adopted.

Table 6.3: Main parameters of natural seawater at T= 25°C and S = 35 g kg^{-1}.

Parameter	u.m.	Value
pH	-	8.2
pK_w^*	-	13.2
$[H^+]$	µmol L^{-1}	0.0063
$[OH^-]$	µmol L^{-1}	10
pCO_2	ppm	420
DIC	mmol L^{-1}	2

Additional calculations are fundamental to obtain the concentration of bicarbonate $[HCO_3^-]$ and carbonate $[CO_3^{2-}]$ ions. These values are needed to find the CA, which can be assumed equal to the TA as a preliminary evaluation. $[HCO_3^-]$ and $[CO_3^{2-}]$ are a fraction of the DIC, and

their value depends on the stoichiometric dissociation constants of carbonic acid (K_1^* and K_2^*), (formula (6.4), (6.5), (6.6)).

$$CO_2 + H_2O \overset{K_1^*}{\leftrightarrow} HCO_3^- + H^+ \overset{K_2^*}{\leftrightarrow} CO_3^{2-} + 2\mathrm{H}^+ \tag{6.4}$$

$$K_1^* = \frac{[HCO_3^-][H^+]}{[CO_2]} \tag{6.5}$$

$$K_2^* = \frac{[CO_3^{2-}][H^+]}{[HCO_3^-]} \tag{6.6}$$

K_1^* and K_2^* depend both on temperature T and salinity S. Many formulations are available in literature studies to determine such constants; here below are reported the equations (6.7) and (6.8) suggested by Hansson (1973) and refitted by Dickson and Millero (1987).

$$pK_1^* = \frac{851.4}{T} + 3.237 - 0.0106\,\mathrm{S} + 0.000105\,\mathrm{S}^2 \tag{6.7}$$

$$pK_2^* = -\frac{3885.4}{T} + 125.844 - 18.141\,ln(T) - 0.0192\,S + 0.000132\,S^2 \tag{6.8}$$

Knowing the DIC and after evaluating these equilibrium constants, it is possible to determine the concentration of bicarbonate and carbonate ions thanks to the following formulations (6.9) and (6.10); in the current study the presence of CO_2 is almost negligible in the DIC evaluation if compared to bicarbonates and carbonates, because of the actual pH level (Zeebe and Wolf-Gladrow, 2003).

$$[HCO_3^-] = DIC\,\frac{[H^+]K_1^*}{[H^+]^2 + [H^+]K_1^* + K_1^*K_2^*} \tag{6.9}$$

$$[CO_3^{2-}] = DIC\,\frac{K_1^*K_2^*}{[H^+]^2 + [H^+]K_1^* + K_1^*K_2^*} \tag{6.10}$$

After obtaining the values of $[HCO_3^-]$ and $[CO_3^{2-}]$, it is possible to calculate the CA, according to equation (2.3). This value of CA is also evaluated in equivalent g$CaCO_3$, multiplying the alkalinity (expressed in mol kg^{-1}) by 50 equivalent g$CaCO_3$. Table 6.4 reports the results.

Table 6.4: Carbonate alkalinity and its constituent parameters at T = 25°C and S = 35 g kg^{-1}.

Parameter	u.m.	Value
$[HCO_3^-]$	mmol kg^{-1}	1.69
$[CO_3^{2-}]$	mmol kg^{-1}	0.31
CA	μmol kg^{-1}	2308
	mg$CaCO_3$ kg^{-1}	115.4

The CA value obtained shows that it is the principal constituent of the total alkalinity; in fact, Zeebe and Wolf-Gladrow (2003) assigned a TA value in seawater of about 2300 μmol kg^{-1}. The different ionic compositions cause the deviation in total alkalinity between artificial and natural seawater. In such water, there is a low unbalance in conservative cations and anions,

offset by the presence of alkalinity (mainly bicarbonates, carbonates, and hydroxyl groups). The result is that seawater is an overall neutral solution.

As described in Chapter 6.2, the calcium concentration in seawater is rather significant. Natural $[Ca^{2+}]$ in seawater is very similar to the one calculated in synthetic water. Indeed, Zeebe and Wolf-Gladrow (2003) assigned Ca^{2+} a concentration value of about 0.01 mol L^{-1} (more precisely 418 mg L^{-1}).

These evaluations are carried out for a set of temperature T, so Table 6.5 reports the main parameters adopted.

Table 6.5: Different seawater characteristics for different temperature T.

Parameter	**u.m.**	**Value**		
Temperature	°C	15	22	25
Density, ρ_w	kg m^{-3}	1,026.0	1,024.3	1,023.4
Viscosity, μ_w	Pa s	1.22 10^{-3}	1.03 10^{-3}	9.59 10^{-4}
K_1^*	mol kg^{-1}	1.12 10^{-6}	1.32 10^{-6}	1.41 10^{-6}
K_2^*	mol kg^{-1}	7.79 10^{-10}	1.02 10^{-9}	1.14 10^{-9}
K_w^*	mol^2 kg^{-2}	2.38 10^{-14}	4.62 10^{-14}	6.07 10^{-14}
TA	µmol kg^{-1}	2212	2275	2308

K_1^* and K_2^* values in Figure 6.4 show that the bicarbonate concentration $[HCO_3^-]$ is predominant on carbonates $[CO_3^{2-}]$ in seawater. Both of them increase with temperature because H_2CO_3 dissociates strongly at higher T. Furthermore, even TA increases with T because of the higher dissolution rates. However, the distribution of these ionic species is strictly related to the pH level. Figure 1.11 shows that high pH values are related to a majority of carbonate ions, while neutral pH levels cause a predominance of bicarbonates.

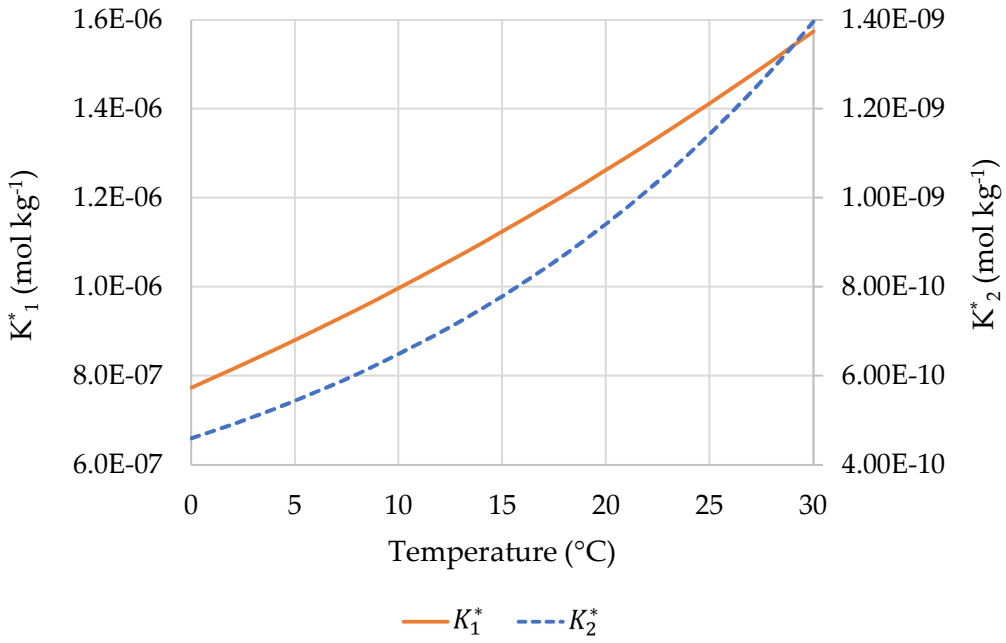

Figure 6.4: Variation of K1 and K2* with temperature T. Graph shows that bicarbonate concentration is higher rather than carbonate ions concentration.*

6.3 PHYSICAL MODEL FOR SLAKED LIME DISSOLUTION IN SEAWATER

The following chapters investigate the behaviour of SL when discharged in a saline environment. A literature review of proper dissolution models aims to find the best way to describe SL dissolution. Later, the discussed models are run into appropriate calculation programs, to compare the results with experimental data. A correction of empirical constants is subsequently operated, to find the best kinetic behaviour of the examined reactions in the specific operating system. In addition to the dissolution models, this study evaluates different ways to consider the particle radius decrease. SL particles (as powder or slurry) reduce their size according to their dissolution. This fact is relevant because the surface of the SL particles in contact with water determines the dissolution rate; the larger the contact area, the faster is the reaction.

For the sake of simplicity, in the following models SL particles are mainly represented by the mass median diameter d_p (9 μm). However, sensitivity analyses aim to analyse various particles' sizes.

Later, the study aims to realize a fluid dynamic model describing SL dissolution and dispersion when poured in a beaker, comparing these results with laboratory experiments from Colombo and Crisanto's study (2021).

6.3.1 JOHANNSEN AND RADEMACHER DISSOLUTION MODEL

In 1999, Johannsen and Rademacher developed a model to describe the SL dissolution in water. They aimed to examine better the usage of SL in water treatments such as softening, decarbonization techniques, and stabilization processes. According to previous studies, they assessed that the dissolution rate depends on the concentration of undissolved particles and the degree of saturation.

The first assessment of Johannsen and Rademacher (1999) is the formulation of the net rate of dissolution R_d (formula (6.11)), which depends on the activity (denoted by curly brackets) of calcium ions $\{Ca^{2+}\}$ and hydroxyl groups $\{OH^-\}$, because they are the ions which form a SL molecule, and their presence increases in seawater during the SL dissolution, according to reaction (2.4). In particular, the relationship with OH^- ions is squared, because a SL molecule releases two hydroxyl groups.

$$R_d = k_f - k_b\{Ca^{2+}\}\{OH^-\}^2 = \frac{d[Ca^{tot}]}{A\,dt} \tag{6.11}$$

where:

R_d: net rate of dissolution [mol L^{-1} s^{-1} m^{-2}];
A: total surface of the particles [m^2];
k_f: forward constant rates of the SL dissolution reaction [mol L^{-1} s^{-1} m^{-2}];
k_b: backward constant rates of the SL dissolution reaction [L^2 mol^{-2} s^{-1} m^{-2}].

To compare laboratory results with the intended modelled increase of calcium ions in water, to subsequently link it to a specific pH increase, the initial concentration of calcium ions $[Ca^{2+}]_0$ is fundamental. Such value is shown in Table 6.2, and it is equal to 0.01 mol L^{-1} (about 420 mg L^{-1}). The importance of this value is due to the fact that the dissociation of SL in Ca^{2+} and OH^- depends also on $[Ca^{2+}]$ value at the beginning of the reaction.

The ions activities can be linked to the ions' concentration by the usage of a practical activity coefficient f, which is itself a function of the ionic strength I; so, the net rate of dissolution R_d can be written as follow (6.12). The practical activity coefficient f used by Johannsen and Rademacher differs from the typical ionic-specific activity coefficient γ_i definition (1.5). In more details, in Johannsen and Rademacher model, f is not an ionic-specific coefficient, so it is subsequently raised to the power of a value related to the ion charge number (equation (6.13)). Usually, this relationship linking the charge number z_i and the activity coefficient f is already included in the formulation of γ_i.

$$R_d = k_f - k_b\, f^4\, [Ca^{2+}]\, f^2\, [OH^-]^2 \tag{6.12}$$

$$log(f) = \frac{-0.5\,\sqrt{I}}{1 + 1.4\,\sqrt{I}} \tag{6.13}$$

$$I = 0.5 \sum c_i\, z_i^2 = 0.5\,(\,4[Ca^{2+}] + [CaOH^+] + [H^+] - [OH^-]\,) \tag{6.14}$$

where:

f: practical activity coefficient [-];
I: ionic strength [-];
c_i: ion concentration [mol L^{-1}];
z_i: ion charge number [-], assumed 2 for Ca^{2+} and 1 for the other species.

In equation (6.14), ionic strength is obtained by the sum of the concentration c_i of each ion i in the solution, multiplied by the square of its charge number z_i. Ionic strength I is a quantity used to characterize aqueous solutions which contain different ions: it could be stated that I describes the number of electrical charges in the solution (Atkins and de Paula, 2006); and it can be also considered as a function of seawater salinity (Zeebe and Wolf-Gladrow, 2003), and in such a medium it is generally about 0.7. The right side of the reaction (6.14) shows the theoretical ionic strength definition in a solution composed of SL and distilled water: this defines how Johannsen and Rademacher (1999) calculated such parameter (not managing with seawater). The reaction (6.15) shows the formulation of ionic strength according to salinity, S, as described by Zeebe and Wolf-Gladrow (2003). This latter equation is more suitable for a seawater solution. It is worth noting that salinity has an average value of 35 g kg^{-1}, both in artificial seawater (illustrated in Chapter 6.1) and in natural seawater.

$$I = \frac{19.924\,S}{1000 - 1.005\,S} \tag{6.15}$$

where:

S: seawater practical salinity [g kg^{-1}].

Even the activity coefficient formulation must be further examined. The equation (6.13) derives from the Debye-Hückel formula, which is suitable for a dilute solution where the ionic strength is less than 0.1 (Appelo and Postma, 2005). Because the current model aims to analyse a saline environment, a different equation is used; Truesdell and Jones (1974), Plummer et al. (1976), and later Parkhurst (1990), fitted a different version of the Debye-Hückel formulation suitable for seawater, the so-called Truesdell-Jones equation (6.16).

$$\log(\gamma_i) = -\frac{A'\, z_i^2\, \sqrt{I}}{1 + B'\, a_i\, \sqrt{I}} + b_i\, I \tag{6.16}$$

where:

γ_i: ionic-specific activity coefficient [-];
A': temperature-dependent coefficient [-];
z_i: ion charge number [-], assumed 2 for Ca^{2+} and 1 for OH^-;
B': temperature-dependent coefficient [Å^{-1}];
a_i: ionic-specific fit parameter [Å], assumed 4.86 Å for Ca^{2+}(Langmuir, 1997) and 3.5 Å for OH^-(Truesdell and Jones, 1974);
b_i: ionic-specific fit parameter [-], assumed 0.15 for Ca^{2+} and 0.08 for OH^- (Langmuir, 1997).

The ionic-specific fit parameters a_i and b_i are determined from experimental data. In particular, the term a_i is linked to the effective size of the ion and so it is a function of the Debye length, which is the measure of how far the electrostatic effect of an ion persists in a solution (Debye and Hückel, 1923). As a result, it is correlated to the degree of ionic hydration, which is roughly proportional to its ionic potential (Appelo and Postma, 2005).

Langmuir (1997) gave the definitions for the temperature-dependent coefficients A' and B' calculation (formula (6.17) and (6.18)); they are temperature and water density dependent, but their value slightly varies when temperature T ranges between 5-35 °C.

$$A' = 1.824928\ 10^6\ \sqrt{\rho_w}\ (\varepsilon\, T)^{-3/2} \tag{6.17}$$

$$B' = 50.3\ (\varepsilon\, T)^{-1/2} \tag{6.18}$$

where:

ε: dielectric constant of water [-].

It is worth noting that in the equation (6.17) and (6.18) seawater density ρ_w should be expressed in kg L^{-1} while T in K.

The dielectric constant of water ε is a measure of the effect of water (versus a vacuum) in decreasing the force of the electrical field between ionic species in solution; it can be expressed as a function of temperature T as expressed in the following relationship (6.19):

$$\varepsilon = 2727.586 + 0.6224107\,T - 466.9151\,ln(T) - 52000.87\,T^{-1} \quad (6.19)$$

According to this later evaluation, an activity coefficient γ_i specific for each ion can substitute the generic activity coefficient f used in equation (6.12). So, the net rate of dissolution R_d can be written as follow (6.20).

$$R_d = \frac{d[Ca^{tot}]}{A\,dt} = k_f - k_b\,\gamma_{Ca^{2+}}\,[Ca^{2+}]\,\gamma_{OH^-}^2\,[OH^-]^2 \quad (6.20)$$

A fraction of SL dissolves in seawater forming $CaOH^+$ ions, and not only Ca^{2+} and OH^-. Johannsen and Rademacher (1999) consider a parameter Ca^{tot}, which is the sum of Ca^{2+} and $CaOH^+$. For the sake of simplicity, and from a conservative point of view (the aim of this study is the evaluate the maximum value of the pH spike), in the present evaluation it is assumed that SL dissociates completely in Ca^{2+}, neglecting a possible $CaOH^+$ portion. Furthermore, $CaOH^+$ is not a stable species in seawater, since it reacts with different ionic compounds as it was present as $Ca^{2+}$and OH^- ions: in solutions made by SL and seawater, $CaOH^+$is present in a very low amount if compared to the other ions derived from the SL dissolution (Justnes et al., 2020).

It is possible to describe the trend of Ca^{2+} in water managing with the previous equations (6.20). This modelling study uses the following formulation (6.21), to compare its results with laboratory experiments.

$$\frac{d[Ca^{2+}]}{dt} = A\left(k_f - k_b\,\gamma_{Ca^{2+}}\,[Ca^{2+}]\,\gamma_{OH^-}^2\,[OH^-]^2\right) \quad (6.21)$$

where:

A: total surface of the particles [m^2];
k_f: forward constant rates of the SL dissolution reaction [mol L^{-1} s^{-1} m^{-2}];
k_b: backward constant rates of the SL dissolution reaction [L^2 mol^{-2} s^{-1} m^{-2}];
$\gamma_{Ca^{2+}}$: calcium ion activity coefficient [-];
γ_{OH^-}: hydroxyl ion activity coefficient [-].

Consequently, an evaluation of the particles' surface behaviour is necessary. The area A decreases according to the time because, while the dissolution takes place, SL particles reduce their size. Such decrease could be described with formulations showing the radius shrinkage. This is possible because, assuming the particles spherical in shape, their area is a function of the radius, r_p. Different equations describing the radius reduction are defined in the following sections. It is fundamental to note that Johannsen and Rademacher assumed all the particles of the same size; for this reason, the dissolution rate is the same for each particle, and so the particles' total number remains the same till total SL dissolution.

It is possible to obtain the total surface A value by multiplying the single particle's surface by the total number of particles (formula (6.22)).

$$A = A_p\,n_0 = 4\,\pi\,r_p^2\,n_0 \quad (6.22)$$

where:

n_0: number of dosed SL particles [-];
A_p: surface area of each particle [m^2].

A critical step in the intended evaluation is the definition of the forward k_f and backward k_b rate constants. In their study, Johannsen and Rademacher (1999) defined an average value for k_f, while k_b showed a dependence on SL initial concentration Z_0 as expressed in the relationship (6.23).

$$log(k_b) = -7 - 0.9\, Z_0 \tag{6.23}$$

However, k_b and k_f values must be modified according to the present study situation. Their results on dissolution rates were indeed based on a system with neutrally buoyant particles, and that's not the case of SL particles discharged for carbon sequestration (Tannenberger and Klein, 2009). New constant rates could be obtained after calibration of this model with laboratory results. Moreover, it emerges that temperature T has effects on the rate constants so, Johannsen and Rademacher (1999) adopted the Arrhenius relationship for temperature calibration; here it is reported only the relationship for the forward constant k_f rate (6.24), but it is the same for the backward constant rate k_b:

$$ln\left(\frac{k_{f_2}}{k_{f_1}}\right) = \frac{E_{A\,f}}{R}\left(\frac{T_2 - T_1}{T_1\, T_2}\right) \tag{6.24}$$

where:

k_{i_2}: forward/backward constant rate at the simulated temperature T_2;
k_{i_1}: forward/backward constant rate at the reference temperature T_1;
$E_{A\,i}$: Activation energy of the forward/backward reaction [kJ mol^{-1}], $E_{A\,f}$ is assumed 29.7 kJ mol^{-1} while $E_{A\,b}$ is equal to 52.8 kJ mol^{-1} (Johannsen and Rademacher, 1999);
R: universal gas constant [kJ mol^{-1} K^{-1}], assumed 8.3144 10^{-3} kJ mol^{-1} K^{-1};
T_1: reference temperature [K], assumed equals to 295.15 K (22 °C);
T_2: simulated temperature [K].

Finally, laboratory experiments from Colombo and Crisanto's study (2021) allowed calibrating the values of k_f and k_b for a temperature T of 22°C. Such results are later modified according to the different temperatures simulated, as described by equation (6.23), and validated with experimental analyses at such temperatures (5-25°C).

From Figure 6.5 is worth stating that at 22°C k_f has a value of 3.2 10^{-4} mmol L^{-1} s^{-1} cm^{-2}, while k_b is 3.5 10^{-9} L^2 mmol^{-2} s^{-1} cm^{-2}. According to the different forward and backward rates, a different SL saturation concentration is obtained. Furthermore, it is worth noting that the equilibrium constant K_{SL} of reaction (2.4) is obtained as the ratio between the forward rate k_f and backward rate k_b, as expressed by the following relationship (6.25).

$$K_{SL} = \frac{k_f}{k_b} \tag{6.25}$$

The result is that the solubility changes as a function of the temperature: in laboratory experiments, it is shown that at 22°C the SL concentration at saturation is about 4.15 gSL L^{-1}. It is important to note that the rate constants obtained are different from the ones calculated by Johannsen and Rademacher (1999) dealing with different conditions. In a temperature range from 5 to 30°C, Johannsen and Rademacher obtained k_f values that vary between 0.58 10^{-5} to 1.90 10^{-5} mmol L^{-1} s^{-1} cm^{-2}, while k_b values from 0.51 10^{-9} to 6.34 10^{-9} L^{-2} $mmol^{-2}$ s^{-1} cm^{-2}. On the other hand, k_f values calculated in the current study range between 1.21 10^{-4} and 3.61 10^{-4} mmol L^{-1} s^{-1} cm^{-2}, while k_b values vary between 9.40 10^{-10} and 4.35 10^{-9} L^{-2} $mmol^{-2}$ s^{-1} cm^{-2}. The Johannsen and Rademacher model allows evaluating the changes in dissolution kinetics when approaching the saturation level. In fact, the dissolution total rate drops to zero when Ca^{2+} and OH^- concentrations in water become too high, according to the condition (6.26).

$$k_f = k_b\,[Ca^{2+}]\,[OH^-] \tag{6.26}$$

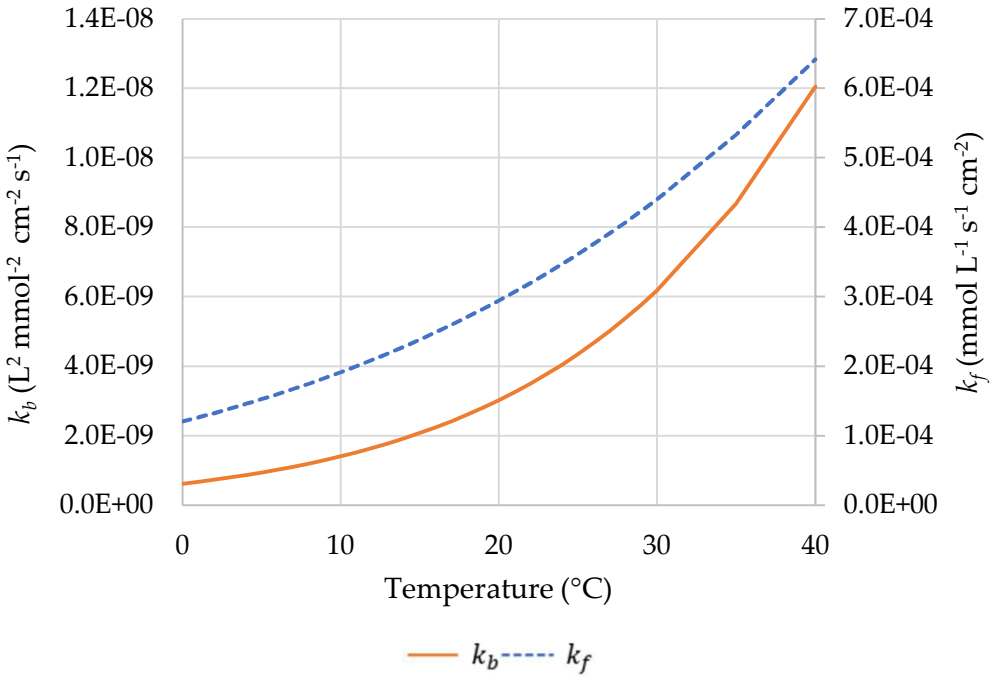

Figure 6.5: Forward k_f and backward k_b constant rate trend as a function of temperature T.

In order to examine the approach to saturation level, a couple of parameters could be used: the saturation state Ω and the saturation index SI. Ω is defined as the ion activity product of the species actually in solution, divided by the solubility product K_{SL} (formula (6.27)). SI is instead the logarithm of Ω (formula (6.28)).

$$\Omega = \frac{\{Ca^{2+}\}\{OH^-\}^2}{K_{SL}} \tag{6.27}$$

$$SI = log_{10}(\Omega) \tag{6.28}$$

An Ω value equal to 1 means that the reaction is in equilibrium. Otherwise, when Ω is less than one, there is a situation of subsaturation. As a result, equilibrium is reached when SI approaches 0, while negative SI values reflect subsaturation (Appelo and Postma, 2005).

When the equilibrium is reached, the dissolution rate drops to zero, and the SL stops dissolving.

An analysis of the SL saturation concentration at different temperatures is necessary to understand how this value varies while changing such initial conditions. Many parameters have to be calculated according to different temperatures: seawater density, forward and backward dissolution rates, ionic water product, dielectric water constant, and ion activity coefficients. The solubility at different temperatures has been obtained thanks to equation (6.24), and later equations (6.25) and (6.26), evaluating which dosed SL mass provides an Ω value equal to one. In order to do that, the ion activity product after the dissolution must be the same as the K_{SL} value. The results of this evaluation are graphically reported in Figure 6.6.

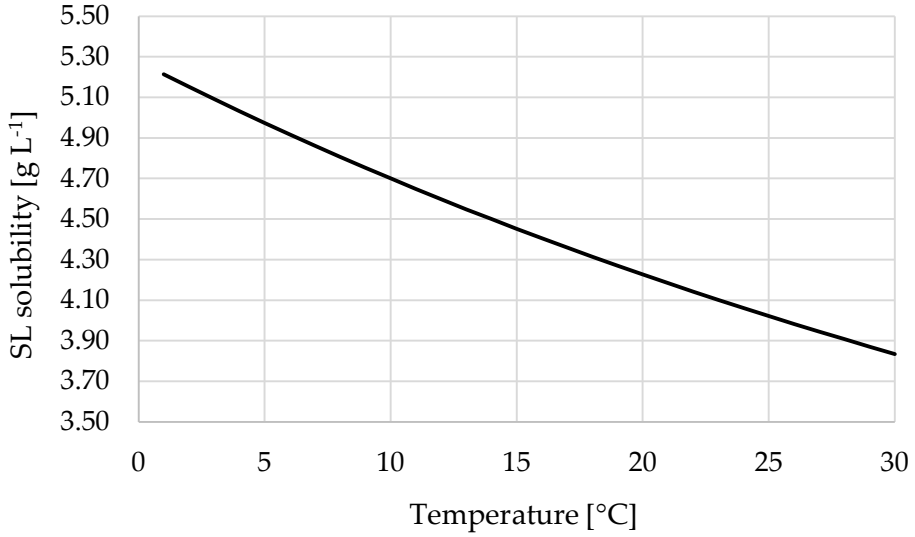

Figure 6.6: SL solubility, in terms of gSL L^{-1}, as a function of temperature T.

Figure 6.6 shows that SL concentration at saturation decreases according to temperature. Despite higher temperatures speed up the dissolution rate (approaching the equilibrium in shorter terms) the solubility of this compound decreases with temperature. This concentration at saturation decrease is not so large in the investigated temperatures, ranging from about 5.21 gSL L^{-1} to 3.84 gSL L^{-1} between 0°C and 30°C. It is worth noting that even if a temperature increase increments the dissolution rates, it doesn't imply an overall acceleration of the process. Such process speeding-up occurs only when the dosed SL is far from the saturation condition because a temperature increase reduces the SL concentration at saturation. In such conditions, high-temperature levels tend to increment the dissolution kinetics, but the solubility drop-off buffers this acceleration.

6.3.2 BERNARD DISSOLUTION MODEL

In 2000, Bernard et al. developed a kinetic model for describing SL dissolution in the preparation of hydroxyapatite by neutralization. Their main objective was to understand the mechanisms ruling the steps of dissolution and the evolution of particles size, assuming shrinking spherical particles. It is fundamental noting that Bernard built this model assuming to discharge QL in water, which reacts quickly forming SL. Consequently, his model describes

the transformation of lime particles, but it is based on the initial QL mass. In this chapter, the QL mass is replaced by SL initial values, assuming that the dissolution kinetics is the same after the transformation of QL in SL: literature studies (Justnes et al., 2020) validate such an assumption demonstrating that burnt lime reacts in seawater almost immediately forming calcium hydroxide. However, this could be a key point whose correctness is evaluated in Chapter 6.3.4.

Bernard et al. (2000), firstly introduced the concept of the linear dissolution rate D of SL particles into seawater (formula (6.29)).

$$D = -\frac{dr_p}{dt} = k_d \frac{M_p}{\rho_p}([Ca^{2+}]_{sat} - [Ca^{2+}]) \tag{6.29}$$

where:

D: linear dissolution rate of SL particles [m s^{-1}];
k_d: mass transfer coefficient [m s^{-1}];
M_p: SL molar mass [g mol^{-1}], assumed 74.10 g mol^{-1};
ρ_p: SL density [g L^{-1}];
$[Ca^{2+}]_{sat}$: concentration of calcium ions into seawater at saturation [mol L^{-1}];
$[Ca^{2+}]$: concentration of calcium ions into seawater at time t [mol L^{-1}].

After the described preliminary analyses, an evaluation about the mass balance on calcium ions is necessary. The mass of calcium ions at time t is equal to the sum of the mass of calcium ions already present in at the beginning (so at time 0) and the calcium ions mass deriving from SL dissolution (formula (6.30)). Assuming that the volume of the liquid phase V_L is constant, the mass balance equation is then derived as a function of time t (formula (6.31)).

$$[Ca^{2+}]\, V_L = [Ca^{2+}]_0\, V_L + \frac{m_p^0 - m_p}{M_p} \tag{6.30}$$

$$\frac{dm_p}{dt} = -V_L\, M_p \frac{d[Ca^{2+}]}{dt} \tag{6.31}$$

where:

V_L: volume of the liquid phase [L];
$[Ca^{2+}]_0$: concentration of calcium ions into seawater at time 0 [mol L^{-1}];
m_p^0: mass of SL present at time 0 inside the reactor [g];
m_p: mass of SL presents in the reactor at time t [g].

A description of the SL particles radius is required in the current model; as stated previously, they are assumed uniform and with the same size r_p. At the beginning particles radius is r_0 and at time t it can be expressed as reported in the following equation (6.32):

$$r_p = r_0 \left(\frac{m_p}{m_p^0}\right)^{\frac{1}{3}} = r_0 \left[1 + \frac{M_p\, V_L\, ([Ca^{2+}]_0 - [Ca^{2+}])}{m_p^0}\right]^{\frac{1}{3}} \tag{6.32}$$

In this way, the variation of the SL mass can be expressed through the following equation (6.33):

$$\frac{dm_p}{dt} = \frac{3\, m_p^0\, r_p^2}{r_0^3} \frac{dr_p}{dt} \tag{6.33}$$

Thanks to the combination of the equation (6.31) and (6.33) it is possible to obtain a differential equation for the description of SL particles radius behaviour during time (6.34):

$$\frac{dr_p}{dt} = -V_L\, M_p \frac{r_0^3}{3\, m_p^0\, r_p^2} \frac{d[Ca^{2+}]}{dt} \tag{6.34}$$

So, combining the dissolution rate equation (6.29), the radius equation (6.32) and the specific expression for radius particles description (6.34), it is possible to obtain a total differential equation describing the variation of calcium ions during time (6.35):

$$\frac{d[Ca^{2+}]}{dt} = \frac{3\, m_p^0}{V_L\, \rho_p\, r_0} \left[1 + \frac{M_p\, V_L\, ([Ca^{2+}]_0 - [Ca^{2+}])}{m_p^0}\right]^{\frac{2}{3}} k_d\, ([Ca^{2+}]_{sat} - [Ca^{2+}]) \tag{6.35}$$

In more details, the mass transfer coefficient k_d is calculated thanks to the formulation of mass transfer from suspended solids to a liquid in agitated vessels is proposed by Boon-Long et al. (1978); it is worth noting that such mass transfer coefficient depends on the particle size (6.36):

$$k_d = 0.046 \frac{D_f}{d_p}\, Re^{0.283}\, Ga^{0.173}\, U^{-0.011} \left(\frac{d_R}{d_p}\right)^{0.019} Sc^{0.461} \tag{6.36}$$

where:

D_f: seawater calcium ion diffusivity coefficient [$m^2\, s^{-1}$], assumed 6.32 10^{-10} $m^2\, s^{-1}$ (Li and Gregory, 1974);
Re: Reynolds number [-];
Ga: Galileo number [-];
U: solid concentration [-];
d_R: vessel diameter [m];
Sc: Schmidt number [-].

Expressing in more details each term, the mass transfer coefficient k_d can be also written as expressed by the following equation (6.37):

$$k_d = 0.046 \frac{D_f}{d_p} \left(\frac{d_p\, d_R\, \pi\, \omega\, \rho_w}{\mu_w}\right)^{0.283} \left(\frac{g\, d_p^3\, \rho_p^2}{\mu_w^2}\right)^{0.173} \left(\frac{m_c}{\rho_p\, d_p^3}\right)^{-0.011} \left(\frac{d_R}{d_p}\right)^{0.019} \left(\frac{\mu_w}{D_f\, \rho_w}\right)^{0.461} \tag{6.37}$$

where:

ω: stirrer angular velocity [-].

The vessel diameter d_R and the stirrer angular velocity ω are strictly referred to the specific laboratory or *in situ* experiment. If the aim is to compare the model with the mentioned laboratory tests, d_R is considered as the diameter of the beaker (so it is equal to 0.128 m), while ω represent the impeller angular velocity and accounts to 10.47.

Defining the concentration at saturation of calcium ions, the so-called solubility, is a fundamental step of the proposed model. It sets the concentration at which Ca^{2+} ions stay in a dissociated phase, without forming compounds such as carbonates or hydroxides. This value could be assessed as the driving force of the dissolution, because the higher the difference between the concentration and the saturation condition, the higher is the dissolution rate (Costa and Lobo, 2000). It is clearly a function of many variables, such as temperature, and its definition is not a simple evaluation. Tannenberger and Klein (2009) describe the solubility of calcium ions according to the solubility of slaked lime. They stated that SL solubility is 1.85 g L^{-1} in an average defined ocean seawater, which corresponds to 0.025 mol L^{-1} of calcium ions. Laboratory studies show a different behaviour, because they result in a significantly higher solubility, assessed as 4 mg L^{-1} or more at a temperature between 20-25°C. All these values are significantly higher than SL solubility in freshwater, which is evaluated as about 1.60-1.73 mg L^{-1} (NIH, 2021) at a 20°C temperature. However, to calculate the effective Ca^{2+} ions solubility, it is important to consider that calcium ions are already present in seawater, with an average concentration of 418 mg L^{-1} at 25°C (about 0.01 mol L^{-1}), (Zeebe and Wolf-Gladrow, 2003). Therefore, considering that SL concentration at saturation is evaluated in seawater rich in Ca^{2+} ions, the overall calcium ions solubility is calculated as the sum of natural Ca^{2+} concentration and SL solubility. Even Bernard et al. (2000) made some considerations regarding the Ca^{2+} saturation. They showed that this value differs significantly according to the operating conditions, such as temperature. Calculations were made through the usage of dosed acid: the results demonstrated that the overall calcium ions concentration at saturation varies significantly according to the added acidity, in a range between 0.45-0.65 mol L^{-1}, but it appears to be more stable around a value of 0.50 mol L^{-1}, almost constant for a great range of temperatures. However, SL solubility in a not acidic system has been considered by Bernard et al. (2000) equal to 0.025 mol L^{-1}.

According to laboratory experiments, supported also by the results of the Johannsen and Rademacher model, a SL solubility of 4.15 gSL L^{-1} has been chosen for a temperature of 22°C. This corresponds to a calcium saturation concentration of 0.067 mol L^{-1}, where 0.011 mol L^{-1} is the initial calcium concentration, and 0.056 mol L^{-1} derives from a complete SL dissolution.

6.3.3 RADIUS REDUCTION MODELS

As mentioned in previous sections, an analysis of models describing the decrease of SL particles' size during dissolution process is required. These models play an outstanding role because the reduction of the particles' radius causes a decrease in the contact surface between SL particles and water, thus reducing the reaction rate.

Johannsen and Rademacher radius reduction model

Johannsen and Rademacher (1999), in the previously analysed model in Chapter 6.3.1, provide a calculation process that would define the behaviour of the particles' radius. Many other researchers analysed such radius reduction model; for instance, it could be found in Appelo and Postma (2005) studies, and in many chemical software as PHREEQC (USGS, 2021).

First of all, for the sake of simplicity they made a strong assumption, considering that the reacting particles have all the same dimension, as mentioned in Chapter 6.3.1. Under this assumption, all the SL particles have the same dissolution rate, and therefore the total number of SL particles n_0 remains constant. It is possible to obtain this total number of particles n_0 by dividing the dosed amount of SL m_p^0 by their density ρ_p (formula (6.38)) and the initial volume of each particle V_0 (formula (6.39)).

$$n_0 = \frac{m_p^0}{\rho_p V_0} \tag{6.38}$$

$$V_0 = \frac{4}{3} \pi r_p^3 \tag{6.39}$$

where:

n_0: number of dosed SL particles, constant during the dissolution [-];
V_0: initial volume of each SL particle [m^3].

Equation (6.22) allows obtaining the total surface area A. Later, it is possible to assess the total undissolved SL volume during the dissolution (formula (6.40)): it decreases as well as the volume and the diameter of each single particle. The undissolved amount of SL is obtained by the knowledge of the initially dosed and the total dissolved SL (formula (6.41)). After that, the volume of the particles during the dissolution is calculated, through which the subsequent particles' radius is evaluated (formula (6.42)).

$$V_{und} = \frac{m_p}{\rho_p} = \frac{m_p^0 - m_d}{\rho_p} = \frac{Mol_p^0 - Mol_d}{\rho_p}\left(\frac{M_p}{1000}\right) \tag{6.40}$$

$$V_p = \frac{V_{und}}{n_0} \tag{6.41}$$

$$r_p = \left(\frac{3\,V_p}{4\,\pi}\right)^{\frac{1}{3}} \tag{6.42}$$

where:

V_{und}: total undissolved slaked lime volume during the dissolution [m^3];
V_p: volume of each particle [m^3];
m_d: total dissolved mass of SL [kg];
Mol_p^0: moles of slaked lime at time 0 [mol];
Mol_d: total moles of dissolved SL [mol];
M_p: SL molar mass [g mol^{-1}].

It is worth noting that the Johannsen and Rademacher model provides concentrations in terms of moles. According to that, in order to obtain the value of dissolved calcium hydroxide, it is necessary to multiply the amount of dissolved SL expressed in moles by its molecular weight.

Bernard radius reduction model

Chapter 6.3.2 previously investigated the Bernard et al. (2000) model describing the radius reduction of calcium-based particles. It could be also used in other dissolution models, giving an alternative in formulating the changes of the particles' size. The intended differential equation (6.34), also present in Chapter 6.3.2, is reported below for completeness (6.34a).

$$\frac{dr_p}{dt} = -V_L \, M_p \frac{r_0^3}{3 \, m_p^0 \, r_p^2} \frac{d[Ca^{2+}]}{dt} \tag{6.34a}$$

Tannenberger and Klein radius reduction model

Tannenberger and Klein (2009) developed a model describing the SL particles' behaviour after discharge in seawater. Their model includes many particles-water interaction characteristics, such as dilution, sinking, and particles aggregation. Recent studies used the so-called shrinking-core model (i.e.: Caserini et al., 2021) to assess the variation of SL concentration in seawater. However, it cannot offer itself an evaluation of the pH increase after the discharge.

Of particular interest is the characterization of the radius decrease of SL particles, and the investigation of the dissolution rate is fundamental to define such radius decrease. Relying on Csanady (1986) studies, the dissolution rate is expressed by a mass balance (6.43), assuming that the mass transferred to the liquid phase is equal to the particles' mass loss, according to the following equation.

$$\frac{d}{dt}\left(\frac{4}{3} \, \pi \, \rho_p \, r_p^3\right) = -\alpha \, \dot{\mathrm{M}} \tag{6.43}$$

where:

r_p: slaked lime particles radius [μm];
Ṁ: total mass transfer [kg s^{-1}];
α: ratio between mass transfer to the bulk and mass loss of the particle [-], assumed 0.54 (Weast et al., 1989).

Managing such total mass loss, it is possible to modify the previous equation in order to obtain a simpler one (formula (6.44) and (6.45)).

$$r_p \frac{dr_p}{dt} = -D_f \, \phi_0 \tag{6.44}$$

$$\phi_0 = \frac{\alpha \, \chi_0}{\rho_p} \tag{6.45}$$

where:

ϕ_0: diffusion potential [-];
χ_0: chemical gradient for calcium ions dissolution [kg m^{-3}], assumed 0.5781 kg m^{-3} (Csanady, 1986).

ϕ_0 is a dimensionless value, which is to be considered constant; χ_0 is the difference between the saturation concentration at particle's surface and the calcium concentration in the medium. Solving equation (6.45) it is easy to get another one, not differential, which describes particle radius r_p as a function of time t (4.46).

$$r_p = \sqrt{r_0^2 - 2\, D_f\, \phi_0\, t} \tag{6.46}$$

6.3.4 MATHEMATICAL ANALYSIS OF THE BEST DISSOLUTION MODEL

This chapter briefly evaluates the suitability of each model, in order to find out the optimal mathematical dissolution model. The adopted implementation code of the decided models is later deeply investigated in Chapter 6.3.5.

Two different main sections compose each model: a first part describing the variation of SL moles (and the consequent increase of Ca^{2+} and OH^- moles in water), and a second part defining the radius reduction of each SL particle. Table 6.6 shows the different combinations adopted.

Table 6.6: Different combinations of dissolution and radius reduction models.

Model	Dissolution model adopted	Radius reduction model adopted
B-B Model	Bernard	Bernard
B-T Model	Bernard	Tannenberger and Klein
J-J Model	Johannsen and Rademacher	Johannsen and Rademacher
J-T Model	Johannsen and Rademacher	Tannenberger and Klein

The Bernard models have been implemented through the Simulink software, a MATLAB-based graphical programming environment for modelling, simulating, and analysing multidomain dynamical systems. Instead, the Johannsen and Rademacher models have been built via MATLAB's workspace itself (MathWorks, 2021).

The initial parameters assumed in the calculating software are those defined in Chapter 6.1, describing the laboratory experiments. In more detail, a 0.2 gSL discharge per litre of seawater (in form of slurry 1.5 M) permits defining such initial parameters. Therefore, the following graphics and figures refer to a temperature of 22°C and initial pH value almost near to neutrality, of about 6.75. It is worth noting that the modelized systems provide a complete SL dissolution, so the final calcium concentration must be equal to 13.3 mmol L^{-1}, since the initial seawater has a calcium content of 10.6 mmol L^{-1}, and 0.2 gSL L^{-1} correspond to 2.7 mmol L^{-1} of Ca^{2+} ions. The second key point to evaluate the accuracy of the models is the dissolution time. To assess this latter topic, it has been analysed the time needed to reach the pH peak in the laboratory experiments. In Figure 6.7 are reported the results of the laboratory tests, showing the pH changes during dissolution process. It is worth noting that the pH peak is reached in

about 40 seconds after the beginning, but the dissolution is completed at least for 90% after only 20 seconds.

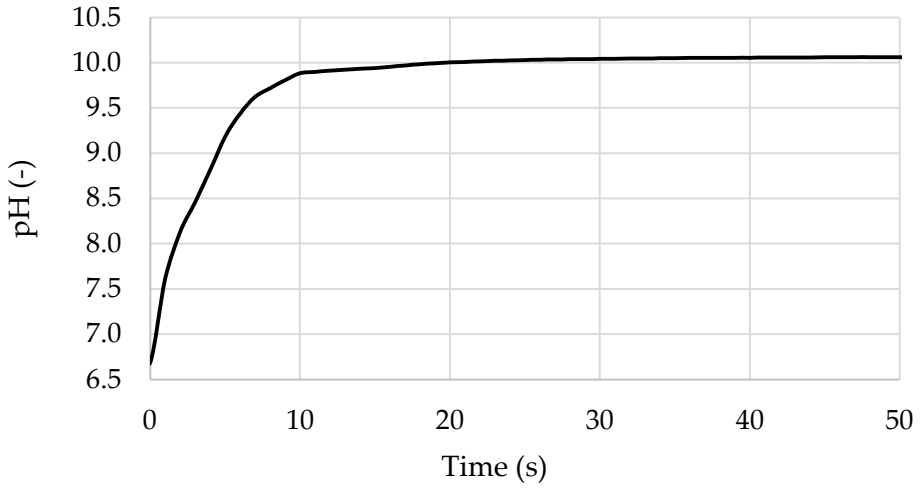

Figure 6.7: pH trend after 0.2 g L^{-1} SL discharge in laboratory experiments.

Figure 6.8 reports the results of radius reduction models, Figure 6.9 presents the calcium concentration trends.

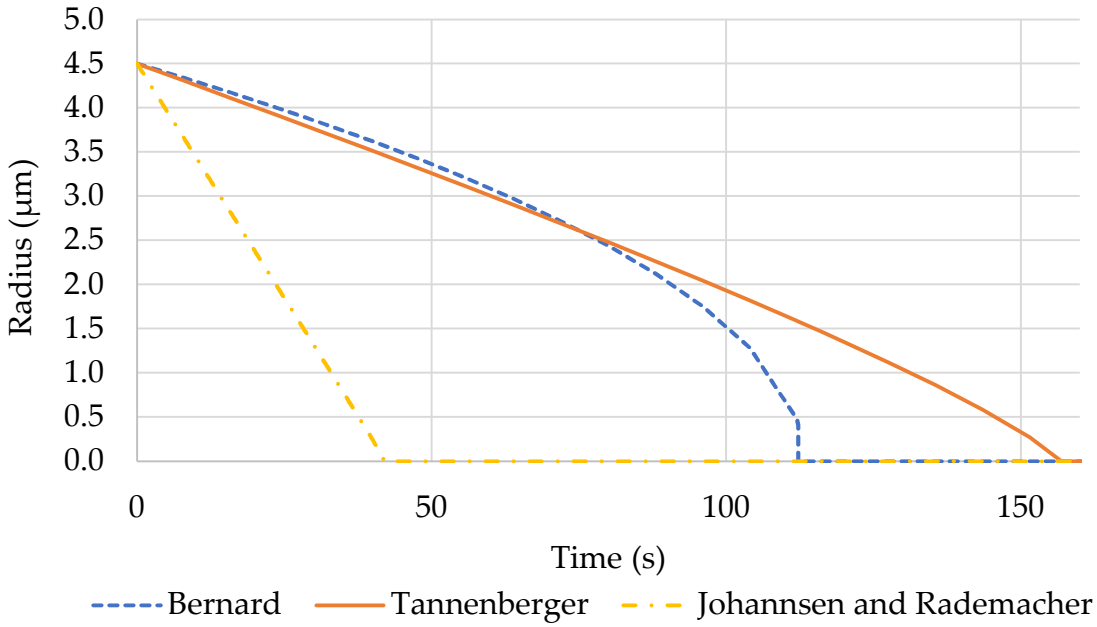

Figure 6.8: Results of the different radius reduction models.

Different models show various particles' radius behaviour as shown in Figure 6.8; Tannenberger and Bernard models show a reduction that slows down when particles are sufficiently small, while the Johannsen and Rademacher model describes an almost linear decrease. Generally, this trend is caused by the reduction of the total area since lower surfaces lead to slower reaction speeds. The differences among the trends are due to the different mathematical relationships present in the various physical models between the dissolution

rate and the total particles surface. However, the linearity of the third model changes when the concentration approaches the saturation level, as later described in Chapter 6.3.5.

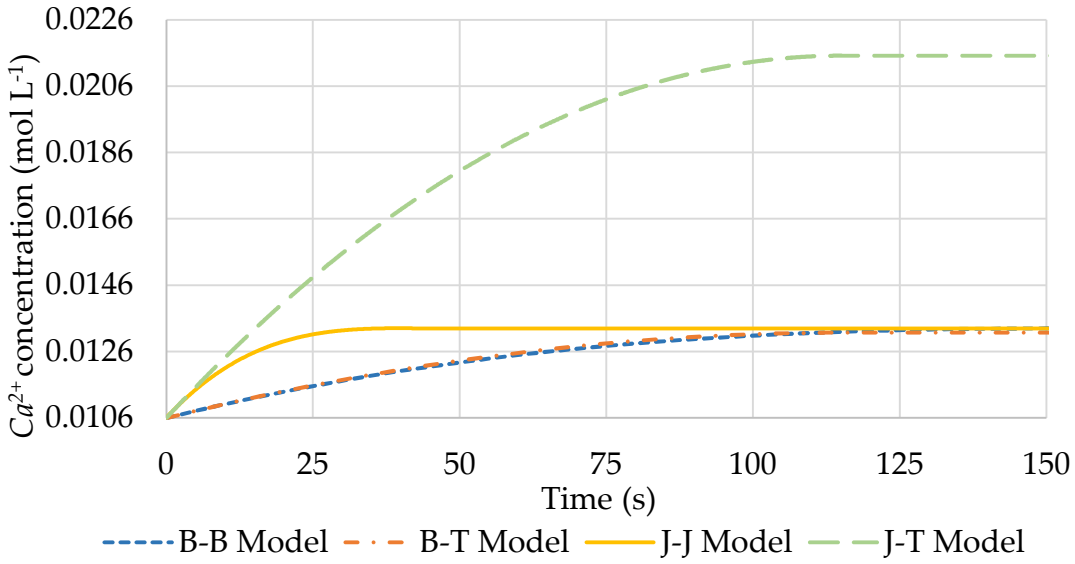

Figure 6.9: Calcium ions trend for all the different implemented models.

It is worth noting that the model built using the Johannsen and Rademacher model with the Tannenberger radius reduction model (J-T Model) appears significantly incorrect, giving a total calcium concentration of 0.022 mol L^{-1} at the end of the dissolution. Such a result is almost twice the maximum theoretical Ca^{2+} concentration, so this model is rejected. Such an issue is probably due to the fact that the Johannsen and Rademacher model describes a SL moles reduction that is strongly linked to the radius reduction function, which in the Tannenberger model is instead independent from the other variables.

Figure 6.10 focuses on the other dissolution models, which appear to be more correct.

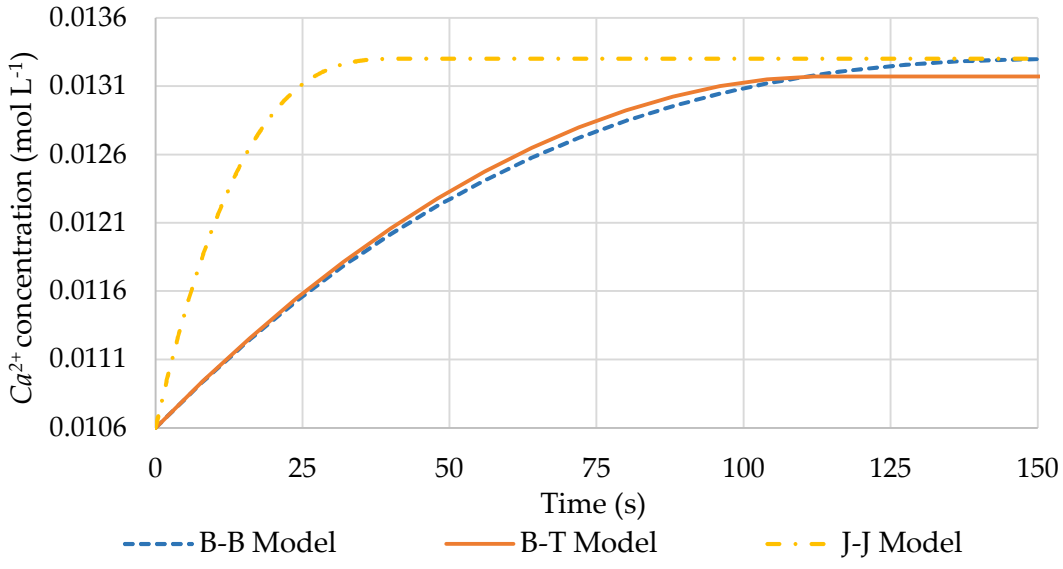

Figure 6.10: Focus on calcium ions trends for B-B, B-T, and J-J Models.

The other models show a similar qualitative Ca^{2+} concentration increasing trend (Figure 6.10), but they highlight some fundamental differences; for instance, the two Bernard models (B-B Model, B-T Model) approach a complete dissolution later than the Johannsen and Rademacher model (J-J Model), in about 150 s. Moreover, the Bernard model with the Tannenberger radius reduction model (B-T Model) does not reach the theoretical calcium concentration since such maximum value obtained is slightly less than 0.0133 mol L^{-1}, as Figure 6.11 shows.

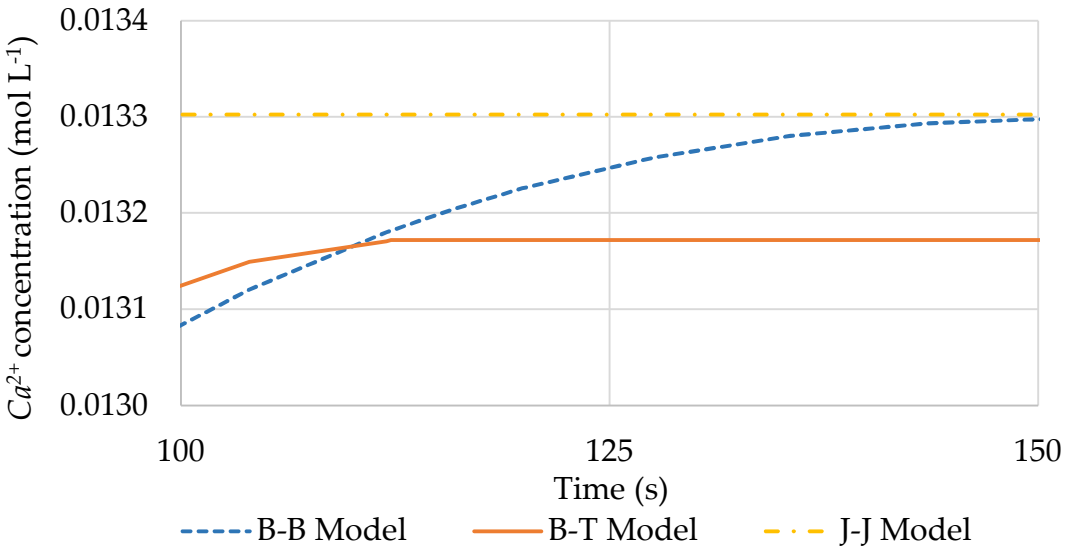

Figure 6.11: Details on the last 50 seconds of the dissolution process.

In light of this, the Johannsen and Rademacher model (J-J Model) appears to be the most suitable because the Ca^{2+} concentration reaches the expected value corresponding to total SL dissolution. Furthermore, the dissolution time is similar to the time shown in Figure 6.7, since it is between 20 and 40 s. As a result, following evaluations and calculations are based exclusively on the Johannsen and Rademacher model.

6.3.5 CODE IMPLEMENTATION AND DISCUSSION

Thanks to the results obtained from the mathematical analysis, Johannsen and Rademacher model is deeply investigated. This chapter aims to describe and examine in detail the MATLAB implementation code; for the sake of simplicity the script is divided in different parts and each of it is analysed in more details: tables from 6.7 to 6.14 accurately describe all the parameters present in the code, while in the code description parameter values are provided for illustrative purposes only.

The parameters implemented in the MATLAB script reported below, describe the laboratory experiments during which 0.2 gSL L^{-1} are poured in the form of a slurry. Seawater has a temperature of 22 °C and an initial pH value of 6.75. A monodisperse SL powder distribution is assumed, and the calculations consider the median mass diameter. The script below reports the water volume in the beaker, which is a key parameter for evaluating the total mass of dosed SL.

As a first step, it is necessary to define the initial parameters characterizing both SL slurry and seawater.

```
Vol = 1;

r0 = 4.5e-6;
Ca0 = 0.010;
SLin = 0.2;
S = 35;
SL0 = SL*Vol;

T = 273.15+22;
Ta = 273.15+22;

MSL = 74.01;
MCa = 40.08;
rhop = 2240;
rhow = 1024.3;
```

Table 6.7 reports the initial parameters presented in the code above.

Table 6.7: Code implementation parameters: initial parameters characterizing slurry and seawater.

Symbol	Parameter	u.m.	Reference
Vol	Water volume in the beaker	L	Text Chapter 6.1
r0	Initial median particle radius	m	Text Chapter 2.4.3
Ca0	Calcium concentration in seawater	mol L^{-1}	Table 6.2
SLin	Concentration of dosed SL	g L^{-1}	Text Chapter 6.1
SL0	Mass of dosed SL	g	Text Chapter 6.1
S	Seawater salinity	g kg^{-1}	Text Chapter 6.1
T	Simulated temperature	K	Text Chapter 6.2
Ta	Reference temperature	K	Text Chapter 6.1
MSL	SL molecular weight	g mol^{-1}	Text Chapter 2.4.3
MCa	Calcium ion molecular weight	g mol^{-1}	Table 6.2
rhop	SL density	kg m^{-3}	Text Chapter 2.4.3
rhow	Seawater density at simulated temperature T	kg m^{-3}	Text Chapter 6.2

It is worth noting that, while the temperature T could be changed according to different simulations, the reference temperature Ta should not be modified; that's because the forward and backward rates have been calibrated at a 22°C temperature. Moreover, it is important to denote that in the later simulations shown, salinity S is constant since it represents an average value of oceans and seas: it has been assumed that the dosed SL is negligible in incrementing such a salinity value: for instance, a dosage of 0.2 gSL in a litre of solution increments salinity and ionic strength by a fraction of 0.005. Otherwise, activity coefficients formulations could change, considering very different values of salinity, because the ionic strength formulation (6.16) is affected.

```
pH0 = 6.75;
H0 = 10^(-pH0);
```

```
lnKw = 148.96502-13847/T-23.6521*log(T)+(118.67/T
5.977+1.0495*log(T))*S^(0.5)-0.01615*S;
Kw = exp(lnKw);
OH0 = Kw/H0;
```

Table 6.8 reports the parameters presented in the code above.

Table 6.8: Code implementation parameters: acidity system.

Symbol	Parameter	u.m.	Reference
pH0	Initial seawater *pH*	-	Text Chapter 6.3.4
H0	Hydrogen ion initial concentration	mol L^{-1}	Formula (2.1)
Kw	Ionic product of water, K_w^*	mol^2 kg^{-2}	Formula (6.2)
lnKw	Natural logarithm of K_w^*	-	Formula (6.3)
OH0	Hydroxyl ion initial concentration	mol L^{-1}	Formula (6.2)

The initial parameters allow the calculation of a set of other starting conditions entirely related to the seawater acidity. It is worth noting that the great importance of temperature `T` and salinity S in such evaluations because the ionic water product `Kw` is strongly affected by such parameters.

```
tmax = 200;
dt = 1e-1;
t = linspace(0, tmax, round(tmax/dt));

Ca = zeros(1, length(t));
r = zeros(1, length(t));
OH = zeros(1, length(t));
SL = zeros(1, length(t));
H = zeros(1, length(t));
SI = zeros(1, length(t));
omega = zeros(1, length(t));

r(1) = r0;
Ca(1) = Ca0;
OH(1) = OH0;
SL(1) = SLin/M;
H(1) = H0;
```

Table 6.9 reports the parameters presented in the code above.

Table 6.9: Code implementation parameters: array creation.

Symbol	Parameter	u.m.	Reference
tmax	Maximum simulation time	s	-
dt	Simulated time step	s	-
t	Time array length	-	-
Ca	Calcium ion concentration array	mol L^{-1}	-
r	Particle radius array	mol L^{-1}	-
OH	Hydroxyl ion concentration array	mol L^{-1}	-
SL	Undissolved SL ion concentration array	mol L^{-1}	-
H	Hydrogen ion concentration array	mol L^{-1}	-

SI	Saturation index array	-	-
omega	Saturation state array	-	-

Later, a group of arrays is created, aiming to contain the evolution of such parameters during the dissolution time. The code necessitates the setting of a maximum simulation time `tmax`, that can be easily changed according to the different simulations, and a time simulation step `dt`; this later parameter describes the level of desired accuracy: increasing it the model becomes more precise but even more complex and slower. Such arrays are created by building matrices with one row and as many columns as the maximum simulation time `tmax` divided by the time step value `dt`. Then, thanks to the values previously indicated, the initial value of such simulated parameters is set. It is worth noting that the model is built with concentration expressed in mol L^{-1}, so the undissolved SL array is created converting SL initial mass into moles.

```
Z0 = SL0/1000;
V0 = (4/3)*pi*r0^3;
Npart = Z0/(rhop*V0);
```

Table 6.10 reports the parameters presented in the code above.

Table 6.10: Code implementation parameters:

Symbol	Parameter	u.m.	Reference
Z0	Total SL initial mass	kg	Text Chapter 6.1
V0	Initial volume of each SL particle	m^3	Formula (6.39)
Npart	Number of SL particles	-	Formula (6.38)

After calculating the SL initial mass `Z0`, the total particles' number `Npart` is obtained; the analysis of a single particle volume `V0` allows its calculation, thanks to the knowledge of the initial radius `r0`. The total particles' number `Npart` is considered constant during the dissolution because SL particles are assumed with the same size.

```
kfa = 3.2e-4;
kba = 3.5e-9;

Eaf = 29.7;
Eab = 52.8;
R = 8.3144e-3;

lnf = Eaf/R*((T-Ta)/(T*Ta));
lnb = Eab/R*((T-Ta)/(T*Ta));

kfi = exp(lnf)*kfa;
kbi = exp(lnb)*kba;

kf = kfi*10;
kb = kbi*1e10;
```

Table 6.11 reports the parameters presented in the code above.

Table 6.11: Code implementation parameters: forward and backward constant rate calculation.

Symbol	Parameter	u.m.	Reference
kfa	Forward constant rate at reference temperature Ta	mmol L^{-1} s^{-1} cm^{-2}	Text Chapter 6.3.1
kba	Backward constant rate at reference temperature Ta	L^2 $mmol^{-2}$ s^{-1} cm^{-2}	Text Chapter 6.3.1
Eaf	Activation energy of the forward reaction	kJ mol^{-1}	Formula (6.24)
Eab	Activation energy of the backward reaction	kJ mol^{-1}	Formula (6.24)
R	Universal gas constant	kJ mol^{-1} K^{-1}	Formula (6.24)
kfi	Forward constant rate at simulated temperature T	mmol L^{-1} s^{-1} cm^{-2}	Formula (6.24)
kbi	Backward constant rate at simulated temperature T	L^2 $mmol^{-2}$ s^{-1} cm^{-2}	Formula (6.24)
kf	Forward constant rate at simulated temperature T	mol L^{-1} s^{-1} m^{-2}	-
kb	Backward constant rate at simulated temperature T	L^2 mol^{-2} s^{-1} m^{-2}	-

The forward kf and backward kb dissolution rates in the script relate to a reference temperature Ta of 22°C. In order to change them according to the different simulated temperatures T, Chapter 6.3.1 provides the necessary parameters and formulations. The latest step in the previously reported script is the change of the dissolution rates unity of measure because the initial rates are estimated in mmol and cm^2, as in the Johannsen and Rademacher (1999) study.

```
eps = 2727.586+0.6224107*T-466.9151*log(T)-52000.87/T;
A = 1.824928e6*sqrt(rhow/1000)*(eps*T)^(-1.5);
B = (50.3*(eps*T)^(-0.5));
I = 19.94*S/(1000-1.005*S);

aCa = 4.86;
bCa = 0.15;
aOH = 3.5;
bOH = 0.08;
zCa = 2;
zOH = 1;

gammaCa = 10^((-(A*zCa^2)*sqrt(I))/(1+B*aCa*sqrt(I))+bCa*I);
gammaOH = 10^((-(A*zOH^2)*sqrt(I))/(1+B*aOH*sqrt(I))+bOH*I);
```

Table 6.12 reports the parameters presented in the code above.

Table 6.12: Code implementation: activity coefficient calculation.

Symbol	Parameter	u.m.	Reference
eps	Dielectric constant of water	-	Formula (6.19)
A	Temperature-dependent coefficient	-	Formula (6.17)
B	Temperature-dependent coefficient	m^{-1}	Formula (6.18)
I	Ionic strength	-	Formula (6.15)
aCa	Ionic-specific fit parameter for Ca^{2+} ion	Å	Formula (6.16)
bCa	Ionic-specific fit parameter for Ca^{2+}ion	-	Formula (6.16)
aOH	Ionic-specific fit parameter for OH^{-} ion	Å	Formula (6.16)
bOH	Ionic-specific fit parameter for OH^{-} ion	-	Formula (6.16)
zCa	Calcium ion charge number	-	Formula (6.14)
zOH	Hydroxyl ion charge number	-	Formula (6.14)
gammaCa	Calcium ion activity coefficient	-	Formula (6.16)
gammaOH	Hydroxyl group activity coefficient	-	Formula (6.16)

Truesdell-Jones equation (6.16) allowed obtaining the activity coefficients for the calcium and hydroxyl ions, `gammaCa` and `gammaOH`; they are needed to later calculate the activity of such ions, as required in the Johannsen and Rademacher model. They vary according to temperature `T`, salinity `S`, and ionic strength `I`.

```
K = kf/kb;
SI0 = log10(gammaCa*Ca0*((gammaOH)^2)*((OH0)^2)/K);
SI(1) = SI0;

omega0 = 10^(SI0);
omega(1) = omega0;
```

Table 6.13 reports the parameters presented in the code above.

Table 6.13: Code implementation parameters: saturation state parameters.

Symbol	Parameter	u.m.	Reference
K	Equilibrium constant of SL dissolution	-	Formula (6.25)
SI0	Initial saturation index	-	Formula (6.28)
omega0	Initial saturation sate	-	Formula (6.29)

After the SL equilibrium constant `K` calculation, the evaluation of the saturation index `SI` and the saturation state `omega` is carried out at each instant `i`. Such values are helpful to understanding the gap to approach the saturation concentration.

```
for i = 1:length(t)-1

    Surf(i) = Npart*4*pi*r(i)^2;
    Rate(i) = Surf(i)*(kf-kb*gammaCa*gammaOH^2*Ca(i)*OH(i)^2);
    SL(i+1) = SL(i) - Rate(i)*(t(i+1)-t(i));

    Ca(i+1) = Ca(i) + Rate(i)*(t(i+1)-t(i));
    OH(i+1) = OH(i) + 2*Rate(i)*(t(i+1)-t(i));

   V(i+1) = SL(i+1)*M/(rhop*1000);
   r(i+1) = (3/(4*pi)*V(i+1)/Npart)^(1/3);
```

```
    SI(i+1) = log10((gammaCa*Ca(i+1)*(gammaOH*OH(i+1))^2)/K)
    omega(i+1) = 10^(SI(i+1));
end
```

Table 6.14 reports the parameters presented in the code above.

Table 6.14: Code implementation parameters: parameters for iterative dissolution modelling.

Symbol	Parameter	u.m.	Reference
`i`	Loop index	-	-
`Surf(i)`	Particle surface at time `i`	m^2	Formula (6.22)
`Rate(i)`	Net rate of SL particle dissolution at time `i`	mol L^{-1} s^{-1}	Formula (6.21)
`V(i)`	Particle volume at time `i`	m^3	Formula (6.39)

To describe the dissolution process of SL during time, and thus the reduction of particle size, it is necessary to adopt an iterative method. This could be implemented thanks to a for-loop, a control flow statement for specifying iteration which allows executing the code repeatedly; in this specific case, the number of iterations coincides with time array length `t`. To do this, it is necessary to define a loop index `i`, that counts the numbers of iteration done.

It is possible to calculate the values of the changing parameters at every time step `dt`; in particular, the for-loop recalculates Ca^{2+}concentration, undissolved SL concentration, OH^- concentration, volume of the undissolved particles, particle radius, total particles area, saturation index and state. As can be seen from the code above, undissolved SL in water at time `i+1` is obtained as the previous SL concentration value `SL(i)` minus the `Rate(i)` multiplied by the time step. `Rate(i)` is indeed the quantity of SL moles dissolved per time unit. Such value is equal to the increase of calcium ion moles in water `Ca(i+1)`, while the hydroxyl concentration `OH(i+1)` raises by to time this value because two OH^- ions are released during the dissolution of one SL molecule (as already shown in reaction (2.4) and in equation (6.11)).

As expected, the undissolved SL concentration decreases while Ca^{2+} and OH^- concentrations increase during time.

6.3.6 SENSITIVITY ANALYSES

This chapter carries out some sensitivity analyses thanks to the previously described dissolution model to understand the influence of different parameters on the overall process.

Many simulations are made, varying the temperature and the SL dosage; this aspect helps to investigate SL solubility deeply. The results of each simulation are given in terms of particles radius, total SL mass, saturation index, and total calcium ions concentration. Finally, different particle size classes are simulated, rather than a monodisperse powder, to enrich the model and better describe the real SL particles dissolution process.

Temperature analysis

The first step aims to study the influence of temperature on the dissolution process. Indeed, the model contains many temperature-changing parameters like seawater density ρ_w, forward k_f and backward k_b dissolution rates, ionic product of water K_w^*, dielectric water constant ε and other parameters that affects the ion activity coefficients γ_i. As mentioned above in Chapter 6.2, this evaluation simulates three different temperatures characterizing different seas (respectively 15 °C, 22 °C and 25 °C).

Figure 6.12, 6.13, and 6.14 present the first comparison; it represents a dosage of 0.2 g L^{-1} for three different temperatures T. Table 6.5 exhibits the different seawater densities ρ_w adopted, and it is clear that such density decreases with a temperature increase. However, the main parameters are the dissolution forward and backward rates, that increase with temperature (Figure 6.5), thus causing an acceleration of the overall process. Figure 6.12 confirms that a temperature increase accelerates dissolution, with the calcium ions concentration incrementing during time and approaching its maximum value after about 30 seconds during the 25 °C test, and in 50 seconds for the 15°C simulation; these outcomes are demonstrated also in Figures 6.13 and 6.14. The temperature increase has a positive effect in accelerating the process because the dosed SL is far from the concentration at saturation. Such acceleration could not less significant if approaching the saturation level, because the overall solubility of SL decreases with temperature.

The trends at different temperatures reach the same final calcium ions concentration, while the dissolution time differs. All these results show a quite linear radius reduction trend, that's because the dosed SL mass is far from the saturation point.

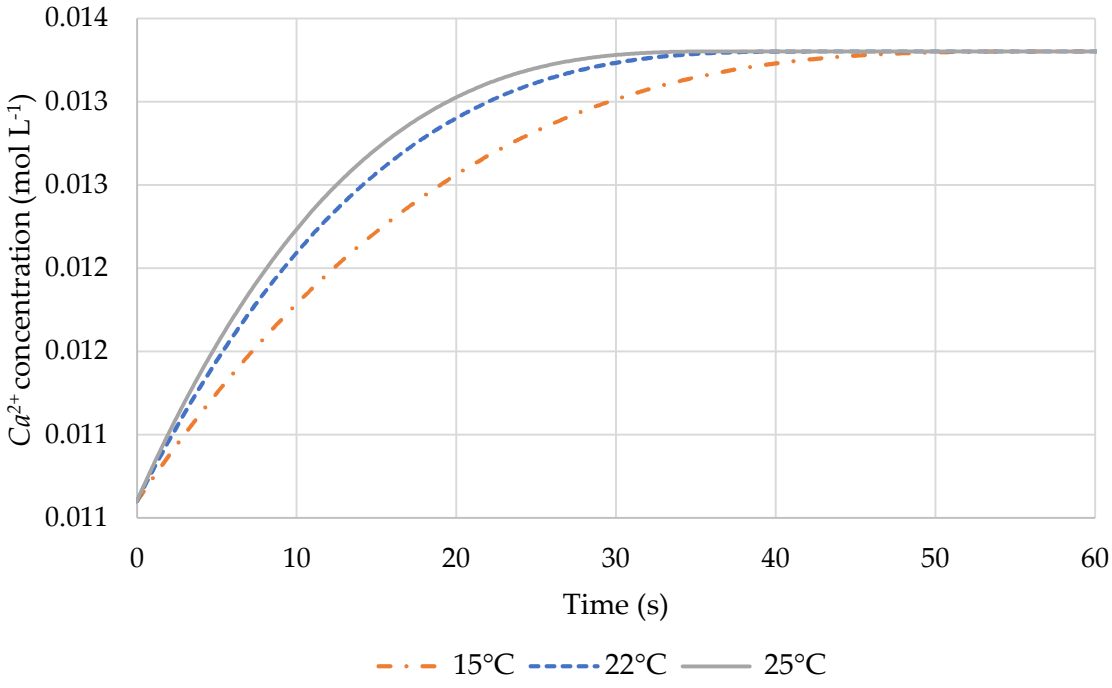

Figure 6.12: Calcium ions concentration trend for different temperatures T; dosed SL: 0.2 g L^{-1}.

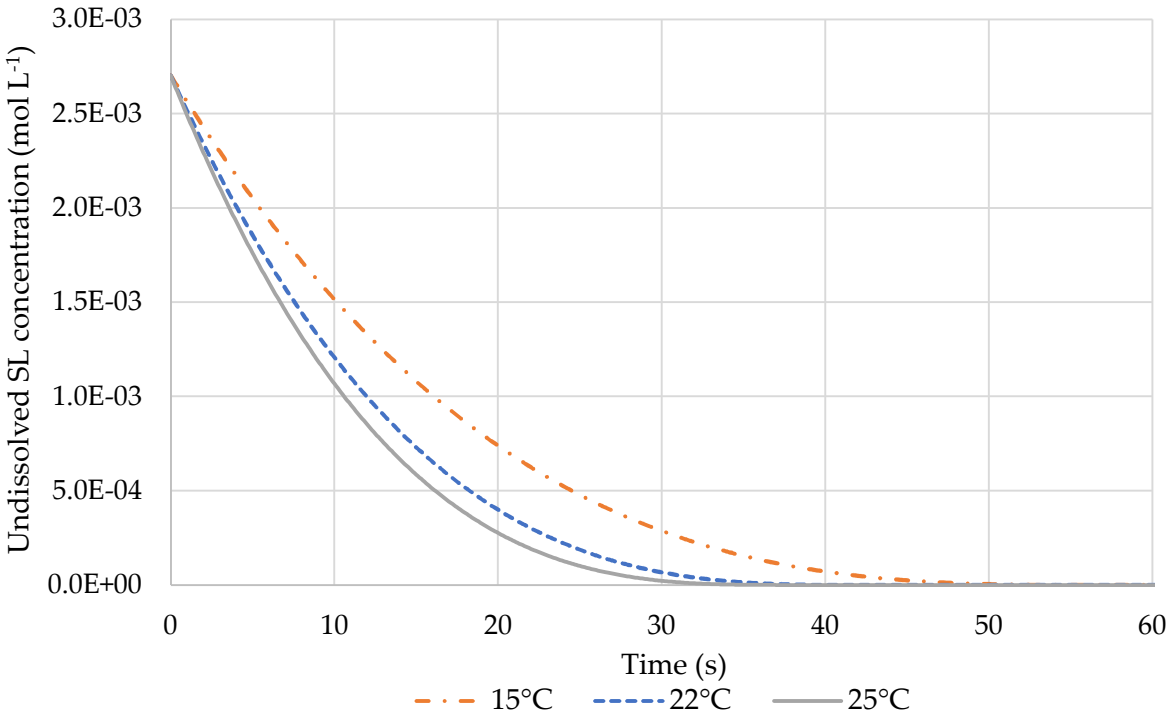

Figure 6.13: Undissolved SL concentration trend for different temperatures T; dosed SL: 0.2 g L^{-1}.

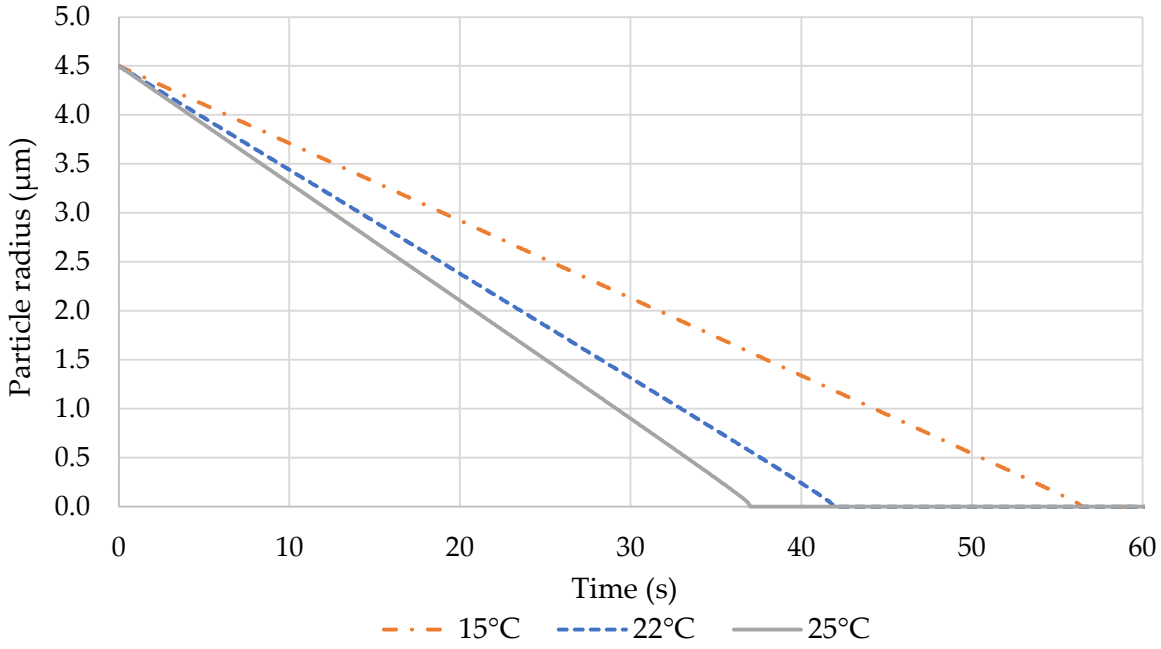

Figure 6.14: Particles' radius trend for different temperatures T; dosed SL: 0.2 g L^{-1}.

SL dosage analysis

Subsequently, further analysis shows the influence of SL dosages; the simulations are carried out at a 22°C temperature for four different SL initial concentrations at discharge: 0.2, 2, 4, and 8 gSL L^{-1}. Figures 6.15, 6.16, and 6.17 present the results; in more details, three different

parameters are graphically reported: the total calcium ions Ca^{2+} concentration, the solution saturation index SI, and the particles' radius r.

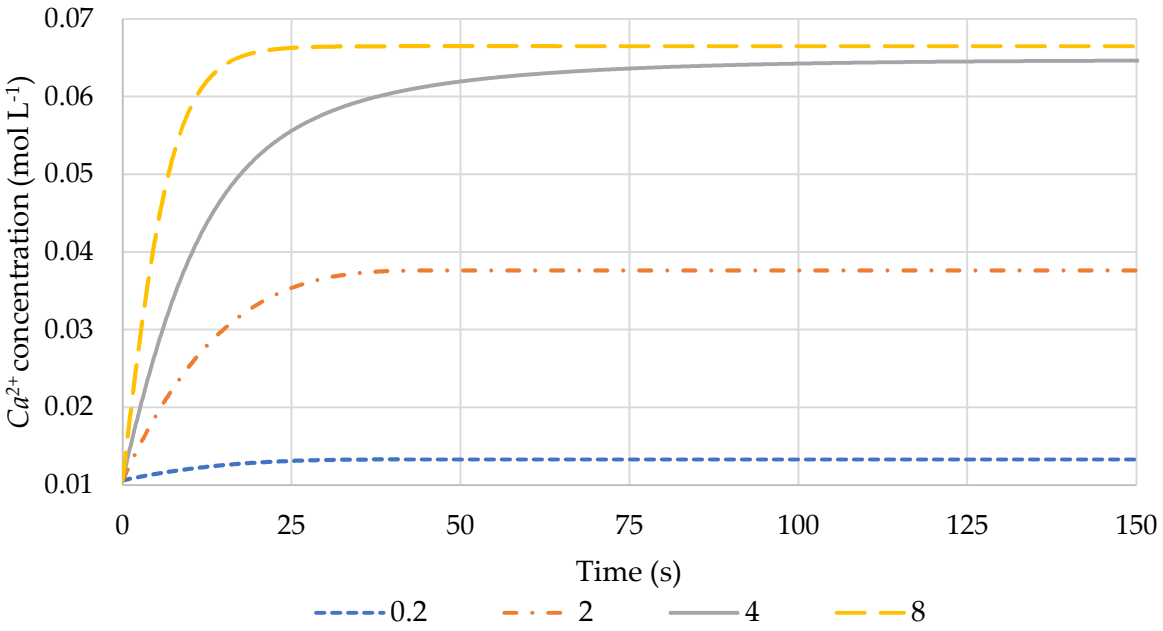

Figure 6.15: Trend of calcium ions in water as the amount of SL poured varies (expressed in g L^{-1}).

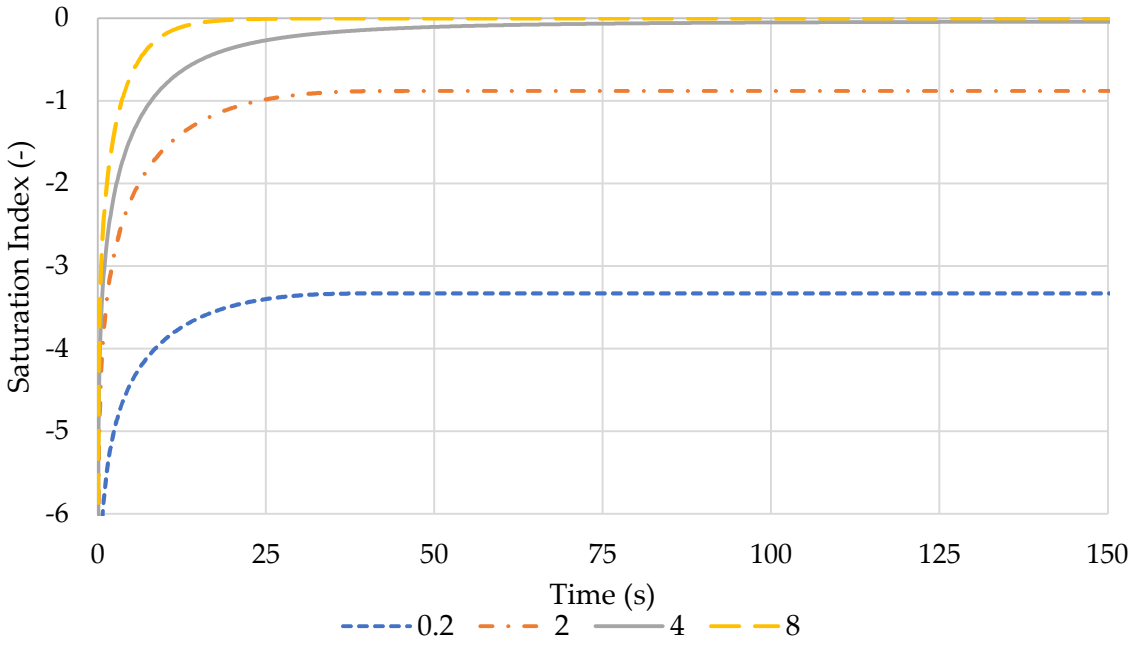

Figure 6.16: Saturation Index trends as the amount of SL poured varies (expressed in g L^{-1}).

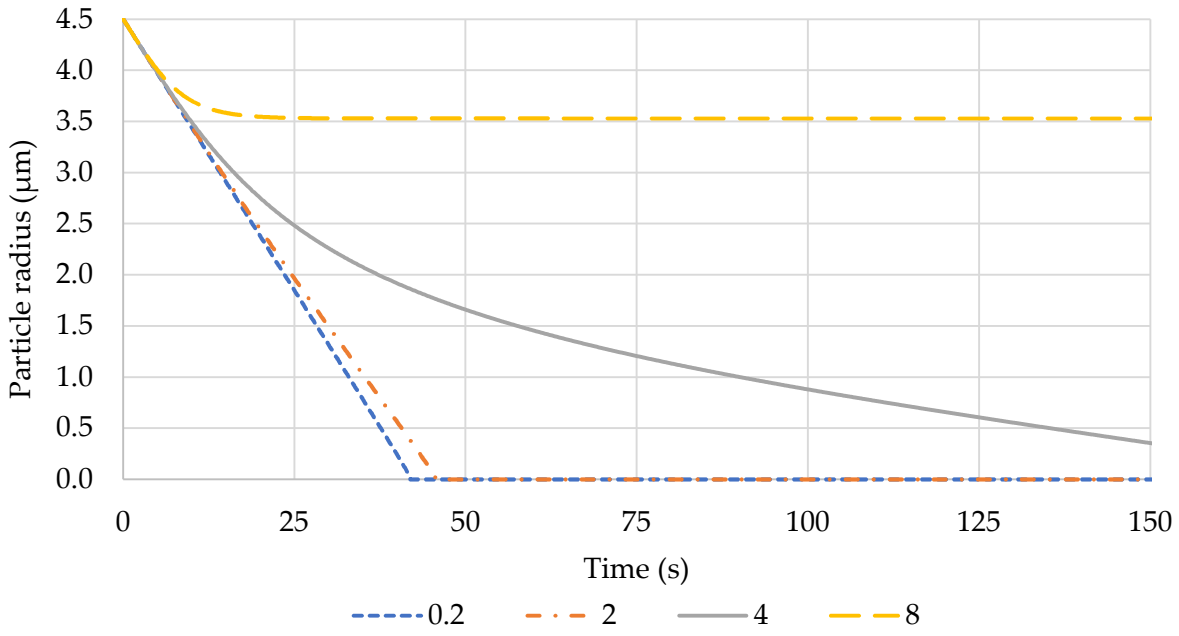

Figure 6.17: Particles' radius trends as the amount of SL poured varies (expressed in g L^{-1}).

Such graphs are interesting in presenting the different behaviours when approaching the SL solubility. While the 0.2 and 2 gSL L^{-1} dosage simulations act similarly, some differences are instead observed in the other cases because of the proximity to the saturation concentration, equals to 4.15 gSL L^{-1} at 22 °C. During the 4 gSL L^{-1} dosage simulation, particles' radius does not decrease linearly but its shrinkage velocity slows down during the dissolution. This is because the process forcing is the difference between the SL concentration and its solubility. Such behaviour is highlighted even in Figure 6.16: at 4.15 gSL L^{-1}, the saturation index SI approaches asymptotically the 0 value but without reaching it (almost achieving saturation conditions). Rather, the 8 gSL L^{-1} dosage is almost twice the SL solubility; as a result, in Figure 6.17 is possible to notice that the particles' radius decreases not linearity, and it does not reach the 0 value; that means that SL mass does not dissolve completely even if the dissolution process ends, and many particles remain suspended and undissolved in the solution. As can be also seen, the SI has a fast increase and reaches the 0 value. Figure 6.15 shows another peculiarity of pouring a SL quantity larger than the solubility: while in other cases, the maximum Ca^{2+} value is reached in higher times for higher SL dosages, when the poured SL mass is higher than the solubility such trend is reversed. The calcium ions concentration increases rapidly, and it reaches its maximum value earlier than the other dosages. This is caused by the large number of particles dissolving, which compensates the low dissolving speed due to the gap from the saturation point.

An in-depth simulation concerning SL dosages close to solubility has been conducted; the main aim is to explore deeply the SL behaviour when the concentration approaches the solubility, considered 4.15 gSL L^{-1} at 22°C as shown in Figure 6.6. Three different initial concentrations are examined: 3.5, 4, and 4.5 gSL L^{-1}. Undissolved SL concentration and the saturation index SI trends are shown respectively in Figure 6.18 and in Figure 6.19.

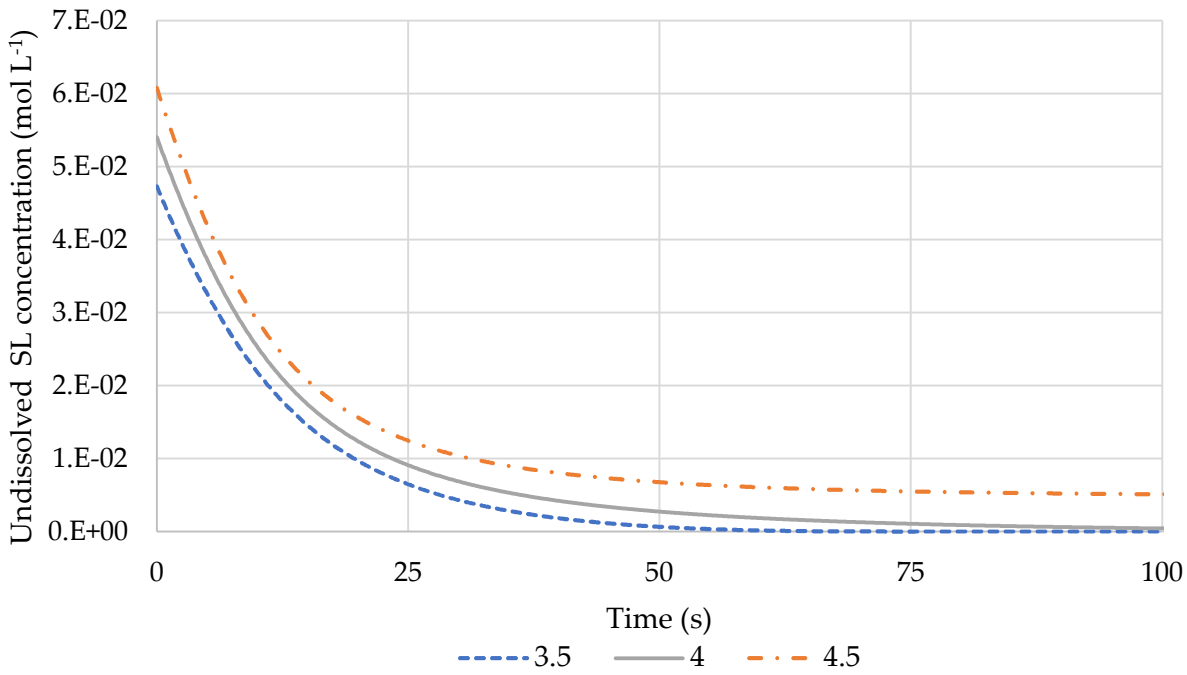

Figure 6.18: Undissolved SL concentration analysis as the amount of SL poured varies near saturation condition (expressed in g L^{-1}).

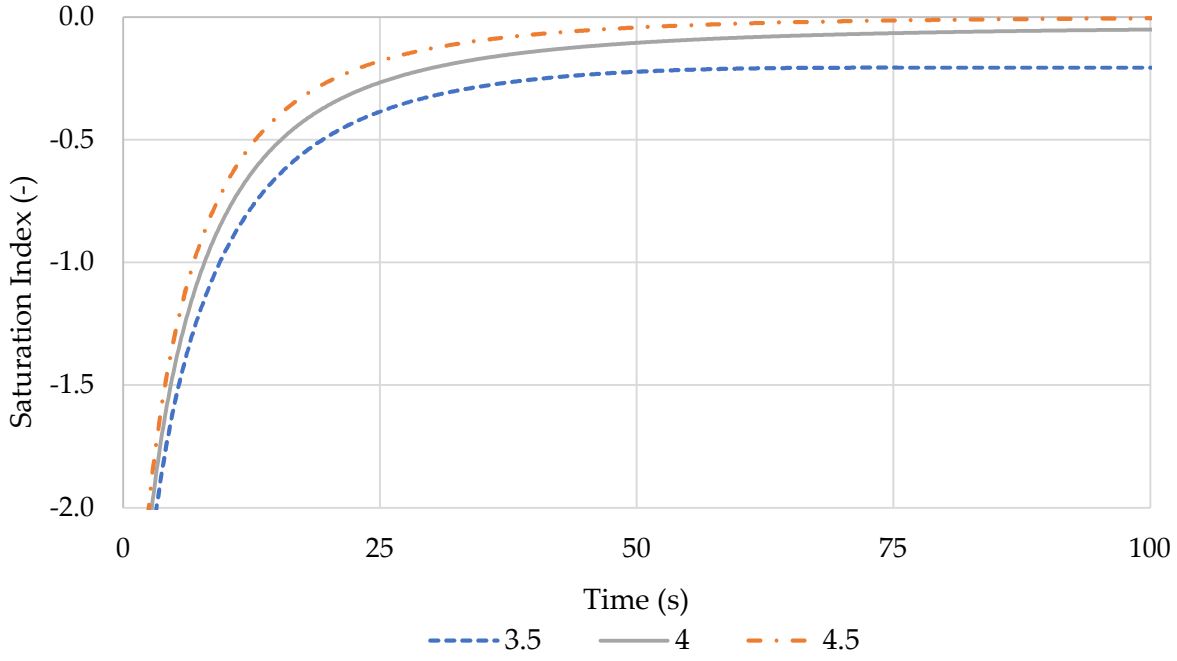

Figure 6.19: Saturation Index analysis as the amount of SL poured varies near saturation value (expressed in g L^{-1}).

As expected, the 4 gSL L^{-1} dosage brings the solution approaching saturation, but the SL mass dissolves completely and the *SI* value remains slightly lower than 0; the same trend is shown by the 3.5 gSL L^{-1} dosage. Otherwise, the 4.5 gSL L^{-1} simulation behaves in a different way, reaching saturation (*SI* = 0), and not dissolving completely. However, the most interesting point is the dissolution time. The graphs show that slightly incrementing the initial concentration, the dissolution time increases significantly. The dissolution time in the 3.5 gSL L^{-1} simulation is about 50 s, while in the 4 gSL L^{-1} dosage it is roughly 100 s, almost doubled.

It is possible to highlight such behaviour only when the initial dosages approach the solubility.

Particle size classes analysis

All the previous simulations considered a monodisperse SL powder characterized by a median particle radius of 4.5 μm. As already explained in the previous chapters, the SL used for OAE is actually a polydisperse powder, so further analyses considering different size classes are necessary.

The following simulation analyse ten different diameters characterizing the SL granulometry percentile distribution (reported previously in Figure 2.9). Each diameter corresponds to a specific relative frequency (reported in Table 6.15), and each undertaken simulation reports the result for a specific size class.

It should be underline that in this case, all the simulations refer to a temperature T of 22 °C with a seawater pH of 7 and a SL dosage of 0.2 gSL L^{-1}.

Table 6.15: Percentile distribution and relative frequency for SL powder.

Percentile	**Particle diameter**	**Relative frequency**
%	μm	%
10	4.09	3.5
20	4.93	5.0
30	6.01	3.8
40	7.71	3.7
50	9.22	5.2
60	10.81	5.4
70	13.16	4.1
80	16.65	3.5
90	24.86	1.6
95	38.99	0.7

The results of the assessment of the calcium ions trend during the SL dissolution process are graphically reported in Figure 6.20. As can be expected, the smallest SL particles dissolve in a shorter period, because of the higher specific surface.

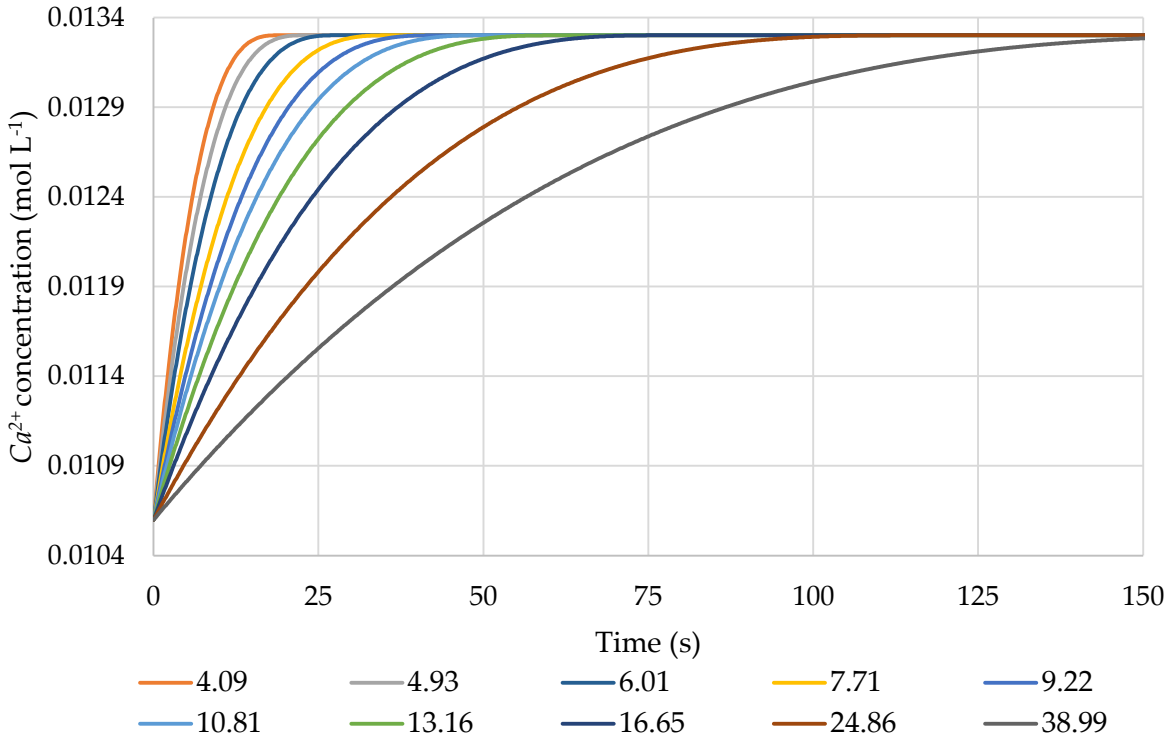

Figure 6.20: Trend of Ca^{2+} ions in seawater for different diameters.

Later, other modelled evaluations describe the behaviour of a polydisperse powder. The conditions are the same as the previously described simulation. In more detail, another analysis is carried out by subdividing the overall distribution into different number of granulometric classes, as also reported in Table 6.16:

1. three classes: they have different dimensions to emphasize that size classes far from the median value have a limited number of elements, so they account for a small percentage of the total distribution;
2. four classes: they all have the same size.

Both simulations consider all the different classes characterized by the related median diameter.

Table 6.16: Assessed granulometric classes.

Simulation 1	Particle diameter	µm	3.75	10.25	27.50	
	Relative frequency	%	25	50	25	
Simulation 2	Particle diameter	µm	4.50	7.20	11.50	22.00
	Relative frequency	%	25	25	25	25

For each simulation, particles' radius, undissolved SL concentration in seawater and SL dissolution rate behaviours are deeply investigated.

As can be seen from the graphs in Figure 6.21, SL particles' radius shows a decreasing trend over time. It is worth noting that, since we are close to the saturation condition, only for smaller particles the radius reaches the 0 value, while for the other classes after a rapid

decrease, the radius tends to stabilize. Each radius' behaviour has a similar trend, even for different partitioning simulations.

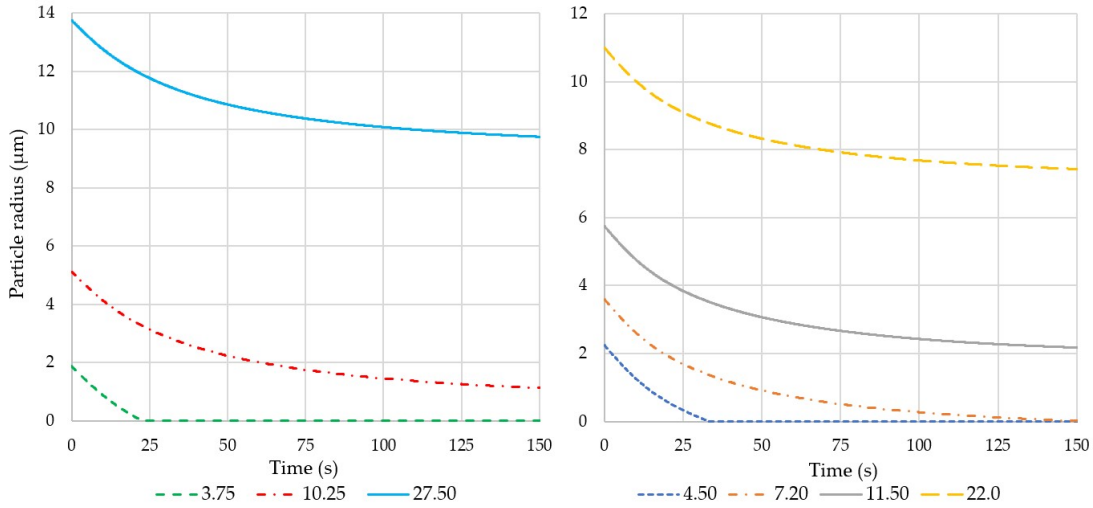

Figure 6.21: SL particle's radius behaviour near saturation conditions for three (left) or four (right) particle size classes (characterized by an initial radius expressed in µm).

The analysis of undissolved SL in each size class shows more interesting results. It is easy to note that bigger particles dissolve slowly, even if they account for a smaller part of the total mass (as in the three different size classes simulation, Figure 6.22). This is caused by the smaller total surface in contact with seawater. The result is that the overall dissolution time is much larger when bigger particles are involved.

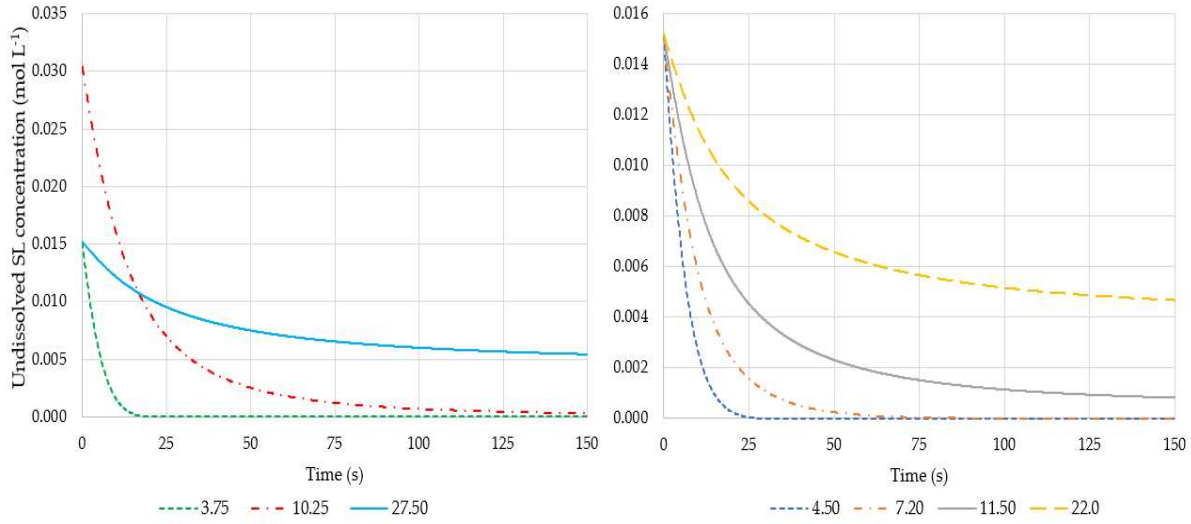

Figure 6.22: Undissolved SL concentration near saturation conditions for three (left) or four (right) particle size classes (characterized by an initial radius expressed in µm).

This chapter carries out also an analysis of the dissolution rates trends, graphically shown in Figure 6.23. Such results are quite interesting because each radius rate develops differently during the dissolution. Smaller particles have a higher dissolution rate, but it drops quickly approaching zero as the dissolution continues. After a few seconds, the smaller particles' rate becomes lower than bigger particles; this happens since the mass of the smaller SL particles becomes significantly lower than the other classes, releasing fewer calcium moles in water.

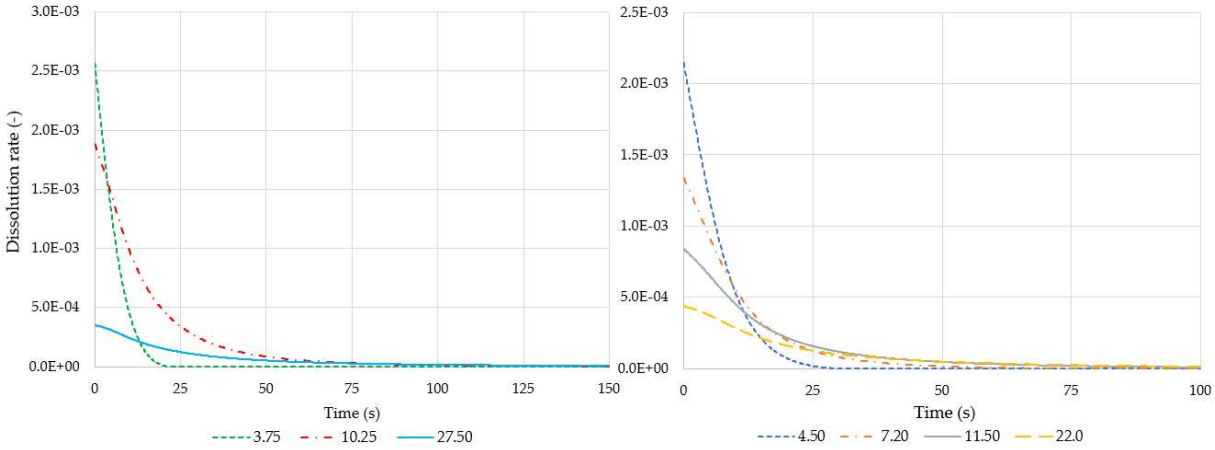

Figure 6.23: SL dissolution rate behaviour near saturation conditions for three (left) or four (right) particle size classes (characterized by an initial radius expressed in μm).

As can be seen in Figure 6.15 and 6.17, the dissolution results for the 4 gSL L^{-1} in the case of median diameter are not so dissimilar from the 4.5 gSL L^{-1} with different size classes. The dissolution time shown in Figure 6.15 is between 125 and 150 seconds, and also in Figure 6.20 the particles stop dissolving after about 150 seconds. Such few seconds' increment could be caused simply by the small amount of extra SL in the later simulation; however, it could be also affected by the larger particles simulated, which take a longer time to dissolve completely. In conclusion, since dissolution times are comparable, it can be stated that the median diameter simulation is quite reliable, and it is not necessary to subdivide the dosed SL into more granulometric classes.

6.4 FLUID DYNAMIC DISSOLUTION MODEL

After the realization of the one-dimensional MATLAB dissolution model, the current thesis work includes a further physical in-depth analysis. A collaboration with two aerospace engineering students permitted the development of a three-dimensional fluid dynamic model describing the SL dissolution process in a stirred beaker, aiming to recreate the laboratory experiments carried out by Colombo and Crisanto (2021), described in Chapter 6.1. This additional study permits to couple the dissolution model with the developed turbulent flow. Bianchi and Abbate's (2022) Master's degree thesis shows the details of such a model. If proven the accuracy of this model, future studies could be implemented to apply this model to a real situation, for instance describing the fluid dynamics of a ship's wake.

This complex model comprises two main parts: the first section describes the water fluid dynamics while the latter includes the MATLAB dissolution model previously described in Chapter 6.3.5. The overall model is created by Bianchi and Abbate (2022) using FORTRAN programming language; for this reason, the MATLAB code has been rewritten and re-elaborated in such a different language. The model purposes to describe a seawater volume in a beaker stirred by a small impeller. Subsequently, a set of comparisons between the fluid dynamics dissolution model and the laboratory experiments results aims to evaluate the correctness of such a model.

The model is three-dimensional, and it comprises the presence of a rotating body in the middle of the simulated beaker, which agitates water forming turbulent structures in the modelled volume. The dissolution implementation provides a SL dosage in a sort of cloud in the centre of the beaker, which is subsequently spread apart by the simulated impeller. The 1 L water volume is divided into half a million smaller cells, whose concentrations of SL, calcium ions, and hydroxyl groups change according to the implemented source term (the SL dissolution model) and water velocity. Each of these cells represents a volume where the SL dissolution occurs according to the kinetics accurately described in the MATLAB code.

6.4.1 GOVERNING EQUATIONS

This chapter aims to briefly present and investigate the equations solved in the fluid dynamic simulations.

Equations solved in the fluid dynamic model are incompressible Navier-Stokes equations (Citrini and Noseda, 1987). They are a set of partial differential equations aiming to define the behaviour of viscous fluid substances, based on mathematical expressions representing the conservation of momentum (equations (6.48), (6.49), and (6.50)) and mass (6.51). It is worth noting that the following equations do not report external volumetric forces because they are negligible in the present case study. Because of the cylindrical symmetry of the beaker, the set of Navier-Stokes equations is written based on cylindrical coordinates and variables. Cylindrical parameters, shown in equations (6.47), helped to recreate a group of Navier-Stokes formulations with specific variables for the case study.

$$q_r = r\,u_r \qquad q_\theta \qquad q_{z_a} \tag{6.47}$$

$$\frac{\partial q_r}{\partial t} + \frac{\partial}{\partial r}\left(\frac{q_r^2}{r}\right) + \frac{\partial}{\partial \theta}\left(\frac{q_r\,q_\theta}{r}\right) + \frac{\partial}{\partial z_a}\left(q_r\,q_{z_a}\right) - q_\theta^2 = -r\frac{\partial p}{\partial r} + \\ + \frac{1}{Re}\left[r\frac{\partial}{\partial r}\left(\frac{1}{r}\frac{\partial q_r}{\partial r}\right) + \frac{1}{r^2}\frac{\partial^2 q_r}{\partial^2 \theta} + \frac{\partial^2 q_r}{\partial^2 z_a} - \frac{2}{r}\frac{\partial q_\theta}{\partial \theta}\right] \tag{6.48}$$

$$\frac{\partial q_\theta}{\partial t} + \frac{1}{r^2}\frac{\partial}{\partial r}\left(r\,q_\theta\,q_r\right) + \frac{1}{r}\frac{\partial}{\partial \theta}\left(q_\theta^2\right) + \frac{\partial}{\partial z_a}\left(q_\theta\,q_{z_a}\right) = -\frac{1}{r}\frac{\partial p}{\partial \theta} + \\ + \frac{1}{Re}\left[\frac{1}{r}\frac{\partial}{\partial r}\left(\frac{1}{r}\frac{\partial q_\theta}{\partial r}\right) - \frac{q_\theta}{r^2} + \frac{1}{r^2}\frac{\partial^2 q_\theta}{\partial^2 \theta} + \frac{\partial^2 q_\theta}{\partial^2 z_a} - \frac{2}{r^3}\frac{\partial q_r}{\partial \theta}\right] \tag{6.49}$$

$$\frac{\partial q_{z_a}}{\partial t} + \frac{1}{r}\frac{\partial}{\partial r}\left(q_{z_a}\,q_r\right) + \frac{1}{r}\frac{\partial}{\partial \theta}\left(q_\theta\,q_{z_a}\right) + \frac{\partial}{\partial z_a}\left(q_{z_a}^2\right) = -\frac{\partial p}{\partial z_a} + \\ + \frac{1}{Re}\left[\frac{1}{r}\frac{\partial}{\partial r}\left(r\frac{\partial q_{z_a}}{\partial r}\right) + \frac{1}{r^2}\frac{\partial^2 q_{z_a}}{\partial^2 \theta} + \frac{\partial^2 q_\theta}{\partial^2 z_a} - \frac{\partial^2 q_{z_a}}{\partial^2 z_a}\right] \tag{6.50}$$

$$\frac{\partial q_r}{\partial r} + \frac{\partial q_\theta}{\partial \theta} + r\,\frac{\partial q_{z_a}}{\partial z_a} = 0 \tag{6.51}$$

where:

r, θ, z_a: cylindrical coordinates - radius, angle, vertical quote;

u_r: velocity of the fluid in the radial direction;
q_r: flux of the fluid in the radial direction;
q_θ, q_{z_a}: velocity of the fluid in the tangential and axial direction;
p: pressure of the fluid.

Furthermore, the described model involves a Large Eddy Simulation (LES) implementation added to the Navier-Stokes equations system (Piomelli, 1999). A LES is a mathematical model for turbulence used in computational fluid dynamics: it simulates the large turbulent scales while modelling the smaller ones. It is a technique intermediate between the exact solution of the turbulent flows and the solution of the Reynolds-averaged equations. The subgrid model applied, which is necessary in solving small scales (Vreman et al., 1995) in each LES implementation, is a "dynamic tensorial eddy viscosity" model developed by Abbà et al. (2022). All the details of this complete model are deeply investigated in Bianchi and Abbate's (2022) thesis, which describes the implementation of the Navier-Stokes equations including a detailed analysis of the LES accomplishment.

The SL dissolution in the previously described fluid dynamics model requires the adoption of a passive scalar equations set. This group of formulations is defined as "passive" since these equations don't affect back the results provided by the fluid dynamics, and it is "scalar" since they represent scalar quantities. The investigated scalar quantities are four: Ca^{2+} and OH^- ions that derive from the dissolution of SL, the undissolved SL in the solution, and the concentration of the particles. An advection-diffusion equation governs the time evolution of scalar quantities in an incompressible turbulent flow: each of the described quantities is ruled by equations with the same structure, represented in formula (6.52).

$$\frac{\partial \phi}{\partial t} + \frac{1}{r}\frac{\partial (q_r\, \phi)}{\partial r} + \frac{1}{r}\frac{(q_\theta\, \phi)}{\partial \theta} + \frac{\partial \left(q_{z_a}\, \phi\right)}{\partial z_a} = \\ = D_\phi \left(\frac{1}{r}\frac{\partial}{\partial r}\left(r\frac{\partial \phi}{\partial r}\right) + \frac{1}{r^2}\frac{\partial^2 \phi}{\partial^2 \theta} + \frac{\partial^2 \phi}{\partial^2 z_a}\right) + S_\phi \qquad (6.52)$$

where:

ϕ: simulated scalar quantity;
D_ϕ: molecular diffusivity of each scalar quantity;
S_ϕ: source term.

Equation (6.52) allows assessing the evolution in space and time of each scalar quantity ϕ investigated (Ca^{2+} and OH^- ions, undissolved SL, and particles' concentration). The source term (S_ϕ) is the MATLAB dissolution model analysed in Chapter 6.3.5, properly adapted in the described passive scalar model, and it is linked to a suitable advection-diffusion model.

6.4.2 VALIDATION SCENARIOS OF THE FLUID DYNAMIC MODEL

The SL dissolution model, coupled with the realization of a developed turbulent fluid dynamics, necessitates the simulation of many scenarios to compare the modelling results with the laboratory experiments from Colombo and Crisanto's (2021) thesis.

This chapter mainly aims to outline the validation methods of the fluid dynamic model deeply described in Bianchi and Abbate's (2022) thesis, with whose collaboration the model has been obtained. Following analyses allow evaluating the robustness of this model, highlighting eventual problems and discrepancies with laboratory results.

Many scenarios necessitate the investigation of multiple initial parameters to examine the influence of the starting conditions in the model. A variety of initial situations constitutes a set of different scenarios; the two main parameters modified to compare the results with laboratory tests are temperature and salinity.

The following simulations represent a set of temperatures T ranging between 5 and 25°C, and salinity S values between 10 and 40 g kg^{-1}. Each of the subsequent scenarios involves a SL dosage of 0.2 g in 1 L of solution, which corresponds to a particles number n_0 of 2.34 10^8, considering a monodisperse powder with the same particle diameter d_p of 9 μm. This matches with a SL concentration of 2.7 mmol L^{-1}. All simulations consider an initial pH level equal to 7 (which allows calculating the starting OH^- concentration, thanks to equations (2.1), (6.2), and (6.3)), and a starting Ca^{2+} concentration obtained by considering a linear relationship between calcium ions concentration and total salinity S. The Arrhenius equation (6.24) allows the calculation of the constant dissolution rates k_f and k_b for different temperatures, while the Truesdell-Jones formulation (6.16) makes it possible to obtain the activity coefficients $\gamma_{Ca^{2+}}$ and γ_{OH^-} in each simulation. Table 6.17 reports the set of initial conditions that characterize each simulated scenario varying temperature and salinity. Moreover, Table 6.17 also shows the molecular diffusion D_ϕ of each calculated scalar quantity, whose necessity can be seen from the formulation (6.53). Literature provides ion molecular diffusion values for different temperatures, including those of Ca^{2+} and OH^- ($D_{Ca^{2+}}$ and D_{OH^-}), (Li and Gregory, 1974), while the Stokes-Einstein equation (Edward, 1970), reported below, permits to obtain SL molecular diffusion (D_{SL}).

$$D_{SL} = \frac{K_B\, T}{6\, \pi\, \mu_w\, r_p} \tag{6.53}$$

where:

D_{SL}: SL molecular diffusivity;
K_B: Boltzmann constant, assumed 1.38065 10^{23} J K^{-1} (Fellmuth et al., 2006);
μ_w: seawater viscosity, that varies according to temperature (Table 6.5).

Table 6.17: Initial parameter for each implemented fluid dynamic scenario.

		Simulated scenarios					
Parameter	**u.m.**	**Test 1**	**Test 2**	**Test 3**	**Test 4**	**Test 5**	**Test 6**
T	°C	5	10	20	25	25	25
S	g kg^{-1}	35	35	35	35	40	10
$[Ca^{2+}]$	10^{-3} mol L^{-1}	10.6	10.6	10.6	10.6	12.1	2.98
$[OH^{-}]$	10^{-7} mol L^{-1}	85.6	1.44	3.84	6.07	6.59	3.10
k_f	mol L^{-1} s^{-1} m^{-2}	0.00153	0.00192	0.00295	0.00361	0.00361	0.00361
k_b	L^2 mol^{-2} s^{-1} m^{-2}	9.396	14.062	30.222	43.460	43.460	43.460
$\gamma_{Ca^{2+}}$	-	0.241	0.239	0.234	0.231	0.228	0.313
$\gamma_{OH^{-}}$	-	0.694	0.692	0.688	0.686	0.686	0.733
$D_{Ca^{2+}}$	10^{-10} m^2 s^{-1}	4.56	5.40	7.08	7.93	7.93	7.93
$D_{OH^{-}}$	10^{-10} m^2 s^{-1}	30.95	36.38	47.20	52.61	52.61 1	52.61
D_{SL}	10^{-14} m^2 s^{-1}	2.79	3.24	4.20	4.72	4.72	4.72

6.4.3 RESULTS OF THE FLUID DYNAMIC MODEL

This chapter aims to investigate the result of the implemented fluid dynamic simulations.

Figure 6.24 graphically shows how the developed turbulence interacts with particles in water. In more detail, it illustrates how molecules are spread apart by the modelled impeller, showing the three-dimensional variation of OH^{-}ions concentration.

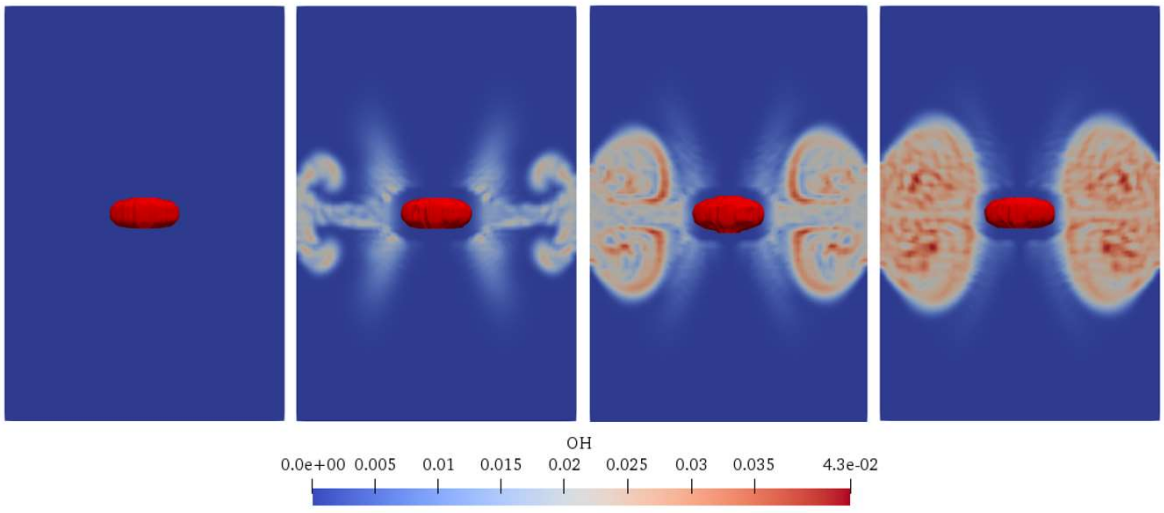

Figure 6.24: OH^{-} ions dispersion inside the beaker over time, expressed in mol L^{-1}.

It should be noted that OH^{-} ions are not homogeneously distributed in the modelled volume because the SL dosage occurs in the middle of the simulated beaker. As a result, there is a lower concentration of OH^{-} ions at the edges of the beaker, where such a concentration could be similar to the initial condition, especially after a few seconds of simulation. Complete dissolution occurs usually in less than a minute, so there is not sufficient time to reach a homogenous distribution in space. This fact is relevant for all the scalar quantities considered.

Figure 6.25 describes this irregular distribution in the volume after the completion of the SL dissolution: it shows the frequency of cells with a different OH^- concentration, demonstrating that about half volume has an extremely low concentration of OH^- ions, very similar to the initial one.

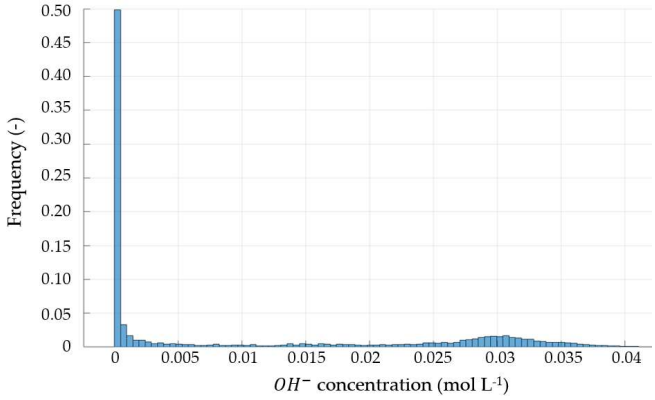

Figure 6.25: Example of the frequency of the OH^- concentration inside the cells of the beaker during Test 1, right after the complete dissolution. It should be noted that at least the 50% of the cells do not contain OH^- ions.

Figure 6.26 show the trends of Ca^{2+} ions, Figure 6.27 reports OH^- ions trends, and Figure 6.28 reports the undissolved SL in the six implemented simulations (Table 6.17). Each graph illustrates the fluid dynamic numerical model results.

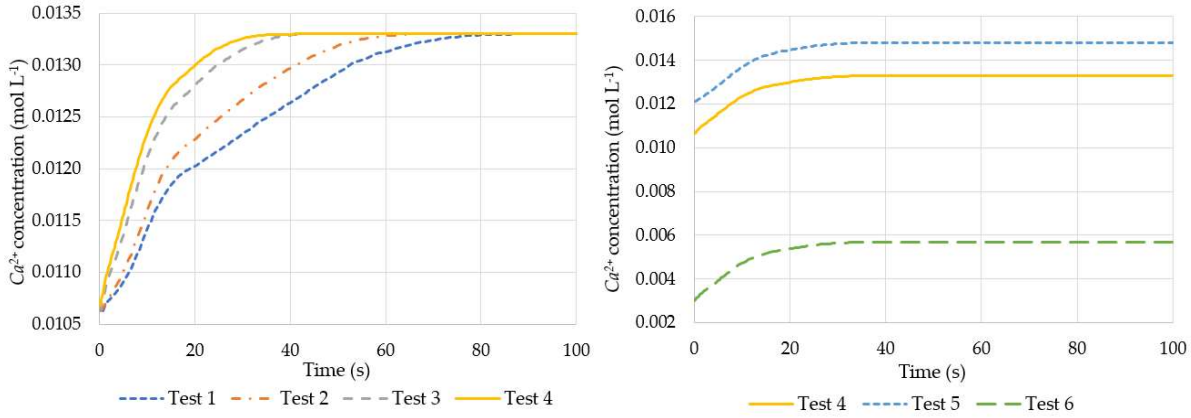

Figure 6.26: Trends of Ca^{2+} ions (in terms of mol L^{-1}) for each implemented scenario.

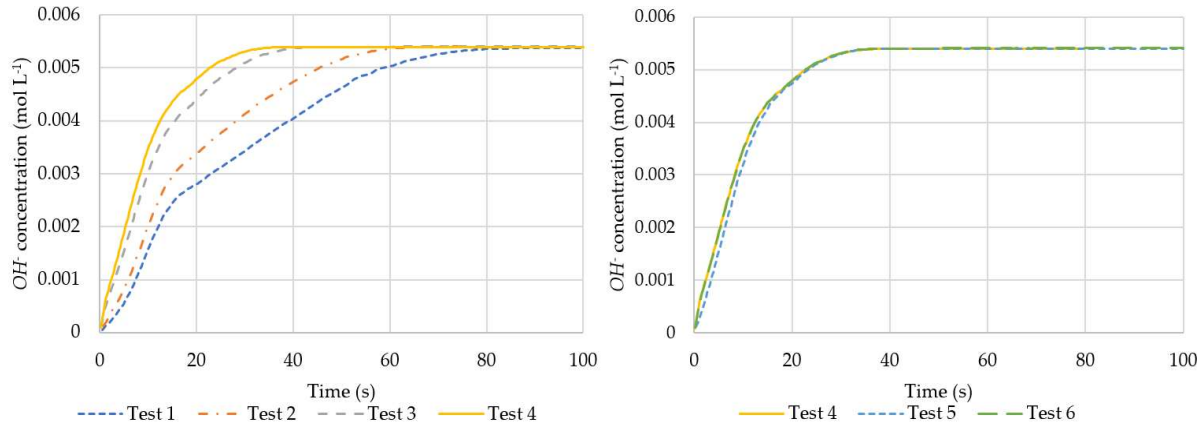

Figure 6.27: Trends of OH^- ions (in terms of mol L^{-1}) for each implemented scenario.

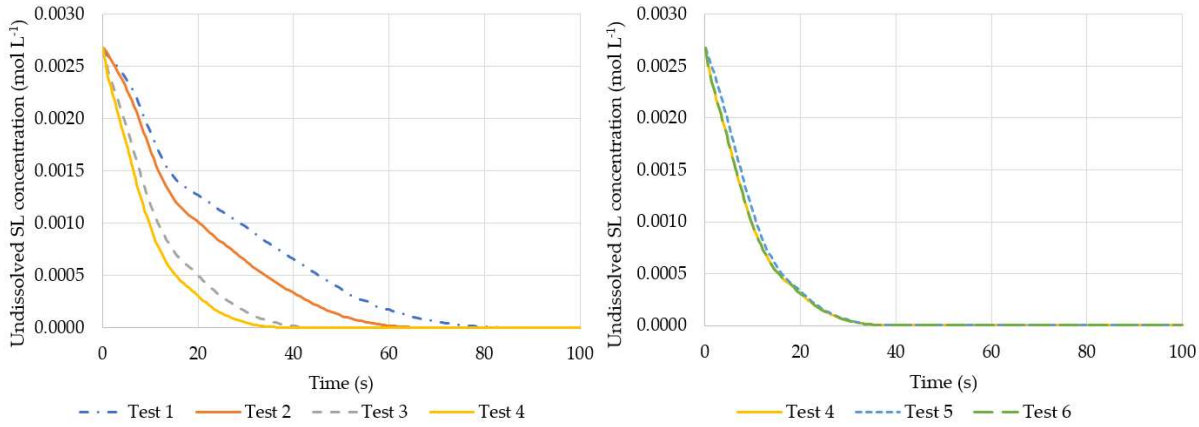

Figure 6.28: Trends of undissolved SL ions (in terms of mol L^{-1}) for each implemented scenario.

Tests from 1 to 4 show the SL behaviour if incrementing the temperature T always at same salinity, while Tests 4 to 6 demonstrate the effect of a salinity variation with a constant seawater temperature T. Additional information of the simulations are reported in Table 6.16. It is worth noting the SL dissolution time decreases for higher T, because of the dissolution kinetics acceleration (Arrhenius equation (6.24)). However, this fact probably displays since the SL dosage is far from the saturation condition, as higher temperatures drop down the SL solubility (Figure 6.6), reversing or balancing the acceleration of the dissolution time. Final values of calcium and hydroxyl ions concentration are the same in all scenarios because starting concentrations are the same, as the SL dosage.

The three-dimensional fluid dynamic model does not show a strong effect of salinity S variation considering the dissolution time. However, in Tests 4 to 6, Ca^{2+} concentration final values are very dissimilar because of their different starting concentration related to seawater composition; on the other hand, there are no differences in OH^- final ions concentration since the initial pH and temperature T are the same in all implemented scenarios.

Knowing the concentration trends allow the comparison between laboratory and simulated results. The fluid dynamic model outcomes are approximate since a large part of the carbonate system reactions are neglected. It is worth noting that the Ca^{2+} trends reach a concentration value of 0.0133 mol L^{-1} in all scenarios from Test 1 to 4. This value derives from a complete SL dissolution without any side reaction (i.e.: Ca^{2+} ions precipitation in form of $CaCO_3$) that could vary such a final concentration value. This result is consistent with all the assumptions made, but it could cause discrepancies with a real situation; however, no laboratory results investigate such ion concentration, so other studies could be necessary to evaluate its correctness. Table 6.18 reports the dissolution time and the pH level useful in comparing laboratory and modelled results to understand how the carbonate system simplifications affect the overall results.

Table 6.18: Comparison of the SL dissolution time and pH level for laboratory analysis and for each implemented scenario.

Parameter	u.m.	Test 1	Test 2	Test 3	Test 4	Test 5	Test 6
Dissolution time - 3D model	s	77.8	61.7	39.5	33.8	33.2	33.8
Dissolution time – Lab	s	72.0	61.5	46.0	39.0	40.0	20.0
Δ dissolution time	s	5.8	0.2	6.5	5.2	6.8	13.8
	%	8.1	0.3	14.1	13.3	17.0	69.0
pH max level - 3D model	-	11.80	11.57	11.15	10.95	10.91	11.25
pH max level – Lab	-	10.86	10.64	10.26	10.07	10.06	10.45
Δ pH max level	-	0.94	0.93	0.89	0.88	0.85	0.80
	%	8.66	8.74	8.67	8.74	8.45	7.66

Table 6.18 shows that the simulated dissolution times are almost the same as the laboratory experiments. Only Test 6 (with a low salinity of 10 g kg^{-1}) behaves quite differently; however, such a salinity value S is a particular condition to be found in the oceans, so it should be noted that such a numerical model is quite reliable in the case of average ocean conditions.

The fluid dynamic model aims to obtain a preliminary concentration of OH^- ions, which allow calculating the pH level (equation (2.1)). Such a concentration is approximate because the model has not yet implemented many reactions of the carbonate systems, as already explained above. The main outcome is that the model overestimates the pH level, as Table 6.18 demonstrates. However, such overestimation is less than 1 pH unit. Results show that increasing temperatures T lead to minor pH levels, while a lower salinity S induces a less acidic situation. Laboratory experiments result in different values, but they confirm such a pH trend.

6.4.4 INVESTIGATION OF THE CARBONATE SYSTEM

Even if previous chapters investigated some of the following reactions of the carbonate system, this chapter performs a more detailed analysis to better evaluate the neglected reactions that could cause the different pH final levels. A variation in OH^- concentration results in a shift of the natural equilibrium of the reactions, affecting the concentrations of the various chemicals in seawater.

Hydration of CO_2

The first reaction taking place in seawater is the CO_2 hydration, already examined in Chapter 1.4. With the intention of summarizing, it can be outlined that CO_2 hydrates producing H_2CO_3, according to the reaction (1.2), while H_2CO_3 dissociates in bicarbonates and H^+ ions, in line with reaction (1.3). It is worth noting that carbonic acid always occurs in very small concentrations compared to CO_2 (Zeebe and Wolf-Gladrow, 2003). Reaction (6.54) illustrates the overall process taking place.

$$CO_2 + H_2O \rightarrow HCO_3^- + H^+ \tag{6.54}$$

While the hydration process (6.54) is predominant at low pH, it is possible to state that a different phenomenon occurs when the pH value is higher, due to the presence of an increasing number of OH^- ions; such reaction (6.55) is termed hydroxylation process.

$$CO_2 + OH^- \rightarrow HCO_3^- \tag{6.55}$$

However, it could be stated that the chemical equilibrium between CO_2 and HCO_3^- does not depend on the happening reactions, since the molecules' energy provides the thermodynamic equilibrium. As a result, the specific chemical pathway that occurs does not affect it.

Recombination of $H^+$and OH^-

Another key reaction in a water system, is the well-known recombination of hydrons and hydroxyl groups (reaction (6.56)). Chapter 6.2 already discussed the dissociation constant of H_2O.

$$H_2O \rightarrow H^+ + OH^- \tag{6.56}$$

The equilibrium constant K_w^* of the reaction is described by formula (6.2). It is worth noting that water molecules' dissociation does not depend on the medium ionic strength because H_2O is an uncharged species.

Protolysis and hydrolysis

In the carbonate system, the acid-base reactions involving bicarbonate, carbonate, and boric acid are a key topic. Firstly, the acid-base system that involves HCO_3^- and CO_3^{2-} as acid and its conjugate base is examined. In this system, there are two reactions paths to achieve equilibrium. The first path is called protolysis (reaction (6.57)), and it states that HCO_3^- dissociates and provides an excess hydron, or alternatively CO_3^{2-} combines with H^+ forming bicarbonate in the backward reaction.

$$HCO_3^- \rightarrow H^+ + CO_3^{2-} \tag{6.57}$$

The second path is called hydrolysis (reaction (6.58)) and provides that HCO_3^- combines with OH^- forming water and CO_3^{2-}. Otherwise, the backward reaction shows that carbonates could form bicarbonates by reacting with water molecules. In typical seawater, with around an 8.2 pH value, hydrolysis is the dominant reaction (Zeebe and Wolf-Gladrow, 2003).

$$HCO_3^- + OH^- \rightarrow CO_3^{2-} + H_2O \tag{6.58}$$

Boric acid – borate equilibrium

A further acid-base equilibrium that has to be evaluated is the reaction between boric acid ($B(OH)_3$) and water (reaction (6.59)), forming borate ions ($B(OH)_4^-$) and H^+ ions. This equilibrium is remarkable because with some other minor species it contributes to the total alkalinity.

$$B(OH)_3 + OH^- \rightarrow B(OH)_4^- \tag{6.59}$$

Bicarbonate concentration has a great effect on the boron relaxation time, showing that there is a significant interaction of boron compounds with HCO_3^- and CO_3^{2-} ions.

Overall carbonate system

Zeebe and Wolf-Gladrow (2003) provide an almost complete set of differential equations (from (6.61) to (6.67)), that comprehends all time scales involved in the relaxation of the carbonate system. These time scales are various, and they range from μs to minutes. This mathematical analysis includes all the reactions described from (6.54) to (6.59). A complete fluid dynamic dissolution model should include all the following differential equations, which affect the concentration of each ion during the dissolution. The previously described model involves only reaction (6.56), aiming to provide a biological conservative value for the pH level reached.

A specific reaction rate characterizes each one of the previous reactions. The reaction rate, r_r, for a given chemical reaction is the measure of the change in concentration of the reactants or the change in concentration of the products per unit time; it increases strongly with temperature T, due to a higher mean energy of the molecules leading to higher numbers of reactions per time interval (Zeebe and Wolf-Gladrow, 2003). The term k indicates instead the rate coefficient or constant rate, and its unit and formulation depend on the order of the reaction. The following formula (6.60) shows the relationship between r_r and k in a reaction involving a single chemical species, denoted as C. In such case, the k unit of measure is s^{-1}. If two different chemical species are involved, the unit of the constant rate becomes kg mol^{-1} s^{-1}.

$$r_r = -\frac{d[C]}{dt} = k[C] \tag{6.60}$$

where:

r_r: reaction rate;
C: chemical species;
k: constant rate.

When considering reversible reactions, it is possible to evaluate two different constant rates. These rates are defined as forward and backward, and they are denoted with k_+ and k_-. Table 6.19 provides a brief description of all the constant rates involved in the carbonate system.

Table 6.19: Constant rates for the reactions of the carbonate system.

Reaction	Forward rate		Backward rate	
		u.m.		u.m.
$CO_2 + H_2O \rightleftarrows HCO_3^- + H^+$	k_{+1}	s^{-1}	k_{-1}	kg mol^{-1} s^{-1}
$CO_2 + OH^- \rightleftarrows HCO_3^-$	k_{+4}	kg mol^{-1} s^{-1}	k_{-4}	s^{-1}
$CO_3^{2-} + H^+ \rightleftarrows HCO_3^-$	$k_{+5}^{H^+}$	kg mol^{-1} s^{-1}	$k_{-5}^{H^+}$	s^{-1}
$HCO_3^- + OH^- \rightleftarrows CO_3^{2-} + H_2O$	$k_{+5}^{OH^-}$	kg mol^{-1} s^{-1}	$k_{-5}^{OH^-}$	s^{-1}
$H_2O \rightleftarrows OH^- + H^+$	k_{+6}	kg mol^{-1} s^{-1}	k_{-6}	kg mol^{-1} s^{-1}
$B(OH)_3 + OH^- \rightleftarrows B(OH)_4^-$	k_{+7}	kg mol^{-1} s^{-1}	k_{-7}	s^{-1}
$CO_3^{2-} + B(OH)_3 + H_2O \rightleftarrows HCO_3^- + B(OH)_4^-$	k_{+8}	kg mol^{-1} s^{-1}	k_{-8}	kg mol^{-1} s^{-1}

$$\frac{d[CO_2]}{dt} = (k_{-1}[H^+] + k_{-4})[HCO_3^-] - (k_{+1} + k_{+4}[OH^-])[CO_2] \quad (6.61)$$

$$\frac{d[HCO_3^-]}{dt} = -(k_{-1}[H^+] + k_{-4})[HCO_3^-] + (k_{+1} + k_{+4}[OH^-])[CO_2] - \\ -\left(k_{-5}^{H^+} + k_{+5}^{OH^-}[OH^-]\right)[HCO_3^-] + \left(k_{+5}^{H^+}[H^+] + k_{-5}^{OH^-}\right)\left[CO_3^{2-}\right] - \\ -k_{-8}[B(OH)_4^-][HCO_3^-] + k_{+8}[B(OH)_3]\left[CO_3^{2-}\right] \quad (6.62)$$

$$\frac{d\left[CO_3^{2-}\right]}{dt} = +\left(k_{-5}^{H^+} + k_{+5}^{OH^-}[OH^-]\right)[HCO_3^-] - \left(k_{+5}^{H^+}[H^+] + k_{-5}^{OH-}\right)\left[CO_3^{2-}\right] - \\ -k_{+8}[B(OH)_3]\left[CO_3^{2-}\right] + k_{-8}[B(OH)_4^-][HCO_3^-] \quad (6.63)$$

$$\frac{d[B(OH)_4^-]}{dt} = +k_{+7}[B(OH)_3][OH^-] - k_{-7}[B(OH)_4^-] + k_{+8}[B(OH)_3]\left[CO_3^{2-}\right] - \\ -k_{-8}[B(OH)_4^-][HCO_3^-] \quad (6.64)$$

$$\frac{d[B(OH)_3]}{dt} = -k_{+7}[B(OH)_3][OH^-] + k_{-7}[B(OH)_4^-] - k_{+8}[B(OH)_3]\left[CO_3^{2-}\right] + \\ +k_{-8}[B(OH)_4^-][HCO_3^-] \quad (6.65)$$

$$\frac{d[H^+]}{dt} = +k_{+1}[CO_2] - k_{-1}[H^+][HCO_3^-] + k_{-5}^{H^+}[HCO_3^-] - k_{+5}^{H+}[H^+]\left[CO_3^{2-}\right] + k_{+6} - \\ -k_{-6}[H^+][OH^-] \quad (6.66)$$

$$\frac{d[OH^-]}{dt} = k_{-4}[HCO_3^-] - k_{+4}[CO_2][OH^-] - k_{+5}^{OH^-}[HCO_3^-][OH^-] + k_{-5}^{OH^-}\left[CO_3^{2-}\right] + \\ +k_{+6} - k_{-6}[H^+][OH^-] - k_{+7}[B(OH)_3][OH^-] + k_{-7}[B(OH)_4^-] \quad (6.67)$$

Future studies aiming to obtain a more accurate model should consider all the carbonate system reactions above. In this way, they would provide better estimates, especially about the final pH value. At least, such a model should consider only reactions whose rate has not a negligible value in the time scale of interest.

6.4.5 FUTURE IMPLEMENTATIONS IN SHIP'S WAKE

Even if this study is circumscribed to the simulation of the dissolution process in a stirred beaker, the related results could be helpful in future works and research, for instance in the case of SL discharge in a ship's wake.

In particular, it is significant to underline that the obtained results are partly conservative when compared to a real situation because of different assumptions considered in this preliminary analysis. First of all, the interaction of Ca^{2+} and OH^- ions with the carbonate system has been strongly simplified, as described in Chapter 6.4.4. This is a conservative assumption, since the neglected reactions (taking place if considering the overall carbonate system) could reduce the presence of OH^- ions in seawater, and the consequent pH spike. These reactions could involve the precipitation of Ca^{2+} and OH^- ions in the form of minerals, such as calcium carbonate, magnesium carbonate or magnesium hydroxide.

Secondly, the ship's wake would provide stronger turbulence and mixing with oceans water, involving molecules dilution that would reduce average Ca^{2+} and OH^{-} ions concentrations in seawater and the consequent pH level. Anyway, future studies and physical models could demonstrate that the implementation of more complex turbulence and mixing would allow an acceleration of the dissolution time. Such a consequence could involve an increase in the local pH peak, since more OH^{-} ions could derive from SL dissolution in the same water volume. This phenomenon could balance the previously analysed effect of turbulence. Furthermore, future fluid dynamic studies could introduce gravitational forces acting on the SL particles in seawater, further reducing its concentration and the related local impact. However, the sedimentation contribution could be minimal, since dissolution occurs in such a short time that particles sink for a negligible depth.

The dissolution time of SL particles is one of the principal outcomes of the fluid dynamic study realized. With the SL concentrations in seawater considered in the study, between 0 and 0.3 mol l^{-1}, far from the saturation condition, the dissolution time is always less than 1 minute. In the real situation of the ship's wake, this time could be consistently lower because of the abovementioned mixing. Indeed, the dissolution speed strongly depends on the Ca^{2+} ions concentration in seawater; diluted concentrations allow faster reactions.

Caserini et al. (2021) consider the discharge in the ship's wake of a SL slurry with an initial concentration of 85 g L^{-1} (1.02 mol L^{-1}); after less than 10 seconds the strong turbulent mixing in the ship's wake lead to SL concentration below 0.3 mol L^{-1}, as shown in Figure 6.29.

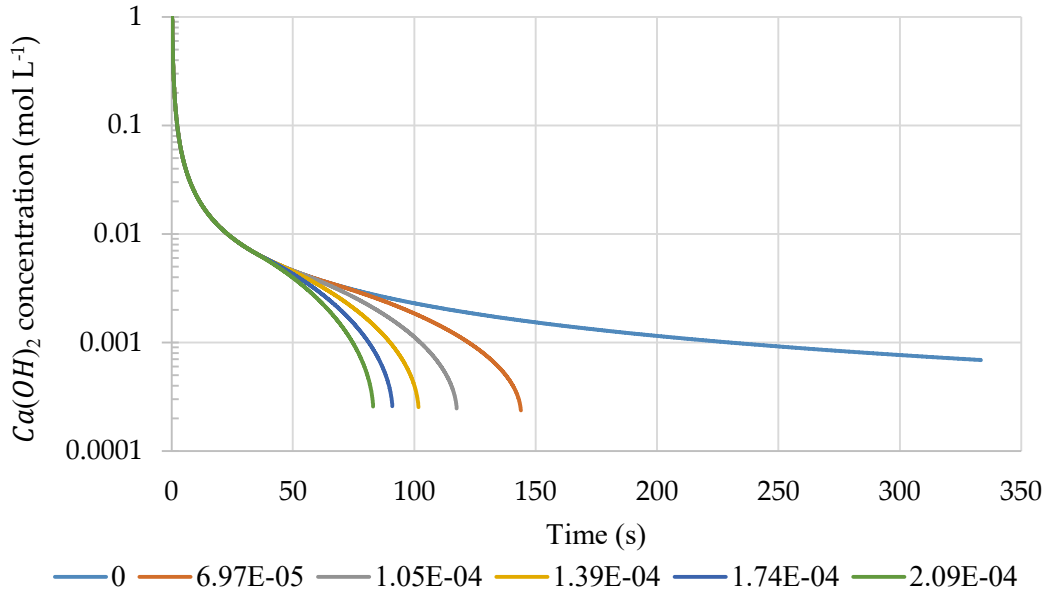

Figure 6.29: $Ca(OH)_2$ concentration for different values of the diffusion potential (reported in the legend) and a discharge rate of 10 kgSL s^{-1} (Caserini et al., 2021).

Such low dissolution time values could involve minor side effects on marine life since they imply short exposure time to SL and the related pH level, unless future studies would demonstrate that further water mixing phenomena could accelerate SL dissolution, causing significant increase in local pH.

7. CONCLUSIONS

The present thesis work has, first of all, allowed the development and the investigation of various SL discharging methodologies for OAE, widening the look towards perspectives not yet analysed, as rainbowing system or airplanes, or studying more in detail others already exiting, like ships.

This chapter provides a comparison of the different scenarios assessed in the previous chapters, with the main aim to understand which is the preferred discharge method to reduce the localized impact of OAE. The goal of the current section is to compare the investigated different aspects (carbon removal efficiency, economic feasibility, and the impact on marine life), assessing the pros and cons of each configuration.

The following sections report a comparison between the scenarios investigated in Chapters 3 to 6, except for the aircraft discharge. This latter case involves too many different scenarios, so this chapter provides detailed information about a specific one; in particular, it describes each aircraft typology but considering the case of a 20 min discharge from 1 km altitude, assuming 75% of yearly available time for the discharge.

Carbon removal efficiency

Previous chapters have described accurately formulations and processes used in calculating the carbon removal efficiency of each option. Basically, they assess the CO_2 emissions related to the spreading technique, neglecting the emissions involved in the SL production process, since they are in common among all the discharging methods. The assessment of the shedding emissions allows evaluating the net amount of CO_2 removed, subsequently compared to the amount of SL discharged.

The most efficient technologies would allow a removal similar to the theoretical maximum removal rate, described in Chapter 2.3 and equal to 0.83 kgCO_2 kgSL^{-1}. The comparison of these different values permits the calculation of the penalty of each specific configuration (equation (3.4)). Figure 7.1 graphically shows the net CO_2 removed per unit of SL and in the labels the annual net CO_2 removed per year in each implemented scenario, while Figure 7.2 illustrates the penalty of each spreading option, showing all the different contributions, and Figure 7.3 provides a focus on the ship's wake and rainbowing scenarios.

CO_2 emissions related to ships and rainbowing can be divided in different terms: navigation emissions and water pumping system emissions; the rainbowing methodology has also an additional emissive term related to the spray jet (indicated as "rainbowing discharging emissions"). On the other hand, aircraft emissions are mainly related to the different flying phases: the Landing and Take-Off cycle (LTO) under about 914 m, and the Climb/Cruise/Descent cycle (CCD) over 914 m.

The results reported in the graphs show that the emissions in the case of aircraft discharge are much more elevated than other methods because of the fuel consumption of the take-off phase. Flying emissions are ever too high if compared to other transport methodologies, even

if the flying phase takes place at high altitudes. Moreover, aircraft have a small transport capacity, discharging a few tons of SL during each fly, minimizing the quantity of CO_2 removed per unit of spread SL. In fact, the best removal rates in the aircraft scenarios could be encountered in the case of MD11 discharge, because they carry higher loads.

CO_2 emissions from a ship's wake discharge and a rainbowing system are quite similar. The major contribution is due to navigation emissions, but compared to the aircraft methodology, they are very low because the specific fuel consumption per travelled km is not so elevated.

In terms of CO_2 penalty of the discharge, the best results are in the case of spreading by existing ships, because emissions are constrained by the normal business of the ships. However, this scenario involves a lower yearly discharge, because each vessel could transport only a small SL quantity. It is worth noting that each transport typology by ships could allow a wider SL discharge since the vessel's capacity is tens of thousands of ton. This significantly affects the total discharge and so the removed CO_2 per trip and per unit of SL mass.

Although the net specific CO_2 removal rate for the scenario with the discharge in ship's wake and rainbowing is similar (about 0.8 tCO_2 tSL^{-1}), the total CO_2 annual removal is substantially higher for the scenario with existing ships and multiple stops (3.3 GtCO_2 yr^{-1}). Differently, the net specific CO_2 removal rate is very dissimilar in each aircraft discharging scenarios, varying from 0.45 to 0.59 tCO_2 tSL^{-1}.

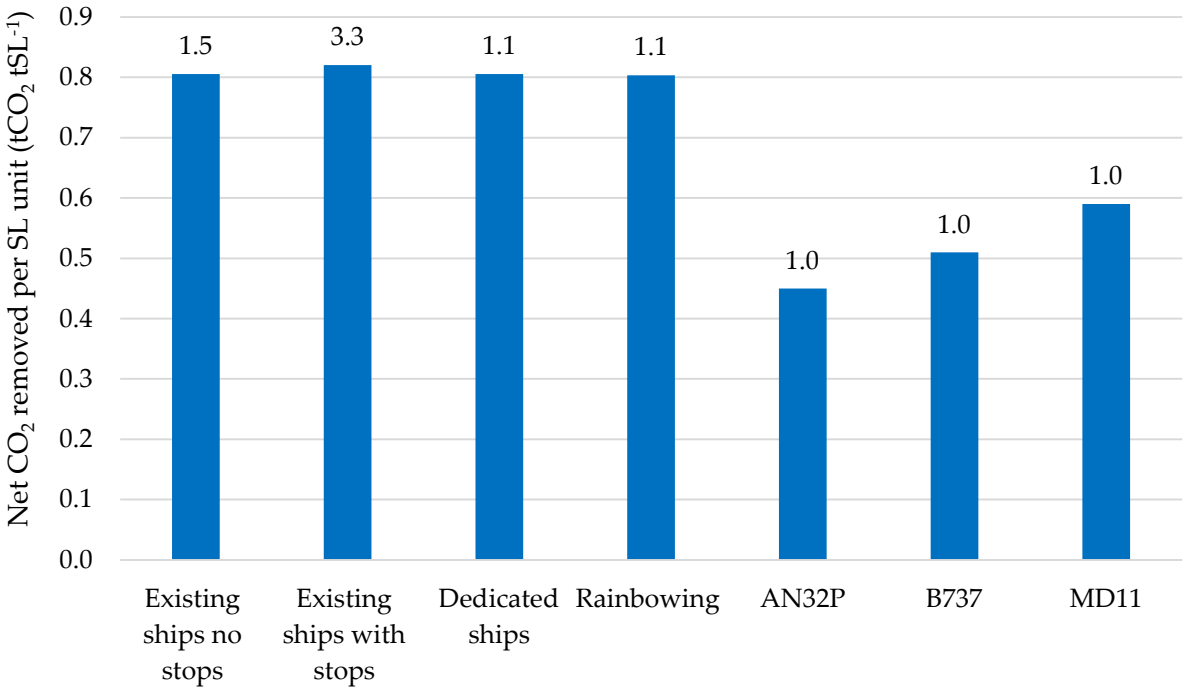

Figure 7.1: Net CO_2 removed per unit of SL discharged for all the implemented discharging configurations. The annual total net CO_2 removed is indicated at the top of the bars in terms of GtCO_2 yr^{-1}.

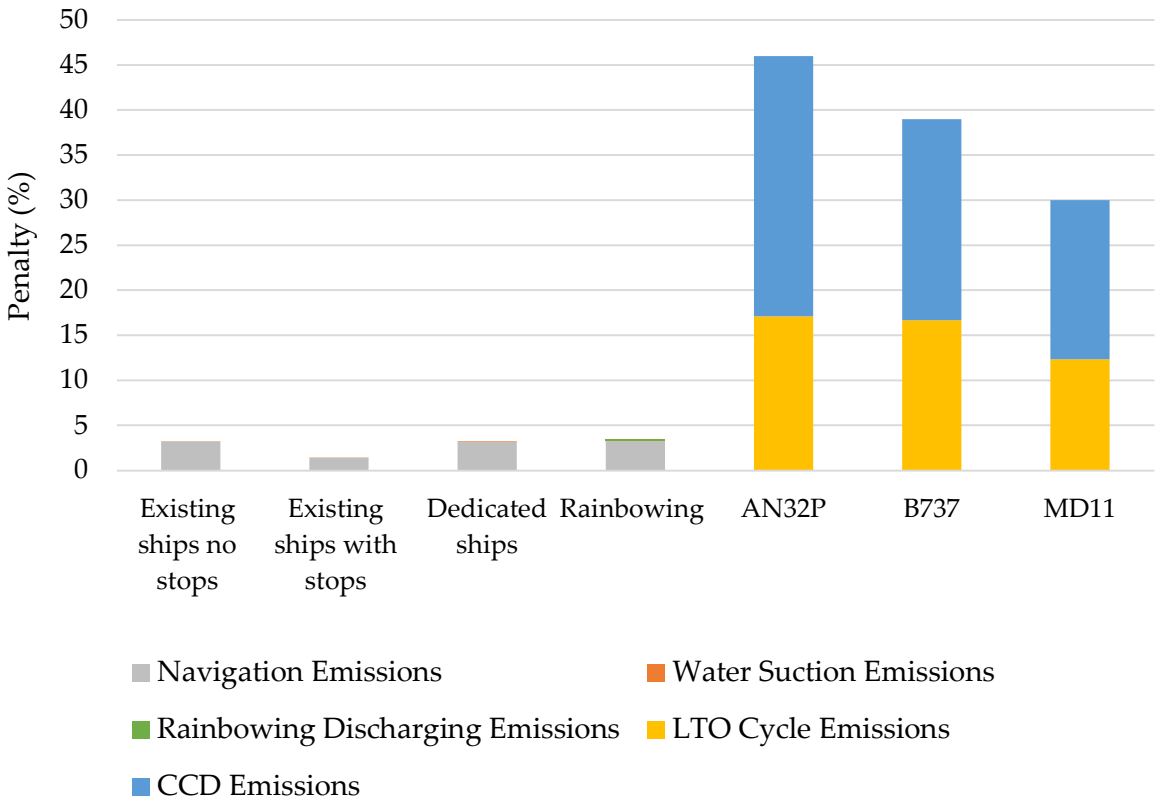

Figure 7.2: Penalty, in term of percentage, for all the implemented discharging configurations.

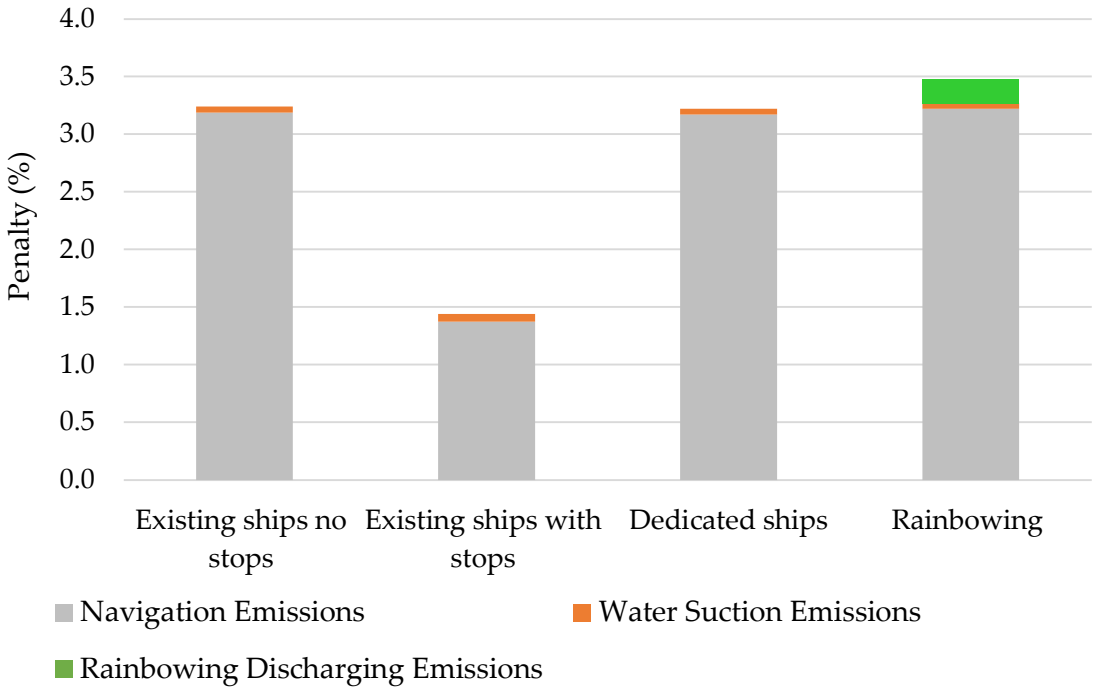

Figure 7.3: Focus on the penalty for the ship's wake configuration and rainbowing system.

Cost analysis

The economic evaluations in Chapters 3 to 6 comprise two main analyses, one which refers to the operative expenditure (Opex) and one referred to the capital expenditure (Capex). Different economic aspects, related to Capex or Opex, affect the costs of each configuration scenario. Figure 7.4 graphically shows the total costs, divided into Capex and Opex, per unit of removed CO_2. Figure 7.5 focuses on the rainbowing and ship's wake scenarios, and the labels reports the annual cost for trip. It also shows how the Opex costs are split in each component, already investigated in detail in dedicated chapters. Additionally, Table 7.1 reports the percentage contribution of Opex and Capex in each scenario.

It should be noted that the main issue in determining the Opex cost is usually the fuel usage, which strongly affects even the specific emissions. Furthermore, the Capex assessment considers average lifespans from all the discharging tools and transporting vehicles, but such values could vary according to the typology of the equipment used.

Table 7.1: Percentage contribution of Opex and Capex in each implemented scenario.

Scenario	Opex percentage	Capex percentage
	%	%
Existing ships no stop	47	53
Existing ships with stops	67	33
Dedicated ships	70	30
Rainbowing	72	28
AN32P	94	6
B737	87	13
MD11	95	5

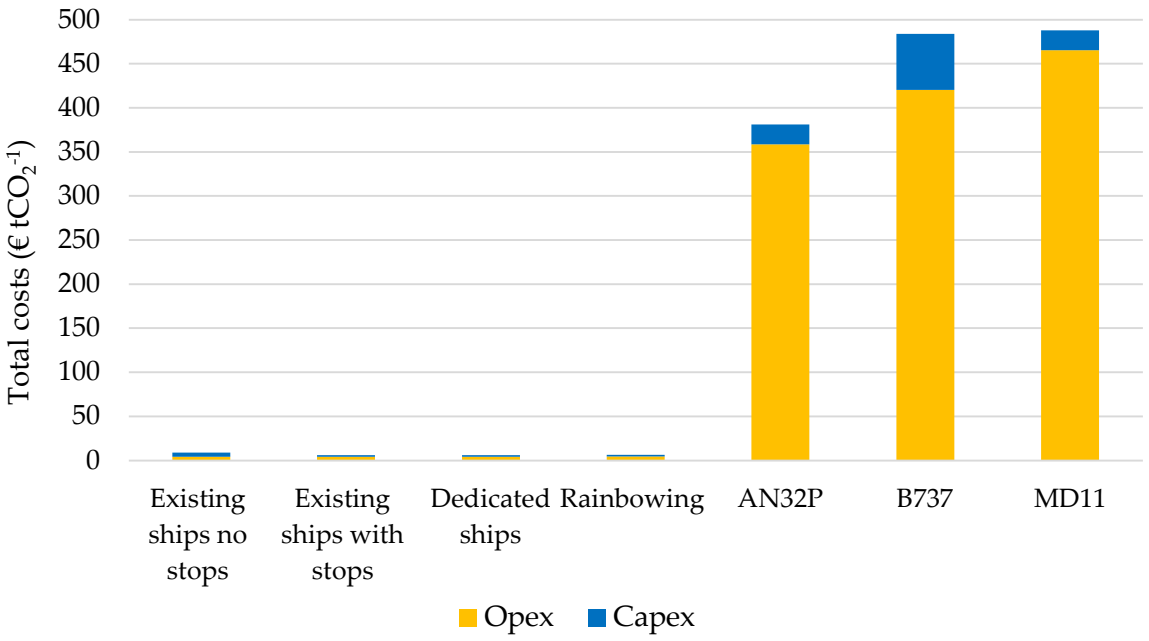

Figure 7.4: Total costs per unit of CO_2 removed for all the implemented discharging configurations.

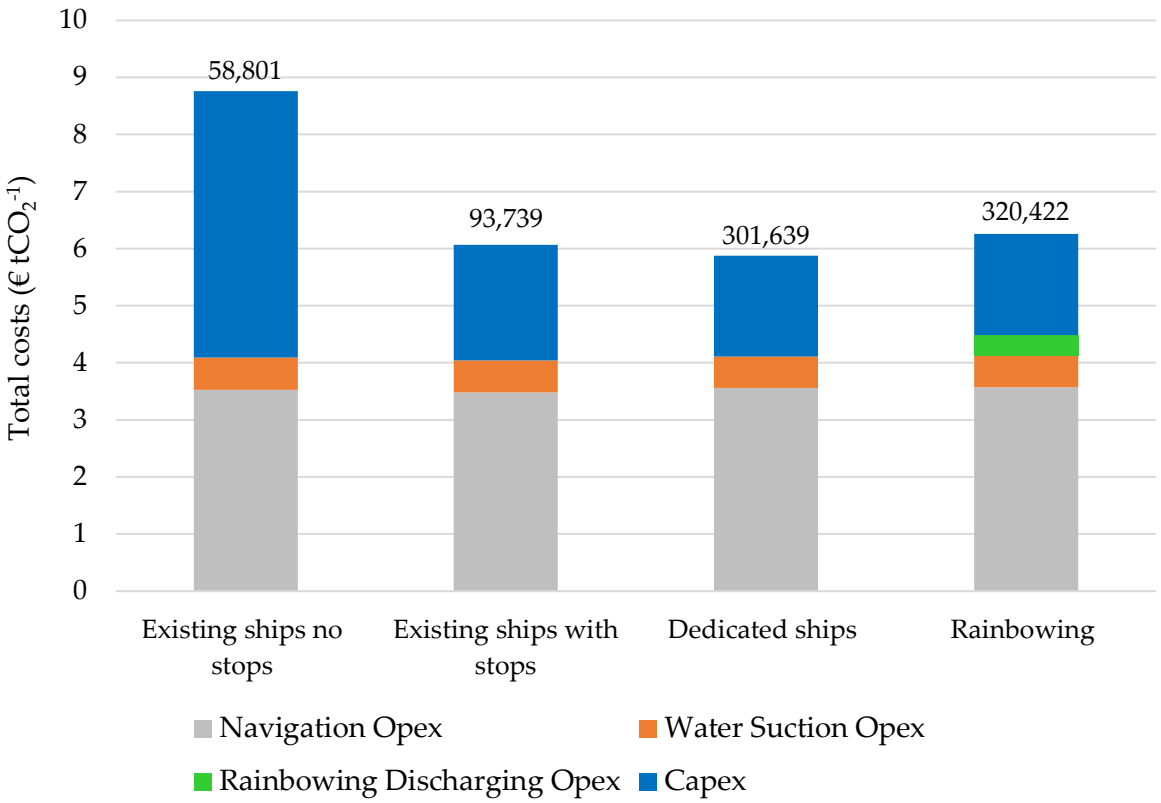

Figure 7.5: Focus on the total cost for the ship's wake configuration and rainbowing system. The total cost per trip is indicated at the top of the bars in terms of € yr⁻¹.

Figure 7.4 also displays a strong difference in specific costs per unit of CO_2 removed. In particular, aircraft methodologies costs are too elevated if compared to the other configurations, ranging between 381 and 488 € tonCO_2^{-1} in the specific scenario. The elevated fuel usage is the cause of such an economic issue, which also affects the emissions previously analysed.

On the other hand, the fuel consumption during vessels navigation is significantly lower, thus implying lower Opex costs. Even the fuel usage during the pumping processes does not affect such a consideration. As a result, Capex is a crucial component of the ship's wake and rainbowing discharge, contrary to the aircraft scenarios. In particular, Capex is a predominant element especially in existing ships, because in dedicated ships it is strongly amortised by the wider SL load, contrary to the Opex which is an almost linear function of the transported SL. The total costs vary between 6.0 and 8.7 € tonCO_2^{-1}.

Moreover, the huge quantity of transported SL by vessels widens the gap with airplanes spreading costs. Also, the specific costs result higher in the case of existing ships rather than dedicated, despite the neglection of the ship's price in the existing ships scenario, whose Capex considers only the contribution of conditioning infrastructures (Chapter 3.3.2). This is due to the less transported SL, reversing the specific cost, even if the total cost per trip remains higher in the case of dedicated vessels.

Impacts on marine life

The comparison between the biological impact, due to SL ecotoxicity, of each shedding methodology is a complex issue. Many conservative assumptions allow a preliminary evaluation of this topic, especially in the case of aircraft and rainbowing discharge systems. It is possible to obtain approximate SL concentration values by considering a specific dissolution time in seawater, thus defining the water volume involved by the discharge and calculating the SL load per unit area.

In the case of rainbowing system spreading, an important parameter is the depth reached by the spray jet. In this way, this calculated preliminary SL concentration provides the first consideration about a possible toxicity level, obtained under the assumption of homogenous dilution in the water volume involved.

A more complex evaluation is that one of the ship's wakes spreading. It is not easy to evaluate the water volume involved in such a discharge since it is highly affected by the propeller rotation and vessel's speed. From this point of view, this thesis work provides a dissolution and fluid dynamic model, which could be useful in future studies to implement the dissolution phenomenon in the fluid dynamic environment of the ship's wake.

Table 7.2 reports maximum preliminary SL load per unit area and concentration in seawater after the discharge, in the case of rainbowing system and aircraft discharge. Ships' scenarios are neglected in the table below since no model aiming to obtain SL concentration in the ship's wake is currently available.

Table 7.2: SL concentration and load per unit area in seawater for aircraft and rainbowing discharging configurations.

Scenario	**Maximum SL concentration in seawater**	**Maximum SL load per unit area**
	mgSL L^{-1}	mgSL m^{-2}
Rainbowing	29.13	$7.30\ 10^{5}$
AN32P	$10\ 10^{-5}$	0.08
B737	$19\ 10^{-5}$	0.15
MD11	$62\ 10^{-5}$	0.50

Knowing the maximum SL concentrations in seawater, it is possible to assess the maximum pH level reached, thanks to equations (2.1) and (6.2), neglecting side reactions in the oceanic carbonate system and further dilutions thanks to ocean currents. These calculated values overestimate the real ones, also in terms of maximum SL concentration.

Figure 7.6 graphically shows the maximum pH level reached in seawater after SL discharge, for the scenarios previously described in Table 7.1. It is worth noting that an initial ocean average pH level of 8.05 has been assumed in this assessment. Additionally, pH maximum level in ship's wake scenarios derives from Caserini et al. (2021) study since the current work does not provide any model for its evaluation; in particular, two scenarios are reported with different SL discharge rate (10 and 100 kgSL s^{-1}).

The SL discharging rates in all the scenarios represented in Figure 7.6 have the same order of magnitude: 10 or 100 kgSL s^{-1} for ship's wake, 50 kgSL s^{-1} for the rainbowing system, and between 10 and 70 kgSL s^{-1} for the aircraft discharge.

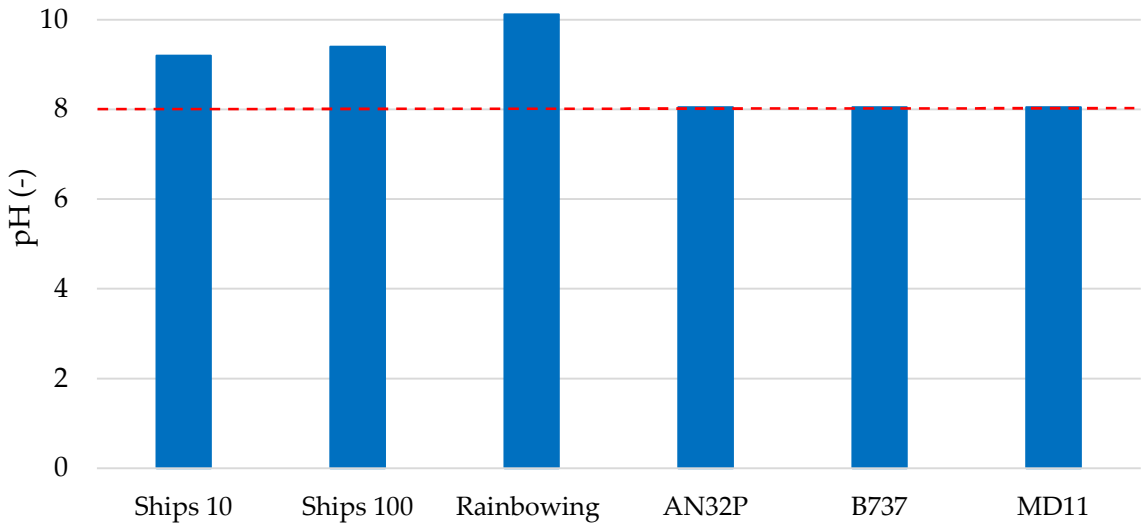

Figure 7.6: Maximum pH level reached after SL discharge for ships (the numbers 10 and 100 represent the discharge rate in terms of kg s^{-1}), rainbowing system and aircraft. The red dashed line represents the initial ocean average pH level of 8.05.

Results in Table 7.2 and in Figure 7.6 clearly show the advantage of an aircraft discharge about the biological impact. Since winds transport the SL powder for huge distances, such particles impact the water surface in very low loads. As a result, the preliminarily evaluated concentration and pH levels demonstrate a minimum and almost negligible increase from the initial seawater pH, far from the toxicity levels.

The rainbowing discharge system provides higher SL loads per unit area and concentration compared to aircraft scenarios, because of the elevated slurry discharge rate of rainbowing systems. The load per unit area is quite elevated, such as the preliminary concentration in seawater, despite the wide volume involved. However, these calculations are strongly conservative, so the possible reached levels could be lower.

Caserini et al. (2021) assessed SL concentrations and the related pH levels in the case of the ship's wake discharging method considering a preliminary fluid dynamic contribution given by a turbulent system. In this regard, it is worth noting that results in Figure 7.6 demonstrate that the current rainbowing and aircraft modelling are conservative; this can be seen if comparing rainbowing and ship's wake scenarios: a rainbowing discharge rate of 50 kgSL s^{-1} induce a pH level of 10, while in the Caserini et al. (2021) ship's wake scenario with a double discharge rate (100 kgSL s^{-1}) the pH level reached is significantly lower (9.4) because of turbulence effects.

Chapter 6 illustrates the maximum theoretical pH level reached in the case of a 0.2 gSL L^{-1} concentration in seawater during the ship's wake spreading. However, these evaluations do not consider side reactions and the strong water exchange occurring in a ship's wake,

overrating the pH level, which varies between 10.9 and 11.8. Anyway, the fluid dynamic model provided could be implemented in future studies considering more complex situations.

The impact of SL discharge on the sea surface micro layer (SML) necessitates a distinctive analysis. It is worth noting that neither literature data are available about the biological and mechanical impacts on SML, for short time exposures (both in terms of SL concentration and pH level). Further studies are necessary for evaluating such information. The aircraft discharge impact on SML could be negligible because the SL load per unit area is very low, between 0.08 and 0.50 mgSL m^{-2} (Table 5.4). Different is the case of the rainbowing system, where the SL load per unit of sea surface is significantly higher, with a maximum value of 0.73 kgSL m^{-2} (Table 4.2). Instead, the ship's wake spreading does not involve the SML since it occurs below the sea surface.

Overall conclusions

Comparing the efficiency of the different SL discharge methods to remove carbon from the atmosphere through OAE, ship's wake and rainbowing discharging systems are more convenient because the emissions related to the ships' navigation are very low. On the other hand, the environmental impacts due to discharging should be investigated since no literature data provide information about toxicity on short time exposures.

Anyway, the aircraft discharge allows in any case lower biological implications in seawater, thanks to the winds' dispersion, but this could lead to impact of SL particle dispersed over a long range. In this specific case, the impact on the ocean ecosystem could be very low in terms of SL toxic concentration, but further studies have to be made to understand SML effects in shorter exposure, including average alkalinity concentration, concentration in the immediate vicinity of the particles, and also with the mechanical action of the surface impact. However, it is worth noting that the ship's wake discharge is the only method that avoids chemical contact with the SML, whose sensibility should be better investigated in future research works.

The assessments demonstrate that a higher potential discharge of SL in the oceans could be achieved by using ships rather than aircraft. In addition, the costs and CO_2 penalties of the aircraft discharge are so high as to make it impracticable.

The best course of action could be to carefully couple the rainbowing and the ship's wake discharge. In this way, each discharging vessel could spread huge quantities of slake lime by subdividing them into different outlets. As a consequence, the localised biological impacts could be strongly lowered, without reducing the overall efficiency. Each propeller at the ship's stern could be combined with a dedicated SL slurry outlet. It should be necessary to properly investigate such a sequence of outlets with an adequate fluid dynamic model, aiming to avoid possible overlapping between different seawater impacted areas. Also, careful studies should examine the suitable slurry concentration to minimize the biological impact. In the same way, rainbowing spray jets on the sides' ship should have appropriate nozzles to reduce the mechanical impact on seawater by increasing the imprint area and reducing the slurry flux

and SL concentration. For instance, two rainbowing systems per side could be installed while inducing a negligible overlapping.

For instance, a ship's wake dispersion could be improved using vessels with more than one propeller: SL could be spread near each of them maximizing the number of outlets. Additionally, different rainbowing discharging systems could be installed on the same vessel. In this case, more than one outlet could be placed on the same vessel's side, always avoiding overlapping between the imprinting areas. However, it is worth noting that some droplets could fall during the rainbowing spray trajectory causing overlapping between the various discharging system; the effect's entity and implications should be better investigated in future studies. In this way, different discharging outlets could divide the overall mass flow rate, minimizing the SL concentration in seawater but without compromising the total carbon removal rate.

For instance, considering the dimensions of a Panamax vessel, as described in Chapter 4.7, a new configuration is reported in Figure 7.7. It consists of eight rainbowing systems at the vessel's sides but with two discharges in the ship's wake instead of two rainbowing systems. This configuration covers a wider area rather than merely discharging in ship's wake, allowing the discharge of a larger SL quantity.

More careful studies should be carried out about the geometrical structure of the ship's wake, which could allow calculating if such a configuration could cause overlapping of the two stern's discharges.

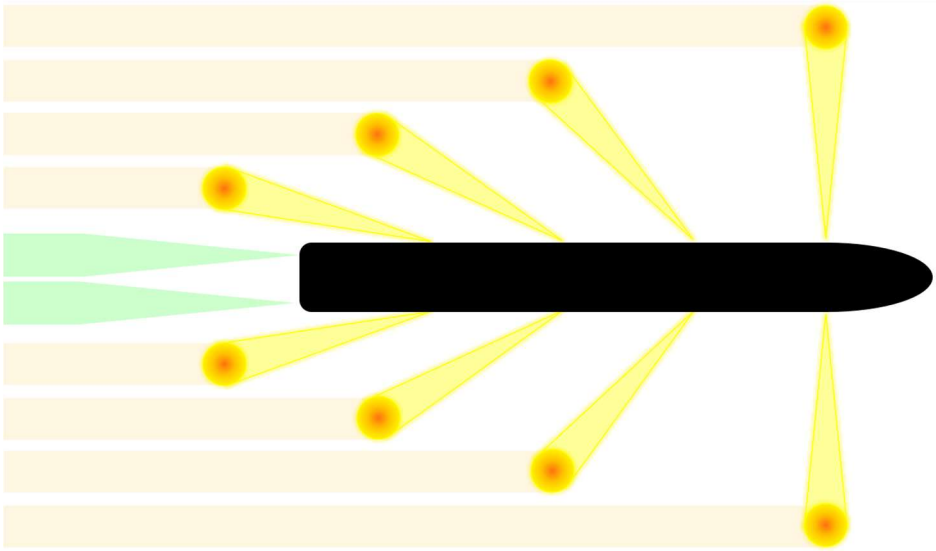

Figure 7.7: Diagram of a multiple discharging rainbowing placed on vessel's side and multiple discharging systems in ship's wake (Panamax vessel in scale).

The application of many modifications to the configuration illustrated in Figure 7.7 could allow the optimization of the system's efficiency. For instance, more powerful rainbowing pumps could permit to discharge SL in longer trajectories, incrementing the number of rainbowing outlets and so the carbon dioxide removed. Furthermore, the usage of larger vessels could allow the installation of more propellers, increasing the SL quantity discharged in the ship's wake.

REFERENCES

Abbà, A., Cimarelli, A., and Germano, M. (2022). Dynamic tensorial eddy viscosity model: Effects of compressibility and of complex geometry. *Physics of Fluids.* 34(2). https://doi.org/10.1063/5.0076341

Airforce Technology (2019). Antonov An-32 Light Multipurpose Transport Aircraft. Available online at: https://www.airforce-technology.com/projects/an32-transport/

Ajayi, T., Gomes, J. S., and Bera, A. (2019). A review of CO_2 storage in geological formations emphasizing modelling, monitoring and capacity estimation approaches. *Petroleum Science*. 16, 1028-1063. https://doi.org/10.1007/s12182-019-0340-8

Alessandrini, A., Guizzardi, D., Janssens-Maenhout, G., Pisoni, E., Trombetti, M., and Vespe, M. (2017). Estimation of shipping emissions using vessel Long Range Identification and Tracking data. *Journal of Maps.* 13(2), 946-954. https://doi.org/10.1080/17445647.2017.1411842

Alterskjær, and K. and Kristjánsson, J. E. (2013). The sign of the radiative forcing from marine cloud brightening depends on both particle size and injection amount. *Geophysical Research Letters.* 40(1), 210-215. https://doi.org/10.1029/2012GL054286

Antonov (2021). Antonov Specifications. Available online at: https://antonov.com/en

Appelo, C. A. J., and Postma, D. (2005). Geochemistry, Groundwater and Pollution. 2nd rev. ed. Amsterdam, NL: *A.A. Balkema Publishers.*

Arpav (2013). Risposta al 3° quesito della Procura di Venezia N. 1257 08 R.G.n.r./Mod. 45. Available online at: https://www.arpa.veneto.it/temi-ambientali/aria/file-e-allegati/porti-aria/Emissioni%20vs%20tonnellaggio.pdf

Atkins, P. W., and de Paula, J. (2006). Atkins' Physical Chemistry. 8th rev. ed. New York, US: *Oxford University Press.*

Baker, A., Kanakidou, M., Nenes, A., Myriokefalitakis, S., Croot, P. L., Duce, R. A., Gao, Y., Guieu, C., Ito, A., Jickells, T. D., Mahowald, N. M., Middag, R., Perron, M. M. G., Sairn, M. M., Shelley, R., and Turner, D. R. (2021). Changing atmospheric acidity as a modulator of nutrient deposition and ocean biogeochemistry. *Science Advances*. 7(28), eabd8800. https://www.science.org/doi/10.1126/sciadv.abd8800

Becker, S. (2017). Experimental study of paraglider aerodynamics. *Imperial College London*. Available online at: https://www.researchgate.net/publication/319702478_Experimental_Study_of_Paraglider_Aerodynamics; https://doi.org/10.13140/RG.2.2.33674.16321

Bednaršek, N., Tarling, G. A., Bakker, D. C. E., Fielding, S., Jones, E. M., Venables, H. J., Ward, P., Kuzirian, A., Lézé, B., Feely, R. A., and Murphy, E. J. (2012). Extensive dissolution of live pteropods in the Southern Ocean. *Nature Geoscience.* 5, 881.885. https://doi.org/10.1038/ngeo1635

Bengtsson, S., Andersson, K., and Fridell, E. (2011). A comparative life cycle assessment of marine fuels: liquefied natural gas and three other fossil fuels. *Journal of Engineering for the Maritime Environment.* 225(2), 97-110. https://doi.org/10.1177/1475090211402136

Bernard, L., Freche, M., Lacout, J. L., and Biscans, B. (2000). Modelling of the dissolution of calcium hydroxide in the preparation of hydroxyapatite by neutralization. 55(23), 5683-5692. https://doi.org/10.1016/S0009-2509(00)00205-0

Bianchi, R., and Abbate, S. (2022). Large eddy simulation of the flow in a stirred tank reactor for calcium hydroxide dissolution. Master of Science, A.Y. 2020-2021. *Politecnico di Milano: Dipartimento di Scienze e Tecnologie Aerospaziali*.

Blunt, M. (2010). Grantham Institute for Climate Change: Briefing paper No 4. Carbon dioxide storage. *Imperial College London*. Available online at: https://www.imperial.ac.uk/media/imperial-

college/grantham-institute/public/publications/briefing-papers/Carbon-dioxide-storage----Grantham-BP-4.pdf

Boccia, L., Pace, P., Amendola, G., and Di Massa, G. (2007). Low multipath antennas for GNSS-based attitude determination systems applied to high-altitude platforms. *Springer-Verlag*. 12(3), 163-171. https://doi.org/10.1007/s10291-007-0075-7

Boeing (2018). About Boeing Commercial Airplanes. Available online at: http://www.boeing.com/

Boon-Long, S., Laguerie, C., and Couderc, J. P. (1978). Mass transfer from suspended solids to a liquid in agitated vessels. *Chemical Engineering Science*. 33, 813-819. https://doi.org/10.1016/0009-2509(78)85170-7

Booth, G. M., Hamilton, J. G., and Molot, L. A. (1985). Liming in Ontario: Short-term biological and chemical changes. *Water, Air, and Soil Pollution.* 31, 709-720. https://doi.org/10.1007/BF00284221

Boskalis (2012). Capability Sheet. Trailing Suction Hopper Dredger (TSHD): a Sea-Going Self-Propelled Free Floating Vessel That Loads Dredged Material into its Hopper Well. Available online at: https://australia.boskalis.com/uploads/media/Trailing_Suction_Hopper_Dredger_-_Capability_sheet_02.pdf

Boutacoff, D. (1990). Working with the watershed. *EPRI Journal.* 15(1), 29-33. Website available online at: https://eprijournal.com/

Bureau of Transportation Statistics (2019). Average Age of Aircraft 2019. Available online at: https://www.bts.gov/average-age-aircraft-2019

Burt, D. J., Fröb, F., and Ilyina, T. (2021). The sensitivity of the marine carbonate system to regional ocean alkalinity enhancement. *Frontiers in climate.* https://doi.org/10.3389/fclim.2021.624075

Butenschön, M., Lovato, T., Grosso, M., Masina, S., and Caserini, S. (2020). Alkalinisation scenarios in the Mediterranean Sea for efficient removal of atmospheric CO_2 and the mitigation of ocean acidification. *Frontiers in Climate*. https://doi.org/10.3389/fclim.2021.614537

Calderoni, A., De Bernardi, R., and Mosello, R. (1994). Recovery of Lago d'Orta by liming. *Verhandlungen des Internationalen Verein Limnologie*. 25, 2016-2020. https://doi.org/10.1080/03680770.1992.11900550

Calderoni, A., and Tartari, G. A. (2000). Evolution of the water chemistry of Lake Orta after liming. *Journal of Limnology.* 60(1), 68-78. https://doi.org/10.4081/jlimnol.2001.69

Cal Fire (2019). California department of forestry and fire protection. Firefighting aircraft recognition guide. Available online at: https://www.fire.ca.gov/media/4950/aviation-guide-2019-access.pdf

Caserini, S., Barreto, B., Lanfredi, C., Cappello, G., Ross Morrey, D., and Grosso, M. (2019). Affordable CO_2 negative emission through hydrogen from biomass, ocean liming, and CO_2 storage. *Mitigation and Adaptation Strategies for Global Change*. 24(7), 1231-1248. https://doi.org/10.1007/s11027-018-9835-7

Caserini, S., Pagano, D., Campo, F., Abbà, A., De Marco, S., Righi, S., Renforth, P., and Grosso, M. (2021). Potential of Maritime Transport for Ocean Liming and Atmospheric CO_2 removal. *Frontiers in Climate*. 3. https://doi.org/10.3389/fclim.2021.575900

Castaño, S. V., La Plante, E. C., Shimoda, S., Wang, B., Neithalath, N., Sant, G., and Pilon, L. (2021). Calcination-free production of calcium hydroxide at sub-boiling temperatures. *RSC Advances*. 11(3), 1762-1772. https://doi.org/10.1039/D0RA08449B

CDIAC (2016). Carbon Dioxide Information Analysis Center. Recent Greenhous Gas Concentrations. Available online at: https://cdiac.ess-dive.lbl.gov/pns/current_ghg.html

Çengel, Y. (1998). Heat Transfer: A Practical Approach. 1st rev. ed. New York, US: *McGraw-Hill series in mechanical engineering*.

Citrini, D., and Noseda, G. (1987). Idraulica. 2nd ed. rev. Milano, IT: *Casa Editrice Ambrosiana.*

Clayton, G., and Clayton, F. (1981). Patty's industrial hygiene and toxicology. 3rd rev. ed. New York, US: *John Wiley & Sons*.

Cleveland, C. J. (2004). Encyclopedia of Energy. *Elsevier Science*. Available online at: https://www.sciencedirect.com/referencework/9780121764807/encyclopedia-of-energy#book-description

Climate Action Tracker (2021). Countries: overview. Available online at: https://climateactiontracker.org/countries/

Cockell, C. S., Izawa, M. R. M., Banerjee, N. R., Osinski, G. R., Flemming,R. L., and Parnell, J. (2011). Weathering of Post-Impact Hydrothermal Deposits from the Haughton Impact Structure: Implications for Microbial Colonization and Biosignature Preservation. *Astrobiology*. 11(6). https://doi.org/10.1089/ast.2011.0612

Colombo, M., and Crisanto, F. (2021). Laboratory study of $Ca(OH)_2$ dissolution dynamics in artificial seawater. Master of Science, A.Y. 2020-2021. *Politecnico di Milano: Dipartimento di Ingegneria Civile e Ambientale*.

Cooke, S. L., and Kim, S. C. (2018). Exploring the "Evil Twin of Global Warming": Public Understanding of Ocean Acidification in the United States. *Science Communication.* 41(1), 66-89. https://doi.org/10.1177/1075547018821434

Cooper, T., Reagan, I., Porter, C., and Franzoni, C. (2021). Global Fleet and MRO Market Forecast 2021-2031. *Oliver Wyman.* Available online at: https://www.oliverwyman.com/content/dam/oliver-wyman/v2/media/2021/feb/Global_FLeet_and_MRO_Market_Forecast_2021-2031_OW.pdf

Costa, P., and Lobo, J. M. S. (2000). Modeling and comparison of dissolution profiles. *European Journal of Pharmaceutical Sciences.* 13(2), 123-133. https://doi.org/10.1016/S0928-0987(01)00095-1

Costello, M. J., and Chaudhary, C. (2017). Marine biodiversity, biogeography, deep-sea gradients, and conservation. *Current biology*. 27(11), 511-527. https://doi.org/10.1016/j.cub.2017.04.060

Crippa, M., Solazzo, E., Huang, G., Guizzardi, D., Koffi, E., Muntean, M., Schieberle, C., Friedrich, R. and Janssens-Maenhout, G. (2020). High resolution temporal profiles in the Emissions Database for Global Atmospheric Research. *Scientific Data.* 7(121). https://doi.org/10.1038/s41597-020-0462-2

Cripps, G., Widdicombe, S., Spicer, J. I., and Findlay, H. S. (2013). Biological impacts of enhanced alkalinity in Carcinus maenas. *Marine Pollution Bulletin*. 71, 190-198. https://doi.org/10.1016/j.marpolbul.2013.03.015

Csanady, G. T. (1986). Mass transfer to and from small particles in the sea. *Limnology and Oceanography.* 31(2), 237-248. https://doi.org/10.4319/lo.1986.31.2.0237

Cunliffe, M., Engel, A., Frka, S., Gasparovic, B., Guitart, C., Murrell, J. C., Salter, M., Stolle, C., Upstill-Goddard, R., and Wurl, O. (2013). Sea surface microlayer: A unified physicochemical and biological perspective of the air-ocean interface. *ScienceDirect*. 109, 104-116. https://doi.org/10.1016/j.pocean.2012.08.004.

Debye, P., and Hückel, E. (1923). The theory of electrolytes. I. Freezing point depression and related phenomena [Zur Theorie der Elektrolyte. I. Gefrierpunktserniedrigung
und verwandte Erscheinungen]. *Physikalische Zeitschrift*. 24, 185-206. Translated and typeset by Braus, M. J. (2020). Available online at: https://minds.wisconsin.edu/handle/1793/79225

Deutsche Flugsicherung DFS (2014). Pilot Info 03/2014: Climb and descent rates. Available online at: https://www.dfs.de/dfs_homepage/en/

Diamond, L. W., and Akinfiev, N. N. (2003). Solubility of CO_2 in water from – 1.5 to 100°C and from 0.1 to 100 MPa: evaluation of literature data and thermodynamic modelling. *Fluid Phase Equilibria.* 208(1-2), 265-290. https://doi.org/10.1016/S0378-3812(03)00041-4

Dickson, A. G. (1981). An exact definition of total alkalinity and a procedure for the estimation of alkalinity and total inorganic carbon from titration data. *Deep Sea Research Part A. Oceanographic Research Papers.* 28(6), 609-623. https://doi.org/10.1016/0198-0149(81)90121-7

Dickson, A. G., and Goyet, C. (1994). Handbook of Methods for the Analysis of the Various Parameters of the Carbon Dioxide System in Sea Water: Version 2. *U.S. Department of Energy.* https://doi.org/10.2172/10107773

Dickson, A. G., and Millero, F. J. (1987). A comparison of the equilibrium constants for the dissociation of carbonic acid in seawater media. *Deep Sea Research Part A. Oceanographic Research Papers.* 34(10), 1733-1743. https://doi.org/10.1016/0198-0149(87)90021-5

Diffenbaugh, N. S., and Field, C. B. (2013). Changes in Ecologically Critical Terrestrial Climate Conditions. *Science*. 341, 486-92. https://doi.org/10.1126/science.1237123

Dowling, A., O'Dwyer, J., and Adley, C. C. (2014). Lime in the limelight. *Journal of Cleaner Production*. 92, 13-22. https://doi.org/10.1016/j.jclepro.2014.12.047

Down, R. D., and Lehr, J. H. (2004). Environmental Instrumentation and Analysis Handbook. *John Wiley & Sons*. https://doi.org/10.1002/0471473332

Dragflow (2021). Big Hydraulic Pumps. Available online at: https://dragflow.it/en/products/pumps/hydraulic-pumps/big-hydraulic-pumps/

Drever, J. I. (1982). The Geochemistry of Natural Waters. 1st rev. ed. Englewood Cliffs, US: *Longman Higher Education.*

Earle, S. (2019). Physical Geology. 2nd rev. ed. Vancouver, CA: *BCcampus Open Education.*

EASAC (2018). European Academies' Science Advisory Council. Negative emission technologies: What role in meeting Paris Agreement targets? European Academies' Science Advisory Council policy report 35. Available online at: https://easac.eu/fileadmin/PDF_s/reports_statements/Negative_Carbon/EASAC_Report_on_Negative_Emission_Technologies.pdf

ECHA (2021). European Chemicals Agency. Calcium carbonate: Aquatic toxicity. Available online at: https://echa.europa.eu/it/registration-dossier/-/registered-dossier/16050/6/2/1

ECOLEX (1972). Convention on the Prevention of Marine Pollution by Dumping of Wastes and Other Matter. Available online at: https://www.ecolex.org/details/treaty/convention-on-the-prevention-of-marine-pollution-by-dumping-of-wastes-and-other-matter-tre-000420/?q=london+protocol+1996&xdate_min=&xdate_max=

ECOLEX (1996). 1996 Protocol to the Convention on the Prevention of Marine Pollution by Dumping of Wastes and Other Matter. Available online at: https://www.ecolex.org/details/treaty/1996-protocol-to-the-convention-on-the-prevention-of-marine-pollution-by-dumping-of-wastes-and-other-matter-1972-tre-001268/?q=london+protocol+1996&xdate_min=&xdate_max=

EDGAR (2018). Global Greenhouse Gas Emission. Available online at: https://edgar.jrc.ec.europa.eu/dataset_ghg60

Edward, J. T. (1970). Molecular volumes and the Stokes-Einstein equation. 47(4), 261-270. *Journal of Chemical Education.* https://doi.org/10.1021/ed047p261

El-Mansy, A. (2020). Evaluation of the Effect of Quicklime on Some Organisms from Different Ecosystems in Egypt: Morphological Perspective. *World Environment*. 10(1), 10-15. https://doi.org/10.5923/j.env.20201001.02

EMEP/EEA (2019). Air pollutant emission inventory guidebook. Available online at: https://www.eea.europa.eu/publications/emep-eea-guidebook-2019

Engel, A., Bange, H. W., Cunliffe, M., Burrows, S. M., Friedrichs, G., Galgani, L., Herrmann, H., Hertkorn, N., Johnson, M., Liss, P. S., Quinn, P. K., Schartau, M., Soloviev, A., Stolle, C., Upstill-Goddars, R. C., Van Pinxtern, M., and Zancker, B. (2017). The ocean's vital skin: toward an integrated understanding of the Sea Surface Microlayer. *Frontiers in Marine Science*. 4, 165. https://doi.org/10.3389/fmars.2017.00165

EPA (2021). U.S. Environmental Protection Agency. Greenhouse Gas Emissions: Overview of Greenhouse Gases. Available online at: https://www.epa.gov/ghgemissions/overview-greenhouse-gases

EUROCONTROL (2016). Method for estimating aviation fuel burns and emissions. Available online at: https://www.eurocontrol.int/publication/eurocontrol-method-estimating-aviation-fuel-burnt-and-emissions

European Commission (2021). Launch by United States, the European Union, and Partners of the Global Methane Pledge to Keep 1.5C Within Reach. Available online at: https://ec.europa.eu/commission/presscorner/detail/en/statement_21_5766

FAA (2021). FAA Guide to Low-Flying Aircraft. Available online at: https://www.faa.gov/about/office_org/field_offices/fsdo/lgb/local_more/media/FAA_Guide_to_Low-Flying_Aircraft.pdf

Feely, R. A., Sabine, C. L., Lee, K., Berelson, W., Kleypas, J., Fabry, V. J., and Millero, F. J. (2004). Impact of anthropogenic CO_2 on the $CaCO_3$ system in the oceans. *Science*. 305(5682), 362-366. https://doi.org/10.1126/science.1097329

Fellmuth, B., Gaiser, C., and Fischer, J. (2006). Determination of the Boltzmann constant – status and prospects. 17(10), 145-159. *Measurement Science and Technology*. https://doi.org/10.1088/0957-0233/17/10/R01

Feng, E. Y., Koeve, W., Keller, D. P., and Oschlies, A. (2017). Model-Based Assessment of the CO_2 Sequestration Potential of Coastal Ocean Alkalinization. *Earth's Future.* 5(12), 1252-1266. https://doi.org/10.1002/2017EF000659

Forecast International (2003). Boeing MD-11 - Archived 4/2003. Available online at: https://www.forecastinternational.com/index.cfm

Fraser, J. E., and Britt, D. L. (1982). Liming of acidified waters: a review of methods and effects on aquatic ecosystems. Final report. 1st rev. ed. Washington D.C., US: *Fish and Wildlife Service, U.S. Department of the Interior*.

Friedlingstein, P., O'Sullivan, M., Jones, M. W., Andrew, R. M., Hauck, J., Olsen, A., Peters, G. P., Peters, W., Pongratz, J., Sitch, S., Le Quéré, C., Canadell, J. G., Ciais, P., Jackson, R. B., Alin, S., Aragão, L. E. O. C., Arneth, A., Arora, V., Bates, N. R., Becker, M., Benoit-Cattin, A., Bittig, H. C., Bopp, L., Bultan, S., Chandra, N., Chevallier, F., Chini, L. P., Evans, W., Florentie, L., Forster, P. M., Gasser, T., Gehlen, M., Gilfillan, D., Gkritzalis, T., Gregor, L., Gruber, N., Harris, I., Hartung, K., Haverd, V., Houghton, R. A., Ilyina, T., Jain, A. K., Joetzjer, E., Kadono, K., Kato, E., Kitidis, V., Korsbakken, J. I., Landschützer, P., Lefèvre, N., Lenton, A., Lienert, S., Liu, Z., Lombardozzi, D., Marland, G., Metzl, N., Munro, D. R., Nabel, J. E. M. S., Nakaoka, S.-I., Niwa, Y., O'Brien, K., Ono, T., Palmer, P. I., Pierrot, D., Poulter, B., Resplandy, L., Robertson, E., Rödenbeck, C., Schwinger, J., Séférian, R., Skjelvan, I., Smith, A. J. P., Sutton, A. J., Tanhua, T., Tans, P. P., Tian, H., Tilbrook, B., van der Werf, G., Vuichard, N., Walker, A. P., Wanninkhof, R., Watson, A. J., Willis, D., Wiltshire, A. J., Yuan, W., Yue, X., and Zaehle, S. (2020). Global Carbon Budget 2020. *Earth System Science Data*. 12, 3269–3340. https://doi.org/10.5194/essd-12-3269-2020, 2020.

Gale, J. (2004). Geological storage of CO_2: what do we know, where are the gaps and what more needs to be done? *Energy*. 29(9-10), 1329-1338. https://doi.org/10.1016/j.energy.2004.03.068

Gao, K., Gao, G., Wang, Y., and Dupont, S. (2020). Impacts of ocean acidification under multiple stressors on typical organisms and ecological processes. *Marine Life Science & Technology*. 2, 279-291. https://doi.org/10.1007/s42995-020-00048-w

Gao, G., Gao, L., Jiang, M., Jian, A., and He, L. (2022). The potential of seaweed cultivation to achieve carbon neutrality and mitigate deoxygenation and eutrophication. *Environmental Research Letters*. 17(1). https://doi.org/10.1088/1748-9326/ac3fd9

Garcia-Reyes, M., Sydeman, W. J., Schoeman, D. S., Rykaczewski, R. R., Black, B. A., Smit, A. J., and Bograd, S. J. (2015). Under pressure: climate change, upwelling, and eastern boundary upwelling ecosystems. *Frontiers in marine science.* https://doi.org/10.3389/fmars.2015.00109

Gasparini, B., McGraw, Z., Storelvmo, T., and Lohmann, U. (2020). To what extent can cirrus cloud seeding counteract global warming? *Environmental Research Letters*. 15(5). https://doi.org/10.1088/1748-9326/ab71a3

Gloss, S. P., and Schofield, C L. (1989). Liming and Fisheries Management Guidelines for Acidified Lakes in the Adirondack Region. 1st rev. ed. Washington D.C., US: *Fish and Wildlife Service, U.S. Department of the Interior.*

Grant, W. M. (1986). Toxicology of the eye. 3rd rev ed. Springfield, IL: *Charles C. Thomas*.

Graver, B., Rutherford, D., and Zheng, S. (2020). CO_2 Emissions from Commercial Aviation. *ICCT: the International Council on Clean Transportation*. Available online at: https://theicct.org/publications/co2-emissions-commercial-aviation-2020

Hansen, B. W., Hansen, P. J., Nielsen, T. G., and Jepsen, P. M. (2017). Effects of elevated pH on marine copepods in mass cultivation systems: practical implications. 39(6), 984-993. *Journal of Plankton Research.* https://doi.org/10.1093/plankt/fbx032

Hansson, I. (1973). A new set of acidity constants for carbonic acid and boric acid in sea water. *Deep Sea Research and Oceanographic Abstracts.* 20(5), 461-478. https://doi.org/10.1016/0011-7471(73)90100-9

Hasan, Y. M. (2018). High altitude platforms in design wireless communication system for cover the specific area. *Al-Qadisiyah Journal for Engineering Sciences*. https://doi.org/10.30772/qjes.v10i4.490

Hassibi, M. (2009). An overview of lime slaking and factor that affect the process. *Chemco Systems*. Available online at: https://vessco.com/wp-content/uploads/2012/12/lime-slaking-process-hassibi-2009.pdf

Hardy, J. T. (1982). The sea surface microlayer: biology, chemistry and anthropogenic enrichment. *Progress in Oceanography*. 11(4), 307-328. https://doi.org/10.1016/0079-6611(82)90001-5

Harper, E. E. (1934). Lime Slaking. *Journal (American Water Works Association). John Wiley & Sons.* 26(6), 750-756. Available online at: https://www.jstor.org/stable/41226062

Harvey, C. (2018). Corals Are Dissolving Away. *Scientific American.* https://www.scientificamerican.com/article/corals-are-dissolving-away1/#

Harvey, L. D. D. (2008). Mitigating the atmospheric CO_2 increase and ocean acidification by adding limestone powder to upwelling regions. *Journal of Geophysical Research*. 113. https://doi.org/10.1029/2007JC00437

Henderson, G., Rickaby, R., and Bounman, H. (2008). Decreasing atmosphere CO_2 by increasing ocean alkalinity. Available online at: https://www.earth.ox.ac.uk/~gideonh/reports/Cquestrate_report.pdf

Heron, S. F., Maynard, J. A., van Hooidonk, R., and Eakin, C. M. (2016). Warming trend and bleaching stress of the world's coral reefs 1985-2012. *Scientific Reports*. 6(38402). https://doi.org/10.1038/srep38402

HHS (1995). U.S. Department of Health and Human Services. Occupational Safety and Health Guideline for Calcium Carbonate. Available online at: https://www.cdc.gov/niosh/docs/81-123/pdfs/0090.pdf

HHS (1995). U.S. Department of Health and Human Services. Occupational Safety and Health Guideline for Calcium Hydroxide. Available online at: https://www.cdc.gov/niosh/docs/81-123/pdfs/0092.pdf?id=10.26616/NIOSHPUB81123

Hoegh-Guldberg, O., Mumby, P., Hooten, A. J., and Steneck, R. S., (2007). Coral reefs under rapid climate change and ocean acidification. *Science*. 318(5857), 1737-1742. https://doi.org/10.1126/science.1152509

Honnegger, M., Michaelowa, A., and Roy, J. (2020). Potential implications of carbon dioxide removal for the sustainable development goals. *Climate policy*. 21(5), 678-698. https://doi.org/10.1080/14693062.2020.1843388

Hua, J., Cheng, C.-W., and Hwang, D.-S. (2018). Total life cycle emissions of post-Panamax containerships powered by conventional fuel or natural gas. *Journal of the Air & Waste Management Association.* 69(2), 131-144. https://doi.org/10.1080/10962247.2018.1505675

Hughes, T. P., Kerry, J. T., Álvarez-Noriega, M., Álvarez-Romero, J. G., Anderson, K. D., Baird, A. H., Babcock, R. C., Beger, M., Bellwood, D. R., Berkelmans, R., Bridge, T. C., Butler, I. R., Byrne, M., Cantin, N. E., Comeau, S., Connolly, S. R., Cumming, G. S., Dalton, S. J., Diaz-Pulido, G., Eakin, C. M., Figueira, W. F., Gilmour, J. P., Harrison, H. B., Heron, S. F., Hoey, A. S., Hobbs, J.-P. A., Hoogenboom, M. O., Kennedy, E. M., Kuo, C.-Y., Lough, J. M., Lowe, R. J., Liu, G., McCulloch, M. T., Malcolm, H. A., McWilliam, M. J., Pandolfi, J. M., Pears, R. J., Pratchett, M. S., Schoepf, V., Simpson, T., Skirving, W. J., Sommer, B., Torda, G., Wachenfeld, D. R., Willis, B. L., and Wilson, S. K. (2017). Global warming and recurrent mass bleaching of corals. *Nature.* 543, 373-377. https://doi.org/10.1038/nature21707

Hussain, A., and Ingole, B. (2020). Massive coral bleaching in the patchy reef of Grande Island, along the eastern Arabian Sea during 2015/16 global bleaching event. *Regional Studies in Marine Science*. 39, 101410. https://doi.org/10.1016/j.rsma.2020.101410

IADC (2014). International Association of Dredging Companies. Facts About: Trailing Suction Hopper Dredgers. Available online at: https://www.iadc-dredging.com/wp-content/uploads/2016/07/facts-about-trailing-suction-hopper-dredgers.pdf

IATA (2021). International Air Transport Association. Jet fuel price monitor. Available online at: https://www.iata.org/en/publications/economics/fuel-monitor/

ICAO (2017). Environment: Local Air Quality Technology Standards. Available online at: https://www.icao.int/environmental-protection/Pages/LAQ_TechnologyStandards.aspx

ICAO (2019). ICAO Environmental Report 2019, Aviation and Environment. Available online at: https://www.icao.int/environmental-protection/pages/envrep2019.aspx

IMO (2006). 1996 Protocol to the Convention on the Prevention of Marine Pollution by Dumping of Wastes and Other Matter, 1972 (as amended in 2006). Available online at: https://wwwcdn.imo.org/localresources/en/OurWork/Environment/Documents/PROTOCOLAmended2006.pdf

IMO (2021). Convention on the Prevention of Marine Pollution by Dumping of Wastes and Other Matter. Available online at: https://www.imo.org/en/OurWork/Environment/Pages/London-Convention-Protocol.aspx

Indar (2021). Case Study: Mega Hopper Suction Dregger, Cristobal Colòn & Leiv Eiriksson. Available online at: https://www.ingeteam.com/Portals/0/Catalogo/Sector/Documento/SSE_2548_Archivo_sse-2548-archivo-sse-2548-archivo-case-study-cristobal-colon-and-leiv-eiriksson-1.pdf

Infras (2006). COMPETE Final Report: Analysis of operating cost in the EU and the US. Annex 1. Available online at: https://ec.europa.eu/ten/transport/studies/doc/compete/compete_annex_01_en.pdf

IPCC (2001). TAR Climate Change 2001: Synthesis Report. WG I: Technical Summary. Available online at: https://www.ipcc.ch/site/assets/uploads/2018/07/WG1_TAR_TS.pdf

IPCC (2005). Special Report on Carbon Capture and Storage [Bert Metz, Ogunlade Davidson, Heleen de Coninck, Manuela Loos and Leo Meyer (Eds.)]. *Cambridge University Press*. Available online at: https://www.ipcc.ch/report/carbon-dioxide-capture-and-storage/

IPCC (2013). Climate Change 2013: The Physical Science Basis. The Working Group I contribution to the Fifth Assessment Report of the Intergovernmental Panel on Climate Change. Available online at: https://www.ipcc.ch/report/ar5/wg1/

IPCC (2014). Climate Change 2014: Synthesis Report. Contribution of Working Groups I, II and III to the Fifth Assessment Report of the Intergovernmental Panel on Climate Change. Available online at: https://www.ipcc.ch/report/ar5/syr/

IPCC (2018). Global Warming of 1.5°C: Summary for PolicyMakers. Available online at: http://report.ipcc.ch/sr15/pdf/sr15_spm_final.pdf

IPCC (2019). Changing Ocean, Marine Ecosystems, and Dependent Communities. In: IPCC Special Report on the Ocean and Cryosphere in a Changing Climate. Bindoff, N.L., W.W.L. Cheung, J.G. Kairo, J. Arístegui, V.A. Guinder, R. Hallberg, N. Hilmi, N. Jiao, M.S. Karim, L. Levin, S. O'Donoghue, S.R. Purca Cuicapusa, B. Rinkevich, T. Suga, A. Tagliabue, and P. Williamson [H.-O. Pörtner, D.C. Roberts, V. Masson-Delmotte, P. Zhai, M. Tignor, E. Poloczanska, K. Mintenbeck, A. Alegría, M. Nicolai, A. Okem, J. Petzold, B. Rama, N.M. Weyer (eds.)]. Available online at: https://www.ipcc.ch/site/assets/uploads/sites/3/2019/11/09_SROCC_Ch05_FINAL-1.pdf

IPCC (2021). Summary for Policymakers. In: Climate Change 2021: The Physical Science Basis. Contribution of Working Group I to the Sixth Assessment Report of the Intergovernmental Panel on Climate Change [Masson-Delmotte, V., P. Zhai, A. Pirani, S. L. Connors, C. Péan, S. Berger, N. Caud, Y. Chen, L. Goldfarb, M. I. Gomis, M. Huang, K. Leitzell, E. Lonnoy, J.B.R. Matthews, T. K. Maycock, T. Waterfield, O. Yelekçi, R. Yu and B. Zhou (eds.)]. *Cambridge University Press*. Available online at: https://www.ipcc.ch/report/ar6/wg1/

ISPRA (2017). Istituto Superiore per la Protezione e la Ricerca Ambientale. La modellistica matematica nella valutazione degli aspetti fisici legati alla movimentazione dei sedimenti in aree marino-costiere. Available online at: https://www.isprambiente.gov.it/it/pubblicazioni/manuali-e-linee-guida/la-modellistica-matematica-nella-valutazione-degli-aspetti-fisici-legati-alla-movimentazione-dei-sedimenti-in-aree-marino-costiere

ITTC (2011). International Towing Tank Conference. Fresh Water and Seawater Properties. Available online at: https://www.ittc.info/media/7989/75-02-01-03.pdf

Jan De Nul (2021). Trailing Suction Hopper Dredgers. Available online at: https://www.jandenul.com/fleet/trailing-suction-hopper-dredgers

Johannsen, K., and Rademacher, S. (1999). Modelling the Kinetics of Calcium Hydroxide Dissolution in Water. *Acta hydrochimica et hydrobiologica.* 27(2), 72-78. https://doi.org/10.1002/(SICI)1521-401X(199902)27:2<72::AID-AHEH72>3.0.CO;2-H

Jokiel, P. L., and Coles, S. L. (1990). Response of Hawaiian and other Indo-Pacific reef corals to elevated temperature. *Coral Reefs*. 8, 166-162. https://doi.org/10.1007/BF00265006

Jones, M. W., Andrew, R. M., Peters, G. P., Janssen-Maenhout, G., De-Gol, A. J., Ciais, P., Patra, O. K., Chevallier, F. and La Quéré. C. (2021). Gridded fossil CO_2 emissions and related O_2 combustion consistent with national inventories 1959-2018. *Scientific Data*. 8(2). https://doi.org/10.1038/s41597-020-00779-6

Juanes, R., Spiter, E. J., Orr, F. M., and Blunt, M. J. (2006). Impact of relative permeability hysteresis on geological CO_2 storage. *Water Resources Research*. 42(12). https://doi.org/10.1029/2005WR004806

Justus, C. G., and Mikhail, A. (1976). Height variation of wind speed and wind distribution statistics. *Advancing Earth and Space Science*. https://doi.org/10.1029/GL003i005p00261

Justnes, H., Escudero-Oñate, C., Garmo, Ø. A., and Mengede, M. (2020). Transformation Kinetics of Burnt Lime in Freshwater and Sea Water. *Materials.* 13(21), 4926. https://doi.org/10.3390/ma13214926

Kaye, G. W. C., and Laby, T. H. (1995). Tables of Physical and Chemical Constants. 16th rev. ed. Essex, UK: *Longman*

Karnozov, V. (2007). Renewed AN-32 in Flight Tests. *AeroWorldNet.* Available online at: https://web.archive.org/web/20070521113555/http://www.aeroworldnet.com/1ra10160.htm

Kecorius, S., Vogl, T., Paasonen, P., Lampilahti, J., Rothenberg, D., Wex, H., Zeppenfeld, S., van Pinxteren, M., Hartmann, M., Henning, S., Gong, X., Welti, A., Kulmala, M., Stratmann, F., Herrmann, H., and Wiedensohler, A. (2019). New particle formation and its effect on cloud condensation nuclei abundance in the summer Arctic: a case study in the Fram Strait and Barents Sea. *Atmospheric Chemistry and Physics.* 9, 14339–14364. https://doi.org/10.5194/acp-19-14339-2019

Keller, D. P., Feng, E. Y., and Oschilies, A. (2014). Potential climate engineering effectiveness and side effects during a high carbon dioxide-emission scenario. *Nature Communications*. 5(3304). https://doi.org/10.1038/ncomms4304

Kheshgi, H. S. (1995). Sequestering atmospheric carbon dioxide by increasing ocean alkalinity. *Energy*. 20(9), 915-922. https://doi.org/10.1016/0360-5442(95)00035-F

Kittipongvises, S. (2017). Assessment of Environmental Impacts of Limestone Quarrying Operations in Thailand. *Environmental and Climate Technologies*. 20(1), 67-83. https://doi.org/10.1515/rtuect-2017-0011

Klapper, H. (2003). Technologies for lake restoration. *Journal of Limnology.* 62(1), 73-90. https://doi.org/10.4081/jlimnol.2003.s1.73

Knowlton, N., and Cairns, S. (2018). Ocean: Corals and Coral Reefs. *Smithsonian Institution.* Available online at: https://ocean.si.edu/ocean-life/invertebrates/corals-and-coral-reefs

Köhler, P., Hartmann, J., and Wolf-Gladrow, D. A. (2010). Geoengineering potential of artificially enhanced silicate weathering of olivine. *Proceedings of the National Academy of Sciences of the United States of America.* 107(47), 20228-20233. https://doi.org/10.1073/pnas.1000545107

Köhler, P., Abrams, J. F., Völker, C., Hauck, J., and Wolf-Gladrow, D. A. (2013). Geoengineering impact of open ocean dissolution of olivine on atmospheric CO_2, surface ocean pH and marine biology. *Environmental Research Letters*. 8(1). https://doi.org/10.1088/1748-9326/8/1/014009

Kretschmann L., Burmeister, H. C., and Jahn C. (2017). Analyzing the economic benefit of unmanned autonomous ships: An exploratory cost-comparison between an autonomous and a conventional bulk carrier. *Research in Transportation Business & Management*. 25, 76-86. https://doi.org/10.1016/j.rtbm.2017.06.002

Lane, J., Greig, C., and Garnett, A. (2021). Uncertain storage prospects create a conundrum for carbon capture and storage ambitions. *Nature Climate Change*. 11, 925-936. https://doi.org/10.1038/s41558-021-01175-7

Langmuir, D. (1997). Aqueous Environmental Geochemistry. 1st ed. rev. New Jersey, US: *Prentice Hall.*

Lenton, A., Matear, R. J., Keller, D. P., Scott, V., and Vaughan, N. E. (2018). Assessing carbon dioxide removal through global and regional ocean alkalinization under high and low emission pathways. *Earth System Dynamics*. 9, 339-257. https://doi.org/10.5194/esd-9-339-2018

Leyendekkers, J. V. (1979). Prediction of the density and viscosity seawater, its concentrates and other multicomponent solution using the Tamman-Tait-Gibson model. *Desalination*. 29(3), 263–274. https://doi.org/10.1016/S0011-9164(00)82243-2

Lhoist North America (2008). Material Safety Data Sheet, Hydrated Lime. Available online at: https://assets.greenbook.net/M105512.pdf

Lhoist North America (2012). Material Safety Data Sheet, Quicklime. Available online at: https://www.lhoist.com/sites/lhoist/files/lna_msds_quicklime_2012-3.pdf

Li, Y. H., and Gregory, S. (1974). Diffusion of ions in sea water and in deep-sea sediments. *Geochimica et Cosmochimica Acta.* 38(5), 703-714. https://doi.org/10.1016/0016-7037(74)90145-8

Liu, G., Eakin, C. M., Chen, M., Kumar, A., De La Cour, J. L., Heron, S. F., Geiger, E. F., Skirving, W. J., Tirak, K. V., and Strong, A. E. (2018). Predicting heat stress to inform reef management: NOAA coral reef watch's 4-month coral bleaching outlook. *Frontiers in marine science*. https://doi.org/10.3389/fmars.2018.00057

Liu, J., and Shi, X. (2021). Estimating the potential cooling effect of cirrus thinning achieved via the seeding approach. *Atmospheric Chemistry and Physics.* 21(13), 10609–10624. https://doi.org/10.5194/acp-21-10609-2021

Locke, A., G. Doe, K., Fairchild, W., Jackman, P., and Reese, J. (2009). Preliminary evaluation because invasive tunicate management with acetic acid and calcium hydroxide on non-target marine organisms in Prince Edward Island Canada. *Reabic*. 4(1), 221-236. https://doi.org/10.3391/ai.2009.4.1.23

Mackenzie, F. T., and Andersson, A. J. (2013). The Marine Carbon System and Ocean Acidification during Phanerozoic Time. *Geochemical Perspectives*. 2(1), 1-3. https://doi.org/10.7185/geochempersp.2.1

Maoxiao, P., Bo, Y., Xiaojun, L., Donghong, N., Tianyi, L., Zhiguo, D., and Jiale, L. (2018). Effects of Alkalinity and pH on Survival, Growth, and Enzyme Activities in Juveniles of the Razor Clam, Sinonovacula constricta. 9. *Frontiers in Physiology.* https://doi.org/10.3389/fphys.2018.00552

MarineTraffic (2020). Global Ship Tracking Intelligence. Available online at: https://www.ship.com

Marinov, I., Follows, M., Gnanadesikan, A., Sarmiento, J. L., and Slater, R. D. (2008). How does ocean biology affect atmospheric pCO_2? Theory and models. *Journal of Geophysical Research*. 113. https://doi.org/10.1029/2007JC004598

Marshall, P., and Schuttenberg, H. (2006). A Reef Manager's Guide to Coral Bleaching. *Great Barrier Reef Marine Park Authority.* Available online at: https://www.coris.noaa.gov/activities/reef_managers_guide/reef_managers_guide.pdf

MathWorks (2021). MATLAB - Math. Graphics. Programming. . Available online at: https://mathworks.com/products/matlab.html

MathWorks (2021). Simulink – Simulation and Model-Based Design. Available online at: https://mathworks.com/products/simulink.html

McKinley Ocean Carbon Group (2021). Carbon and Climate: Basic information of the major components of the global carbon cycle. Available online at: https://galenmckinley.github.io/CarbonCycle/

McNamara, S., and Young, W. R. (1991). Inelastic collapse and clumping in a one-dimensional granular medium. *Scripps Institution of Oceanography*. https://doi.org/10.1063/1.858323

Meier, A., Gremaud, N., and Steinfeld, A. (2005). Economic evaluation of the industrial production of lime. *Energy Conversion and Management*. 46(6), 905-926. https://doi.org/10.1016/j.enconman.2004.06.005

Michael, K., Golab, A., Shulakova, V., Ennis-King, J., Allinson, G., Sharma, S., and Aiken, T. (2010). Geological storage of CO_2 in saline aquifers - A review of the experience from existing storage operations. *International Journal of Greenhouse Gas Control*. 4(4), 659-667. https://doi.org/10.1016/j.ijggc.2009.12.011

Minchev, A., Schmidt, M., and Schnack, S. (2013). Contemporary Bulk Carrier Design to Meet IMO EEDI Requirements. *Third International Symposium on Marine Propulsor.* Available online at: https://www.marinepropulsors.com/proceedings/2013/6A.3.pdf

Ming, A., Rowell, I., Lewin, S., Rouse, R., Aubry, T., and Boland, E. (2021). Key Messages from the IPCC AR6 Climate Science Report. *Cambridge Open Engage.* https://doi.org/10.33774/coe-2021-fj53b

Minx, J. C., Lamb, W. F., Callaghan, M. W., Fuss, S., Hilaire, J., Creutzig, F., Amann, T., Beringer, T., Oliveira Garcia, W., Hartmann, J., Khanna, T., Lenzi, D., Luderer, G., Nemet, G. F., Rogelj, J., Smith, P., Vicente, J. L., Wilcox, J., and Mar Zamora Dominguez, M. (2018). Negative emissions-

Part 1: Research landscape and synthesis. *Environmental Research Letters*. 13(6). https://doi.org/10.1088/1748-9326/aabf9b

Mongin, M., Baird, M. E., Lenton, A., Neill, C., and Akl, J. (2021). Reversing ocean acidification along the Great Barrier Reef using alkalinity injection. *Environmental Research Letters.* 16(6). https://doi.org/10.1088/1748-9326/ac002d

Monti, R. (1930). La graduale estinzione della vita nel lago d'Orta. 1st rev. ed. Milano, IT: *Hoepli*.

Moorberg, C. J., and Crouse, D. A. (2021). Soils Laboratory Manual: K-State Edition, Version 2.0. 3rd rev. ed. Manhattan, US: *New Prairie Press.*

Moras, C. A., Bach, L. T., Cyronak, T., Joannes-Boyau, R., and Shulz, K. G. (2021). Ocean Alkalinity Enhancement - Avoiding runaway $CaCO_3$ precipitation during quick and hydrated lime dissolution. *Biogeosciences*. https://doi.org/10.5194/bg-2021-330

Morel, F. M. M., and Hering, J. G. (1993). Principles and Applications of Aquatic Chemistry. 1st rev. ed. New York, US: *John Wiley & Sons.*

Morningstar (2021). Available online at: https://www.morningstar.com/

Morrison, B. (2012). Race-to-the-Top: Easy and Gulf Coast Ports Prepare for a Post-Panamax World. *Nicholas School of the Environment and Earth Sciences, Duke University.* Available online at: https://hdl.handle.net/10161/5201

Mountford, H., Waskow, D., Gonzalez, L., Gajjar, C., Cogswell, N., Holt, M., Fransen, T., Bergen, M., and Gerholdt, R. (2021). COP26: Key Outcomes From the UN Climate Talks in Glasgow. *World Resources Institute.* Available online at: https://www.wri.org/insights/cop26-key-outcomes-un-climate-talks-glasgow

Muri, H., Kristajansson, J. E., Storelvmo, T., and Pfeffer, M. A. (2014). The climatic effects of modifying cirrus cloud in a climate engineering framework. *JGR Atmosphere.* 119(4), 4174-4191. https://doi.org/10.1002/2013JD021063

Narula, K. (2019). The maritime dimension of sustainable energy security. *Lecture Notes in Energy*. 9(68), 187-209. https://doi.org/10.1007/978-981-13-1589-3_9

Nave, R. (2002). Surface Tension and Water. *Georgia State University*. Available online at: http://hyperphysics.phy-astr.gsu.edu/hbase/hframe.html

NFPA (2015). Standard for aircraft rescue and fire fighting vehicles. Available online at: https://www.nfpa.org/assets/files/AboutTheCodes/414/414_FDR_A2016.pdf

Nicol, A., Carne, R., Gerstenberger, M., and Christophersen, A. (2011). Induced seismicity and its implications for CO_2 storage risk. *Energy Procedia*. 4, 3699-3706. https://doi.org/10.1016/j.egypro.2011.02.302

NIH (2021). National Institutes of Health. PubChem - Compound summary: Slaked lime. Available online at: https://pubchem.ncbi.nlm.nih.gov/compound/Calcium-hydroxide

Nikulshina, V., Hirsch, D., Mazzotti, M. and Steinfeld A. (2006). CO_2 capture from air and co-production of H_2 via the $Ca(OH)_2$-$CaCO_3$ cycle using concentrated solar power-thermodynamic analysis. *Energy*. 31(12), 1715-1725. https://doi.org/10.1016/j.energy.2005.09.014

NIOSH (1997). National Institute for Occupational Safety & Health. Registry of Toxic Effects of Chemical Substances (RTECS). Available online at: https://www.cdc.gov/niosh/docs/97-119/default.html

NJDHSS (2003). New Jersey Department of Health and Senior Services. Hazardous substance fact sheet: Calcium Oxide. Available online at: https://nj.gov/health/eoh/rtkweb/documents/fs/0325.pdf

NLM (1991). National Library of Medicine. The hazardous substances data bank: calcium carbonate. Available online at: https://www.nlm.nih.gov/toxnet/index.html

NLM (1992). National Library of Medicine. The hazardous substances data bank: calcium hydroxide. Available online at: https://www.nlm.nih.gov/toxnet/index.html

NOAA (2020). National Oceanic and Atmospheric Administration. Ocean and coast: Ocean acidification. Available online at: https://www.noaa.gov/education/resource-collections/ocean-coasts/ocean-acidification

NOAA (2021). National Oceanic and Atmospheric Administration. Global Monitoring Laboratory: Earth System Research Laboratories. GML Data Finder: MLO Monthly Averages. Available online at: https://gml.noaa.gov/dv/data/?site=mlo

NOAA (2021). What are hydrofluorocarbons (HCFs)?. Available online at: https://gml.noaa.gov/hats/about/hfc.html

Nowak, M., Jasinski, R., and Galant, M. (2018). Implementation of the LTO cycle in flight conditions using FNPT II MCC simulator. *IOP Conference Series: Materials Science and Engineering*. 421(4) https://doi.org/10.1088/1757-899X/421/4/042060

Oates, J. A. H. (2008). Lime and Limestone: Chemistry and Technology, Production and Uses. 2nd rev. ed. Hoboken, US: *John Wiley & Sons.*

Ochoa George, P. A., Sagastume Gutiérrez, A., Cogollos Martinez, J. B., and Vandecasteele, C. (2010). Cleaner production in a small lime factory by means of process control. *Journal of Cleaner Production*. 18, 1171-1176. https://doi.org/10.1016/j.jclepro.2010.03.019

Olem, H. (1991). Liming Acidic Surface Waters. 1st rev. ed. Chelsea, US: *Lewis Publishers.*

OpenLCA (2021). OpenLCA databases. Website available online at: https://www.openlca.org/

Panarello, A. (2020). Personal communications, *Interprogetti Srl*. Website available online at: https://www.interprogetti.it/

Paquay, F. S., and Zeebe, R. E. (2013). Assessing possible consequences of ocean liming on ocean pH, atmospheric CO_2 concentration and associated costs. *International Journal of Greenhouse Gas Control*. 17, 183-188. https://doi.org/10.1016/j.ijggc.2013.05.005

Parkhurst, D. L. (1990). Ion-Association Models and Mean Activity Coefficients of Various Salts. *ACS Symposium Series.* 416(3), 30-43. https://doi.org/10.1021/bk-1990-0416.ch003

Parmeggiani, L. (1983). Encyclopedia of occupational health and safety. 3rd rev. ed. Geneva, CH: *International Labour Organization*.

Pinnegard, J., Cheung, W., Beechinh, A., Soma, K., Grilli, F., Margonski, P., Drinkwater, K. F., and Bernal, M. (2012). Climate change and European fisheries: observed changes and future prospects. *European Fisheries and Aquaculture Research Organisations*. Available online at: https://www.efaro.eu/onewebmedia/2011%20Climate%20change%20and%20fisheries.pdf

Peters, G. (2018). Stylised pathways to "well below 2°C". *KLIMA - Et magasin om klimaforskning fra CICERO*. Available online at: https://www.cicero.oslo.no/no/posts/klima/stylised-pathways-to-well-below-2c

Pinsky, M. L., Reygondeau, G., Caddel, R., Palacios-Abrantes, J., Spijkers, J., and Cheung, W. M. L. (2018). Preparing ocean governance for species on the move. *Science*. 360(6394), 1189-1191. htpps://doi.org/10.1126/science.aat2360

Piomelli, U. (1999). Large-eddy simulation: achievements and challenges. *Progress in Aerospace Sciences.* 35(4), 335-362. https://doi.org/10.1016/S0376-0421(98)00014-1

Plummer, N., Jones, B. F., and Truesdell, A. H. (1976). WATEQF; a FORTRAN IV version of WATEQ: a computer program for calculating chemical equilibrium of natural waters. Water-Resources Investigation 76-13. *U. S. Geological Survey.* https://doi.org/10.3133/wri7613

Polo, G. (2012). On maritime transport costs, evolution, and forecast. *Ship Science & Technology.* 5(10), 19-31. https://doi.org/10.25043/19098642.57

Popova, E., Pierax, M. A., and Napalkova, L. (2015). Staff scheduling in ground handling company. Master of Science, A.Y. 2014-2015. *Universitat autonoma de Barcelona*. Available online at: https://www.mathmods.eu/resources/downloads/master-theses/finish/37-master-s-theses/251-elena-popova-thesis

Ramphull, M., and Surroop, D. (2017). Greenhouse gas emission factor for the energy sector in Mauritius. *Journal of Environmental Chemical Engineering*. 5(6), 5996-6000. https://doi.org/10.1016/j.jece.2017.11.027

Renault, L., Hall, A., and McWilliams, J. C. (2016). Orographic shaping of US West Coast wind profiles during the upwelling season. *Climate Dynamics*. 46, 273-289. https://doi.org/10.1007/s00382-015-2583-4

Renforth, P., and Kruger, T. (2013) Coupling Mineral Carbonation and Ocean Liming. *Energy Fuels*. 27(8), 4199-4207. https://doi.org/10.1021/ef302030w

Renforth, P., Jenkins, B. G., and Kruger, T. (2013). Engineering challenges of ocean liming. *Energy*. 60, 442-452. https://doi.org/10.1016/j.energy.2013.08.006

Renforth, P., and Henderson, G. (2017). Assessing ocean alkalinity for carbon sequestration. *Reviews of Geophysics*. 55(3), 636-674. https://doi.org/10.1002/2016RG000533

Riebesell, U., and Gattuso, J.-P. (2015). Lessons learned from ocean acidification research. *Nature Climate Change*. 5(1), 12-14. https://doi.org/10.1038/nclimate2456

Ringrose, P. S., Furre, A., Gilfillan, S. M. V., Krevor, S., Landro, M., Leslie, R., Meckel, T., Nazarian, B., and Zahid, A. (2021). Storage of carbon dioxide in saline acquifers: physicochemical processes, key constraints, and scale-up potential. *Annual Review of Chemical and Biomolecular Engineering*. 12, 471-494. https://doi.org/10.1146/annurev-chembioeng-093020-091447

Rosseland, B. O., and Hindar, A. (1988). Liming of lakes, rivers and catchments in Norway. *Water, Air, and Soil Pollution*. 41(1), 165-188. https://doi.org/ 10.1007/BF00160350

Roy, R. N., Roy, L. N., Vogel, K. M., Porter-More, C., Pearson, T., Good, C. E., Millero, F. K., and Campbell, D. M. (1993). The dissociation constants of carbonic acid in seawater at salinities 5 to 45 and temperature 0 to 45°C. *Marine chemistry*. 44(2-4), 249-267. https://doi.org/10.1016/0304-4203(93)90207-5

Sabine, C. L., and Tanhua, T. (2010). Estimation of Anthropogenic CO_2 Inventories in the Ocean. *Annual Review of Marine Science*. 2, 175-198. https://doi.org/10.1146/annurev-marine-120308-080947

Safe Work Australia (2019). Calcium Hydroxide. Available online at: https://www.safeworkaustralia.gov.au/

Sagastume Gutiérrez, A., Van Caneghem, J., Cogollos Martìnez, J. B., and Vandecasteele, C. (2012). Evaluation of the environmental performance of lime production in Cuba. *Journal of Cleaner Production*. 31, 126-136. https://doi.org/10.1016/j.jclepro.2012.02.035

Şahin, Ö., and Ağayeva, Ç. (2018). An Approach to Estimate Aircraft Fuel Consumption for the Descent Phase. *Celal Bayar University Journal of Science*. 14(4), 379-383. https://doi.org/10.18466/cbayarfbe.405224

Ship & Bunker (2021). World Bunker Prices: VLSFO. Available online at: https://shipandbunker.com/prices

Shu, Z., and Moan, T. (2011). Ultimate hull girder strength of a bulk carrier under combined global and local loads in the hogging and alternate hold loading condition using nonlinear finite element analysis. *Journal of Marine Science and Technology*. 17(1), 94-113. https://doi.org/10.1007/s00773-011-0147-9

Sigma-Aldrich (2014). Material Safety Data Sheet: calcium oxide. Available online at: https://www.nwmissouri.edu/naturalsciences/sds/c/Calcium%20oxide.pdf

Simpson, S. D., Munday, P. L., Wittenrich, M. L., Manassa, R., Dixson, D. L., Gagliano, M., and Yan, H. Y. (2011). Ocean acidification erodes crucial auditory behaviour in a marine fish. *Biology Letters*. 7(6), 917-920. https://doi.org/10.1098/rsbl.2011.0293

Smith, P., Davis, S., Creutzig, F., Fuss, S., Minix, J., Gabrielle, B., Kato, E., Jackson, R. B., Cowie, A., Kriegler, E., van Vuuren, D. P., Rogelj, J., Ciais, P., Milne, J., Canadell, J. G., McCollum, D., Peters, G., Andrew, R., Krey, V., Shrestha, G., Friedlingstein, P., Gasser, T., Grübler, A., Heidug, W., K.,

Jonas, M., Jones, C. D., Kraxner, F., Littleton, E., Lowe, J., Moreira, J., R., Nakicenovic, N., Obersteiner, M., Patwardhan, A., Rogner, M., Rubin, E., Sharifi, A., Torvanger, A, Yamagata, Y., Edmonds, J., and Youngsung, C. (2016). Biophysical and economic limits to negative CO_2 emissions. *Nature Climate Change*. 6, 42–50. https://doi.org/10.1038/nclimate2870

Stoffel, B. (2015). Assessing the Energy Efficiency of Pumps and Pump Units. 1st rev. ed. Oxford, UK: *Elsevier*

Storni, N., Caserini, S., and Grosso, M. (2021). The availability of limestone and other raw materials for ocean alkalinity enhancement. Under review on *Chief Global Biogeochemical Cycles*.

Strogen, D. P., Arnot, M. J., Bland, K. J., and Griffin, A. G. (2009). Opportunities for underground geological storage of CO2 in New Zealand – Report CCS- 08/7 – Onshore Taranaki Neogene reservoirs. *GNS Science Report*. 104p. Available online at: https://www.researchgate.net/profile/Kj-Bland/publication/268435094_Opportunities_for_underground_geological_storage_of_CO2_in_New_Zealand_-Report_CCS_-087_-Onshore_Taranaki_Neogene_reservoirs/links/5509cf430cf20f127f90ad4a/Opportunities-for-underground-geological-storage-of-CO2-in-New-Zealand-Report-CCS-08-7-Onshore-Taranaki-Neogene-reservoirs.pdf

Stuart Pumps LTD (2021). Used Dredging / Quarry Pumps. Available online at: https://www.stuartgroup.ltd.uk/pumps/dredger.php

Takahashi, T., Sutherland, S. C., Wanninkhof, R., Sweeney, C., Feely, R. A., Chipman, D. W., Hales, B., Friederich, G., Chavez, F., Sabine, C., Watson, A., Bakker, D. C. E., Schuster, U., Metzl, N., Yoshikawa-Inoue, H., Ishii, M., Midorikawa, T., Nojiri, Y., Kortzinger, A., Seinhoff, T., Hoppema, M., Olafsson, J., Arnarson, T. S., Tilbrook, B., Johannessen, T., Olsen, A., Bellerby, R., Wong, C. S., Delille, B., Bates, N. R., and de Baar, H. J. W. (2009). Climatological mean and decadal change in surface ocean pCO_2, and net sea-air CO_2 flux over the global oceans. *Deep-Sea Research Part II: Topical Studies in Oceanography*. 56(8-10), 554-577. https://doi.org/10.1016/j.dsr2.2008.12.009

Tannenberger, M., and Klein, H. (2009). Settling and Dissolution of Calcium Hydroxide Particles. *Technischen Universität München: Lehrstuhl für Anlagen- und Prozesstechnik.*

Taylor, R., Sims, M., Burns, D., and Lyons, K. (2021). What COP26 Means for Forests and the Climate. *World Resources Institute.* Available online at: https://www.wri.org/insights/what-cop26-means-forests-climate

Truesdell, A. H., and Jones, B. F. (1974). WATEQ, a Computer Program for Calculating Chemical Equilibria of Natural Waters. *Journal of Research of the U.S. Geological Survey*. 2(2), 233-248. Available online at: https://pubs.usgs.gov/journal/1974/vol2issue2/report.pdf#page=105

Turgut, E. T., and Rosen, M. A. (2011). Relationship between fuel consumption and altitude for commercial aircraft during descent: preliminary assessment with a generic algorithm. *Aerospace Science and Technology*. 17(1), 65-73. https://doi.org/10.1016/j.ast.2011.03.007

UN (1987). United Nations. Treaty Collections: a Montreal Protocol on Substances that Deplete the Ozone Layer. Available online at: https://treaties.un.org/Pages/ViewDetails.aspx?src=TREATY&mtdsg_no=XXVII-2-a&chapter=27&clang=_en

UNFCCC (2015). Adoption of the Paris Agreement. Available online at: https://unfccc.int/resource/docs/2015/cop21/eng/l09r01.pdf

UNFCCC (2021). Glasgow Climate Pact. Available online at: https://unfccc.int/sites/default/files/resource/cma2021_L16_adv.pdf

UNFCCC (2021). Glasgow Leaders' Declaration on Forests and Land Use. Available online at: https://ukcop26.org/glasgow-leaders-declaration-on-forests-and-land-use/

UNFCCC (2021). Nationally determined contributions under the Paris Agreement: Synthesis report by the secretariat. Available online at: https://unfccc.int/sites/default/files/resource/cma2021_08E.pdf

Unicalce (2021). Rapporto di prova calce idrata fiore 29/4/2021. Personal communication. Unicalce s.p.a., Sedrina (BG), Italy. Website available online at: https://www.unicalce.it/

USGS (1988). United States Geological Survey. USGS yearbook, fiscal year 1988. *United States Government Printing Office*. https://doi.org/10.3133/70046669

USGS (2021). United States Geological Survey. Overview of PHREEQC Version 3. Available online at: https://www.usgs.gov/software/phreeqc-version-3

Vasileiou, V. (2018). Weekly Market Report n.12. *Intermodal Research & Valuations.* Available online at: https://www.investinthefuture.gr/files/data/blog/Intermodal%20Report%20Week%2012%202018.pdf

Vreman, B., Geurts, B., and Kuerten, H. (1995). Subgrid-modelling in LES of compressible flow. *Applied Scientific Research.* 54, 191-203. https://doi.org/10.1007/BF00849116

Wang, F., Yin, J., Zhang, Q., Wang, L., and Han, Z. (2018). A method for calculating the trajectory and extension of a bow-spray for the TSHD. Hydraulic Engineering V: Proceeding of the 5th International Technical Conference on Hydraulic Engineering. 5th rev. ed. Shanghai, CN: *CRC Press.*

Watson, A. J., Schuster, U., Shutler, J. D., Holding, T., Ashton, I. G. C., Landschützer, P., Woolf, D. K., and Goddijn-Murphy, L. (2021). Revised estimates of ocean-atmosphere CO_2 flux are consistent with ocean carbon inventory. *Nature Communications*. 11, 4422. https://doi.org/10.1038/s41467-020-18203-3

Weast, R. C., Lide, D. R., Astle, M. J. K., and Beyer, W. H. (1989). Handbook of Chemistry and Physics. 70th rev. ed. Boca Ratòn, US: *CRC Press*

Webb, P. (2019). Introduction to Oceanography. *Rebus Community.* Available online at: https://geo.libretexts.org/Bookshelves/Oceanography/Book%3A_Introduction_to_Oceanography_(Webb)

West, A. J., Torres, M. A., and Clark, K. E. (2015). Geomorphic regime modulates hydrologic control of chemical weathering in the Andes-Amazon. *Geochimica et Cosmochimica Acta*. 166, 105-128. https://doi.org/10.1016/j.gca.2015.06.007

Whitney, J. L., Gove, J. M., McManus, M. A., Smith, K. A., Lecky, J., Neubauer, P., Phipps, J. E., Contreras, E. A., Kobayashi, D. R., and Asner, G. P. (2021) Surface slicks are pelagic nurseries for diverse ocean fauna. *Nature Communications*. 11, 3197. https://doi.org/10.1038/s41598-021-81407-0

Wolf-Gladrow, D. A., Zeebe, R. E., Klaas, C., Körtzinger, A., and Dickson, A. G. (2007). Total alkalinity: The explicit conservative expression and its application to biogeochemical processes. *Marine Chemistry.* 106, 287-300. https://doi.org/10.1016/j.marchem.2007.01.006

World Bank (2007). World Bank Group: Air Transport, Fiscal Year 2007 Annual Report. Available online at: https://documents.worldbank.org/en/publication/documents-reports/documentdetail/967021468313773774/the-world-bank-air-transport-fiscal-year-2007-annual-report

WHO (2015). WHO calls for urgent action to protect health from climate change – Sign the call. Available online at: https://web.archive.org/web/20210103002854/https://www.who.int/globalchange/global-campaign/cop21/en/

WHO (2017). Internationally Peer Reviewed Chemical Safety Information. Calcium Oxide information. Available online at: http://www.inchem.org/documents/icsc/icsc/eics0409.htm

Wurl, O., and Obbard, J. P. (2004). A review of pollutants in the sea-surface microlayer (SML): a unique habitat for marine organisms. *Marine Pollution Bulletin*. 48(11-12), 1016-1030. https://doi.org/10.1016/j.marpolbul.2004.03.016

Wurl, O., Ekau, W., Landing, W. M., and Zappa, C. J. (2017). Sea surface microlayer in a changing ocean - A perspective. *Elementa: Science of the Anthropocene*. 5(31). https://doi.org/10.1525/elementa.228

Xin, X., Zhang, L., Zhang, L., Fang, Y., and Wu, T. (2013). Climate change projections over East Asia with BCC_CSM1.1 climate model under RCP scenarios. *Journal of the Meteorological Society of Japan Ser II*. 91(4), 413-429. https://doi.org/10.2151/jmsj.2013-401

Zhang, M., Huang, Q., Liu, S., and Zhang, Y. (2019). Fuel Consumption Model of the Climbing Phase of Departure Aircraft Based on Flight Data Analysis. *Multidisciplinary Digital Publishing Institute*. 11, 4362. https://doi.org/10.3390/su11164362

Zeebe, R. E., Wolf-Gladrow, D. A., and Jansen, H. (1999). On the time required to establish chemical and isotopic equilibrium in the carbon dioxide system in seawater. *Marine Chemistry*. 65, 135-153. https://doi.org/10.1016/S0304-4203(98)00092-9

Zeebe, R. E., and Wolf-Gladrow, D. A. (2003). CO_2 in seawater: equilibrium, kinetics, isotopes. 2nd rev. ed. Amsterdam, NL: *Elsevier Oceanography Series*.